Proton ordering and reactivity of ice

Zamaan Raza
Department of Chemistry
University College London

Thesis submitted for the degree of Doctor of Philosophy

September 2012

I, Zamaan Raza, confirm that the work presented in this thesis is my own. Where information has been derived from other sources, I confirm that this has been indicated in the thesis.

For Chryselle, without whom I would never have made it this far.

I would like to thank my supervisors, Dr Ben Slater and Prof Angelos Michaelides for their patient guidance and help, particularly in light of the fact that I was woefully unprepared when I started.

I would also like to express my gratitude to Dr Florian Schiffmann for his indispensable advice on CP2K and quantum chemistry, Dr Alexei Sokol for various discussions on quantum mechanics, Dr Dario Alfé for his incredibly expensive DMC calculations, Drs Jiri Klimeš and Erlend Davidson for advice on VASP, Matt Watkins for help with CP2K, Christoph Salzmann for discussions on ice, Dr Stefan Bromley for allowing me to work with him in Barcelona and Drs Aron Walsh, Stephen Shevlin, Matthew Farrow and David Scanlon for general help, advice and tolerance. Thanks and also apologies to Stephen Cox, with whom I have collaborated, but have been unable to contribute as much as I should have.

Doing a PhD is an isolating experience (more so in the Kathleen Lonsdale building), so I would like to thank my fellow students and friends for making it tolerable: Richard, Tiffany, and Chryselle.

Finally, I would like to acknowledge UCL for my funding via a DTA and computing time on Legion, the Materials Chemistry Consortium (MCC) for computing time on HECToR and HPC-Europa2 for the opportunity to work in Barcelona.

Abstract

Cubic ice Ic is a rarely-observed ambient pressure phase of water implicated in the catalysis of atmospheric reactions. It forms between 160 K [1] and 243 K [2], in droplets smaller than 5 μm [3] in diameter. It is metastable with respect to hexagonal ice Ih and is poorly characterised both experimentally and theoretically. The proton ordered ground state for cubic ice has $I4_1md$ symmetry and is named ice XIc [4]. We find that the ground state proton ordered configurations of hexagonal and cubic ice, XI and XIc are isoenergetic.

The surface energy of ice is strongly dependent on proton ordering. The "striped" configuration [5] has the lowest surface energy, and clustering of dangling OH bonds increases the surface energy. Cubic ice is has a surface energy approximately 10% higher than hexagonal, and is more reactive. Elementary steps on the ice surface reconstruct to lower the step formation energy; under-coordinated molecules on the step edge relax to form an additional hydrogen bond with the lower terrace. We examine five different steps: the low energy A-and B_1-steps and the high energy B_1^*-, B_2 and B_2^*-steps. Different growth rates for these steps combined with a proton disorder are in part responsible for the isotropic bilayer growth of ice observed by Sazaki *et al* [6].

Glycolaldehyde, the simplest sugar, has been observed recently in the interstellar medium [7;8] and in a solar-type protostar [9]. We evaluate two potential mechanisms for its formation on icy dust grains at 10 K, finding that activation barriers are greatly reduced by the ice surface, and that the most likely route is a reaction between H_2COH and HCO radicals, which are formed by the sequential hydrogenation of carbon monoxide.

Contents

List of Figures

Nomenclature

ASW Amorphous Solid Water

BLYP Becke-Lee-Yang-Parr exchange-correlation functional

BSSE Basis Set Superposition Error

CCSD Coupled Cluster Singles and Doubles

CCSD(T) Coupled Cluster Singles, Doubles and perturbative Triples

CCSDT Coupled Cluster Singles, Doubles and Triples

CI Configuration Interaction

CISD Configuration Interaction Singles and Doubles

CRP Cosmic Ray Particle

DFT Density Functional Theory

DMC Diffusion Monte Carlo

GGA Generalised Gradient Approximation

GTH Goedecker-Teter-Hutter pseudopotentials/basis sets

HF Hartree-Fock Theory

Ic/ice Ic Proton disordered cubic ice

Ih/ice Ih Proton disordered hexagonal ice

ISM Interstellar Medium

MO Molecular Orbital

MP*n* *n*th order Møller-Plesset method

NE6 Nada-van der Eerden six-site potential

NEB Nudged Elastic Band

PAW Projector Augmented Wave pseudopotential method

PBE Perdew-Burke-Ernzerhof exchange-correlation functional

PSC Polar Stratospheric Clouds

QMC Quantum Monte Carlo

SCF Self-Consistent Field method

SPC Simple Point Charge 3-site empirical potential for water

TIP*n*P *n*-site Transferable Interatomic Potential for water

UHF Unrestricted Hartree-Fock

vdW-DF van der Waals Density Functional

XIc/ice XIc Proton ordered ice Ic

XIh/ice XIh Synonym for ice XI, proton ordered ice Ih

Chapter 1

Introduction

1.1 Why study ice?

In spite of its ubiquity, water is a contentious area of research; for example, in 2009, Huang *et al.* asserted that liquid water is inhomogeneous, and consists of 'tetrahedral patches surrounded by thermally excited H-bond distorted structures'[20;21] — a view directly contended by Soper *et al*[22]., who suggest that 'each molecule is typically hydrogen bonded to four others, with rarely more than one additional nonbonded molecule in the first coordination shell'. The simple chemical formula H_2O belies its extensive range of anomalous physical properties (listed in extensive detail on Martin Chaplin's website[23]), including the unusual temperature dependences of its density and phase, its wide range of stable and metastable amorphous and crystalline solid structures and its high viscosity and surface tension. Most of these properties can be generally explained by the ability of each water molecule to form four relatively strong hydrogen bonds, although an accurate theoretical model of water remains elusive; for this reason, the question 'what is the structure of water' was one of the top 125 unanswered questions in the 125th anniversary edition of *Science*[24].

Hexagonal ice is the solid phase of water that is most commonly encountered on Earth and has been extremely well studied, yet new and unusual properties continue to

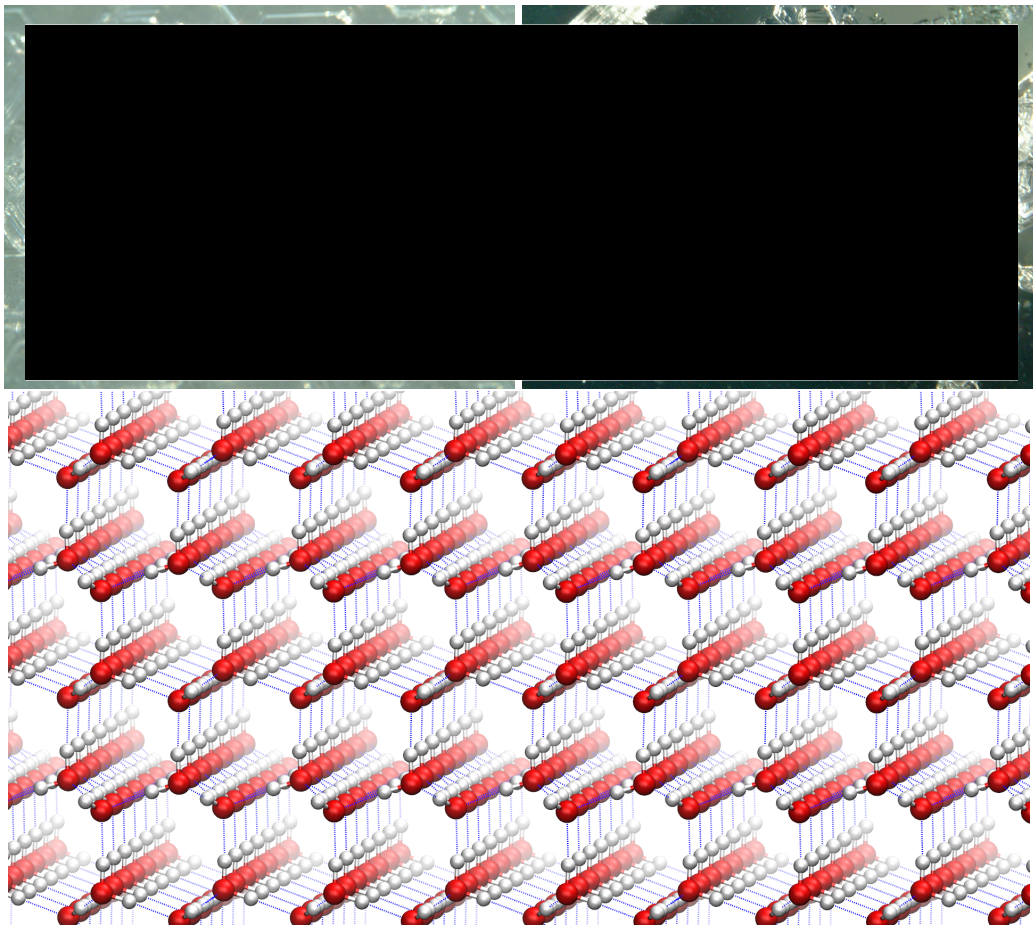

Figure 1.1: Photographs of hexagonal ice Ih crystals[10], and the crystalline structure of orientationally ordered hexagonal ice.

be discovered. For example, it has been recently shown that ice nucleates differently at positively and negatively charged surfaces of pyroelectric materials[25] (materials which become polarised upon temperature change), and that the surface of crystalline ice displays a continuum of vacancy energies[26].

A crystalline ice lattice consists of water molecules bound together by hydrogen bonds; in a crystal free of defects, all water molecules are four-coordinated, donating two hydrogen bonds and accepting two. The ambient pressure ice I polytypes (including the ubiquitous hexagonal ice Ih and cubic ice Ic) discussed in this thesis are comprised of tetrahedrally coordinated water molecules with a HOH bond angle close to 109.5° and hydrogen bonds which are approximately straight and form six-rings.

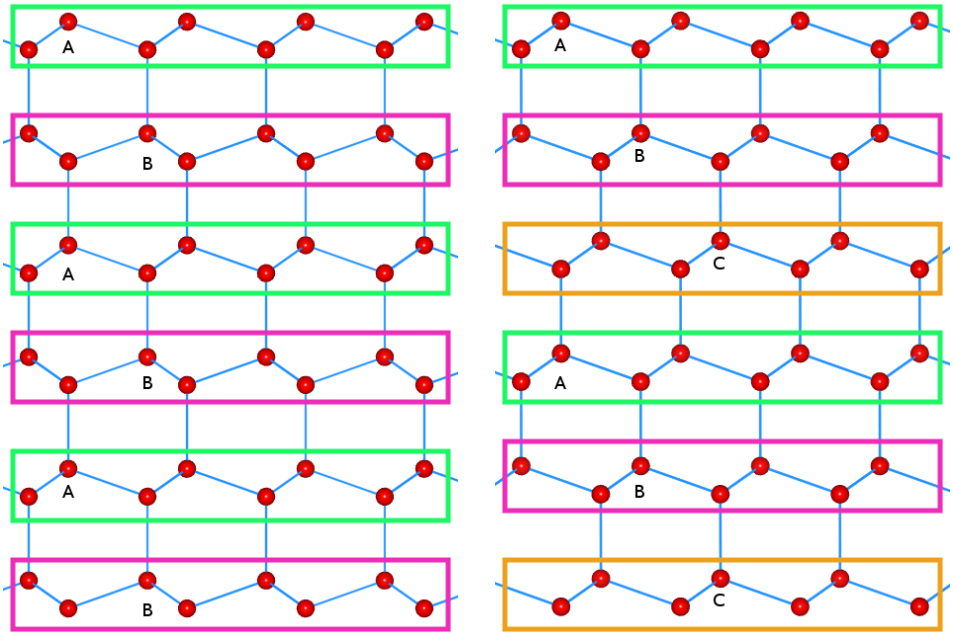

(a) Hexagonal ice (b) Cubic ice

Figure 1.2: Stacking of bilayers in hexagonal and cubic ices. The vertical is normal to the (0001) basal surface of hexagonal ice, and the (111) surface of cubic ice. Only oxygen atoms are shown, connected by hydrogen bonds indicated by blue lines. The coloured boxes indicate the sequences that have translational symmetry in the z-direction (green: A, pink: B, orange: C). It can be seen that hexagonal ice is characterised by a mirror plane, whereas cubic ice contains straight "channels" that run diagonally from this perspective.

There are currently 15 known phases of ice, with ice XV being discovered as recently as 2009[27]. Of the two low pressure proton disordered polytypes, ices Ih (hexagonal) and Ic (cubic) , only hexagonal ice has been studied extensively. Cubic ice — which is studied in this thesis — is metastable (hence the absence of a solid line in the phase diagram, figure 1.3), and has not been synthesised in pure form in the laboratory. These two polytypes differ only in the stacking order of the hexagonal bilayers (figure 1.2).

Experiments have revealed that ice nucleates homogeneously as cubic ice in small droplets with radii in the range 5 nm[28;29] to 5 μm[2] and in confined pores[3] at temperatures between 160 K[1] and 243 K[2]. Whilst it was previously thought that Ic transforms to Ih at temperatures above ∼180 K–200 K, recent studies indicate that Ic remains stable for hours at 228 K with complex time and temperature dependences[2]. There is no well

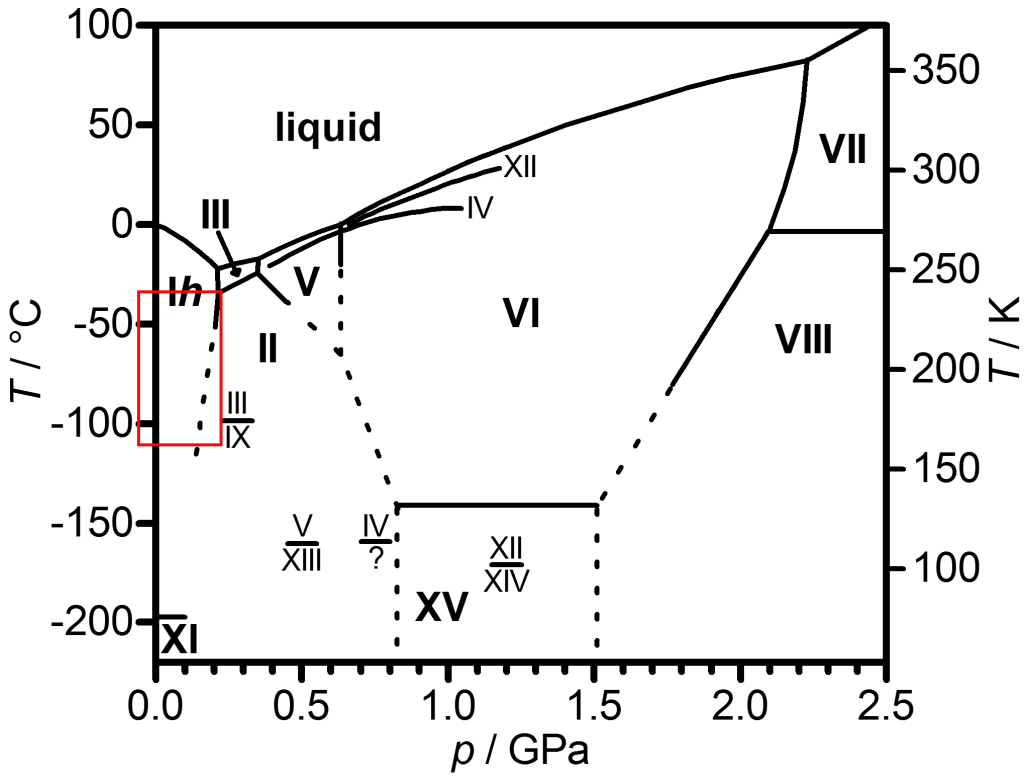

Figure 1.3: The phase diagram of water[11]. There is considerable uncertainty in the temperature bounds of the regime of interest for ice Ic, highlighted with a red box.

defined phase transition. The cohesive energy difference between ices Ic and Ih is tiny by chemical standards. Attempts have been made to measure the heat of transition from ice Ic to ice Ih ($\Delta H_{c\to h}$), with estimates ranging from $-160\,\mathrm{J\,mol^{-1}}$ to $-13\,\mathrm{J\,mol^{-1}}$[30–37]. Murray *et al.* suggest that this is because cubic ice invariably contains some hexagonal sequences, and the cubic sequences anneal to hexagonal ones over a wide range of temperatures such that there is no distinct cubic-hexagonal phase transition — for this reason, there is some debate as to whether cubic ice is actually a distinct phase of water: it could be more accurate to describe it as hexagonal ice with cubic stacking faults. As a result, calorimetric techniques tend to underestimate $\Delta H_{c\to h}$[38], and they suggest that the true value is likely to lie closer to $-155\,\mathrm{J\,mol^{-1}}$, from the 2006 study by Shilling *et al.*[36].

The structural and energetic differences between cubic and hexagonal ice are subtle

but the chemical reactivity of these two phases are distinct and could profoundly effect atmospheric chemistry on Earth. Given the temperature regime and droplet sizes required for cubic ice formation, it seems likely that cubic ice nucleates preferentially in the Earth's upper atmosphere[39], with a significant impact on processes such as cloud formation and ozone depletion as a result of differences in surface chemistry between hexagonal and cubic ices[40–43]. It has also be suggested that cubic ice could be used in cryopreservation of cells, since octahedral Ic crystals are benign, in contrast with the destructive needle-like crystals that can be formed by hexagonal ice[44].

It has been shown experimentally and using quantum chemistry, that a proton ordered (i.e. orientationally ordered) form of hexagonal ice can exist at temperatures below 72 K, even though differences between the cohesive energies of proton ordered configurations are small (up to $\sim$1 kJ mol^{-1})[12]. However, there is no known analogous proton ordered phase of cubic ice. Quantum chemical simulations have shown that proton ordering affects surface energies by an order of magnitude more than it effects bulk energies[5], which is particularly relevant since surface effects will be dominant in the size regime of ice nucleation.

There are very few computational studies (particularly quantum mechanical) of cubic ice in the literature, and given (i) the absence of conclusive experimental data, and (ii) the difficulty in preparing pure samples of cubic ice, modelling offers a route to a better understanding of its structure and chemistry.

In this thesis, three different aspects of the chemistry of ice are examined. First, a characterisation of bulk cubic ice is undertaken, comparing it with the ubiquitous hexagonal ice. In particular, the effect of orientational (proton) ordering will be investigated, and the ground state configuration determined. Next, the effect of proton ordering on both pristine ice surfaces and surfaces with step defects is discussed. Finally, the developed surface models are employed to simulate the reactions which form interstellar glycolaldehyde.

Chapter 2

A review of water ice

2.1 The crystalline structure of ice

There are currently 15 known crystalline structures of ice[23;45], which are identified by the roman numerals I – XV; this does not include a number of amorphous phases including high density and low density amorphous ices. The high pressure phases of ice, which form in excess of 100 MPa, will not be discussed in any detail here, since the main thrust of this study is the simplest ambient pressure polytypes, ices Ih (hexagonal) and Ic (cubic) and their proton ordered variants. Ice XI is the most stable proton ordered form ice Ih, and is formed when KOH-doped ice Ih is cooled to 72 K[46]. Proton ordering is discussed in more detail in chapter 4. Examples of high pressure phases include Ice VII, which consists of two interpenetrating Ic lattices and its stable orientationally-ordered analogue ice VIII, and ice X which is a non-molecular form of the tetrahedral ice lattice with protons equidistant from adjacent pairs of oxygen atoms. These phases all contain approximately straight hydrogen bonds and six-membered rings; this is not necessarily the case for other high pressure phases, which contain four-, five-, seven- and eight-membered rings and bent hydrogen bonds. In the most unusual high pressure phase, ice X, molecular units of H_2O can no longer be discerned — it consists of hydrogen atoms at the midpoint between pairs of oxygen atoms.

Note that to date, no pure proton ordered ices have been formed in laboratory conditions[45], with the exceptions of ice VIII, which can be formed by cooling ice VII[23] and ice II, which has no proton disordered form; they have only been synthesised in the presence of a dopant. There is currently no known proton ordered phase of ice Ic.

Bjerrum made one of the first attempts to deduce the properties of ice from a simple electrostatic model of the H_2O molecule[47]. The oxygen atoms in a hexagonal ice crystal form a tetrahedral structure as a result of the four-coordination of water molecules; each donates and accepts two hydrogen bonds. The resulting structure is a puckered hexagonal layering of oxygen atoms. The stacking order of these layers determines whether the ice has a hexagonal structure (ABAB stacking), or a cubic structure (ABCABC stacking, reminiscent of diamond), as shown in figure 1.2. Ice Ih therefore consists of sheets of hexamers in the chair and boat configurations, whereas Ic contains only the chair configuration; the higher symmetry of cubic ice made it popular for modelling applications in the past[46]. Despite the structural similarities, Ic is metastable with respect to Ih. Hexagonal ice is the familiar structure of ice generally seen in terrestrial conditions, while cubic ice has been shown to nucleate homogeneously at low temperatures and in small droplets[2], yet the difference in energy between cubic and hexagonal is small; experimental estimates of its value vary between $-160\,\mathrm{J\,mol^{-1}}$ and $-13\,\mathrm{J\,mol^{-1}}$[30–37]. Like the energies, the structures are very subtly different; the difference in cohesive energy may be due to the fact that cubic ice has twelve molecules in the second coordination sphere, compared with thirteen for hexagonal ice.

To answer the question of why hexagonal ice forms preferentially to cubic ice, Bjerrum characterised hydrogen bonds as strong or weak, depending on the geometry of the water "dimer" constituting the bond. He identified 6 possible dimer configurations. Taking symmetry into account, there are four unique hydrogen bond configurations (figure 2.1), which I will refer to as they are more commonly and concisely known in the literature[12;47]: c-trans (inverse mirror symmetric), h-cis (oblique mirror symmetric),

c-cis (inverse centre symmetric) and h-trans (oblique centre symmetric).

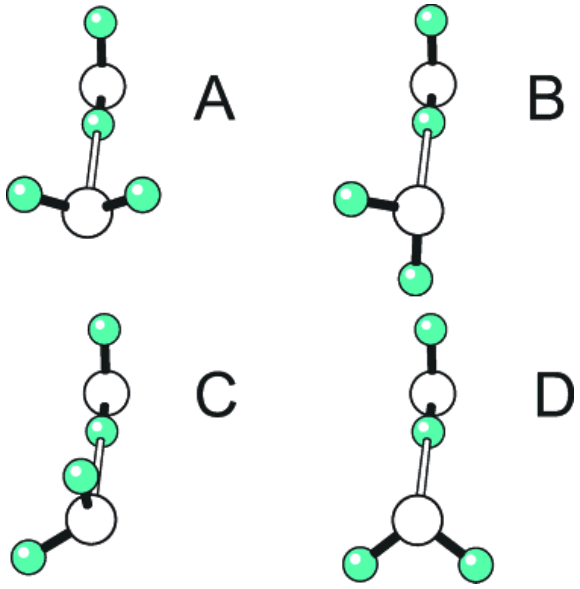

Figure 2.1: (Taken from Hirsch *et al.* [12]) Hydrogen bond types in a tetrahedral ice lattice - h-cis (A), h-trans (B), c-cis (C) c-trans (D).

Bjerrum suggested, not unreasonably, that the trans hydrogen bond configurations would be more energetically favourable, since the distance between repulsive centres is maximised - indeed, his calculations from experimental data indicated that mirror-symmetric bonds are 0.5% shorter than centre-symmetric bonds, and electrostatic calculations showed that 100% centre-symmetric ice is less stable than 25% mirror symmetric; evidence, perhaps that proton ordering does play a role in the formation of ice crystals. If this theory of strong and weak hydrogen bonds was robust, we would expect the relative number of strong (trans-) hydrogen bonds to increase as the temperature decreases, i.e. the most stable proton-ordered structures should have the largest fraction of trans hydrogen bonds. Bjerrum's hypothesis resulted in the prediction of the $Pna2_1$ (figure 2.5b) structure as the lowest energy proton ordered configuration of hexagonal ice. It has since been shown using quantum mechanical calculations that this is incorrect [12], although calculations using classical potentials tend to favour the $Pna2_1$ structure (see, for example, Buch *et al.* [48]). Bjerrum's classification scheme may still be

important; Hirsch and Ojamäe[12] have suggested that the energy of a cell may be related to a linear combination of the hydrogen bond types rather than a simple fraction of bonds with the trans- configurations.

2.2 Cubic ice

2.2.1 Structure: a stacking disordered phase?

Whilst pure hexagonal ice has been isolated within instrumental resolution, pure cubic ice still eludes experimental synthesis; Murray and Bertram[2] have prepared cubic ice that is ∼80% pure, although the coherence of the cubic sequences was not reported. A common trend in the literature regarding laboratory preparation is the assumption of cubic ice formation on the basis of the temperature and pressure regime, rather than spectroscopic analysis. Recently, Malkin *et al*. used X-ray diffraction on ice crystallized from supercooled water droplets suspended in an oil emulsion at temperatures under 232 K[49]. Instead of cubic ice, they observed a stacking disordered phase they named ice I_{sd} with approximately the same proportion of cubic and hexagonal sequences, randomly arranged. These observations were strongly supported by Monte Carlo simulations using the TIP4P model. Earlier molecular dynamics simulations by Moore and Molinero using the mW model (a monatomic water model that mimics hydrogen bonds using a short range anisotropic potential) also predict a stacking disordered phase, albeit with a 2:1 ratio of cubic to hexagonal sequences[50].

2.2.2 Phase transition to hexagonal ice

There is no sharp temperature-dependent phase transition between hexagonal and cubic ice; Ic gradually and irreversibly anneals to Ih as it is heated over approximately −200 K–−180 K, although it has been recently shown to persist for several hours at 228 K. They have almost identical densities, and extremely similar binding energies, with a heat of

transition ($\Delta H_{c\rightarrow h}$) in the range $-160\,\mathrm{J\,mol^{-1}}$ to $-13\,\mathrm{J\,mol^{-1}}$ [30–37]. Yamamuro *et al.*[30] suggested that measurements on the high end of the range had overestimated the energy difference by forming ice Ic from amorphous ice, which resulted in small particles and an exaggerated surface effect; they cite a figure of $37\,\mathrm{J\,mol^{-1}}$ using cubic ice formed from the sequence of transitions III → IX → Ic. Murray *et al.* suggest that the energy difference has been grossly underestimated since pure cubic ice has not been synthesized, and necessarily contains hexagonal sequences[38], and support the value cited by Shilling *et al.*[36], $155\,\mathrm{J\,mol^{-1}}$. Indeed, Kuhs *et al.*[51] assert that the stacking faults are an inherent property of ice Ic; it could be claimed that cubic ice is not a unique phase, but merely hexagonal ice containing a high proportion of cubic stacking faults. On the other hand, it has been proposed that the broad phase transition is a result of the defect energy at interphase grain boundaries when hexagonal crystals grow in bulk cubic ice[52]. Salzmann *et al.* suggest that increasing numbers of hexagonal sequences in cubic ice seem to correlate with a less exothermic transition[53]. The lower free energy of Ih is attributed to an extra water molecule in the second coordination sphere of Ih in comparison to Ic[23]; radial distribution functions confirm that hexagonal stacking gives rise to 13 molecules inside the second coordination sphere, compared with 12 molecules for cubic stacking, resulting from the lack of a mirror plane.

2.2.3 Cubic ice in nature

Although cubic ice is metastable and forms at low temperatures, its effects were first observed as early as 1629 by Christophe Scheiner[54]. Haloes are visible around the sun and moon around 100 times a year; these usually appear at an angle of 22° (figure 2.2) and are a result of light refracted by large quantities of randomly oriented ice Ih crystals in the form of hexagonal prisms. Scheiner's halo was at an angle of 28° and was most probably caused by light refracted by octahedral crystals of ice Ic. The fact that there were only three subsequent sightings of Scheiner's halo in the following 250 years in-

Figure 2.2: A 22° halo around the sun[13]. These are caused by light refracted by large quantities of hexagonal ice crystals in the upper atmosphere. Scheiner's halo appears at 28°, has been observed very infrequently and is evidence of octahedral cubic ice crystals.

dicate just how rare it is. Whalley[54] suggests that the halo will only result from large numbers of octahedral crystals that are small enough to be fully randomly oriented by Brownian motion; larger crystals that are not completely randomly oriented may result in partial haloes. Scheiner's halo was recently observed in Northern Chile in 2000[55]. The formation of dendritic or polycrystalline snow flakes with their c-axes at 70° to one another is further evidence of the influence of cubic ice in nature. Studies[56;57] suggest that this is a result of the growth of ice Ih on an octahedral ice Ic nucleus.

It is thought that cubic ice is influential in processes occurring in the earth's atmosphere, particularly in ice cirrus clouds (from aqueous ammonia and sulphuric acid droplets), and in polar stratospheric clouds (from aqueous nitric and sulphuric acid droplets), which play a key role in stratospheric ozone depletion[39]. Murphy[40] has proposed a mechanism by which ice nucleates to Ic, then converts to Ih, with the resulting vapour pressure differential resulting in the formation of larger ice crystals; larger crys-

tals have higher terminal velocities and are therefore more effective at dehydrating air. This dehydration mechanism is only important at temperatures below 200 K, which happens to be the temperature range present in tropical tropopause and polar stratospheric clouds.

2.2.4 Formation conditions

Cubic ice was first created under laboratory conditions by Dewar in 1905[54], who observed a phase change to a 'milk-white' crystalline form when slowly heating compressed ice at 15 kbar and 193 K. Dowell and Rinfret later prepared amorphous ice by condensation of water on to a surface maintained below 110 K, which transformed to cubic ice (identified by X-ray diffraction) on heating above 110 K[58]. Bertie *et al.*[59] claimed to be the first to prepare large quantities of ice Ic in 1963, by heating samples of high pressure ice phases (ices II, III and V) from 77 K at zero pressure. Mayer and Hallbrucker[33] succeeded in preparing cubic ice from liquid water in 1987 (it had previously only been formed via the amorphous ice phase) by rapidly quenching aqueous aerosol droplets with a diameter of roughly 3 μm to 190 K–200 K on a cryoplate. They found that cubic ice formed in this way annealed to ice Ih slower than ice Ic formed from amorphous ice, perhaps as a result of the higher surface area to volume ratio, which allowed faster heat dissipation. This would suggest that cubic ice crystals formed in the atmosphere must be more stable, since they are thermally isolated from each other. Steytler *et al.* cooled heavy water trapped in porous silica (with pores of mean diameter 9 nm) to 260 K and identified cubic ice using neutron diffraction[60], demonstrating that cubic ice could be stabilised at higher temperatures by formation in confined geometries.

Johari[61] argues that water droplets will freeze to ice Ih or Ic depending on their size. His thermodynamic calculations yield a 'critical radius' of 15.1 nm, suggesting that water droplets smaller than this will freeze to ice Ic, and larger droplets will freeze to ice Ih. He also calculates the 'critical thickness' of a water film to be 10 nm (water films

thinner than 10 nm will freeze to ice Ic). These results are borne out by experiment, to an extent; a number of studies (for example, Dunn *et al*. (1988)[3]) on ice formation in the pores of nanoporous materials indicate that ice Ic is indeed formed in these confined geometries. Johari adds that the critical radius (or thickness, for a water film) is affected by the temperature and shape of the droplets, and that it is expected to be affected by the presence of impurities and, crucially, the degree of proton ordering in the ice formed since heat capacity is affected by proton ordering.

2.2.5 Attempts to prepare pure cubic ice

Murray *et al.*[39] attempted to experimentally simulate the conditions present in the atmosphere during cloud formation, namely homogeneous nucleation of ice in water droplets. Aqueous droplets of 2 μm–20 μm were suspended in an oil matrix by emulsification, and the ice phase formation was monitored using X-ray diffraction. Aqueous droplets containing ammonia, sulphuric acid and nitric acid among other solutes were all found to freeze to ice Ic containing hexagonal stacking faults at 190 K, a temperature representative of the tropical tropopause and stratosphere, while 10 μm droplets of pure water were shown to contain significant proportions of ice Ic (∼67%) at 235 K. Sufficient heating of these ice particles caused the ice Ic to anneal to ice Ih. The authors of the study estimated that heat transfer is approximately ten times slower in the atmosphere than it is in the emulsion, so a 10 μm droplet in the atmosphere is unlikely to contain much ice Ic after freezing.

Murray and Bertram[2] conducted similar experiments, with an emphasis on determining the proportion of cubic ice formed in emulsified pure water droplets as a function of droplet size, and investigating the stability of the droplets after freezing. They found that as the median diameter of the droplets increased from 5.6 μm to 17 μm, the fraction of ice Ic present decreased from almost 100% (with some hexagonal stacking faults), indicating a strong inverse size dependence. This can be rationalised in terms of

heat transfer: crystallisation is an exothermic process, so heat is produced on freezing. Smaller crystals have a larger surface area to volume ratio, and can therefore dissipate the heat to their surroundings more rapidly; this heat would otherwise result in the ice Ic to Ih transition. They conclude that ice Ic is the phase that nucleates, and the final amount of Ic in the droplet is governed by the variation in the temperature of the droplet after freezing.

As part of the same study, they also looked at ice Ic stability as a function of temperature. Using a similar experimental setup, an emulsion of 10 μm water droplets was cooled to 228 K–263 K, then the temperature increased, and the diffraction pattern monitored. It was found that ice Ic is extremely stable at 228 K, but at 263 K it is rapidly converted to ice Ih; there is a clear disparity with previous studies, with indicated that ice Ic is rapidly converted to Ih at 205 K. Murray and Bertram rationalise this by suggesting that the transition is highly dependent on the surface area of droplet, and the results of previous experiments were dominated by gas phase transfer which is blocked by the emulsion. This theory is corroborated by studies on freezing in porous silica, in which ice Ic was also observed at higher temperatures[3].

Murray and Bertram's results conflict with predictions from Johari's[61] thermodynamic calculations, which predicted that only droplets of <10 nm would freeze to ice Ic, a difference of almost 3 orders of magnitude. One order of magnitude can be accounted for by the increased heat transfer from the droplets in the emulsion; in the atmosphere, heat dissipation would occur at approximately a tenth of the rate in the emulsion so a 10 μm droplet in the emulsion will behave as a 1 μm droplet in the atmosphere.

2.3 Proton ordering in bulk ice

Linus Pauling's seminal 1935 paper[62] was the first to quantify orientational effects on entropy in ice. It was known that the oxygen atoms in an ice crystal form a tetrahedral structure from X-ray diffraction studies; however there was still uncertainty regarding

the positions of the hydrogen atoms because X-rays are scattered by electrons, and the bulk of the electron density surrounds the oxygen atoms leaving the hydrogen positions poorly characterised. Pauling deduced that the hydrogens must not be midway between the oxygens since this would require a much larger change in properties than is observed between the gas, liquid and solid phases of water; for example, the melting points of most ionic crystals are several hundred degrees higher than that of ice[63]. Additionally, there must be a constraint forcing the hydrogen atom to occupy one of the two available positions between a pair of neighbouring oxygens, since the concentration of H_3O^+ and OH^- ions in water is low. These orientational constraints are summarised by the "ice rules," formalised by Bernal and Fowler[64], which stipulate that:

1. there may only be two hydrogen atoms bonded to each oxygen (formally, a water molecule)

2. there may only be one hydrogen atom per hydrogen bond (that is, one hydrogen atom between each pair of neighbouring oxygen atoms).

Two types of defects arise from the violation of these rules[45]: ionic defects resulting in the violation of the first rule, which are responsible for the formation of H_3O^+ and OH^- ions, and Bjerrum L (no proton on a hydrogen bond axis) and D (two protons on a hydrogen bond axis) defects, resulting from the violation of the second rule.

Thus ice crystals can exist in a number of configurations with differing molecular orientations, subject to the ice rules. Each molecule can assume one of six orientations (figure 2.3) — a constraint imposed by the underlying tetrahedral structure — and according to Pauling[62], the chance that the adjacent molecules will permit that orientation is $\frac{1}{4}$, hence there are $(\frac{6}{4})^N = (\frac{3}{2})^N$ ways of arranging N molecules, therefore the molar entropy (S) of ice at 0 K is given by,

$$S = R \ln W = NR \ln \left(\frac{3}{2} \right), \tag{2.1}$$

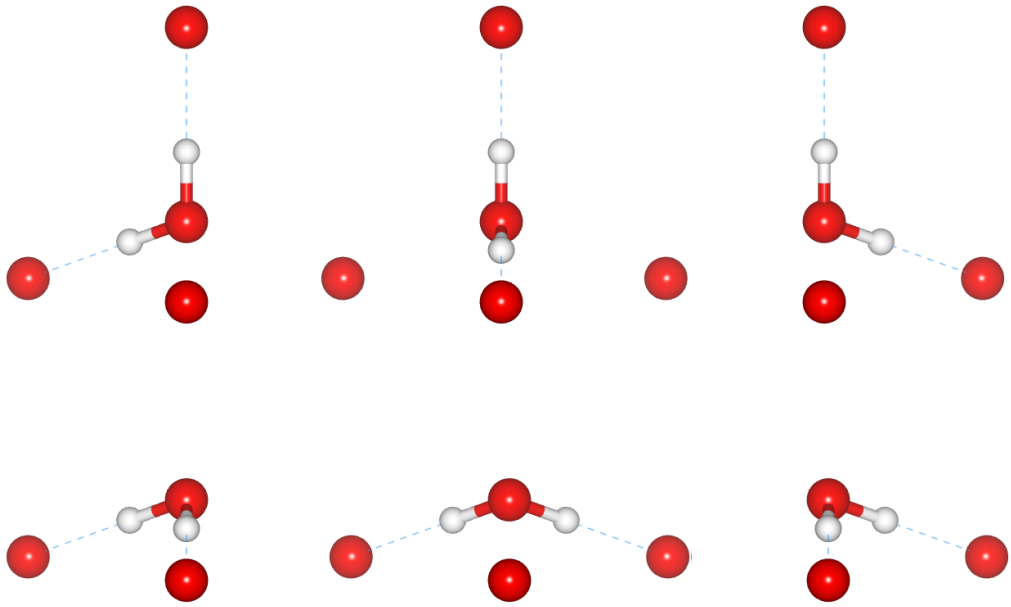

Figure 2.3: The six canonical orientations of a water molecule in a tetrahedral ice lattice.

where R is the molar gas constant and W is the number of ways of arranging the molecules.

Pauling calculated that there are $(\frac{3}{2})^N$ ways of arranging N water molecules in an ice crystal, but speciously argued that these configurations would all be degenerate at low temperatures, perhaps based on the assumption that all configurations contribute equally to the entropy. Petrenko and Whitworth suggest that long range interactions between molecules are negligible; they quote Pauling: 'under ordinary conditions the interaction of non-adjacent molecules is not such as to stabilise one of the many configurations satisfying the ice rules with respect to the others'[46]. It seems intuitive that variations in proton ordering would affect the electrostatic energy, making some configurations more favourable than others. However, the energy differences between proton ordered structures with the same underlying oxygen lattice can be small (as low as $10\,\mathrm{J\,mol^{-1}}$)[65], so their resolution requires the application of extremely precise modelling techniques.

Ice therefore has a finite entropy at 0 K, and must have a large number or proton-ordered and disordered configurations. It is now known that proton ordered phases of

ice can form under certain conditions, indicating that the different configurations are non-degenerate.

Although Pauling's entropy calculation is exact for dendritic (branching) structures, closed loops of hydrogen bonds introduce an error. For example, it has been shown that in a closed loop of six hydrogen bonds (the shortest closed loop present in ice I), assuming the first five bonds are correctly formed with probability $\frac{1}{2}$, the probability that the sixth bond is correctly formed is slightly greater than $\frac{1}{2}$. As a result, Pauling's calculation underestimates W and therefore the entropy[46;63].

To date, there is a considerable body of computational work on proton ordering in bulk hexagonal ice, but very little on cubic ice or the ice surface. There have been attempts at determining the structure of a possible proton ordered phase of ice Ic in the literature: Silvi compares the $I4_1md$ cubic ice and ice XIII structures, identifying the former as a "prototype"[66], and Lekner generates an exhaustive set proton ordered configurations from the cubic cell[67;68]. Casassa *et al.* compare the configurational energies of different hexagonal and cubic proton ordered and disordered structures[69]. However, it would seem that there has been no published work on cubic ice analogous to Hirsch and Ojamäe's on hexagonal ice[12]: an exhaustive study of proton ordered polymorphs of ice Ic in order to determining the most viable candidate for a proton ordered cubic ice phase using DFT.

2.4 Modelling ice using empirical potentials

One of the striking features of the ice (and water) literature is the sheer number of models that have been constructed in attempts to reproduce small subsets of the anomalous properties of water. In his 2002 review, Guillot lists 46 different forcefield models; this value has increased considerably in the interim[70]. The most common are rigid body models, which have no internal degrees of freedom; these models generally differ in terms of geometry, charge distribution, polarisation, etc. Flexible (in which bond

lengths and angles are degrees of freedom) and polarisable (in which charge distribution is a degree of freedom) models are also available, but do not offer any significant advantage over simpler models considering the added computational cost[71].

One of the most simple models is SPC (simple point charge) [72]; it is a three site model with the tetrahedral geometry of ice, point charges located on the atomic positions, and a Lennard-Jones potential centred on the oxygen site. A reparameterisation of this model that has been extremely successful in reproducing the properties of ice is the SPC/E variant. It is identical to SPC, except that it includes a polarisation correction with the aim of reproducing the enthalpy of vaporisation.

The popular TIP*n*P (*n*-point transferable intermolecular potential) family of models is characterised by the use of the gas phase geometry of water molecules[73]. The simplest member is the three site TIP3P model, which is is similar to SPC in terms of charge distribution and the potential, but adopts the geometry of the gas phase molecule. Jorgensen *et al.* developed the four site TIP4P model in an attempt to better reproduce the oxygen-oxygen radial distribution function[74]; it differs from TIP3P primarily in terms of charge distribution: the charge is moved off the oxygen atom, and onto the massless 'M-site' along the HOH angle bisector in the direction of the hydrogen atoms, with the Lennard-Jones potential remaining at the oxygen site. This allows the dipole moment to be varied without altering the geometry of the molecule. The TIP5P model resembles TIP3P, but with additional negative charges at the 'L-sites,' located at the positions of the oxygen lone pairs. These models are parameterised to reproduce experimental values for the enthalpy of vaporisation and density at ambient conditions, and crucially in the case of TIP5P, the temperature at which the density of water is at a maximum (T_{MD})[75].

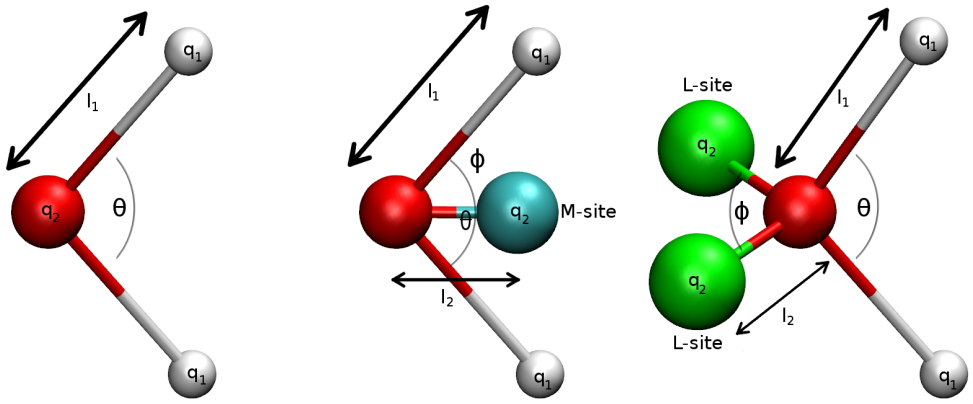

(a) TIP3P (b) TIP4P (c) TIP5P

Figure 2.4: The three basic TIP*n*P forcefield models, with geometries and charges. TIP4P contains an imaginary "M"-site at the bisector of the HOH angle, and TIP5P has two imaginary "L"-sites at the positions of the lone pairs on the oxygen.

Model	Type	σ (Å)	ϵ (kJ mol^{-1})	l_1 (Å)	l_2 (Å)	q_1 (e)	q_2 (e)	θ (°)	ϕ (°)
SPC	a	3.16600	0.6500	1.0000	—	+0.410	−0.820	109.47	—
TIP3P	a	3.15061	0.6364	0.9572	—	+0.417	−0.834	104.52	—
TIP4P	b	3.15365	0.6480	0.9572	0.15	+0.520	−1.040	104.52	52.26
TIP4P/ice	b	3.1668	0.8822	0.9572	0.1577	+0.5897	−1.1794	104.52	52.26
TIP4P/2005	b	3.1589	0.7749	0.9572	0.1546	+0.5564	−1.1128	104.52	52.26
TIP5P	c	3.12000	0.6694	0.9572	0.70	+0.241	−0.241	104.52	109.57
NE6	b + c	3.115_{OO} 0.673_{HH}	0.715_{OO} 0.115_{HH}	0.9800	0.8892_{L} 0.2300_{M}	+0.477	-0.044_{L} -0.866_{M}	108.00	111.00

Table 2.1: Geometries and parameters for some relevant rigid body forcefield models[23] (NE6 refers to the Nada-van der Eerden six-site model). The type and geometric quantities correspond to those indicated in figure 2.4; σ and ϵ are Lennard-Jones parameters.

There have been many attempts to reparameterise the TIP4P model, including several with the specific aim of reproducing ice properties. Even though TIP4P molecules assume the gas phase geometry, it generates a qualitatively correct phase diagram, for which reason Abascal *et al.* attempted to modify it to model ice[71]. They noted that it is impossible to simultaneously fit the melting temperature and the enthalpy of vaporisation for rigid models, choosing to prefer fitting to the melting temperature. The resulting potential, named TIP4P/ice, demonstrated excellent agreements for the melting point of ice Ih (272.2 K), the densities of most ice phases, and the enthalpy of melting, but an unsurprisingly bad fit for the enthalpy of vaporisation. However, it provided a

poor representation of the extremely dense forms of ice (VII and VIII), perhaps a consequence of the model having only one repulsive site per molecule.

Abascal *et al.* later proposed a new variation of dubbed TIP4P/2005[76] which was, like TIP4P/ice, designed to model the condensed phases of water. In contrast with TIP4P/ice, it does not sacrifice the ability to predict the enthalpy of vaporisation, for which it uses a corrective term. It was also taken into account that many empirical models overestimate the stability of ice II; SPC/E, in particular does this unless it is transformed into a four site model. They used a larger number of target parameters than most other potentials, notably including T_{MD}, and the distance between the oxygen atom and the M-site was modified. The resulting potential represented a significant improvement in terms of accuracy of predictions (for the liquid phase as well as the solid), and reproducing a wider range of properties than many other potentials. It proved to be a better model than SPC/E, TIP3P, TIP4P and TIP5P[73] over a wide range of properties which notably included densities of ice polymorphs, melting points and structure predictions. Vega *et al.*[73] note that although the dipole moments of the models examined are similar, the quadrupole moments differ greatly, TIP4P/2005 having the highest, and TIP5P having the lowest. This may be a clue as to why TIP4P/2005 is so much better at modelling the condensed phases, where there is a strong short range orientational dependence between molecules.

McBride *et al.*[77] have attempted to modify TIP4P/2005 to include quantum delocalisation effects which are responsible for (to name one example) the discrepancy in the maximum density temperature between H_2O (∼4°C) and D_2O (∼7°C). Empirical models which are tailored to reproduce experimental results at 273 K tend to fail as the temperature is reduced since classical models do not account for one of the consequences of the third law of thermodynamics, namely that the thermal expansion coefficient α tends to zero as the temperature tends to zero. Quantum effects are thus significant at low temperatures, particularly in the 77 K regime, where many experiments are con-

ducted using liquid nitrogen cooling. The TIP4P/2005 and the "quantum compensated" TIP4PQ/2005 models are identical, except that the latter has a larger dipole moment achieved by a 0.02e shift in charge from each of the hydrogen sites to the M site. Simulations on all ice phases other than ice X suggested that the new model was 'clearly superior.'

Empirical models allow the reproduction of limited sections of the phase diagram of water, and are computationally inexpensive way of calculating relative thermodynamic potentials and configurational energies, but they clearly fall short when attempting to resolve the subtle energy differences between proton ordered polymorphs. This underlines the need for more precise modelling techniques, such as density functional theory (DFT, discussed in detail in chapter 3).

It should be noted that the success of classical methods in predicting the relative energies of proton ordered configurations depends largely on the complexity of the model. The most widely used potentials, namely SPC and the TIP*n*P family, have failed in predicting the structure of ice XI, favouring the antiferroelectric $Pna2_1$ configuration instead of the experimentally verified $Cmc2_1$ configuration[48;78]. Only the six-site Nada-van der Eerden six-site model (NE6)[79] has been successful in this respect[78].

2.5 Ice XI

Ice XI is the proton ordered form of ice Ih. Although there has been some debate regarding its crystalline structure, the consensus is that it is the ferroelectric $Cmc2_1$ variant, as opposed to the antiferroelectric configuration predicted by Davidson and Morokuma[14], the $Pna2_1$ structure (figure 2.5a).

Tajima *et al.*[80] reported a phase transition in KOH-doped ice Ih at 72 K, associated with a loss of approximately 70% of its configurational entropy, indicating a transition to a proton ordered phase; later experiments indicate an entropy loss of up to 82%[46]. They noted that the phase transition is remarkably insensitive to the KOH concentra-

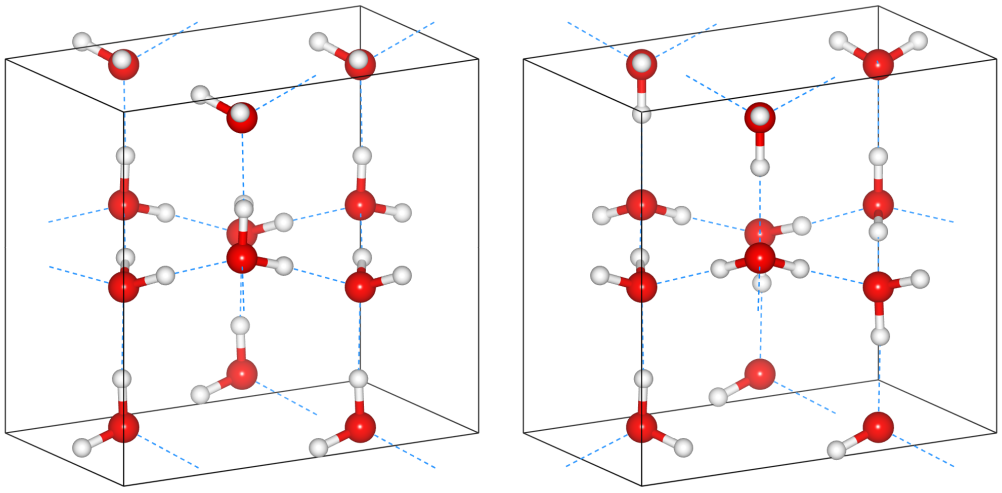

(a) $Cmc2_1$ (b) $Pna2_1$

Figure 2.5: The ferroelectric $Cmc2_1$ structure of ice XI and the antiferroelectric $Pna2_1$ structure predicted by Davidson and Morokuma[14].

tion (it could be varied by at least two orders of magnitude without losing the transition), perhaps indicating the role of the OH^- ions as a catalyst. Howe and Whitworth[81] suggested that the Ih $\longleftrightarrow$ XI transition does not occur in pure ice because it does not contain the point defects that allow orientational reconfiguration. Leadbetter *et al.*[82] performed neutron diffraction experiments on KOH-doped D_2O, and concluded that only the lattice spacings in the $Cmc2_1$ structure could account for the diffraction pattern.

Jackson and Whitworth[83] later addressed the fact that the proposed $Cmc2_1$ structure is ferroelectric by investigating the transition of KOH-doped ice Ih under the influence of an applied electric field. They used a 'thermally stimulated depolarisation' (TSD) technique, in which KOH-doped ice was cooled in an electric field, causing the induced polarisation to become 'frozen in.' Upon removal of the applied electric field and heating, a 'TSD' current was observed. They determined that ice XI is ferroelectric parallel to the c-axis, consistent with the $Cmc2_1$ structure, and crucially, that when no electric field was applied, no TSD current was observed. This indicated that the summed contributions to the electric field over bulk ice XI must average to zero, that is, without an applied electric field, ice XI forms from ferroelectric domains with op-

posing orientations resulting in a non-polar macroscopic structure. This was supported by the observation that increasing the applied electric field resulted in a larger TSD current (although they did not increase it enough to reach a saturation point, which would indicate a single domain limit).

According to Petrenko and Whitworth[46], there are six possible domain orientations in ice XI, and there must be equal proportions of domains polarised in opposite directions in order to avoid a net polarisation. They suggest that there are 'incompatibilities' between certain domain orientations - for example, it is impossible for two domains oppositely polarised along their c axes to join without violating the ice rules at the boundary; for this reason there will always be some residual ice Ih and it is impossible to form a single-domain phase pure ice XI crystal. This is supported by the failure of calorimetric experiments to recover the full Pauling entropy; OH^- ions would have to follow an improbably exact path through the ice lattice in order to remove all remaining disorder.

2.6 Generating ice simulation cells

Howe[84] devised a scheme for generating the symmetry-unique proton ordered configurations of the 8-molecule cell of ice Ih. By independently fixing the orientations of specific molecules in one of the two hexagonal layers of the cell, and working out the permutations of orientations of the dependent molecules subject to the constraints of the ice rules, she was able to determine that there are 13 unique configurations of molecules in one of the layers. By considering the combinations of ways in which the two layers could be connected, she concluded that there are 57 configurations permissible by the ice rules. This differs from the number of 114 configurations independently arrived at by Hirsch and Ojamäe by a factor of two, but can be explained by the fact that there are two possible positions for a proton on every hydrogen bond, and for every one of the 57 configurations predicted by Howe there is a 'converse' configuration in which

each proton is the alternate position. Hayward and Reimers[85] developed a method of generating proton disordered hexagonal ice cells with minimised multipole moments by the application of orientational constraints. However, it seems that the most efficient method of generating hydrogen bond topologies is that of Kuo, Knight, Singer *et al.*[86–88]. They demonstrate the use of graph invariants in generating proton ordered configurations, and show that graph invariants may also be used to predict various physical properties.

Lekner[67;68] calculates the electrostatic energies of various proton ordered configurations of ice Ic, based on the conjecture that any energy difference as a result of differences in proton ordering will be purely electrostatic. It is a fairly primitive study, since it only considers the Hartree component of the total energy, and uses ideal (unrelaxed) ice lattices with straight hydrogen bonds, ignoring quantum effects. By using the proton position on the hydrogen bond as a coordinate, and what appears to be a similar method to Howe's[84], Lekner concludes that there are 90 configurations of the cubic eight-molecule $Fd\bar{3}m$ cell that satisfy the ice rules. In a later study[68], Lekner explicitly calculates the number of valid configurations for the eight-molecule ice Ih cell as 114 in agreement with Hirsch and Ojamäe[12].

Lekner's calculations suggest that the electrostatic energy is linearly related to the dipole moment of the cell squared, so the degeneracy of the configurations can be worked out on the basis of the cell dipole moment; in this way, he determines that there are 17 distinct energies for the Ih cell (in agreement with Howe[84]), and 4 for the Ic cell. He goes on to suggest that antiferroelectric configurations for both hexagonal and cubic cells would be energetically favoured on the basis of electrostatic considerations. In an analogous study of diamond[68], he shows using purely electrostatic arguments that the cubic structure for a lattice of carbon atoms is the energetically favourable compared with a hexagonal lattice. Although his method makes qualitatively correct predictions, it is highly unlikely that it is robust considering the coarseness of the approximations;

he used unrelaxed structures and did not take quantum mechanical effects into consideration.

It is impossible to use atomistic periodic models of ice to simulate macroscopic proton disordered systems since they are ordered by construction (although it is possible to simulate proton disorder using surprisingly small cells of a few hundred molecules); any non-periodic system would have to be intractably large in order to capture the macroscopic properties of ice, and would include surface effects. Rick and Haymet[89] used ensembles of quasi-disordered ice configurations generated by their 'Move Algorithm' in order to simulate disorder, with the aim of reproducing experimental values of the exceptionally high dielectric constant of water. The Move Algorithm essentially uses random walks to identify closed loops of hydrogen bonds, then reorienting the molecules on the loop using the Metropolis Monte Carlo scheme to accept or reject the new arrangement on the basis of configurational energy. Of the three empirical potentials used, they found TIP4P-FQ (a TIP4P variant that allows fluctuating charge, and therefore induced polarisation[90]) to give a dielectric constant closest to the experimental value; it also showed signs of a transition to a proton ordered phase at 50 K–100 K which would make it consistent with the ice Ih $\longleftrightarrow$ ice XI transition.

2.7 Proton ordering in ices Ih and Ic

Buch, Sandler and Sadlej[48] approach the problem of proton ordering in ice with a view to constructing a potential that favours the ferroelectric $Cmc2_1$ as the most stable proton ordered form of ice Ih, rather than Bjerrum's $Pna2_1$ structure. They used a Rick and Haymet's 'Move Algorithm'[89] to generate quasi-random proton-disordered configurations for large unit cells containing up to 1600 water molecules. Cells were generated containing the oxygen sub-lattice for ice Ic or Ih, and a hydrogen atom placed at one of the two possible positions on each oxygen-oxygen axis, at which point each oxygen atom would be 'bonded' to between zero and four hydrogen atoms. At each

Monte Carlo step, a bond was picked at random, and the hydrogen atom moved to the alternative position on the oxygen-oxygen axis with a probability favouring a configuration with all oxygen atoms bonded to exactly two hydrogen atoms. The fact that they found 16 distinct eight-molecule ice 1h configurations (in agreement with Hirsch and Ojamäe[12]) vindicates their method. The energies of the ideal cells displayed a linear correlation with the fraction of trans hydrogen bonds (f_t), with more stable structures having a higher f_t as predicted by Bjerrum; however full geometry optimisation broke the correlation. Rick and Haymet[89] have used f_t as an order parameter in an earlier study, but this only makes sense when using rigid body models such as SPC and TIP4P.

One limitation of studying proton-ordered configurations of ice is that for a cell containing a given oxygen sub-lattice, the fraction of trans hydrogen bonds can only take certain discrete values. Bartók and Baranyai[65] performed Monte Carlo simulations on quasi-disordered ice configurations, in order to effectively make the trans fraction a continuous variable, within limits prescribed by the geometric constraints - for example, the fraction of h-cis and h-trans bonds in ice Ih is 0.75. They noted that it was only possible to generate disordered configurations with the trans fraction in a narrow range, and it was not generally possible to expand this range substantially by increasing the cell size; for example, in a 432 molecule cell, $0.56 < f_t < 0.75$. They found that the energy and trans fraction were (more or less) correlated, as expected, and suggested that the distribution of hydrogen bond isomers can be used to uniquely identify phases for the tetrahedral structures examined (ices Ih, XI, VII and VIII), but the hydrogen bonding structures of other phases were too complicated for this approach. They conclude by estimating that there are generally small energy differences of $10\,\mathrm{J\,mol^{-1}}$–$1000\,\mathrm{J\,mol^{-1}}$ between pairs of proton ordered and disordered polymorphs, which is consistent with DFT calculations.

Bartók and Baranyai used several empirical potentials in their aforementioned study, including TIP5P-EW (a re-parameterised TIP5P with better representation of long range

forces), TIP4P-EW and TIP4P/2005. In a previous paper[91], they simulated the ice phases I-XII (an exhaustive set at the time) using the popular SPC/E and TIP4P potentials and a Monte Carlo method. The results suggested that these coarse models are unable to predict the subtle energy differences between low pressure phases (notably ices Ih and Ic), and they significantly overestimate the energies of the high pressure phases. This is not entirely surprising when one considers the physical origin of these models as Baranyai and Bartók do in a subsequent paper[92]. They are both rigid body models based on opposite extremes of the phase diagram: SPC/E is 3-site model based on the perfect tetrahedral structure of crystalline ice, and TIP4P is a 4-site model with geometry based molecules in the gas phase. In this study, they repeated the calculations on thirteen phases of ice using the TIP4P potential and two of its variations, TIP4P-EW and TIP4P/ice, as well as an 'average' model, with geometry compromised between those of SPC/E and TIP4P. It was found that none of these models resulted in a significant improvement over SPC/E and TIP4P, although TIP4P-EW yielded the best results. It therefore seems that no single simple rigid-body model is sufficient to model all phases of water, and are not capable of resolving the energy differences between ices Ic and Ih, let alone their proton ordered configurations, although constant refinement and reparameterisation may eventually yield a usable potential.

The group of Casassa, Pisani *et al.* has written a number of papers on proton ordering energetics in hexagonal and cubic ice[69;93–96]. In their 1996 paper[93], they use periodic Hartree-Fock (HF) calculations to determine the energy difference between two proton ordered forms of ice Ih, denoted C-ice (which is the actual structure of Ice XI, space group $Cmc2_1$) and P-ice (a hypothetical anti-ferroelectric proton-ordered ice structure proposed by Davidson and Morokuma[14], in space group $Pna2_1$). According to Davidson and Morokuma's three-body potential calculations, P-ice has a lower energy than C-ice because all of the hydrogen bonds have the trans-configuration, maximising the distances between repulsive centres; however the HF calculations of Pisani *et al.* sug-

gest that C-ice and P-ice are 'essentially iso-energetic', and while their binding energies were in good agreement with experimental results (allowing for the characteristic under-binding of HF calculations), Hirsch and Ojamäe's later work[12] demonstrates that HF calculations using the fairly extensive 6-31G** basis set are not accurate enough to resolve energy differences between proton ordered polymorphs of ice, most likely due to the omission of electron correlation.

Whilst there are no studies that examine an exhaustive set of proton valid proton ordered configuration in cubic ice in the vein of the Hirsch and Ojamäe study[12], there are details of possible ground state structures. In a neutron diffraction study of ice Ic, Kuhs *et al.* mentioned candidates for a hypothetical proton orrdered phase with space groups $I4_1md$ and $P2_12_12_1$[51]. Casassa *et al.* examined two configurations with space groups $I4_1md$ (ferroelectric) and $P4_12_12$ (antiferroelectric)[69]. In this paper, they take a step up from HF methods and apply GGA and hybrid periodic DFT methods to calculate the energies of four different proton ordered configurations of ice: the aforementioned $Cmc2_1$ (polar hexagonal) and $Pna2_1$ (apolar hexagonal) structures, and two different cubic ice configurations: $P4_12_12$ (apolar cubic) and $I4_1md$ (polar cubic). By performing DFT calculations on water molecules and dimers using various basis sets, it was shown that HF tends to under-bind and DFT tends to over-bind, with the B3LYP hybrid functional yielding results closer to experimental values cited by Petrenko and Whitworth[46] than the PW91 GGA functional. Their results indicated that ice XI ($Cmc2_1$) is metastable with respect to proton ordered cubic ice ($I4_1md$) by 880 J mol^{-1}–3517 J mol^{-1}, a fact they described as 'contrary to intuition.' They conclude that the cubic structure is more stable than the hexagonal, and ferroelectric structures are more stable than anti-ferroelectric; the latter assertion is widely supported in the literature (for example, Knight *et al.*[88]), but the former has interesting implications, and again raises the question as to why hexagonal ice structures are preferred in nature. Note that in contradiction with the CRYSTAL calculations in this paper, the VASP calculations

suggest that the anti-ferroelectric structure should be more stable; they also disagree with the analogous CASTEP calculations of Hirsch and Ojamäe, which are considered to be robust - indeed, they acknowledge that the VASP results are erroneous in a later publication[96].

In their 2009 papers[94–96], Erba *et al.* perform essentially the same calculations as in the 2005 paper[69] on the $Cmc2_1$ and $Pna2_1$ structures, but with a different computational setup. HF, post-HF (local-MP2) and DFT (PW91, B3LYP) with two different basis sets. In this case, the GGA calculations were in agreement with those of Hirsch and Ojamäe. The B3LYP results are in such good agreement with experimental data that Erba *et al.* significantly conclude that dispersive interactions are insignificant in ice (since DFT is known not to model long range interactions well); however, unpublished results suggest that a dispersion correction adds 5–10% to total absolute energies, which would take the B3LYP energies significantly away from the experimental values; in this case, perhaps a 'fortuitous cancellation of errors'[69] is responsible for the excellent agreement.

Tribello and Slater[97] revisited the 16 symmetry-inequivalent proton ordered structures of Hirsch and Ojamäe in an attempt to determine what effect the exchange-correlation functional recipe has on their relative energies, the answer being "surprisingly little". By performing DFT calculations using the CASTEP code, they showed that the relative energies were similar for two GGA functionals, PW91 and RPBE, and even an LDA functional - leading to the conclusion the proton ordering energetics are determined solely by electrostatic effects; this was confirmed by a multipolar analysis, which also demonstrated that an accurate description of the electrostatics in ice requires 'surprisingly high order multipoles.'

Labat *et al.* performed a detailed study of the $Pna2_1$ and $Cmc2_1$ configurations of hexagonal ice, their assertion being that the energy of the $Pna2_1$ structure is close to the approximate average energy of the ensemble of structures comprising ice Ih[98].

They examine the relative energies using several density functionals including GGA, hybrid, meta-GGA and hybrid meta-GGA with differing fractions of Hartree-Fock exchange. Whilst the structure and band gap are sensitive to the choice of functional, they show that the energy difference is only weakly affected, by $\sim$2 meV, supporting the notion that the energetics of proton ordering is well-described by a range of functional[97]. They conclude that although non-local exchange has a significant effect on the electronic structure and energetics of hexagonal ice, it does not significantly affect the *relative* energies of proton ordered configurations, and that the relative energy is insensitive to changes in the exchange-correlation functional recipe. They also note that only the M06-L (meta-GGA) and B3LYP (hybrid) functionals reproduce the formation energies, and only B3LYP is capable of accurately describing the electronic structure.

Calculating the dipole moment of a water molecule in an ice crystal is a non-trivial task, since it is necessary to take into account the dipoles induced by neighbouring molecules (and perhaps even those in higher coordination shells). Batista *et al.*[99] developed an ingenious 'induction model' which uses an individual water molecule to calculate high order multipole moments of water molecules in ice crystals. Starting with the dipole moment of an isolated molecule, a first order correction is added for dipoles, quadrupoles, octapoles and higher order multipoles induced by neighbouring molecules, then this process is repeated using the updated multipoles to generate a second order correction, and so forth. Each molecule is then represented by multipole tensors at its centre of mass. The electric field of the molecule is then calculated using experimental values for the dipole and quadrupole, and results obtained from *ab initio* calculations for higher order multipoles. They found that by using such a multipole expansion up to and including the hexadecapole, they were able to reproduce the electric field as calculated using DFT. This goes some way to explaining why empirical potentials have been so unsuccessful at correctly predicting the structure of ice XI (they tend to show a preference for the $Pna2_1$ structure predicted by Bjerrum instead of the ferro-

electric $Cmc2_1$ structure) - most of these potentials do not expand beyond the dipole term.

2.8 Proton ordering in the ice surface

Faraday's famous experiment in which a length of cheese wire with weights at either end cuts through a block of ice demonstrated that there is something 'special' about the ice surface; as the wire descends, the two surfaces above it fuse together, leaving a single block of ice, a phenomenon known as 'regelation' that cannot simply be accounted for by pre-melting[46]. The ice surface is characterised by three different types of surface molecule: dangling OH bonds, notionally dangling hydrogen bonds (the lone pair on the oxygen atom, or the hydrogen bond site not occupied by a proton) and four-coordinated water molecules with distorted geometry. Dangling bonds tend to destabilise the surface, so there is great interest in how surface reconstructs itself in order to (at least partially) mitigate their effect.

Fletcher's 1992 paper[100] considers proton ordering on the ice surface. His intuitive analysis of electrostatic interactions in basal and prism surfaces led him to conclude that these surfaces should undergo a transition to a proton-ordered phase. One candidate for an ordered phase was the distinctive 'striped' phase (see figure 5.2 for the atomic structure), consisting of alternating rows of dangling OH bonds and lone pairs. He proposed a mechanism for this reconstruction, based on the motion of Bjerrum L ("empty" hydrogen bonds) and D (hydrogen bonds occupied by two protons) defects which can form in bulk ice in pairs, but singly at the surface. The surface acts as a sink and a source for these defects, and at a reduced energy cost since the surface reduces the elastic strain associated with these defects.

Proton transfer can also occur in ice via the motion of ionic defects. In the absence of impurities, these defects are formed by water autoionisation, in which a pair of water molecules forms a H_3O^+ ion and an OH^- ion; charge transfer occurs as a result of pro-

tons hopping between ions because the H_3O^+ is more mobile. Note that this is not a conduction mechanism; the passage of a proton along a path results in molecular reorientations which would require violations of the second ice rule for additional protons to follow the same path. Devlin and Buch[101] used an isotopic exchange technique to examine this phenomenon. The spectra of three unique species were observed in D_2O-doped ice nanocrystals: D_2O, coupled $[HDO]_2$ dimers and isolated HDO molecules. Measurements of proton transfer rate suggested that it occurred 20 times faster in the surface than in the bulk, and that there is an energy barrier to the penetration of surface-originating protons which increases with depth into the crystal — perhaps a result of coulombic attraction to the much less mobile OH^- ions which are "frozen" into the surface. Intriguingly, they found that the proton exchange rate could be made to vary wildly with the addition of an adsorbate. For example, a surface monolayer of a proton source such as H_2S greatly increased the exchange rate by injecting protons into the crystal. A 1% monolayer of NH_3 almost stopped proton exchange due to the trapping of surface protons by a strong acceptor, whereas a full monolayer induced an increased exchange rate since the high OH^- ion concentration restarted exchange in spite of the low mobility of OH^- ions. A 40% monolayer of SO_2 caused an extreme acceleration in proton exchange; this was attributed to a reduction in surface strain due to the incorporation of the adsorbate into the surface. The SO_2 adsorbate also eliminated orientational defects, supporting the hypothesis that Bjerrum defects are injected from the surface.

Buch *et al.*[102] performed a series of surface calculations using two empirical potentials, TIP4P/ice and EMP (a modification of the MCY *ab initio* potential designed to include induced polarisation effects[103]), and sets of ice slabs with orientational disorder in the bulk. Each slab had one of three surface ordered pattern on the two basal planes that formed the slab surfaces; it was found that the sets using the fletcher "striped" phase had the lowest mean energy. Monte Carlo simulations of fully disordered surfaces indicated a tendency for clusters of dangling OH bonds to "unclump" - although the surface

atoms did not assume the Fletcher striped phase, they did arrange themselves in a 'meandering stripe pattern,' which was locally reminiscent of the striped phase, and almost iso-energetic. This is qualitatively in agreement with the DFT calculations of Pan *et al.*, whose order parameter (which is directly correlated with surface energy) assigns the striped and meandering striped phase the same value, whilst the less favourable "honeycomb" phase has a higher order parameter. It is important to note that the model Buch *et al.* used in this study does not predict the correct structure for ice XI, which is not a convincing basis for a study on surface effects; however, the only significant surface effect is the Coulomb repulsion of dangling protons, which is modelled. Another possible criticism of this study is the lack of an order parameter to quantify the degree of order in the ice surface.

One of the defining characteristics of the many DFT calculations of the energies of proton ordered configurations of bulk ice is how small the range of energy differences is: slightly less than 1 kJ mol^{-1} separates the most and least stable or the 16 symmetry-unique proton ordered configurations of Hirsch and Ojamäe[12]. In their study on proton order of the ice Ih surface, Pan *et al.*[5;104] estimate that the proton-ordered configurations of bulk ice Ih are within ∼5 meV/H_2O of each other, compared with ∼100 meV/H_2O for the surface. It therefore seems that proton ordering affects the energetics of the ice surface by an order of magnitude more than it affects the bulk. Indeed, according to their calculations, the studied ice surfaces (the basal [0001] and prism [10$\bar{1}$0]) will not become fully disordered at any meaningful temperature, i.e. before the onset of premelting. They also determined, using an order parameter, that surface energy increases as the degree of proton ordering in the surface increases, although they were not able to identify a unique surface that could be said to be the most stable - instead there appears to be a family of highly ordered degenerate surfaces, including Fletcher's 'striped phase,' in which the repulsive electrostatic energy of dangling OH bonds is minimised. They go on to suggest that the charge-charge interactions between dangling OH bonds

on the ice surface is analogous to the much weaker dipole-dipole interactions "notionally dangling" hydrogen bonds (i.e. an oxygen lone pair that acts as a hydrogen bond acceptor) in the bulk ice, which may explain why proton ordering affects energetics on the surface so much more dramatically than it does in the bulk.

Computational modelling has clearly taught us a great deal about the relationship between the sub-nanometre scale structure of ice and its properties, but many gaps in our knowledge remain. The calculations described in this thesis to further our understanding of ice primarily use electronic structure methods, for which the theoretical background is discussed in the next chapter.

Chapter 3

Theoretical background

3.1 Introduction

At the atomic level, all interactions between non-relativistic particles are governed by quantum mechanics, as prescribed by the time-dependent Schrödinger equation.

$$i\hbar\frac{d\Psi(\{\mathbf{r}_i\};t)}{dt} = \hat{H}\Psi(\{\mathbf{r}_i\};t) \tag{3.1}$$

Here, the particle wavefunctionΨ is a function of its position $\mathbf{r}_i$ and time t, and $\hat{H}$ is the Hamiltonian. The wavefunction can be decomposed into time-dependent and independent parts, and written $\Psi(\{\mathbf{r}_i\};t) = \Psi(\{\mathbf{r}_i\})e^{-\frac{iE}{\hbar}t}$. If the wavefunction does not evolve with time, equation (3.1) simplifies to the time-independent Schrödinger equation,

$$H\Psi(\{\mathbf{r}_i\}) = E\Psi(\{\mathbf{r}_i\}) \tag{3.2}$$

This is an eigenvalue equation; the eigenstates correspond to stationary points on the potential energy surface, and the eigenvalues at those points are their energies. The ground state energy can in principle be determined by minimising the total energy E with respect to the independent variables $\{\mathbf{r}_i\}$. In practice, this is a very difficult prob-

lem for all but the simplest systems; for many-body systems, it is intractable unless approximations are made. The most basic of these is the Born-Oppenheimer approximation: since the mass of an electron is so much smaller than the mass of a nucleus, their motions can be decoupled by treating the nuclear mass as infinite when solving the Schrödinger equation for the electrons, and using the gradient of the electronic energy to calculate the forces on the nuclei.

This section discusses the means by which the Schrödinger equation can be recast into a form which can in practice be used to explore the potential energy landscapes of systems of many atoms. These methods can be used to evaluate clusters of atoms, or when periodic boundary conditions are applied, bulk solids. With a judicious choice of models, they can also be used to model (among many other things) infinite two-dimensional surfaces and to study reaction chemistry and catalysis.

3.2 General polyelectronic systems

The basic Hamiltonian for a system of interacting electrons and nuclei is (using atomic units of $\hbar = m_e = e = \frac{4\pi}{\epsilon_0} = 1$):

$$\hat{H} = -\frac{1}{2}\sum_i \nabla_i^2 - \sum_{i,I} \frac{Z_I}{|\mathbf{r}_i - \mathbf{R}_I|} + \frac{1}{2}\sum_{i \neq j} \frac{1}{|\mathbf{r}_i - \mathbf{r}_j|} - \frac{1}{2}\sum_{I \neq J} \frac{Z_I Z_J}{|\mathbf{R}_I - \mathbf{R}_J|} \tag{3.3}$$

$$= \hat{T} + \hat{V}_{\text{ext}} + \hat{V}_{\text{int}} + E_{II} \tag{3.4}$$

where Z_I is the charge of the I^{th} nucleus, r_i is the position of the i^{th} electron and R_I is the position of the I^{th} nucleus. Note that the nuclear kinetic energy operator $-\sum_I \frac{1}{M_I}\nabla_I^2$ is omitted via application of the Born-Oppenheimer approximation ($M_I \gg m_e$, where M_I is the mass of nucleus I). The terms in equation (3.3) are, in order, the kinetic energy operator ($\hat{T}$), the potential energy of an electron in the nuclear potential ($\hat{V}_{\text{int}}$), the potential energy arising from electron-electron interactions

($\hat{V}_{\text{ext}}$) and the nuclear-nuclear potential energy (E_{II}).

The total energy of the system is the expectation value of the Hamiltonian acting on the total electronic wavefunction:

$$E = \langle \hat{H} \rangle = \frac{\langle \Psi | \hat{H} | \Psi \rangle}{\langle \Psi | \Psi \rangle} = \langle \hat{T} \rangle + \langle \hat{V}_{\text{int}} \rangle + \int d^3 r \, V_{\text{ext}}(\mathbf{r}) n(\mathbf{r}) + E_{II} \tag{3.5}$$

Here, E_{II} is a classical additive term. The eigenstates of this equation are stationary points of E, and can be found using the variational method and Lagrange multipliers.

A naïve first guess at the total wavefunction Ψ of a N electron system is a simple product of the single electron spin orbitals, the Hartree product:

$$\Psi(1,2,\ldots,N) = \chi_1(1)\chi_2(2)\ldots\chi_N(N) \tag{3.6}$$

where χ_N is the single electron spin orbital of the N^{th} electron. This choice is inappropriate because it does not satisfy the antisymmetry principle (or Pauli exclusion principle), which requires the sign of the total wavefunction to change under the exchange of two electrons. To state this in a more intuitive way, the Hartree product assumes that the probability of finding an electron at a specific point is independent of the probability of finding any other electron there.

The most convenient way of writing an antisymmetric polyelectronic wavefunction is a Slater determinant.

$$\Psi = \frac{1}{\sqrt{N!}} \begin{vmatrix} \chi_1(1) & \chi_2(1) & \cdots & \chi_N(1) \\ \chi_2(1) & \chi_2(2) & \cdots & \chi_N(2) \\ \vdots & \vdots & \ddots & \vdots \\ \chi_N(1) & \chi_N(2) & \cdots & \chi_N(N) \end{vmatrix} \tag{3.7}$$

Interchanging any two rows of the determinant represents the exchange of two electrons and is associated with a change of sign. Additionally, a multiple of any column can be

added to any other column without altering the determinant, i.e. spin orbitals can be constructed from linear combinations of other spin orbitals.

3.3 Hartree-Fock theory (HF)

The expression for the energy of a general polyelectronic system (3.3) can be cast in a more concise form by decomposing the energy into the three main contributions:

1. The potential and kinetic energy of the electrons moving in the nuclear potential:

$$H_{ii}^{\text{core}} = \int d\tau_1 \chi_i(1) \left(-\frac{1}{2}\nabla_i^2 - \sum_{a=1}^{M} \frac{Z_A}{r_{iA}} \right) \chi_i(1) \tag{3.8}$$

2. The pairwise electrostatic repulsion between electrons 1 and 2 in spin orbitals i and j:

$$J_{ij} = \int \int d\tau_1 d\tau_2 \chi_i(1)\chi_j(2) \frac{1}{r_{12}} \chi_i(1)\chi_j(2) \tag{3.9}$$

   The total electrostatic interaction between electrons in orbital χ_1 and the other $(N-1)$ electrons is therefore,

$$E_i^{\text{Coulomb}} = \sum_{j \neq i}^{N} \int d\tau_1 d\tau_2 \chi_i(1)\chi_i(1) \frac{1}{r_{12}} \chi_j(2)\chi_j(2) \tag{3.10}$$

   Hence the total Coulomb contribution for all electrons is:

$$E_{\text{total}}^{\text{Coulomb}} = \sum_{i=1}^{N} \sum_{j=i+1}^{N} \int d\tau_1 d\tau_2 \chi_i(1)\chi_i(1) \frac{1}{r_{12}} \chi_j(2)\chi_j(2) \tag{3.11}$$

$$= \sum_{i=1}^{N} \sum_{j=i+1}^{N} J_{ij} \tag{3.12}$$

3. The energy of the exchange interaction between electrons 1 and 2 in orbitals i and j. This is a manifestation of the Pauli exclusion principle, and it has no classical analogue. The physical consequences are that there is a finite probability of

finding two electrons with the opposite spins at the same position, but there is a zero probability of finding two electrons with the same spin at the same position. The exchange interaction always lowers the total energy, and is therefore sometimes interpreted as the interaction of an electron with a positive "exchange hole" surrounding it.

$$K_{ij} = \int\int d\tau_1 d\tau_2 \chi_i(1)\chi_j(2)\frac{1}{r_{12}}\chi_i(2)\chi_j(1) \tag{3.13}$$

This quantity is only non-zero if the electrons in spin orbitals χ_i and χ_j have the same spin. The interaction energy between an electron in spin orbital χ_i and the other $N-1$ electrons is:

$$E_i^X = \sum_{j\neq i}^{N}\int\int d\tau_1 d\tau_2 \chi_i(1)\chi_j(2)\frac{1}{r_{12}}\chi_i(2)\chi_j(1) \tag{3.14}$$

Hence the total exchange energy for the system is:

$$E_{\text{total}}^X = \sum_{i=1}^{N}\sum_{j'=i+1}^{N}\int\int d\tau_1 d\tau_2 \chi_i(1)\chi_j(2)\frac{1}{r_{12}}\chi_i(2)\chi_j(1) \tag{3.15}$$

$$= \sum_{j=1}^{N}\sum_{j'=i+1}^{N} K_{ij} \tag{3.16}$$

where the j' label indicates a sum over electrons with the same spin as i.

These terms can be incorporated into the Schrödinger equation as follows:

$$\left[-\frac{1}{2}\nabla_i^2 \sum_{A=1}^{M}\frac{Z_A}{r_{12}}\right]\chi_i(1) + \sum_j\left[\int d\tau_2 \chi_j(2)\chi_j(2)\frac{1}{r_{12}}\right]\chi_i(1) - \sum_j\left[\int d\tau_2 \chi_j(2)\chi_i(2)\frac{1}{r_{12}}\right]\chi_i(1) = \sum_j^N \epsilon_{ij}\chi_j(1) \tag{3.17}$$

$$H^{\text{core}}(1)\chi_i(1) + \sum_j^N J_i(1)\chi_i(1) - \sum_j^N K_j(1)\chi_i(1) = \sum_j^N \epsilon_{ij}\chi_j(1) \tag{3.18}$$

Note that the sums in equation (3.17) include spurious "self-interaction" terms where $i = j$; in the full Hartree-Fock expression, these conveniently cancel out between the Coulomb and Exchange terms (the second and third terms in equation (3.17)). Using the fact that $\{J_i(1) - K_i(1)\}\chi_i(1) = 0$, we arrive at the Hartree-Fock equations:

$$\left[H^{\text{core}}(1) + \sum_{j=1}^{N} \{J_j(1) - K_j(1)\} \right] \chi_i(1) = \sum_{j=1}^{N} \epsilon_{ij} \chi_j(1) \tag{3.19}$$

$$\mathscr{F}_i(1)\chi_i(1) = \sum_{j=1}^{N} \epsilon_{ij} \chi_j(1) \tag{3.20}$$

Where the Fock operator $\mathscr{F}_i$ is an effective one-electron Hamiltonian for a polyelectronic system. For the less general closed shell case, it becomes,

$$\mathscr{F}_i(1) = H^{\text{core}}(1) + \sum_{j=1}^{N/2} \{2J_j(1) - K_j(1)\} \tag{3.21}$$

The Fock operator is invariant under unitary transformations, and as long as ϵ_{ij} is hermitian, it is always possible to transform the Hartree-Fock equations (3.20) to a canonical eigenvalue equation $\mathscr{F}_i\chi_i = \epsilon_i\chi_i$. The integro-differential equations (3.19) can be recast as a set of algebraic equations by representing wavefunctions using a set of spatial basis functions (for example, Gaussians). Introducing a general basis $\{\phi_\mu\}, \mu = 1, \ldots, K$, the spatial orbitals φ are:

$$\varphi_i = \sum_{\mu=1}^{K} C_{i\mu}\phi_\mu \quad i = 1, 2, \ldots, K \tag{3.22}$$

Substituting into the canonical Hartree-Fock equations:

$$\mathscr{F}(1) \sum_{\nu} C_{i\nu}\phi_\nu(1) = \epsilon_i \sum_{\nu} C_{i\nu}\phi_\nu(1) \tag{3.23}$$

Multiplying by ϕ_ν^* and integrating:

$$\sum_\nu C_{i\nu} \int \phi_\nu^*(1)\mathscr{F}(1)\phi_\nu(1)d\mathbf{r}_1 = \epsilon_i \sum_\nu C_{i\nu} \int \phi_\nu^*(1)\phi_\nu(1)d\mathbf{r}_1 \tag{3.24}$$

$$\sum_\nu C_{i\nu}\langle\phi_\mu|\mathscr{F}|\phi_\nu\rangle = \epsilon_i \sum_\nu C_{i\nu} \int \phi_\mu^*(1)\phi_\nu(1)d\mathbf{r}_1 \tag{3.25}$$

$$\sum_\nu C_{i\nu}\mathscr{F}_{i\nu} = \epsilon_i \sum_\nu C_{i\nu}S_{\mu\nu} \tag{3.26}$$

In matrix form, these are the Roothan-Hall equations, $\mathscr{F}\mathbf{C} = \mathbf{S}\mathbf{C}\epsilon$; $\mathscr{F}$, $\mathbf{C}$, $\mathbf{S}$ and ϵ are $K \times K$ matrices and ϵ is diagonal. In order to solve the Roothan-Hall equations must be transformed into an eigenvector equation using the transformation matrix $\mathbf{X}$, which generates an orthonormal basis $\{\phi'\}$ from the initial basis $\{\phi\}$. This orthogonal transformation satisfies $\mathbf{X}^\dagger\mathbf{S}\mathbf{X} = \mathbf{I}$ such that $\mathbf{C}' = \mathbf{X}^{-1}\mathbf{C}$ and $\mathbf{C} = \mathbf{X}\mathbf{C}'$. Thus the Roothan-Hall equations become:

$$\mathscr{F}\mathbf{X}\mathbf{C}' = \mathbf{S}\mathbf{X}\mathbf{C}'\epsilon \tag{3.27}$$

$$(\mathbf{X}^\dagger\mathscr{F}\mathbf{X})\mathbf{C}' = (\mathbf{X}^\dagger\mathbf{S}\mathbf{X})\mathbf{C}'\epsilon \tag{3.28}$$

$$\mathscr{F}'\mathbf{C}' = \mathbf{C}'\epsilon \tag{3.29}$$

Many properties of they system can be derived using the electron density, so the electron density matrix $\mathbf{P}_{\mu\nu}$ can be derived from the electron density $\rho(\mathbf{r})$ as follows:

$$\rho(\mathbf{r}) = 2\sum_{i=1}^{N/2}|\varphi_i(\mathbf{r})|^2 = 2\sum_{i=1}^{N/2}\varphi_i(\mathbf{r})\varphi_i^*(\mathbf{r}) \tag{3.30}$$

$$= 2\sum_{i=1}^{N/2}\left(\sum_\mu^K C_{\mu i}\phi_\mu(\mathbf{r})\right)\left(\sum_\nu^K C_{\nu i}\phi_\nu(\mathbf{r})\right)^* \tag{3.31}$$

$$= \sum_{\mu,\nu}^K\left[2\sum_{i=1}^{N/2}C_{\mu i}C_{\nu i}^*\right]\phi_\mu(\mathbf{r})\phi_\nu^*(\mathbf{r}) \tag{3.32}$$

$$\mathbf{P}_{\mu\nu} = 2\sum_{i=1}^{N/2}C_{\mu i}C_{\nu i} \tag{3.33}$$

Each equation represents the motion of a single electron in the *fixed* field resulting from the $N-1$ other electrons in the system — clearly, any solution found for the single electron Hamiltonian will alter the solutions of the remaining $N-1$ equations — thus the overall solution must be found using the self-consistent field (SCF) approach. The following iterative procedure[105] is generally used when solving the Hartree-Fock equations:

1. Calculate the integrals comprising the Fock matrix
2. Construct the overlap matrix **S**
3. Diagonalise **S**
4. Guess or calculate initial density matrix **P**
5. Construct the Fock matrix $\mathscr{F}$ using integrals and density matrix
6. Transform $\mathscr{F} \rightarrow \mathscr{F}' = \mathbf{X}^{\dagger}\mathscr{F}\mathbf{X}$
7. Diagonalise $\mathscr{F}'$ to solve the eigenvalue equation (3.29) with respect to $\mathbf{C}'$
8. Calculate $\mathbf{C} = \mathbf{X}\mathbf{C}^{T}$
9. Re-evaluate density matrix **P** using **C**
10. Repeat from step 5 until self-consistency is achieved

Hartree-Fock is an *ab initio* method; its strength lies in the fact that in principle, it calculates the exact exchange energy. However, it neglects all correlation other than the two-body correlation required by the Pauli exclusion principle, and this usually constitutes a significant error. Although Hartree-Fock calculations on small systems are tractable, it scales poorly with size; $3N$ coordinates are required to describe a closed shell system containing N electrons ($4N$ for an open shell system); it also scales as b^4 for a system described by b basis functions.

3.4 Open shell systems: unrestricted Hartree-Fock (UHF)

The restricted Hartree-Fock (RHF) as described above assumes all molecular orbitals are fully occupied; the most general formulation, Unrestricted Hartree-Fock, relaxes this requirement.

A major shortcoming of RHF can be demonstrated by considering the hydrogen molecule (H_2) with a minimal basis set, i.e. the atomic orbitals consist of one s-function on each centre, χ_A and χ_B. An RHF calculation will result in a doubly occupied bonding MO, ϕ_1, and an unoccupied anti-bonding MO, ϕ_2:

$$\phi_1 = \chi_A + \chi_B \tag{3.34}$$

$$\phi_2 = \chi_A - \chi_B \tag{3.35}$$

The ground state can be expressed as a Slater determinant, Φ_0:

$$\Phi_0 = \begin{vmatrix} \phi_1(1)\alpha(1) & \phi_1(1)\beta(1) \\ \phi_1(2)\alpha(2) & \phi_1(2)\beta(2) \end{vmatrix} \tag{3.36}$$

$$= \phi_1(1)\alpha(1)\phi_1(2)\beta(2) - \phi_1(1)\beta(1)\phi_1(2)\alpha(2) \tag{3.37}$$

$$= \phi_1(1)\phi_1(2)[\alpha(1)\beta(2) - \alpha(2)\beta(1)] \tag{3.38}$$

The first excited state Φ_1 can be written,

$$\Phi_1 = \begin{vmatrix} \phi_2(1)\alpha(1) & \phi_2(1)\beta(1) \\ \phi_2(2)\alpha(2) & \phi_2(2)\beta(2) \end{vmatrix} \tag{3.39}$$

$$= \phi_2(1)\alpha(1)\phi_2(2)\beta(2) - \phi_2(1)\beta(1)\phi_2(2)\alpha(2) \tag{3.40}$$

$$= \phi_2(1)\phi_2(2)[\alpha(1)\beta(2) - \alpha(2)\beta(1)] \tag{3.41}$$

The Hamiltonian is spin-independent in the RHF approximation, so the spin functions

α and β can be ignored, and the MOs expanded in terms of the atomic orbitals (equation (3.34)).

$$\Phi_0 = (\chi_A(1) + \chi_B(1))(\chi_A(2) + \chi_B(2)) = \chi_A\chi_A + \chi_B\chi_B + \chi_A\chi_B + \chi_B\chi_A \tag{3.42}$$

$$\Phi_1 = (\chi_A(1) + \chi_B(1))(\chi_A(2) - \chi_B(2)) = \chi_A\chi_A + \chi_B\chi_B - (\chi_A\chi_B + \chi_B\chi_A) \tag{3.43}$$

The final expressions for Φ_0 and Φ_1 can be divided into two separate contributions. The first is the ionic contribution to the wavefunction, with both electrons on the same atomic centre ($\chi_A\chi_A + \chi_B\chi_B$) and the second is the covalent contribution with electrons on opposite atomic centres ($\chi_A\chi_B + \chi_B\chi_A$). These expressions demonstrate that in the RHF approximation, the wavefunctions contain equal ionic and covalent character at all atomic separations, when in fact, in the case of the H_2 molecule, the wavefunction should have 100% covalent character at large separations. This is known as the RHF dissociation problem: when the atomic centres are pulled apart, the ionic character results in heterolytic rather than the desired homolytic dissociation.

The RHF dissociation problem can be corrected using an *unrestricted* Hartree-Fock wavefunction:

$$\phi_1\alpha(1) = (\chi_A + c\,\chi_B)\alpha(1) \tag{3.44}$$

$$\phi_1\beta(1) = (c\,\chi_A + \chi_B)\beta(1) \tag{3.45}$$

The coefficient c is determined using the variational principle. A value of $c = 1$ recovers the RHF wavefunction. Thus the ground state UHF wavefunction can be written by

expanding its Slater determinant:

$$\Phi_0^{\mathrm{UHF}} = \begin{vmatrix} \phi_1(1)\alpha(1) & \phi_1(1)\beta(1) \\ \phi_1(2)\alpha(2) & \phi_1(2)\beta(2) \end{vmatrix} \tag{3.46}$$

$$= c(\chi_A\chi_A + \chi_B\chi_B)(\alpha\beta - \beta\alpha) + (\chi_A\chi_B\alpha\beta - c^2\chi_B\chi_A\beta\alpha) \tag{3.47}$$

$$+ (c^2\chi_B\chi_A\alpha\beta - \chi_A\chi_B\beta\alpha) \tag{3.48}$$

$$= [c(\chi_A\chi_A + \chi_B\chi_B) + (\chi_A\chi_B + \chi_B\chi_A)](\alpha\beta - \beta\alpha) \tag{3.49}$$

$$+ (1 - c^2)(\chi_A\chi_B\beta\alpha - \chi_B\chi_A\alpha\beta) \tag{3.50}$$

Expanding the first four RHF determinants in terms of AOs gives,

$$\Phi_0^{\mathrm{RHF}} = [\chi_A\chi_A + \chi_B\chi_B + \chi_A\chi_B + \chi_B\chi_A](\alpha\beta - \beta\alpha) \tag{3.51}$$

$$\Phi_1^{\mathrm{RHF}} = [\chi_A\chi_A + \chi_B\chi_B - \chi_A\chi_B - \chi_B\chi_A](\alpha\beta - \beta\alpha) \tag{3.52}$$

$$\Phi_2^{\mathrm{RHF}} = [\chi_A\chi_A + \chi_B\chi_B](\alpha\beta - \beta\alpha) - [\chi_A\chi_B](\alpha\beta + \beta\alpha) \tag{3.53}$$

$$\Phi_3^{\mathrm{RHF}} = [\chi_A\chi_A - \chi_B\chi_B](\alpha\beta - \beta\alpha) + [\chi_A\chi_B - \chi_B\chi_A](\alpha\beta + \beta\alpha) \tag{3.54}$$

The excited states Φ_2^{RHF} and Φ_3^{RHF} can be combined to construct the singlet and triplet states, ${}^1\Phi_-$ and ${}^3\Phi_+$ respectively:

$${}^1\Phi_- = \Phi_2^{\mathrm{RHF}} - \Phi_3^{\mathrm{RHF}} = [\chi_A\chi_A - \chi_B\chi_B](\alpha\beta - \beta\alpha) \tag{3.55}$$

$${}^3\Phi_+ = \Phi_2^{\mathrm{RHF}} + \Phi_3^{\mathrm{RHF}} = [\chi_A\chi_B - \chi_B\chi_A](\alpha\beta + \beta\alpha) \tag{3.56}$$

Thus the first term in the expansion of Φ_0^{UHF} (3.49) can be expanded as a linear combination of the Φ_0^{RHF} and Φ_1^{RHF} determinants and therefore describes a *pure* singlet state. The second term (3.50) has terms in common with the triplet state ${}^3\Phi_-$. Thus the ground state UHF determinant contains both singlet and triplet states, and is not a pure spin state — this phenomenon is known as spin contamination. Spin contamination is gen-

erally most significant near transition states, where bonds are stretched and are not at the RHF limits. The UHF description overestimates biradical character in homolytic dissociation (i.e. the tendency for a bond to break into two radicals rather than two ions). Spin contamination is not constant along the reaction coordinate, which can lead to the actual transition state appearing as a bogus local minimum on the UHF potential energy surface. In addition, the UHF solution is often too flat near saddle points, which can lead to UHF barriers being lower than RHF barriers. The UHF wavefunction lowers the energy by allowing some occupation of excited states (i.e. introduces some correlation), but increases the energy by higher energy spin states. The point at which these two effects are equal is known as the instability point: as a bond is stretched, the correlation energy increases until it exceeds the spin contamination energy at this point.

For pure spin states, the expectation value of the $\hat{S}^2$ operator is given by the expression $\langle \hat{S}^2 \rangle = \hat{S}_z(\hat{S}_z + 1)$. This equality no longer holds when spin contamination is involved; it is evaluated by taking the spatial overlap between all pairs of α and β spin orbitals:

$$\langle \hat{S}^2 \rangle = \hat{S}_z(\hat{S}_z + 1) + N_\beta - \sum_{ij}^{N_{MO}} \langle \phi_i^\alpha | \phi_j^\beta \rangle^2 \tag{3.57}$$

Therefore if α and β are identical, there is no spin contamination.

3.5 Electron correlation and post-Hartree-Fock methods

The Hartree-Fock method captures approximately 99% of the total energy of a system; the remaining 1% is called the "correlation energy" and although relatively small, is often important in describing chemical interactions. Mean field models such as Hartree-Fock and density functional theory assume that the probability of an electron classically

occupying a specific point in space is *independent* of the position of all other electrons in the system, and instead depends on an all-encompassing potential. Lewars uses the analogy of an individual walking through a crowd[106]: given the knowledge of the positions and motions of every other person in the crowd, it is possible to avoid collisions by adjusting, or correlating one's route accordingly; this information is not available in the case of a "mean field." Since interactions are not treated in a pairwise manner in the HF approximation, they are allowed to get too close to each other on average, resulting in an energy that is too high, even in the limit of an infinite basis set.

Löwdin defines the correlation energy in the following terms:[106;107]

> "The correlation energy for a certain state with respect to a specified Hamiltonian is the difference between the exact eigenvalue of the Hamiltonian and its expectation value in the Hartree-Fock approximation for the state under consideration"

In other words, the correlation energy is defined as the difference between the true energy of the system and the Hartree-Fock energy with an infinite basis set — thus the correlation energy will always be negative. In Lewars' words, the correlation energy is the "energy that the Hartree-Fock procedure fails to account for"[106].

$$E_{\text{correlation}} = E_{\text{exact}} - E_{\text{HF limit}} \tag{3.58}$$

Hartree-Fock theory only includes correlation arising as a result of the Pauli exclusion principle, and there is no correlation between two electrons in the same molecular orbital (MO). Correlation between electrons with opposite spins (Coulomb correlation) has both intra- and inter-orbital contributions, and will therefore be more significant than correlation between electrons with the same spin (Fermi correlation). Electron correlation is the tendency for electrons to "avoid" each other, thereby reducing the energy of the system. Even notional uncharged electrons would be surrounded by

a region that cannot be occupied by another uncharged electron of the same spin (the Fermi hole); there is a similar exclusion zone which arises from electrostatic repulsion (the Coulomb hole). Thus correlation energy arises from two distinct effects. Dynamic correlation is the "instantaneous" correlation (electrons in the same spatial orbital), and static correlation is where electrons avoid each other on a more "permanent" basis (electrons in different spatial orbitals). By way of example, correlation between the two electrons in a helium atom is purely dynamic, whereas correlation between the electrons in a hydrogen molecule is purely static. There is no convenient way of decomposing the correlation energy into dynamic and static contributions.

There are three general strategies for adding correlation effects to the Hartree-Fock formalism:

- Explicitly include interelectronic distances as a variable in the Schrödinger equation. This is usually computationally intractable.
- Explicitly include the wavefunction of electron configurations other than the ground state, i.e. excited states. This forms the basis for the configuration interaction and coupled cluster methods.
- Treat the real system as a perturbed Hartree-Fock system, as in many body (Møller-Plesset) perturbation theory.

3.5.1 Configuration interaction (CI)

It is possible to improve on the Hartree-Fock description by allowing electrons to occupy virtual molecular (anti-bonding) orbitals, essentially giving them more room to avoid each other. This can be achieved using a multi-determinant wavefunction. In the HF method, the components ψ_i of the many body wavefunction ψ are constructed as

a linear combination of M basis functions, χ_s.

$$\psi_i = \sum_{s=1}^{M} c_{is}\chi_s \tag{3.59}$$

Using the CI method, the components Ψ_i of the wavefunction Ψ are built using a linear combination of N Slater determinants ϕ_s:

$$\Psi_i = \sum_{s=1}^{N} c_{is}\phi_s \tag{3.60}$$

In this representation, ϕ_1 is the ground state HF determinant, and the rest represent excited states formed by promoting one or more electrons from occupied MOs to virtual MOs. Just as M basis functions result in M MOs, L determinants result in L wavefunctions. Ψ_1 is the ground state wavefunction, and $\Psi_{i>1}$ are wavefunctions for excited states. Thus electron correlation methods are "two dimensional," requiring two bases: the basis set used to expand electronic wavefunctions, and the set of determinants to model correlation. This makes them prohibitively expensive for all but the smallest systems.

Excited Slater determinants are generated by replacing MOs that are occupied in the HF determinant with MOs that are unoccupied. The excitation level depends on the number of such replacements: singles (S), doubles (D) triples (T) and quadruples (Q) denote one, two, three and four occupied orbitals in the determinant replaced with virtual MOs respectively, up to a potential L excitations. For any basis set larger than minimal, there are more virtual MOs than occupied MOs, thus number of excited Slater determinants increases factorially with the number electrons *and* basis functions.

The CI method is uses a variational approach comparable to Hartree-Fock. A set of *fixed* HF MOs are used to build Slater determinants (ϕ), and a trial wavefunction is

written as a linear combination of these determinants:

$$\Psi_{\mathrm{CI}} = a_0\phi_{\mathrm{HF}} + \sum_S a_S\phi_S + \sum_D a_D\phi_D + \sum_T a_T\phi_T + \ldots \tag{3.61}$$

$$= \sum_i a_i\phi_i \tag{3.62}$$

Where ϕ_{HF} is the HF determinant, ϕ_S are singly excited determinants, ϕ_D are double excited and so on. Without going into the mathematics in detail, this is solved variationally using Lagrange multipliers, subject to the constraint that the CI wavefunction is normalised. The Lagrangian L is therefore,

$$L = \langle\Psi_{\mathrm{CI}}|H|\Psi_{\mathrm{CI}}\rangle - \lambda(\langle\Psi_{\mathrm{CI}}|\Psi_{\mathrm{CI}}\rangle - 1) \tag{3.63}$$

where the first bracket is the energy of the CI wavefunction, and the second bracket is its norm. Exploiting the orthogonality of the MOs, this reduces to,

$$L = \sum_{i=0} a_i^2 E_e + \sum_{i=0}^{j\neq 0} a_i a_j \langle\phi_i|H|\phi_j\rangle - \lambda(\sum_{i=0} a_i^2 - 1) \tag{3.64}$$

The variational procedure requires that all derivatives of the Lagrangian with respect to a_i are set to zero:

$$\frac{\partial L}{\partial a_i} = 2\sum_i a_j\langle\phi_j|H|\phi_j\rangle - 2\lambda a_i = 0 \tag{3.65}$$

$$a_i(E_i - \lambda) + \sum_{j\neq 0} a_j\langle\phi_i|H|\phi_j\rangle = 0 \tag{3.66}$$

Here, it turns out that the Lagrange multiplier λ is the CI energy. The variational problem has become the set of secular CI equations, which can be written as a matrix equation (using $H_{ij} = \langle\phi_i|H|\phi_j\rangle$) and solved by diagonalising:

$$(\mathbf{H} - E\mathbf{I})\mathbf{a} = 0 \tag{3.67}$$

The lowest eigenvalue is the CI energy, the second lowest is the energy of the first excited state, and so on.

In principle, the full CI energy is exact in the limit of an infinite basis set; however, as mentioned, the number of determinants increases factorially with the number of electrons and basis functions, so only extremely small systems are computationally tractable. In practice, the excitation level as in equation (3.61) must be truncated. Truncation at the singles level results in the configuration interaction with singles method (CIS), which gives no improvement over HF energies. Inclusion of only doubles (CID) results in an improvement, but is only marginally more expensive than including singles and doubles (CISD). CISD is the normal practical limit for calculations, and scales as M^6 (where M is the number of basis functions).

The CI method generates excited electron states from a single reference state,the Hartree-Fock determinant. In many cases this is not an appropriate choice for the reference state, for example, ozone (O_3) formally resembles a closed shell singlet species, but in fact has significant open shell biradical character (figure 3.1). In such cases, a multireference wavefunction must be used by invoking such methods as multiconfiguration SCF (MCSCF), multireference CI (MRCI), complete active state SCF (CASSCF) and restricted active space SCF (RASSCF).

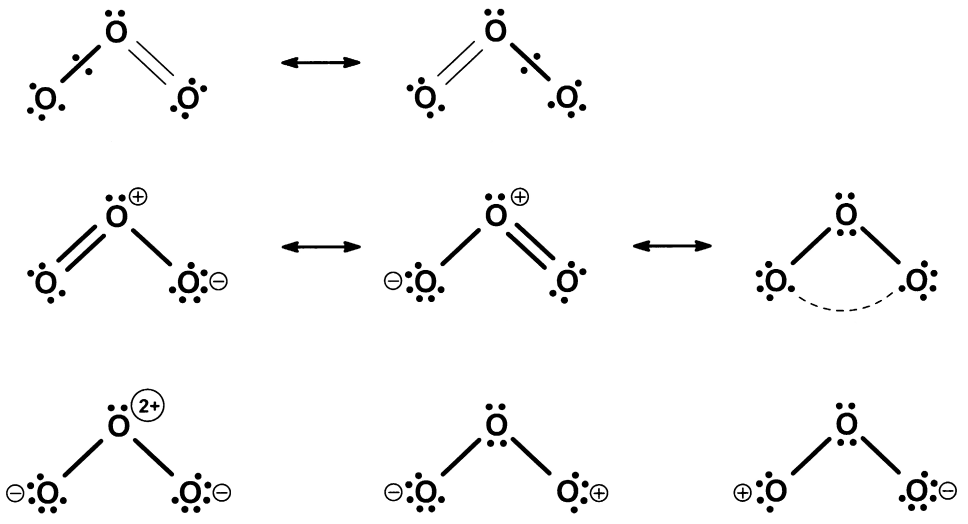

Figure 3.1: Resonance structures ozone[15]. The presence of *non-equivalent* resonance structures requires the use of multireference methods in order to recover all of the correlation energy.

3.5.2 Møller-Plesset perturbation theory

In perturbation theory, it is assumed that the problem at hand differs only slightly from a "reference" problem that has already been solved. In the case of the Schrödinger equation, the perturbed Hamiltonian H is written,

$$H = H_0 + \lambda H' \tag{3.68}$$

where H_0 is the reference Hamiltonian for the solved reference problem, H' is the perturbation, and the parameter λ varies from 0 to 1 such that $\lambda = 0$ corresponds to the reference problem, which is:

$$H_0 \phi_i = E_i \phi_i \tag{3.69}$$

where ϕ_i is a complete set of orthonormal solutions. The perturbed Schrödinger equation is then,

$$H\psi = W\psi \tag{3.70}$$

As the perturbation is increased by varying λ, the energy and wavefunction increase continuously, and can be expressed as a Taylor expansion in terms of λ:

$$W = W_0 + \lambda W_1 + \lambda^2 W_2 + \dots \tag{3.71}$$

$$\psi = \psi_0 + \lambda \psi_1 + \lambda^2 \psi_2 + \dots \tag{3.72}$$

Substituting these into the perturbed Schrödinger equation (3.70):

$$(H_0 + \lambda H')(\psi_0 + \lambda\psi_1 + \lambda^2\psi_2 + \dots) = (W_0 + \lambda W_1 + \lambda^2 W_2 + \dots) \tag{3.73}$$

Collecting terms with the same powers of λ:

$$H_0\psi_n + H'\psi_{n-1} = \sum_{i=0}^{n} W_i \psi_{n-i} \tag{3.74}$$

It can be show that the nth order wave function can be used to calculate the $(2n+1)$th order energy:

$$W_{2n+1} = \langle \psi_n | H' | \psi_n \rangle - \sum_{k,J=0}^{n} W_{2n-1-k-l} \langle \psi_k | \psi_l \rangle \tag{3.75}$$

The corrections to the unperturbed energy and wavefunction become more and more complicated to express as the perturbation order is increased, so I will only mention the first and second order corrections. Bearing in mind that the nth order corrections to the energy and wavefunction can be expressed in terms of the matrix elements of the perturbation operator over the *unperturbed* wavefunction ϕ_0 and the *unperturbed* energy E_0. Starting from equation (3.74),

1. First order: $H_0\psi_1 + H'\phi_0 = W_0\psi_1 + W_1\phi_0$ where $\psi_1 = \sum_i c_i \phi_i$

$$W_1 = \langle \phi_0 | H' | \phi_0 \rangle \tag{3.76}$$

$$c_j = \frac{\langle \phi_j | H' | \phi_0 \rangle}{E_0 - E_1} \tag{3.77}$$

2. Second order: $H_0\psi_2 + H'\psi_1 = W_0\psi_2 + W_1\psi_1 + W_2\phi_0$ where $\psi_2 = \sum_i d_i\phi_i$

$$W_2 = \sum_{i=0} \frac{\langle\phi_0|H'|\phi_i\rangle\langle\phi_i|H'|\phi_0\rangle}{E_0 - E_1} \tag{3.78}$$

$$d_j = \sum_{i=0} \frac{\langle\phi_j|H'|\phi_i\rangle\langle\phi_i|H'|\phi_0}{(E_0 - E_j)(E_0 - E_i)} - \frac{\langle\phi_j|H'|\phi_0\rangle\langle\phi_0|H'|\phi_0\rangle}{(E_0 - E_j)^2} \tag{3.79}$$

Møller-Plesset perturbation theory is formulated by choosing a sum over Fock operators (equation (3.21)) to be the unperturbed Hamiltonian; this is the only choice that results in a size-extensive method, although it is not necessarily consistent with the requirement that the perturbation is small compared with H_0. For an N electron system:

$$H_0 = \sum_{i=1}^{N} \mathscr{F}_i = \sum_{i=1}^{N} (h_i + \sum_{j=1}^{N} (J_j - K_j)) \tag{3.80}$$

$$= \sum_{i=1}^{N} h_i + \sum_{i=1}^{N}\sum_{j=1}^{N} \langle g_{ij}\rangle \tag{3.81}$$

$$= \sum_{i=1}^{N} h_i + 2\langle V_{ee}\rangle \tag{3.82}$$

$$H' = H - H_0 = \sum_{i=1}^{N}\sum_{j=1}^{N} g_{ij} - \sum_{i=1}^{N}\sum_{j=1}^{N} \langle g_{ij}\rangle \tag{3.83}$$

$$= V_{ee} - 2\langle V_{ee}\rangle \tag{3.84}$$

Here, V_{ee} is the interelectronic potential, and the final expression for H' is referred to as the "fluctuation potential." The zeroth order wavefunction is therefore simply the Hartree-Fock determinant, and the zeroth order energy is,

$$W_0 = \langle\phi_0|H_0|\phi_0\rangle = \langle\phi_0|\sum_{i=1}^{N} F_i|\phi_0\rangle = \sum_{i=1}^{N} \epsilon_i \tag{3.85}$$

which is the sum of HF molecular orbital energies. The MO energy is the energy of an electron in the field of all nuclei and *all other electrons*, therefore at zeroth order, electron-electron repulsion is double counted. Using equation (3.76), the first order

correction is,

$$W_1 = \langle \phi_0 | H' | \phi_0 \rangle = \langle V_{ee} \rangle - 2\langle V_{ee} \rangle = -\langle V_{ee} \rangle \tag{3.86}$$

which corrects the spurious double counting. Therefore the first order Møller-Plesset (where MPn denotes the nth order Møller-Plesset method) recovers the total energy from the Hartree-Fock method, and in this scheme, the lowest level of approximation for electron correlation occurs at the second order. The second order energy correction is,

$$W_2 = \sum_{i<j}^{\text{occ}} \sum_{a<b}^{\text{vir}} \frac{\langle \phi_0 | H' | \phi_{ij}^{ab} \rangle \langle \phi_{ij}^{ab} | H' | \phi_0 \rangle}{E_0 - E_{ij}^{ab}} \tag{3.87}$$

$$E(\text{MP2}) = \sum_{i<j}^{\text{occ}} \sum_{a<b}^{\text{vir}} \frac{\langle \phi_i \phi_j | \phi_a \phi_b \rangle - \langle \phi_i \phi_j | \phi_b \phi_a \rangle}{\epsilon_i + \epsilon_j - \epsilon_a - \epsilon_b} \tag{3.88}$$

The Møller-Plesset method essentially allows electrons to partially occupy virtual MOs, giving them more room to "avoid" each other, thus lowering the total energy. The denominator of equation (3.88) shows that as the energy difference between the occupied and virtual MOs increases the second order contribution to the energy becomes smaller since it becomes harder to promote electrons, meaning that higher order excitations have a smaller contribution to the correlation energy.

The perturbation is a two-electron operator, so all matrix elements involving triples, quadruples and higher order excitations are zero. It can be shown that the contribution from singly excited states is zero, leaving only contributions from doubles. This appears as a sum over doubly excited determinants, where two electrons are promoted from occupied (occ) MOs i and j to virtual (vir) MOs a and b. MP2 generally accounts for 80–90% of the correlation energy[108]. It is relatively cheap, since the energy correction is calculated as a sum of two electron integrals over HF MOs, which scale as M^4, but there is a transformation from the atomic orbital basis to the molecular orbital basis which pushes this up to M^5. This makes MP2 the cheapest post-Hartree-Fock method

of introducing correlation effects. MP3 and MP4 scale as M^6 and M^7 respectively, and are still computationally feasible; MP4 requires a similar amount of effort to a CISD calculation, and captures 95-98% of the correlation energy.

MPn methods are not variational, and as such do not represent an upper bound to the energy; this may result in some error cancellation. The main limitation is the assumption that the zeroth order wavefunction is a good approximation to the real system, which in turn allows the assumption that the perturbation is small. This assumption does not hold for systems that are not well described in the HF approximation (for example, systems with significant multireference character). A poor reference state description can result in slow or erratic convergence. Another problem arises as a consequence of the theory of infinite series convergence: the perturbation coefficient λ is allowed to take complex values, and the series is only convergent inside the "convergence radius" $|\lambda| < R$, which allows for non-physical states such as $\lambda < 0$, representing an attractive force between electrons. These "intruder states" can prevent the convergence.

3.5.3 The coupled cluster method

Whilst perturbation theory adds all types of correction (single, double, triple etc.) to nth order, the coupled cluster method includes all corrections of a given type to infinite order. The method defines an "excitation operator" T,

$$T = T_1 + T_2 + \ldots + T_N \tag{3.89}$$

such that T_i acting on the HF reference wavefunction generates all ith excited Slater determinants. For example,

$$T_1\phi_0 = \sum_{i}^{\text{occ}}\sum_{a}^{\text{vir}} t_i^a \phi_i^a \tag{3.90}$$

$$T_2\phi_0 = \sum_{k<j}^{\text{occ}}\sum_{a<b}^{\text{vir}} t_{ij}^{ab} \phi_{ij}^{ab} \tag{3.91}$$

The expansion coefficients t are called "amplitudes." An intermediate normalisation generates the CI wavefunction.

$$\psi_{\text{CI}} = (1+T)\phi_0 = (1+T_1+T_2+\ldots)\phi_0 \tag{3.92}$$

The coupled cluster wavefunction is,

$$\psi_{\text{CC}} = e^T\phi_0 = (1+T+\frac{1}{2}T^2+\frac{1}{6}T^3+\ldots)\phi_0 = \sum_{k=0}^{\infty}\frac{1}{k!}T^K \tag{3.93}$$

Substituting equation (3.89) and collecting all singles, doubles, triples etc. gives,

$$e^T = 1+T_1+(T_2+\frac{1}{2}T_1^2)+(T_3+T_2T_1+\frac{1}{6}T_1^3)+(T_4+T_3T_1+\frac{1}{2}T_2^2+\frac{1}{2}T_2T_1^2+\frac{1}{24}T_1^4)+\ldots \tag{3.94}$$

These terms represent the HF reference, all singles, all doubles, all triples, all quadruples and so forth. Terms in this expansion can be "connected" (for example, T_4, which represents four electrons interacting simultaneously) or "disconnected" (T_2^2 representing two non-interacting pairs of electrons interacting). The key difference between the coupled cluster and CI methods is that the coupled cluster equations contain "product" states such as T_2T_1 and T_1^3, whereas the CI equations only contain "true" states such as T_2 and T_3. The formal coupled cluster Schrödinger equation is:

$$He^T\phi_0 = Ee^T\phi_0 \tag{3.95}$$

The energy can be evaluated as the expectation value of the coupled cluster wavefunction, and the variational principle used to find the amplitudes.

$$E_{\mathrm{CC}}^{\mathrm{var}} = \frac{\langle \psi_{\mathrm{CC}} | H | \psi_{\mathrm{CC}} \rangle}{\langle \psi_{\mathrm{CC}} | \psi_{\mathrm{CC}} \rangle} = \frac{\langle e^T \phi_0 | H | e^T \phi_0 \rangle}{\langle e^T \phi_0 | e^T \phi_0 \rangle} \tag{3.96}$$

The expansion of the exponential operator according to equation (3.93) contains non-vanishing terms up to $\frac{1}{N!}T^N$, where N is the number of electrons. Therefore, this method is tractable only for very small systems. When the HF orbitals are used to construct the Slater determinants, the one-electron integrals vanish due to Brillouin's theorem, and the only non-vanishing terms are two-electron integrals.

$$E_{\mathrm{CC}} = E_0 + \sum_{i<j}^{\mathrm{occ}} \sum_{a<b}^{\mathrm{vir}} (t_{ij}^{ab} + t_i^a t_j^b - t_i^b t_j^a)(\langle \phi_i \phi_j | \phi_a \phi_b \rangle - \langle \phi_i \phi_j | \phi_b \phi_a \rangle) \tag{3.97}$$

This is the general coupled cluster equation.

The equations above are exact, containing all terms up to T^N where N is the number of electrons, and give results identical to a full CI calculation. In practice, it is necessary to truncate the expansion to include only terms up to the nth excitation. Truncating the series at $T = T_1$ offers no improvement over the HF description due to Brillouin's theorem. Including only $T = T_2$ (coupled cluster doubles, CCD) significantly improves the description, and scales as M^6 (for M basis function). However, singles can be included in a CCD calculation, improving the description without increasing the cost significantly (scaling as M^6), resulting in coupled cluster singles and doubles (CCSD). Truncating the series at $T = T_3$ gives coupled cluster singles, doubles and triples (CCSDT), which scales as M^8. CCSD(T) involves calculating the triples perturbatively rather than iteratively, using the MP4 formula with CCSD amplitudes, and scales as M^7. The CCSD(T) approach is regarded as the benchmark for moderately sized molecular calculations[106].

3.6 Density Functional Theory (DFT)

Density functional theory has revolutionised condensed matter theory fields by allowing the replacement of intractable systems of many-body wave mechanics equations with relatively simple sets of equations based on electron density. It has been shown to usually outperform Hartree-Fock theory in terms of accuracy.

In their 1964 paper[109], Hohenberg and Kohn made the first step towards a workable density functional theory with their theorems[110]:

1. For any system of interacting particles in an external potential $V_{\text{ext}}(\mathbf{r})$, the potential $V_{\text{ext}}(\mathbf{r})$ is defined uniquely by the ground state particle density $n(\mathbf{r})$.

2. It is possible to define a universal energy functional of the density, $E[n]$, valid for any $V_{\text{ext}}(\mathbf{r})$. For any particular V_{ext}, the ground state energy is the global minimum of this functional.

The computational expediency gains from using DFT stem from the fact that for a N electron system, the electron density is the square of the wavefunction integrated over $N-1$ coordinates, depends on three coordinates, and is independent of the number of electrons (N). This is in contrast with wavefunction methods, which use $3N$ coordinates ($4N$ if the spin is included) and are therefore scale less favourably with system size.

The problem can be formulated as follows: the Hamiltonian (H) for a system of interacting electrons is the sum of the kinetic (T) and mutual interaction (V) energy of the electrons, and an external potential (U) representing the influence of nuclear attraction.

$$H = T + U + V = H_0 + V \tag{3.98}$$

H_0 is the "fixed" part of the Hamiltonian, the sum of the internal and kinetic energies of the system, whilst V is a sum of electronic potentials $v(\mathbf{r}_i)$ and is determined by the

Kohn-Sham theory.

$$V = \sum_{i=1}^{N} v(\mathbf{r}_i) \tag{3.99}$$

If the many-body wavefunction is ψ, then the ground state energy E_g is given by the integral,

$$E_g = \langle \psi | H_0 + V | \psi \rangle \tag{3.100}$$

The electron density $n(\mathbf{r})$ is in fact a sum of two spin polarised electron densities in the open shell case, $n(\mathbf{r}) = n_\uparrow(\mathbf{r}) + n_\downarrow(\mathbf{r})$. The density is defined as:

$$n(\mathbf{r}) = \sum_\sigma n(\mathbf{r}, \sigma) = \sum_\sigma \sum_{i=1}^{N^\sigma} |\psi_i^\sigma(\mathbf{r})|^2 \tag{3.101}$$

where σ is the spin. Although I have dropped the spin superscript in the remaining equations, they are straightforward to generalise from the closed shell case.

Since E_g is uniquely determined by the electron density, it can be written in the following functional form, with the external field interaction separated from the inter-electron interactions:

$$E_g[n(\mathbf{r})] = \int \mathrm{d}\mathbf{r} v(\mathbf{r}) n(\mathbf{r}) + F[n(\mathbf{r})] \tag{3.102}$$

Here, $F[n(\mathbf{r})]$ is the ground-state expectation value of H_0 when the electron density is $n(\mathbf{r})$. Given the correct density, E_g will be the ground state energy. The minimisation can be achieved using the variational principle and the constraint that the number of electrons is fixed, namely:

$$N[n] = \int n(\mathbf{r}) d\mathbf{r} = N \tag{3.103}$$

It is convenient to extract the long-range Coulomb interaction (the Hartree energy) from $F[n]$:

$$F[n] = \frac{1}{2} \int \int \frac{n(\mathbf{r}) n(\mathbf{r}')}{|\mathbf{r} - \mathbf{r}'|} \mathrm{d}\mathbf{r} \mathrm{d}\mathbf{r}' + G[n], \tag{3.104}$$

where $G[n]$ is another functional. Thus the energy functional (3.102) can be expanded:

$$E[n] = \int v(\mathbf{r})n(\mathbf{r})\mathrm{d}\mathbf{r} + \frac{1}{2}\int\int \frac{n(\mathbf{r})n(\mathbf{r}')}{|\mathbf{r}-\mathbf{r}'|}\mathrm{d}\mathbf{r}\mathrm{d}\mathbf{r}' + G[n] \tag{3.105}$$

Kohn and Sham developed a method by which the Hohenberg-Kohn theorems could be employed practically to determine the properties of a many body system using the electron density as a basic variable in their 1965 paper[111]. Their strategy was to construct a more tractable 'auxiliary system' via the Kohn-Sham ansatz[110]:

- The ground state density of the interacting system is the same as that of some chosen non-interacting system.

By this assumption, Kohn and Sham showed that it is possible to reduce a complicated many-body problem to an easier set of single-body problems. The many-body problem is recast as a set of Schrödinger-like single-body equations under the influence of an effective potential, V_{eff}. Starting from equation (3.104), the functional $G[n]$ is expressed as a sum of the kinetic energy of non-interacting electrons ($T_s[n]$) and a term (which is exact by definition) encompassing the exchange and correlation components of the electron-electron interactions, $E_{\mathrm{XC}}[n]$:

$$G[n] = T_s[n] + E_{\mathrm{XC}}[n] \tag{3.106}$$

Applying the variational principle to (3.105), and requiring that the number of electrons remains constant,

$$\int \delta n(\mathbf{r})\mathrm{d}\mathbf{r} = 0, \tag{3.107}$$

one obtains the equation,

$$\int \delta n(\mathbf{r})\left\{\varphi(\mathbf{r}) + \frac{\delta T_s[n]}{\delta n(\mathbf{r})} + \mu_{\mathrm{XC}}(n(\mathbf{r}))\right\}\mathrm{d}\mathbf{r} = 0, \tag{3.108}$$

where

$$\varphi(\mathbf{r}) = v(\mathbf{r}) + \int \frac{n(\mathbf{r}')}{|\mathbf{r}-\mathbf{r}'|}\mathrm{d}\mathbf{r}', \tag{3.109}$$

and μ_{XC} is the chemical potential of a uniform electron gas of density $n(\mathbf{r})$, and depends on the choice of functional $E_{\mathrm{XC}}[n]$. It can be shown that (3.108) is exactly the same as for a non-interacting electron gas under the influence of an effective external potential V_{ext}:

$$V_{\mathrm{eff}} = \varphi(\mathbf{r}) + \mu_{\mathrm{XC}}(n(\mathbf{r})) \tag{3.110}$$

Applying the Lagrange undetermined multipliers method to the variational problem results in a set of Schrödinger-like equations, the Kohn-Sham equations:

$$H_{\mathrm{KS}}\psi_i(\mathbf{r}) = \epsilon_i\psi_i(\mathbf{r}) \tag{3.111a}$$

$$H_{\mathrm{KS}} = -\frac{1}{2}\nabla^2 + V_{\mathrm{eff}}(\mathbf{r}) \tag{3.111b}$$

$$V_{\mathrm{eff}}(\mathbf{r}) = V_{\mathrm{ext}}(\mathbf{r}) + V_{\mathrm{Hartree}}(\mathbf{r}) + V_{\mathrm{XC}}(\mathbf{r}) \tag{3.111c}$$

The electron density is related to the Kohn-Sham orbitals $\psi_i(\mathbf{r})$ by the relationship

$$n(\mathbf{r}) = \sum_{i=1}^{N} |\psi_i(\mathbf{r})|^2 \tag{3.112}$$

The Schrödinger-like Kohn-Sham equation is complicated by the fact that the electron density, $n(\mathbf{r})$ appears on both sides — it must therefore be solved self consistently. The following procedure[110] is generally used:

1. Make an initial guess of electron density $n(\mathbf{r})$.
2. Calculate the effective potential V_{eff}.
3. Solve the Kohn-Sham equations (3.111).
4. Calculate the electron density (3.112).

5. If $n(\mathbf{r})$ is not self-consistent, return to step 2. If self-consistency has been achieved, proceed.

6. Calculate the relevant quantities: energy, forces, stresses, eigenvalues etc.

The Kohn-Sham equations, in principle, are exact. The difficulty arises in the choice of the exchange-correlation functional, $E_{\mathrm{XC}}[n]$. After the local spin-density approximation, there is no established analytical or consistent method for generating new and more accurate functionals. As established in equation (3.17), the spurious self-interaction terms cancel between the Coulomb and exchange terms in Hartree-Fock theory; DFT exchange-correlation functionals, in contrast, contain self interaction terms that can only be corrected at great computational expense (although, in the limit of exact DFT, these would vanish).

The advantage DFT has over HF theory is the inclusion of correlation terms beyond exchange, namely the van der Waals energy. This is a long range effect, and can be physically explained as the tendency of separate electron densities to "avoid" each other, resulting in transient dipoles, which weakly attract each other. Whilst significant, it is by far the smallest contribution to the total energy, constituting around 1%. In practice, it is very difficult to calculate the exact correlation contribution, so a convenient (but not the only) definition of the correlation energy is:

$$E_{\mathrm{C}} = E_{\mathrm{XC}}^{\mathrm{DFT}} - E_{\mathrm{X}}^{\mathrm{HF}} \tag{3.113}$$

i.e. the difference between the exchange correlation energy as calculated by DFT and the *exact* exchange energy as calculated by HF.

There are several levels of approximation used in the construction of the exchange-correlation functional (3.114), which treat it with varying degrees of complexity; these are rungs of what Perdew and Schmidt call the 'Jacob's ladder of density functional approximations'[112]. Higher rungs of the ladder incorporate theory from lower rungs with

improvements, and generally (but not necessarily) represent a higher level of accuracy at greater computational expense.

$$E_{\mathrm{XC}}[n(\mathbf{r})] = \int \mathrm{d}\mathbf{r} n(\mathbf{r}) \epsilon_{\mathrm{XC}}(n(\mathbf{r}); \mathbf{r}) \tag{3.114}$$

The five rungs of the ladder are (from highest to lowest)[112]:

- Exact exchange and exact partial correlation (hybrid)
- Exact exchange and compatible correlation (hybrid)
- Meta-generalised gradient approximation (meta-GGA)
- Generalised gradient approximation (GGA)
- Local spin density approximation (LSDA/LDA)

The computational costs for the first three rungs are fairly similar, but they rapidly increase thereafter[113]. Post Hartree-Fock methods such as MP2 and CCSD offer even higher accuracies at extreme computational costs.

The lowest level is the local spin density approximation (LSDA), which simplifies to the local density approximation (LDA) in closed shell systems. Starting from the ansatz that the density is a slowly varying function, it can be assumed that the density can be treated *locally* as a uniform electron gas, i.e. truncating the expansion of $E_{\mathrm{C}}[n]$ in terms of the energy of homogeneous electron gas after the first term:

$$E_{\mathrm{XC}}[n] = \int \epsilon_{\mathrm{XC}}(n) n \mathrm{d}\mathbf{r} + \int \epsilon^{(2)}_{\mathrm{XC}}(n) |\nabla n|^2 \mathrm{d}\mathbf{r} + \ldots \tag{3.115}$$

where ϵ_{XC} is the energy per electron in a *homogeneous* electron gas. The rationale for this approximation is that the range of exchange and correlation effects is short for densities characteristic of solids. One would expect it to work best where the electron gas is close to homogeneous as in solids, but fail in inhomogeneous cases where the electron density

tends to zero outside atoms. In practice, the LDA tends to underestimate exchange energy by $\sim 10\%$, and overestimate the correlation energy by a factor of ~ 2, resulting in significant overbinding[108]. The performance of LDA models is similar to that of HF theory.

The next level of approximation is the generalised gradient approximation (GGA), in which the density and its derivatives are used to construct the exchange-correlation functional (this is more complicated that the simple Taylor expansion in equation (3.115), hence "generalised"). These methods are sometimes known as "semi-local," because they use the require the density at position $\mathbf{r}$, and in and infinitesimal neighbourhood surrounding $\mathbf{r}$. GGA models generally perform much better than LDA methods, giving better geometries and vibrational frequencies; the performance is comparable to *ab initio* second order Møller-Plesset (MP2) methods.

The third rung of the ladder, meta-GGA, uses kinetic energy densities $\tau_\sigma(\mathbf{r})$, and sometimes the Laplacian of the electron density, $\nabla^2 n(\mathbf{r})$, as ingredients of the exchange-correlation functional. Meta-GGA is the highest rung that does not utilise full non-locality, instead using a non-local functional of electron density and a semi-local functional of orbitals. It is thus potentially not much more expensive than a pure GGA but has the advantage of eliminating self-correlation, which can have a severe effect in low density systems. Meta-GGA functionals generally result in better atomisation energies, metal surface energies and lattice constants, but bond lengths (especially hydrogen bonds) can be worse than for pure GGA functionals.

The highest level of approximation involving density functional theory is the "hybrid" model, which takes elements of both HF theory and DFT. The exchange-correlation energy is related to the potential connecting a non-interacting "reference" system and a real interacting system by the adiabatic connection formula (ACF):

$$E_{\mathrm{XC}} = \int_0^1 \langle \psi_\lambda | V_{\mathrm{XC}}(\lambda) | \psi_\lambda \rangle \mathrm{d}\lambda, \tag{3.116}$$

where V_{XC} is the exchange-correlation potential, and the integration coupling constant λ can be considered to "turn on" electron-electron correlation interactions. The $\lambda = 1$ case corresponds to the real, fully interacting system, whilst $\lambda = 0$ represents a system of non-interacting electrons in an effective one body potential with the same density as the real system (the Kohn-Sham auxiliary system)[114], and exact exchange as prescribed by HF theory. Becke proposed a simple correction to the $\lambda = 0$ case to incorporate correlation into an exact exchange framework:

$$E_{\mathrm{XC}} = E_{\mathrm{XC}}^{\mathrm{DFT}} + a_0(E_{\mathrm{X}}^{\mathrm{exact}} - E_{\mathrm{X}}^{\mathrm{DFT}}), \tag{3.117}$$

where $E_{\mathrm{XC}}^{\mathrm{DFT}}$ is approximate DFT exchange-correlation energy, $E_{\mathrm{X}}^{\mathrm{exact}}$ is the exact exchange energy from HF theory, $E_{\mathrm{X}}^{\mathrm{DFT}}$ is the contribution to exchange energy contribution from DFT, and a_0 is a parameter determining the 'Hartree-Fock character'[114]. Empirical fitting atomisation energies suggest that a value of $a_0 \simeq \frac{1}{4}$ is optimal[114]; Perdew *et al.* later justified this value using fourth order perturbation theory[115] — thus the PBE0 hybrid functional incorporates 25% exact exchange into the PBE GGA functional. There are various other recipes for incorporating exact exchange using different numbers of parameters, for example, B3LYP uses three mixing parameters in a variation of equation (3.117). Although such hybrid functionals are generally more accurate than pure GGA functionals (especially at predicting reaction barriers, which GGA functionals tend to grossly underestimate), they require the solution of the Hartree-Fock equations and are therefore much more computationally expensive.

DFT calculations require a similar amount of computational effort to HF calculations, but have the potential to be much more accurate due to the implicit inclusion of correlation effects. It has been shown (for example, in Feibelman (2008)[116]) that DFT methods can characterise hydrogen bonding well (when HF theory fails, for example, in Casassa *et al.* (2005)[69]), which is an important consideration when modelling ice. One of its main shortcomings is the failure of current functionals to characterise disper-

sion (Van der Waals-type) interactions; for example, the inherent overbinding in LDA models results in an attraction between rare gas atoms which is inaccurate. Errors associated with DFT calculations include, the basis set superposition error (BSSE) arising from the use of local basis sets (but not unique to DFT), self-interaction and unphysical effects arising from certain functionals, such as the existence of correlation energy in one-electron systems.

Unlike HF theory, DFT is considered by some not to be an *ab initio* method. In principle it is exact, but only in the limit of a complete basis set and with an exact exchange-correlation functional. There is currently no functional that works for all systems, which means that choosing the correct functional for a system is as much of an art as a science. Additionally, many functionals (excluding LDA and many GGA) contain empirical fitting parameters and tabulated data for the sake of expediency.

3.7 Quantum Monte Carlo (QMC)

Variational (VMC) and Diffusion (DMC) Monte Carlo are stochastic techniques for evaluating the expectation values of many body Hamiltonians and wavefunctions. Although they are computationally expensive, they scale well with system size, and are currently regarded as the most accurate method of evaluating the energies of large numbers of interacting quantum mechanical particles[117]. Both methods are variational, and as such yield an upper bound to the ground state energy.

3.7.1 Variational Monte Carlo

The energy calculated via the variational principle, E_{var}, for an approximate many-body trial wavefunction, Ψ_T, can be written,

$$E_{\text{var}} = \frac{\int d\mathbf{R}\Psi_T(\mathbf{R})\hat{H}\Psi_T(\mathbf{R})}{\int d\mathbf{R}\Psi_T^2(\mathbf{R})} \tag{3.118}$$

$$= \int d\mathbf{R}E_{\text{local}}(\mathbf{R})p(\mathbf{R}), \tag{3.119}$$

where the local energy $E_{\text{local}}(\mathbf{R})$ and probability function $p(\mathbf{R})$ are defined,

$$p(\mathbf{R}) = \frac{\Psi_T^2(\mathbf{R})}{\int d\mathbf{R}'\Psi_T^2(\mathbf{R}')} \tag{3.120}$$

$$E_{\text{local}}(\mathbf{R}) = \Psi_T^{-1}\hat{H}\Psi_T \tag{3.121}$$

The variational energy E_{var} can be evaluated by randomly sampling the probability distribution $p(\mathbf{R})$ within the integration limits using the Metropolis Monte Carlo algorithm. E_{var} is then the average of the local energies of configurations $\mathbf{R}_i$ over M sampling points:

$$E_{\text{var}} = \frac{1}{M}\sum_{i=1}^{M} E_{local}(\mathbf{R}_i) \tag{3.122}$$

The main problem with this process is the difficulty in preparing trial wavefunctions of equivalent accuracy for different systems. Thus the VMC approach is often used to optimise the parameters in trial wavefunctions for DMC calculations.

3.7.2 Diffusion Monte Carlo

In the diffusion Monte Carlo method, the imaginary time operator $e^{-\tau\hat{H}}$ is used to project out the ground state from the initial state. This is equivalent to solving the imaginary time Schrödinger equation, where the time t is replaced with the imaginary

time $\tau = it$ in the time dependent Schrödinger equation (3.1):

$$-\frac{\partial}{\partial \tau}\Phi(\mathbf{R},\tau) = (\hat{H} - E_T)\Phi(\mathbf{R},\tau) \tag{3.123}$$

$$= (-\frac{1}{2}\nabla_R^2 + V(\mathbf{R}) - E_T)\Phi(\mathbf{R},\tau) \tag{3.124}$$

Here, E_T is an arbitrary offset called the reference energy. Equation (3.124) has the form of a generalised diffusion equation, hence the name diffusion Monte Carlo. If the approximate wavefunction $\Phi(\mathbf{R},\tau)$ is expanded in terms of the exact wavefunction ϕ_i,

$$\Phi(\mathbf{R},\tau) = \sum_i c_i(\tau)\phi_i(\mathbf{R},\tau) = \sum_i c_i\phi_i(\mathbf{R})e^{-E_i\tau}, \tag{3.125}$$

it can be seen that states with a high energy (E_i) decay faster than low energy states, and as a result, only the ground state survives.

3.7.3 Some QMC caveats

QMC techniques rely on sampling from a probability distribution, but fermionic wavefunctions can not generally be treated as such because they contain positive and negative regions due to antisymmetry. This results in $3N-1$ dimensional hypersurfaces called nodes, on which the wavefunction and therefore probability is zero; excessive sampling of nodal regions will reduce the accuracy of the calculation. This problem can be overcome using the fixed node approximation, which effectively places an infinite repulsive potential on the nodal surface, or by using a more computationally efficient importance sampling transformation.

The accuracy of a QMC calculation is very sensitive to the trial wavefunction, in particular, the nodal structure, which is not trivial to determine. Most electronic systems use a trial wavefunction of the Slater-Jastrow type, Ψ_{SJ}, which is a product of the Jastrow factor $e^{J(\mathrm{R})}$ and spin up and down determinants (which are often obtained from

DFT or HF calculations):

$$\Psi_{SJ}(\mathbf{R}) = e^{J(\mathbf{R})}\det[\psi_n(\mathbf{r}_i^{\uparrow})]\det[\psi_n(\mathbf{r}_j^{\downarrow})] \tag{3.126}$$

$$J(\mathbf{R}) = \sum_{i}^{N_e}\chi(\mathbf{R}_i) - \sum_{i>j}^{N_e} u(\mathbf{R}_i, \mathbf{R}_j) \tag{3.127}$$

The parameters in $J(\mathbf{R})$ are chosen to reproduce nuclear-electron and electron-electron cusps. In this formulation, correlation is introduced through the explicit dependence on electron separation.

In a QMC geometry optimisation, peak computational efficiency is achieved by moving a single atom at a time. This allows a faster evaluation of the trial wavefunction. Many particle wavefunctions satisfy Bloch's theorems, but it is only possible to perform many particle calculations on a single k-point, resulting in a poor representation of bulk systems. Therefore, a supercell is usually required.

QMC methods are associated with an inherent statistical error which decreases with the inverse square of the sampling frequency. The statistical error makes evaluation of derivatives for geometry optimisations and vibrational frequencies problematic.

3.8 A note on nomenclature

For all DFT and *ab initio* calculations, the standard nomenclature for representing the levels of theory is used. For example, CCSD(T)/cc-pVDZ//MP2/cc-pVTZ means that the geometry of the system was optimised at the MP2 level using the cc-pVTZ basis set, and the calculated energy is a CCSD(T) single point using the cc-pVDZ basis set.

3.9 Dispersion corrections in DFT

One of the main shortcomings of common GGA and hybrid functionals is their inability to describe the long range correlation effects responsible for Van der Waals-type

interactions. DFT works well for systems under extremes of temperature or pressure since the repulsive part of the potential is sampled at high pressures, but is less accurate for weakly interacting systems at ambient conditions, notably hydrogen bonded liquids. Two different dispersion corrections have been used in this thesis, the DFT-D method of Grimme[118;119] and the van der Waals DFT method of Langreth *et al.*[120;121]. Langreth *et al.* note that it is impossible to construct a GGA that will mimic van der Waals interactions because there is not enough information in the small overlap region utilised by the functional, and atoms that can affect van der Waals interactions may not be nearest neighbours[120].

3.9.1 DFT-D

Grimme[118] proposed the solution of limiting the density functional description to short range, and describing medium to long range interactions with damped C_6R^{-6} terms, where C_6 is the 'dispersion coefficient.' The scheme is limited to the C_6 term because it was found that the higher order C_8 and C_{10} terms interfered with the short range description. Compared with other dispersion correction schemes, Grimme's (named DFT-D2) is less empirical and requires fewer fitting parameters; it is reported to give good results when implemented with the B97-D functional, and to a lesser extent, PBE (although it is not explicitly tested with bulk water in the literature).

A recent revision to Grimme's DFT-D scheme is detailed in his 2010 paper[119], offering an improved description of inter- and intra-molecular dispersion for the most commonly used functionals. It implements a consistent description of all chemically relevant elements with atomic number 1–94, specifying dispersion coefficients and cut-off radii for element pairs, and coefficients that are dependent on coordination number derived from *ab initio* calculations on simple molecules. The only other new ingredients are the C_8 term representing a shorter range contribution to the dispersion, and a C_9 term for three-body interactions. There are only two parameters that must be

determined empirically, the $s_{r,6}$ and s_8 factors, which allow the seamless merging of correlation contributions from different length scales; the rest can be determined ab initio (although this is not necessarily done for expediency).

On the basis of the WATER27 benchmark — a 'tough test for the description of strong hydrogen bonds'[119], using 27 neutral $(H_2O)_n$, negative $OH^-(H_2O)_n$ and positive $H^+(H_2O)_n$ clusters — it seems that PBE is a poor choice of functional, displaying clear overbinding which is only exacerbated by the dispersion correction. Grimme *et al.* therefore recommend the BLYP, revPBE or B97-D functionals for modelling water[119] because they underbind in the absence of a dispersion correction.

3.9.2 Van der Waals DFT (vdw-DFT)

Van der Waals DFT[120] is a cheap yet sophisticated treatment of long range correlation effects in which a standard GGA functional is used to calculate exchange, but the correlation part is replaced with a "van der Waals density functional" (vdW-DF). Many common GGA functionals exhibit a binding effect between rare gas dimers; this has been shown to arise from the exchange interaction instead of correlation, and is not present when exact exchange is used[122]. Whilst this long range exchange effect mitigates the lack of long range correlation to some extent, it has been shown to be unreliable in general[123] (although it should be noted that this refers to *long range* exchange; the overall exchange energy is accurate to within 1% in the majority of cases).

Langreth *et al.* recast the exchange-correlation functional as follows:

$$E_{\mathrm{XC}}[n] = E_{\mathrm{X}}^{\mathrm{GGA}} + E_{\mathrm{C}}^{0} + E_{\mathrm{C}}^{\mathrm{nl}} \tag{3.128}$$

where the terms on the right hand side represent respectively the GGA exchange energy, the short range (but still non-local) correlation term, and the term encompassing non-local correlation terms that give rise to long range van der Waals interactions. The short range correlation term is approximated to the LDA correlation, $E_{\mathrm{C}}^{\mathrm{LDA}}$, which is

valid for slowly varying systems.

In its original incarnation, the exchange part of the vdW-DF consists of the LDA exchange energy with the gradient correction term from the revPBE functional, which does not exhibit the attractive long range exchange interaction typical of many GGAs. Klimeš *et al.* were able to improve the accuracy of the vdW-DF by replacing revPBE exchange with a different, optimised GGA functional[124]. They achieved substantially improved accuracy for the S22 dataset (of weakly interacting biologically important dimers) using van der Waals density functionals with reparameterised B88 and PBE exchange, dubbed optB88-vdW and optPBE-vdW. Significantly, coupled cluster calculations predict the ground state of the water hexamer to adopt a "prism" configuration, whilst PBE and BLYP give rise to six-ring and "book" configurations. The optPBE-vdW functional recovers the prism configuration, along with a dissociation energy that is essentially identical to that obtained with CCSD(T).

3.10 The Gaussian and plane waves (GPW) representation

The main difference between the DFT code used for this research, the QUICKSTEP module of CP2K[125] and its contemporaries is the use of the Gaussian and plane waves (GPW) representation of wavefunctions and electron density — it utilises the strengths of both representations to allow better algorithmic efficiency.

3.10.1 The Gaussian representation

Atomic orbitals can be represented as Slater-type orbitals (STO), which consist of wavefunctions constructed from Slater determinants. STOs are a faithful representation of electronic wavefunctions; however integrals involving STOs are difficult to calculate, especially when the atomic orbitals in question are centred on different nuclei. Such

integrals can be made analytic by expanding the atomic orbitals as linear combinations of Gaussian functions[105;126] of the form $x^a y^b z^c e^{-\alpha r^2}$, where the exponent α determines the spread of the function. The product of two Gaussians is another Gaussian with an intermediate centre, which offers the advantage of allowing two-electron integrals to be reduced to the integral of a single Gaussian.

The accuracy of calculations depends on the number and types of functions in the basis set. Increasing the number of basis functions generally (but not invariably) improves accuracy; a minimal basis set includes a single Gaussian contraction (a sum of Gaussian functions with fixed exponents and coefficients) per atomic orbital, whilst a double-zeta set would contain two contractions, a triple-zeta set would contain three contractions, and so on. Adding functions beyond the minimal basis set allows the description of non-spherical aspects of the electron distribution required for higher angular momenta (p-orbitals and above). Split valence sets use a simpler set for modelling core electrons, with a more diverse set for the chemically interesting valence electrons. Polarisation functions can be added for a better description of molecules, where the charge distribution is often perturbed from the nuclear centres, and highly diffuse functions are useful for situations where there is a significant charge density in the internuclear region, for example, lone pairs. An increase in the quality of the basis set obviously comes at the expense of computational cost.

A fundamental difficulty that arises from the necessity of using incomplete basis sets is the basis set superposition error (BSSE). When interacting species approach each other, their basis functions overlap, effectively increasing the size of their basis sets, resulting in a difference in energy between the composite species and its individual part, beyond the cohesive energy. This becomes less significant when larger basis sets are used, and disappears in the limit of a complete basis set.

3.10.2 The plane wave representation

When modelling ordered, highly symmetric condensed matter systems such as metals, the most natural representation for electrons is in terms of plane waves, which are periodic by definition, as opposed to Gaussian functions, which are localised. According to Bloch's theorem, a wavefunction can be expanded in a plane wave basis using a wave-like component and a cell-periodic component [127]:

$$\psi_i(\mathbf{r}) = f_i(\mathbf{r}) e^{i\mathbf{k}\cdot\mathbf{r}}, \tag{3.129}$$

where $\mathbf{k}$ is a reciprocal vector. The cell periodic part, f, can be expanded using a basis set of discrete plane waves with coefficients c:

$$f_i(\mathbf{r}) = \sum_{\mathbf{G}} c_{i,\mathbf{G}} e^{i\mathbf{G}\cdot\mathbf{r}}, \tag{3.130}$$

where $\mathbf{G}$ are reciprocal lattice vectors. Thus each electronic wavefunction can be written as a sum of plane waves:

$$\psi_i(\mathbf{r}) = \sum_{\mathbf{G}} c_{i,\mathbf{k}+\mathbf{G}} e^{i(\mathbf{k}+\mathbf{G})\cdot\mathbf{r}} \tag{3.131}$$

As a result of the reciprocal space representation, coefficients c with a small kinetic energy ($\frac{\hbar}{2m}|\mathbf{k}+\mathbf{G}|^2$) are more important, so that only plane waves with an energy lower than a pre-determined cutoff energy are included. Bloch's theorem ensures that there is a finite number of plane waves (for a continuous plane wave basis set, there would be an infinite number of plane waves regardless of the cutoff); it is then possible to increase the cutoff until convergence is achieved.

A problem with the plane wave method is that all-electron calculations are much more expensive. Core electrons are tightly bound, and have rapidly oscillating wavefunctions in the vicinity of the nucleus due to the strong ionic potential. In addition, valence electron wavefunctions oscillate rapidly in the core region to maintain orthogo-

nality with the core electrons. A large number of plane waves is necessary to represent these rapidly varying wavefunctions accurately. This problem is usually overcome using the pseudopotential approximation: instead of including the chemically irrelevant core electrons in the calculation, their influence is folded into a smooth potential that only excludes valence electrons; it is constructed such that the scattering properties of pseudo-wavefunctions are identical to the cumulative scattering properties of the nuclei and core electrons, but critically, have no radial nodes in the core region. Outside the core region, the pseudo-wavefunctions are indistinguishable from the actual wavefunctions.

3.10.3 The GPW representation

The plane wave representation has several advantages over the Gaussian representation[128]. Plane waves are independent of atomic positions, which simplifies calculation of forces; there is no associated BSSE; calculation of exchange-correlation and Hartree potentials are much more straightforward, and the use of Fourier transforms simplifies algebraic manipulations (fast Fourier transform (FFT) algorithms make this even more efficient). However, the BSSE is replaced by the degree of approximation inherent in the use of pseudopotential and the computational cost of modelling the vacuum is the same as for populated regions, making surface calculations more expensive.

The GPW approach involves explicit treatment of valence electrons only, with pseudopotentials accounting for the effect of core electrons. Plane waves are used to represent electron density, thereby simplifying calculations of the Hartree and exchange-correlation potential, whilst Gaussians are used to represent wavefunctions. In this

formulation, the energy functional (3.104) becomes:

$$E[n] = \sum_i f_i \langle \psi_i | -\frac{\nabla^2}{2} + V_{\mathrm{loc}}^{\mathrm{PP}}(\mathbf{r}) | \psi_i \rangle + \sum_i f_i \langle \psi_i(\mathbf{r}) V_{\mathrm{nl}}^{\mathrm{PP}}(\mathbf{r}, \mathbf{r}') | \psi_i(\mathbf{r}') \rangle + 4\pi\Omega \sum_{|\mathbf{G}|<G_c} \frac{\overline{n}^*(\mathbf{G})\overline{n}(\mathbf{G})}{\mathbf{G}^2} + \int \mathrm{d}\mathbf{r} \overline{n}(\mathbf{r}) \varepsilon_{\mathrm{XC}}[n](\mathbf{r}) \tag{3.132}$$

Here, the pseudopotential is split into local ($V_{\mathrm{loc}}^{\mathrm{PP}}$) and non-local ($V_{\mathrm{nl}}^{\mathrm{PP}}$) parts, f_i is the occupancy of orbital ψ_i defined by

$$n = \sum_i f_i |\psi_i|^2, \tag{3.133}$$

Ω is the volume and G_c is the wave vector corresponding to the cutoff energy. n is the density evaluated in the primary (Gaussian) basis, and $\overline{n}$ is the density evaluated in the auxiliary (plane wave) basis, the two being equal if both basis sets are complete. The pseudopotentials of Goedecker, Teter and Hutter (GTH)[129] are appropriate for this method since they are constructed such that all matrix elements can be calculated analytically in a Gaussian basis. The numerical accuracy in the GPW scheme as prescribed by Lippert *et al.*[128] is dependent on only two parameters: the plane wave cutoff G_c and the screening parameter ε_s.

Vandevondele *et al.*[125] note that DFT is generally efficient for up to about 100 atoms, but for larger systems, the computation of the Hartree energy and orthogonalisation of wavefunctions do not scale linearly with system size — Gaussians are localised, so the representations of the Kohn-Sham, overlap and density matrices become sparse as the system size increases; together with a real space integration scheme, linear scaling is achieved.

3.11 Using DFT to model hydrogen bonding in water and ice

There has been a great number of studies in the literature on the ability of DFT to characterise hydrogen bonds, notably for the case of this project, the water dimer. It has been noted[130] that the LDA overbinds the dimer by ∼70%, and results in an oxygen-oxygen separation that is ∼10% too short; use of the GGA results in significant improvements.

Santra *et al.*[131] evaluated the performances of 16 different functionals on small (≤5 molecules) water clusters using the large aug-cc-PV5Z basis set, with a view to minimising basis set incompleteness errors. Since there is limited available experimental data on such clusters, results were compared with MP2 benchmarks extrapolated to the complete basis set limit, which are accurate to within a few meV, and bond lengths to within 0.01 Å. They observed that with sufficiently large basis sets, all of the functional considered are capable of chemical accuracy (1 kcal mol^{-1} ≃ 43 meV/H bond), although this is a fairly weak constraint, considering hydrogen bond strengths vary from 10 meV–30 meV/H bond. The best performance for dissociation energies and geometries were achieved by the X3LYP and PBE0 hybrid functionals, with X3LYP giving results almost identical to MP2 in some cases. Dissociation energies for these functionals were within 7 meV/H bond of MP2 benchmarks. The best pure GGAs were mPWLYP and PBE1W, achieving dissociation energies within 12 meV/H bond of the benchmarks. BLYP and B3LYP consistently underbound clusters by 35 meV/H bond and 20 meV/H bond respectively, whilst PBE displayed a tendency to overbind more as the size of the cluster increased (overbinding the dimer by 5 meV/H bond, and the pentamer by ∼20 meV/H bond).

Dimer and cluster energies and geometries are a good test case for functionals, but these quantities are not representative of hydrogen bonding in ice. The phenomenon of cooperativity has been demonstrated on water clusters[131] — as the number of molecules

in a cluster increases, the average hydrogen bond strength increases, resulting in a length contraction. Hamann[130] systematically compares one LDA and four GGA functionals, including B86, PW91, PBE and B-loc, applied to the Bernal-Fowler ice cell. He concludes that PW91 and PBE give by far the best agreement for the cohesive energy and the volume, but they significantly underestimate the bulk modulus — an effect which is mitigated by adding a correction to model the zero-point motion of hydrogen atoms.

In his study on the *ab initio* calculation of the lattice constant mismatch between β-AgI and ice Ih, Feibelman[116] compares the performances of eight GGA functionals. It has been suggested that as a result of the similarity in lattice parameters between β-AgI and ice Ih, AgI smoke might be used to "seed" cloud formation by acting as a catalyst for ice nucleation. Experiments have shown that the mismatch between the a and c lattice parameters is 2.2%, whilst PBE predicts a 5.9% mismatch. He notes that PBE results in the best lattice energy (5% overbinding), and BLYP gives the best volume (2.8% too large). However, DFT tends to under-represent Van der Waals interactions, whilst arguably the best GGA functional for modelling ice, PBE, overbinds — thus adding an attractive dispersion correction would only exacerbate the overbinding. From this perspective, the GGA functionals that underbind, namely BLYP, RPBE and revPBE, are the most promising. However, none of the functionals adequately calculates the lattice mismatch factor; RPBE comes closest, but is still out by a factor of two.

The majority of the calculations in chapters 4 and 5 employ the PBE functional, which has been shown by Hirsch and Ojamäe to predict the correct proton ordered ground state for ice Ih[12].Feibelman also demonstrates that of the GGA functionals, it yields a good agreement with experiment for the lattice energy and geometry in spite of a small but consistent overbinding[116]. I have used the underbinding BLYP functional in conjunction with the D3 dispersion correction, since using D3 with PBE would exacerbate the overbinding. It was necessary to use a hybrid functional for the reaction chemistry in chapter 6 to correctly evaluate barriers. The choice of hybrid functional

used in these calculations is discussed in detail in section 6.7.1.

Chapter 4

Proton ordering in bulk ice

4.1 Introduction

Hexagonal ice is the most prevalent phase of ice on Earth, accounting for ∼10% of its surface area, thus giving it an important role in climatic regulation via albedo. Although hexagonal ice is one of the most studied materials in science, new properties are being discovered, with implications for both ice and other materials. For example, it has been shown that ice nucleates differently at positively and negatively charged surfaces of pyroelectric materials[25], and that the surface of crystalline ice displays a continuum of vacancy energies[26].

Cubic ice has not been studied to the same extent, and its existence in nature is a subject of debate since it is known that proton disordered ice Ic is metastable with respect to Ih[52]. Scheiner's halo is interpreted as evidence of cubic ice in the upper atmosphere, but it has only been observed a few times over the past 200 years[132], perhaps suggesting that cubic ice is not important in nature. However, recent work suggests that ice Ic forms readily and persists under conditions characteristic of the Earth's atmosphere. Experiments have shown that water droplets homogeneously freeze to cubic ice at ambient pressure and temperatures between 160 K[1] and 240 K[2], and in droplets with radii in the range 5 nm[28;29] to 5 μm[2]. Whilst it was previously believed that Ic transforms

rapidly to Ih at temperatures above ∼180 K–200 K, recent studies indicate that Ic remains stable for hours at 228 K[2]. It has also been argued that differences in the surface chemistry of cubic and hexagonal ice could influence processes such as cloud formation and dehydration[40] and ozone depletion[39].

The proton ordered ground state of hexagonal ice is well characterised. It forms when ice Ih is cooled to 72 K in the presence of a KOH dopant[80], since the OH^- ions generate the Bjerrum defects necessary for orientational reordering. A stacking defect-free sample of cubic ice has yet to be prepared in the laboratory, so observation of a proton ordered cubic ice ground state is unlikely for the foreseeable future. In fact, on the basis of X-ray diffraction experiments and Monte Carlo simulations, Malkin *et al.*[49] suggest that cubic ice sequences only exist in a stacking disordered phase, ice I_{sd}. Hirsch and Ojamäe[12] demonstrated that DFT methods predict the correct structure of ice XI, so we attempt a similar analysis here.

This chapter is motivated by these recent developments, and consists of a basic characterisation of bulk cubic ice. We first generate an exhaustive set of proton ordered, symmetry-unique cells for cubic ice in order to determine the proton ordered ground state, analogous to ice XI. We then compare the proton ordered ground states (ices XI and XIc) in order to gain some insight into their relative abundances and the unusual phase transition.

4.2 Methodology and computational setup

4.2.1 Constructing unit cells

In section 2.3, it was noted that there are six ways of orienting each water molecule within the constraints of a tetrahedral ice lattice. Therefore, there are 6^N ways of orienting the molecules in a N molecule ice cell. Hence, for an eight-molecule cubic or hexagonal ice cell, there are $6^8 = 1679616$ ways of orienting the molecules, most of

which are forbidden by the ice rules. A computer code developed by the author (available on request) which employed the Hayward-Reimers algorithm[85] was used to generate all valid eight-molecule cells for cubic and hexagonal ice; in both cases, it was found that there are only 114 valid configurations for each phase. It should be noted that this algorithm yields an exhaustive list of valid configurations and as a result is computationally intractable for cells of approximately 16 molecules and larger. Most of the 114 valid cells are related by symmetry operations; the set of symmetry-unique structures was found using graph invariant software developed by Knight, Singer and Beck[86–88;133], resulting in 16 hexagonal ice cells, in agreement with Hirsch *et al.*[12]

The cubic ice cell listed generally mentioned in the literature contains eight molecules, and is cubic with a side of length 6.358 Å and space group $Fd\bar{3}m$. This cell only has 4 symmetry-unique proton ordered configurations, one of which is anti-ferroelectric. By cutting through the (011) plane, it is possible to construct a four molecule tetragonal cell of dimensions 4.4958 Å × 4.4958 Å × 6.3580 Å, which also has four proton ordered configurations; this can be used to construct a $2 \times 1 \times 1$ supercell which has 11 symmetry-unique proton ordered configurations, two of which are antiferroelectric, and is comparable to the eight molecule orthorhombic cell used by Hirsch and Ojamäe. This cell was used to examine proton ordering in cubic ice.

4.2.2 Setup for DFT calculations

DFT calculations were conduced using the VASP plane wave code and the QUICKSTEP[125] module of the CP2K suite, which uses the computationally efficient Gaussian/plane wave representation.

Initial calculations on all symmetry-unique proton ordered configurations of the aforementioned eight molecule hexagonal and cubic ice cells were conducted using CP2K. Wavefunctions were constructed using the triple-ζ doubly polarised (TZV2P) basis set, and the electron density using a plane wave expansion with a 450 Ry cut-

off with Goedecker-Teter-Hutter (GTH) norm-conserving pseudopotentials[129] and basis sets. For calculations without a dispersion correction, the Perdew-Burke-Ernzerhof (PBE) GGA exchange-correlation functional was used, since it has been shown to describe hydrogen bonding energetics in ice Ih well[5;130], with a small but consistent 5% overbinding[116].

Applying a dispersion correction in conjunction with PBE would only exacerbate the overbinding; however, the Becke-Lee-Yang-Parr (BLYP) GGA functional consistently underbinds ice, and has been shown to perform well for hydrogen bonded systems when dispersion is taken into account[134]. The long range dispersive forces were accounted for using Grimme's DFT-D3 correction[119] with a dispersion cutoff of 12 Å, and the repulsive three-body C9 term was omitted from the calculations since it considerably increases the computational cost without significantly improving the accuracy.

CP2K only supports Γ-point sampling, so the unit cells were replicated to construct $3 \times 2 \times 2$ hexagonal ice supercells (with a smallest lattice parameter of 13.48 Å) and $2 \times 3 \times 2$ cubic ice supercells (with smallest side 12.46 Å), both containing 96 molecules. In all cases, full cell relaxation and geometry optimisation were performed in the absence of any symmetry constraints.

In order to gauge the impact of basis set completeness and basis set superposition error (BSSE), the CP2K calculations were repeated using VASP. The projector-augmented wave (PAW) method was used[135] with a plane wave cutoff of 550 eV and a $6 \times 3 \times 3$ Monkhorst-Pack grid of 54 k-points for hexagonal ice or $3 \times 6 \times 4$ grid of 72 k-points for cubic ice. Additional high precision calculations were performed on the ground state cubic and hexagonal ice configurations using hard PAW potentials, a plane wave cutoff of 1000 eV and 128 k-points (a $8 \times 4 \times 4$ grid for hexagonal ice or $4 \times 8 \times 4$ for cubic ice). For the high precision calculations, a number of approaches were used to examine the importance of van der Waals interactions and electron delocalisation between the two ground state polytypes, including the PBE GGA functional, the van der Waals density

functional[121] using PBE exchange (optPBE-vdW[124]) and the PBE0 hybrid functional, which includes 25% Hartree-Fock exchange. The van der Waals DFT calculations were performed in VASP, using the self-consistent implementation of Klimeš *et al.*[136]

4.2.3 Setup for DMC calculations

As an independent quantum mechanical reference point, diffusion Monte Carlo (DMC) calculations were performed on the ground state hexagonal and cubic configurations by Dario Alfè[4]. His calculations employed the CASINO code[117] with Dirac-Fock pseudopotentials[137] using core radii of 0.4 Å and 0.26 Å for oxygen and hydrogen respectively, and trial wavefunctions of the Slater-Jastrow type, with a single Slater determinant. The single particle orbitals were obtained from plane wave DFT calculations in the local density approximation using the PWscf code[138] with a plane wave cutoff of 300 Ry, and re-expanded in B-splines[139]. Extensive tests on the ice VIII and ice II primitive cells, close to their equilibrium volumes[140] demonstrated that a time step of 0.002 a.u., together with the locality approximation[141], resulted in cohesive energy differences converged to within 5 meV per molecule; this setup was therefore used in the calculations described. The 96-molecule hexagonal and cubic ground state supercells described for the CP2K calculations were used for the DMC calculations. The model periodic Coulomb technique was used to treat electron-electron interactions, significantly reducing DMC size errors[142]. Size tests performed on the ice VIII and II cells showed that finite size errors are reduced to less than 5 meV per molecule for cells containing 96 molecules or more[140].

4.2.4 Setup for empirical forcefield calculations

Although previous computational studies have shown that the commonly used empirical potentials lack the precision required to describe proton ordering in ice[48;65;91;92] there are still some reasons to be interested in them, particularly from a methodological per-

spective. What is the magnitude of the difference in energy between proton ordered configurations when using empirical potentials, and can we expect to see evidence of proton ordering during a simulation of nucleation? And perhaps more importantly, do these commonly used models display a bias towards nucleation of a specific phase? The latter question may have considerable repercussions, for example, in the field of biological simulations, where the TIP3P model is very frequently used.

All calculations were carried out using the GROMACS molecular dynamics code[143] using 596 molecule supercells of the orthorhombic eight-molecule hexagonal and cubic ice cells mentioned in the previous section ($6 \times 3 \times 4$, with a shortest side of 24.92 Å for cubic and $6 \times 4 \times 3$, with a shortest side of 22.01 Å for hexagonal). Simulations were run in the isothermal-isobaric (NPT) ensemble; the temperature was maintained at 0.01 K using a velocity rescaling thermostat with a 1 ps period in lieu of a zero-temperature energy minimisation, and the pressure was maintained at 1 bar using an anisotropic Berendsen barostat with a period of 5 ps. For each proton ordered configuration considered, a leapfrog integrator was run for 100 ps with a timestep of 1 fs (100000 steps), and a cutoff of 10 Å was used when calculating neighbour lists, and van der Waals and Coulomb interactions. Coulomb interactions were treated using the particle-mesh Ewald (PME) method.

4.3 Results and discussion

Here the cohesive energy E_c (synonymous with "sublimation energy") is defined as the energy released when n (non-interacting) water molecules, each of energy E_{molecule} in the gas phase are brought together to form the unit cell of an ice lattice with energy E_{cell}, i.e.

$$E_c = E_{\text{cell}} - nE_{\text{molecule}} \tag{4.1}$$

When phase transition energies are discussed, it is important to distinguish between the internal energy U and the enthalpy H, which is defined as:

$$H = U + pV \tag{4.2}$$

For a cell of volume V at pressure p. Assuming a pressure of 1 bar and a cell volume of 250 Å^3, the contribution from the pV term is of the order of 2 J mol^{-1}. Considering the cell volume varies by no more than 1% between proton ordered configurations, it can be deduced that the contribution of the pV term to the enthalpic difference will be less than a negligible 0.01 J mol^{-1}. Therefore the enthalpy of transition as discussed below is approximated to the internal energy change of transition.

Tables 4.1 and 4.2 list the cohesive energies of each of the 27 proton ordered configurations for the orthorhombic eight-molecule unit cells of hexagonal and cubic ice using the PBE exchange-correlation functional and the BLYP-D3 dispersion-corrected functional using the GPW method of CP2K, and the PBE functional using a BSSE-free plane wave basis in VASP. The cohesive energies relative to structure number 1 for hexagonal and cubic ice have been plotted in figure 4.1. The structures numbered in order of symmetry, 1 having the highest symmetry. In both cases, structure 1 is found to be the ground state proton ordered configuration. For hexagonal ice, this corresponds to the $Cmc2_1$ structure of ice XI, in agreement with the calculations of Hirsch and Ojamäe[12] and Tribello and Slater[97]. It should be noted that this structure has been experimentally verified[82] (see section 2.5).

Cohesive energies for the TIP4P and TIP3P forcefields are tabulated in tables 4.3 and 4.4, and their energies relative to the $Cmc2_1$ configuration for hexagonal ice and $I4_1md$ for cubic ice are plotted in figures 4.2a and 4.2b. Relative energies for TIP3P in the figures have been scaled down by a factor of ten in the graphs to allow easy comparison. Surprisingly, the TIP3P model agrees with DFT on the ground state configuration of cubic ice, but not for hexagonal ice. In agreement with other studies[48;78], both the

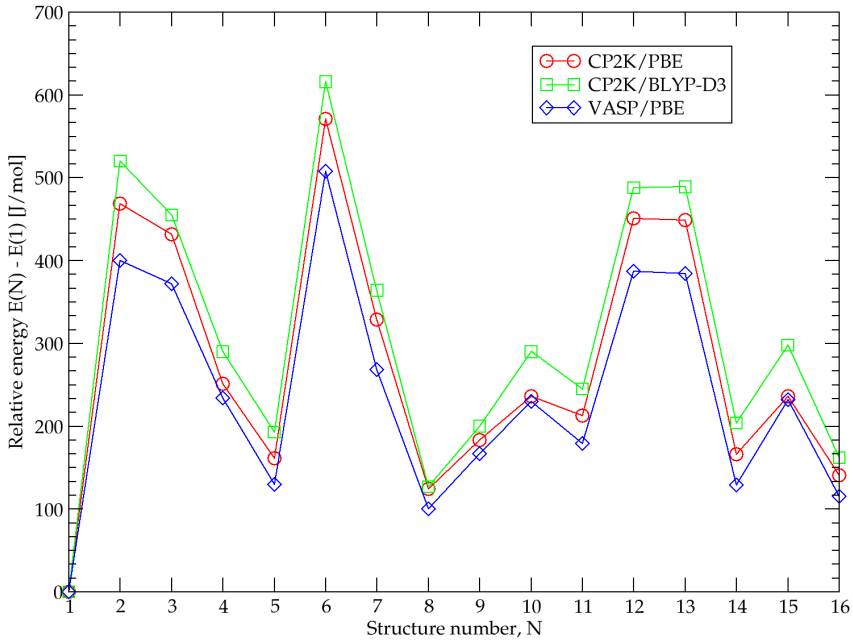

(a) Hexagonal ice

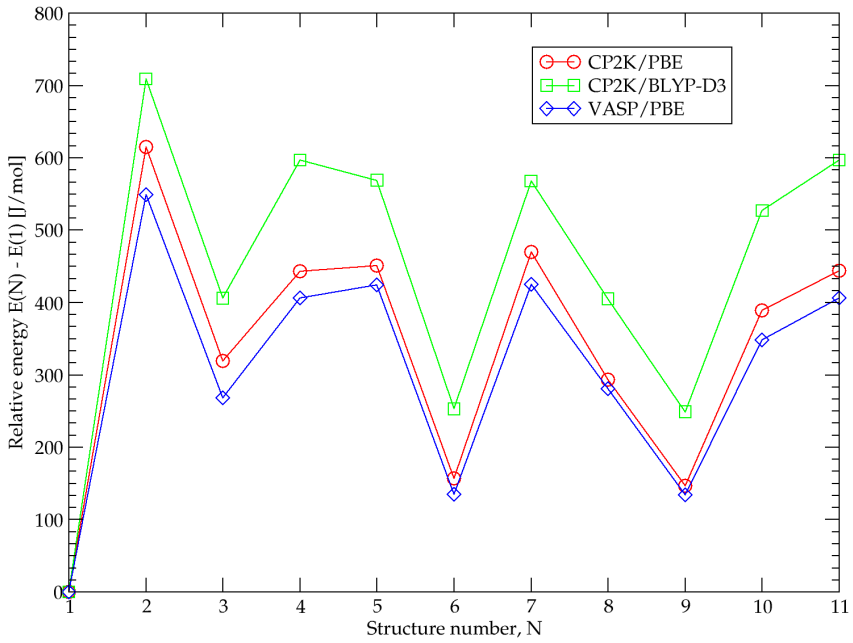

(b) Cubic ice

Figure 4.1: Relative energies for 16 hexagonal and 11 cubic symmetry-unique proton ordered configurations, as calculated using DFT. Energies are shown relative to structure 1 in both cases. The connecting lines have no physical meaning, and are present to guide the eye. In 4.1a, structure 1 is the experimentally verified $Cmc2_1$ structure of ice XI, and 2 is the antiferroelectric $Pna2_1$ configuration predicted by Davidson and Morokuma[14]. In 4.1b, structure 1 is the ground state $I4_1md$ structure, according to PBE and BLYP-D3 calculations, and can be considered the cubic analogue of ice XI.

TIP4P and TIP4P/2005 models favour the $Pna2_1$ structure for hexagonal ice, and the $P4_12_12$ structure for cubic ice, in both cases the antiferroelectric configuration with the highest symmetry. The range of energies for proton ordered configurations is considerably lower for the TIP4P calculations, up to $\sim$150 J mol^{-1}, which in turn is considerably lower than the range for the DFT calculations. These models are useful in many situations, but when they are used to attempt to resolve energy differences on the scale of 40 J mol^{-1} (the TIP4P energy difference between the $Cmc2_1$ and $Pna2_1$ configurations), they are clearly insufficient. The preference for antiferroelectric phases (in the case of TIP4P) suggests an underlying problem with the model; this has been addressed by Tribello and Slater, who established that widely used potential models such as TIP4P lack the description of high order multipole moments required to capture proton ordering energetics[97].

4.3.1 Hexagonal ice

All three datasets for hexagonal ice (figure 4.1a) agree with each other with regards to the ground state and the general shape; they are also in broad agreement with calculations by Hirsch and Ojamäe[12], with differences perhaps attributable to their choice of functional (PW91), k-point sampling and lower plane wave cutoff. The similarity between the VASP and CP2K results confirms that the GPW method is reliable for discriminating the extremely small (on the J mol^{-1} scale) energy differences involved in proton ordering. Grimme's D3 dispersion correction uses an empirically parameterised function with a $\frac{1}{r^6}$ dependence to simulate long and short range dispersive forces[119]. It can be seen that the relative energies calculated using BLYP-D3 (the red line in figure 4.1a) have a similar distribution, suggesting that to a first approximation, long range dispersion has a negligible effect on proton ordering energetics. The inherent overbinding of PBE at hydrogen bonding distances mimics the effect of short range dispersive forces on the cohesive energy. The cohesive energy of -67.76 kJ mol^{-1} compares favourably

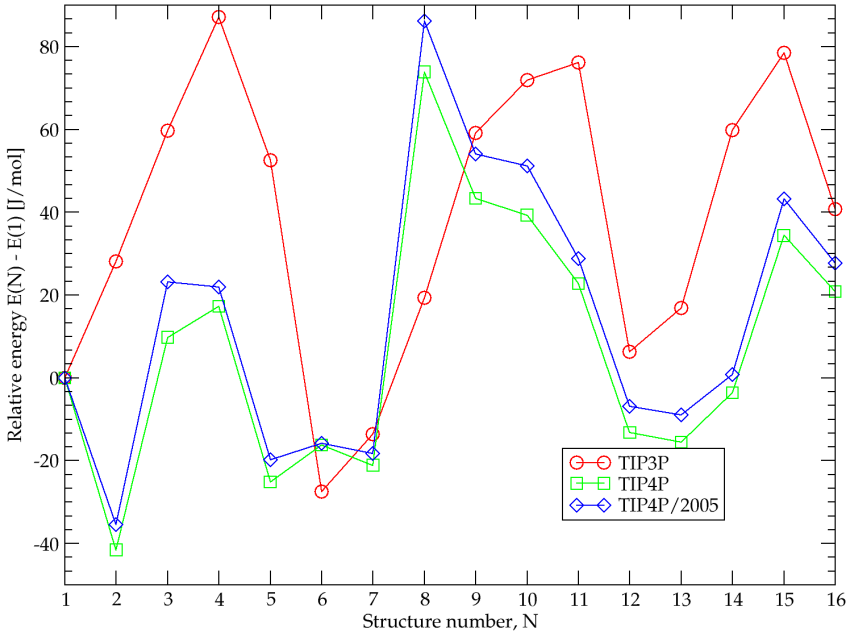

(a) Hexagonal ice

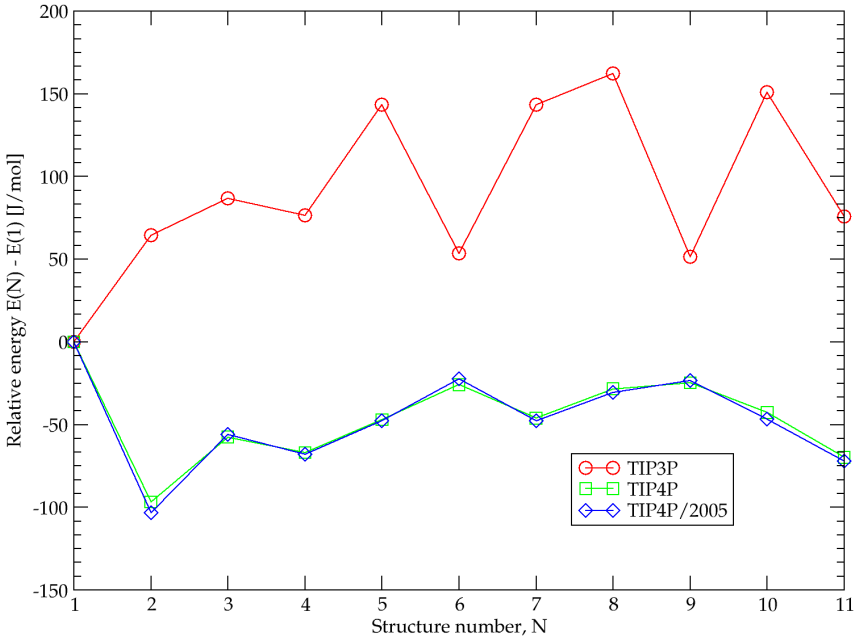

(b) Cubic ice

Figure 4.2: Relative energies for 16 hexagonal and 11 cubic symmetry-unique proton ordered configurations, as calculated using MM. Energies are shown relative to structure 1 in both cases. The connecting lines have no physical meaning, and are present to guide the eye. In 4.2a, structure 1 is the experimentally verified $Cmc2_1$ structure of ice XI, and 2 is the antiferroelectric $Pna2_1$ configuration predicted by Davidson and Morokuma[14]. In 4.1b, structure 1 is the ground state $I4_1md$ structure, and 11 is the antiferroelectric configuration with the highest symmetry. The relative energies for TIP3P are much larger than for the TIP4P models, and have been scaled down by a factor of 10 for easy comparison.

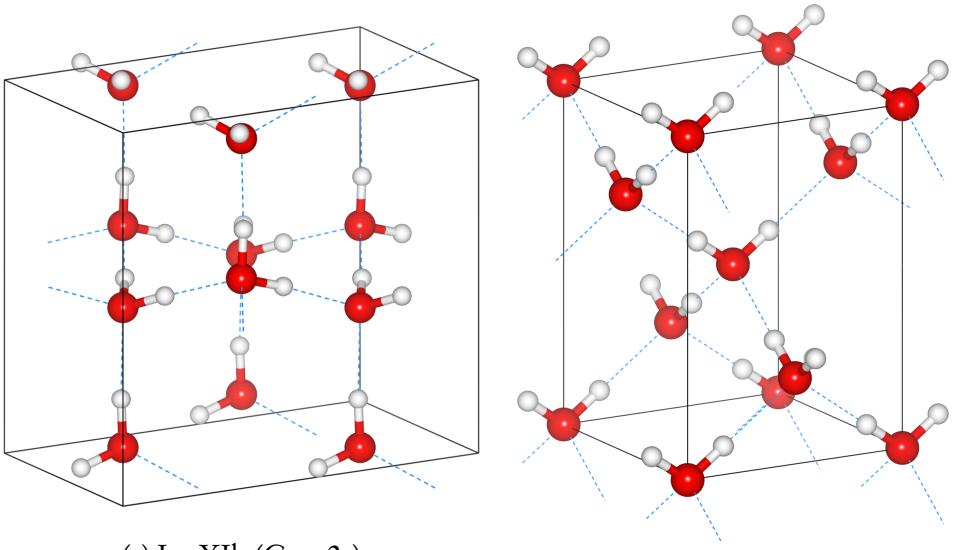

(a) Ice XIh ($Cmc2_1$)

(b) Ice XIc ($I4_1md$)

Figure 4.3: DFT ferroelectric ground state structures of ice Ih (XIh) and ice Ic (XIc). Although the tetragonal four molecule cell of XIc is shown, a $2 \times 1 \times 1$ supercell was generated to enumerate proton ordered configurations and calculate energies.

with the value of $-68.1\,\mathrm{kJ\,mol^{-1}}$ reported by Pan *et al.*[5], who also used CP2K albeit with a lower plane wave cutoff.

To the best of our knowledge, there is no experimental estimate for the cohesive energy of ice XI. According to Petrenko and Whitworth, proton disordered ice Ih is estimated to have a cohesive energy of $-58.95\,\mathrm{kJ\,mol^{-1}}$[46]. Pan *et al.* reported an energy range of $500\,\mathrm{J\,mol^{-1}}$ dependent on the degree of proton disorder, and a recent study yielded a cohesive energy of $67.3\,\mathrm{kJ\,mol^{-1}}$ for Ih[26]. The results presented here suggest, in agreement with Tribello and Slater[97], that the proton ordering energies are not sensitive to the choice of functional, hence it must be predominantly influence by the electrostatic interactions. Note that the energy difference between the $Cmc2_1$ and $Pna2_1$ structures (N = 1 and 2 respectively in figure 4.1) is $400\,\mathrm{J\,mol^{-1}}$, which compares favourably with the $335\,\mathrm{J\,mol^{-1}}$ reported by Labat *et al.*[98].

4.3.2 Cubic ice

Given that results for hexagonal ice are consistent with previous work (notably by Hirsch and Ojamäe[12]), the results for cubic ice can be viewed with confidence. According to all of the DFT recipes used, the ground state is the ferroelectric $I4_1md$ structure (only 2 and 7 are anti-ferroelectric), and consists of 100% inverse centre-symmetric ("h-cis") dimers, according to Bjerrum's classification[47]. This configuration will henceforth be referred to as "Ice XIc," where the "c" suffix is retained from ice Ic to denote the cubic stacking order of the bilayers even though the unit cell is tetragonal. $I4_1md$ is a sub-group of $Fd\bar{3}m$, the space group of the cubic ice cell (in the interest of disambiguation, ice XI will be referred to as "XIh" in this chapter). The hydrogen bond topology is in fact identical to that of the sub-lattices of ice VIII (recall that ice VIII is the proton ordered variant of ice VII, which consists of two interpenetrating ice Ic lattices); however, the ice VIII lattice is antiferroelectric overall, because the dipole moments of the two sub-lattices exactly cancel each other out. The dipole moments of all molecules in the XIc cell are aligned in the *c*-direction, resulting in a higher dipole moment in comparison with XIh.

4.3.3 Estimating the Ic→Ih transition energy

In real terms, a phase transition from cubic ice to hexagonal ice is a transition from the Ic phase to the Ih phase, both of which are disordered. Since simulating proton disorder is computationally expensive, the energy difference between XIh and XIc is used as a first approximation to the transition energy.

Although the hexagonal and cubic dataset are internally consistent, agreeing on the ground state configurations and relative energies of the structures, there is a significant mismatch in the energy difference between XIh and XIc ($\Delta H_{c\to h}$) for the GPW and plane wave datasets. GPW calculations using the PBE functional indicate that XIh has a lower cohesive energy than XIc by 102 J mol^{-1}, but the plane wave calculation yield

a much larger difference of $\Delta H_{c\to h} \simeq -416\,\mathrm{J\,mol^{-1}}$. Note that the order of stability (hexagonal being more stable than cubic) disagrees with the findings of Casassa *et al.*[69] In order to shed light on this discrepancy, additional DMC and high precision plane wave DFT calculations were performed on the XIh and XIc structures, as delineated at the end of section 4.2.2. The results of these calculations are displayed in table 4.5.

The first point to take from the high precision calculations is that regardless of the functional recipe used, $\Delta H_{c\to h}$ is very close to zero; for all of the methods used (with the possible exception of DMC which is subject to a statistical error), the cohesive energies are within $60\,\mathrm{J\,mol^{-1}}$ of each other. The second noteworthy point is that the sign of $\Delta H_{c\to h}$ varies with the recipe used. The GGA functional PBE, the hybrid PBE0 and the BLYP-D2 functional, employing the semi-empirical D2 dispersion correction[118] all suggest that XIc is marginally more stable, with values of $+47$, $+54$, and $+12\,\mathrm{J\,mol^{-1}}$ respectively. (Note that data for BLYP-D2 are not included on table 4.5 because molecular energies could not be reliably calculated as a result of a software bug.) In particular, the PBE0 result suggests that a moderate level of non-local exchange (25%) has very little effect on the energy difference between two proton ordered configurations. The functional with the most sophisticated treatment of long range dispersion, optPBE-vdW, is the only one to yield a negative value for $\Delta H_{c\to h}$ ($-29\,\mathrm{J\,mol^{-1}}$). Together with the lower energy difference from BLYP-D2, it seems likely that long range dispersion stabilises XIh with respect to XIc. Finally, with regards to the DMC calculations, the XIc is slightly ($40\,\mathrm{J\,mol^{-1}}$) more stable, albeit with a substantial error bar; the primary conclusion one can draw from this result is that XIh and XIc are essentially isoenergetic.

There is no clear correlation between the relative cell volumes per molecule and cohesive energies. One would intuitively expect the structure with the lower cohesive energy to be more dense, and therefore have a smaller cell volume; however, the PBE calculations suggest that XIc is more stable and denser, whereas the optPBE-vdW calculations show the opposite trend, with XIh being more stable, but XIc having the higher

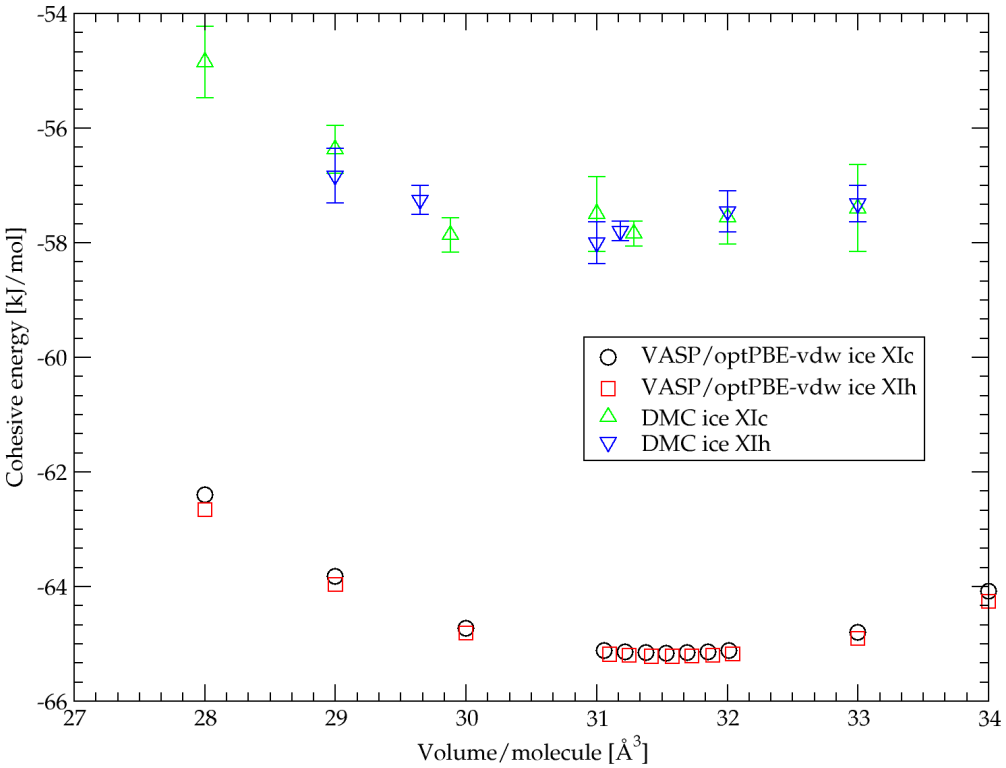

Figure 4.4: Equation of state plot for ices XIc and XIh; calculated using the optPBE-vdW functional and DMC.

density. It has been noted that PBE overbinds at hydrogen bonding distances, which mimics short-range dispersion, but there is no effect that adds long-range dispersion. The optPBE-vdW functional explicitly models both types of dispersion, therefore one might expect it to stabilise XIh with respect to XIc, since XIh has an additional water molecule in the second coordination sphere. PBE0 on its own has no long range dispersion correction, and generates a more localised electron density distribution; this results in a larger electrostatic contribution to the cohesive energy and yields XIh as the denser and more stable phase. This is slightly counterintuitive, since one might expect the larger dipole moment of the XIc cell (by 0.1 Debye) to electrostatically stabilise it with respect to XIh.

The zero point energy is sizeable in ice and could therefore influence the relative stability of XIh and XIc. Four point numerical derivative vibrational mode calculations

were performed on the PBE (hard PAW pseudopotential) optimised structures; at the time, the stress tensor had not been implemented for the optPBE-vdW functional, even though it would have been the natural choice for these calculations). It was found that the zero point energy of XIc is 133.349 kJ mol^{-1}, compared with 133.224 kJ mol^{-1} for XIh — i.e. the zero point energy of XIc is 125 J mol^{-1} greater than for XIh. Thus $\Delta H_{c\rightarrow h}$ is modified to -78 J mol^{-1}, suggesting that XIh is the more stable phase. PBE calculations using ultrasoft pseudopotentials and the plane wave CASTEP code, performed by Ben Slater[4], tell a different story: a zero point energy difference of 467 J mol^{-1} combined with a $\Delta H_{c\rightarrow h}$ of -130 J mol^{-1} stabilise cubic ice. However, considering that several first derivative methods have been unable to reach an agreement as to which phase is more stable, it seems premature to interpret zero point energies, which are derived from the second derivative of the energy.

Turning to configurational entropy, there are six possible orientations of each molecule in the cell within the constraints of the ice lattice, resulting in $6^8 = 1679616$ configurations for an eight molecule cell. Of these, only 114 are allowed by the ice rules, and the majority of the 114 are related by symmetry operations. In the case of hexagonal ice, six of the 114 have the $Cmc2_1$ structure, whilst for cubic ice, six of the 114 have the $I4_1md$ structure. Thus there are the same number of ways of generating both ground state configurations (XIh and XIc), and it can be concluded that they have identical configurational entropies.

For all of the functionals used, the denser phase reassuringly has the lower nearest neighbour oxygen-oxygen separation. It has recently been shown that that the linearity of the O$\hat{\text{H}}$O bond is an extremely good indicator of stability[144] — more stable structures generally correspond to hydrogen bond angles closer to 180°. For all of the functionals used, XIc has a mean O$\hat{\text{H}}$O bond angle closer to 180°, with a smaller variance; this is compelling evidence that XIc should be the more stable phase, and that the order of stability is very subtly influenced by the functional recipe used.

Recently, Kobayashi and Yasuda[145] induced a phase transition from Ic to XI at 95 K in a thin film by irradiation with high energy electrons. It is noteworthy that there was no transition to XIc, and the transition occurred above the 72 K reported by Tajima *et al*[80]. and the Bjerrum defects required for reorientation are created by ionisation of water molecules into H^+ and OH^-. They suggest an intermediate transition to Ih, but do not rule out the possibility of XIc forming.

4.4 Summary and conclusions

The ferroelectric $I4_1md$ configuration (polarised in the *c* direction), dubbed ice XIc, is identified as the unambiguous ground state proton ordered phase of cubic ice according to PBE and BLYP-D3 DFT calculations performed using the Gaussian/plane wave CP2K code. Higher precision plane wave calculations using a variety of functionals (notably the best available approximation to a long range dispersion corrected functional, optPBE-vdW) and hard PAW pseudopotentials in the VASP code suggest that the difference in cohesive energy between XIh and XIc is only a few tens of J mol^{-1}. Considering the error bars in the DMC calculations and the lack of agreement between the high precision plane wave DFT methods, it is only appropriate to conclude that ices XIh and XIc are essentially isoenergetic.

In principle Ic should transform to XIc in a manner similar to the Ih → XIh transition, with the addition of a KOH dopant to allow reorientation. The difference in energy between the most favourable and second most favourable proton ordered configuration for cubic (∼270 J mol^{-1}) and hexagonal (∼130 J mol^{-1}) suggest that the transition may be more facile in the case of cubic ice, since the potential well separating the two most favorable configurations is deeper.

In order to prepare ice XIc, one would need to surmount the considerable obstacle of obtaining a reasonably pure sample of Ic. Ices XIII, XIV[53] and XV[27] have been isolated by cooling very slowly (to prevent transformation to Ih and XIh) in the presence of a

dopant, and it can be tentatively suggested that XIc might be prepared from a good Ic sample in a similar way[4].

		DFT cohesive energy (kJ mol^{-1})		
N	Space group	CP2K/PBE	CP2K/BLYP-D3	VASP/PBE
1	$Cmc2_1$	−67.901	−69.434	−64.503
2	$Pna2_1$	−67.432	−68.914	−64.102
3	$Pna2_1$	−67.470	−68.979	−64.131
4	$Pbn2_1$	−67.650	−69.144	−64.268
5	$Pca2_1$	−67.740	−69.241	−64.373
6	$P2_12_12_1$	−67.330	−68.818	−63.995
7	$P2_12_12_1$	−67.572	−69.070	−64.235
8	Cc	−67.777	−69.307	−64.402
9	Pc	−67.718	−69.234	−64.336
10	Pc	−67.665	−69.144	−64.273
11	Pc	−67.688	−69.189	−64.324
12	$P2_1$	−67.450	−68.946	−64.115
13	$P2_1$	−67.452	−68.945	−64.118
14	$P2_1$	−67.735	−69.230	−64.374
15	$P2_1$	−67.665	−69.136	−64.271
16	$P1$	−67.760	−69.272	−64.387

Table 4.1: DFT cell optimised cohesive energies for all symmetry-unique proton ordered hexagonal ice configurations.

		DFT cohesive energy (kJ mol^{-1})		
N	Space group	CP2K/PBE	CP2K/BLYP-D3	VASP/PBE
1	$I4_1md$	−67.797	−69.021	−64.087
2	$P4_12_12$	−67.182	−68.312	−63.538
3	$Pna2_1$	−67.479	−68.615	−63.818
4	$Pna2_1$	−67.354	−68.424	−63.680
5	$Pmn2_1$	−67.346	−68.452	−63.663
6	$Pca2_1$	−67.640	−68.768	−63.952
7	$P2_12_12$	−67.327	−68.453	−63.662
8	Pc	−67.504	−68.616	−63.806
9	Pc	−67.650	−68.771	−63.953
10	$P2_1$	−67.408	−68.493	−63.738
11	$P2_1$	−67.353	−68.424	−63.681

Table 4.2: DFT cell optimised cohesive energies for all symmetry-unique proton ordered cubic ice configurations.

		MM potential energy (kJ mol^{-1})		
N	Space group	TIP4P	TIP4P/2005	TIP3P
1	$Cmc2_1$	−57.084±0.000	−63.018±0.000	−54.826±0.000
2	$Pna2_1$	−57.125±0.000	−63.053±0.000	−54.544±0.002
3	$Pna2_1$	−57.074±0.000	−62.994±0.000	−54.229±0.005
4	$Pbn2_1$	−57.067±0.000	−62.996±0.000	−53.954±0.003
5	$Pca2_1$	−57.109±0.000	−63.037±0.001	−54.301±0.003
6	$P2_12_12_1$	−57.100±0.001	−63.033±0.001	−55.101±0.002
7	$P2_12_12_1$	−57.105±0.001	−63.036±0.000	−54.963±0.001
8	C1c1	−57.010±0.000	−62.931±0.000	−54.633±0.001
9	P1c1	−57.041±0.000	−62.964±0.000	−54.235±0.002
10	P1c1	−57.045±0.000	−62.966±0.000	−54.108±0.004
11	$P12_11$	−57.061±0.000	−62.989±0.000	−54.065±0.005
12	$P12_11$	−57.097±0.000	−63.024±0.000	−54.763±0.003
13	$P12_11$	−57.099±0.000	−63.026±0.000	−54.658±0.003
14	$P12_11$	−57.087±0.000	−63.017±0.000	−54.228±0.003
15	$P12_11$	−57.050±0.000	−62.974±0.000	−54.041±0.006
16	P1	−57.063±0.000	−62.990±0.000	−54.419±0.003

Table 4.3: MM cell optimised cohesive energies for all symmetry-unique proton ordered hexagonal ice configurations, using 3 common empirical potentials: TIP4P, TIP4P/2005 and TIP3P.

		MM cohesive energy (kJ mol^{-1})		
N	Space group	TIP4P	TIP4P/2005	TIP3P
1	$I4_1md$	−57.032±0.000	−62.961±0.000	−55.564±0.001
2	$P4_12_12$	−57.129±0.000	−63.064±0.000	−54.920±0.064
3	$Pna2_1$	−57.089±0.000	−63.017±0.003	−54.697±0.071
4	$Pna2_1$	−57.099±0.000	−63.029±0.001	−54.800±0.067
5	$Pmn2_1$	−57.079±0.000	−63.009±0.000	−54.129±0.001
6	$Pca2_1$	−57.058±0.001	−62.983±0.002	−55.029±0.035
7	$P2_12_12$	−57.078±0.000	−63.009±0.001	−54.132±0.001
8	Pc	−57.060±0.000	−62.991±0.000	−53.940±0.002
9	Pc	−57.057±0.000	−62.984±0.001	−55.049±0.026
10	$P2_1$	−57.075±0.000	−63.008±0.000	−54.054±0.002
11	$P2_1$	−57.102±0.001	−63.033±0.000	−54.805±0.067

Table 4.4: MM cell optimised cohesive energies for all symmetry-unique proton ordered cubic ice configurations, using 3 common empirical potentials: TIP4P, TIP4P/2005 and TIP3P.

	Cohesive energy (kJ mol^{-1})		Volume/H_2O (Å^3)		OĤO bond angle (°)		$\Delta H_{c\to b}$ (J mol^{-1})
Density Functional	Ice XIh	Ice XIc	Ice XIh	Ice XIc	Ice XIh	Ice XIc	
PBE	−61.312	−61.359	30.41	30.35	177.28	177.66	+47
optPBE-vdW	−65.388	−65.359	31.58	31.53	177.08	177.36	−29
PBE0	−62.630	−62.684	30.02	30.17	177.60	178.25	+54
DMC	−57.80±0.17	−57.84±0.22	31.18±0.22	31.28±0.31	—	—	+40±280

Table 4.5: Comparison of ice XIh and ice XIc energies and structures obtained with VASP using hard PAW potentials and DMC.

Chapter 5

The ice surface

5.1 Introduction

Polar stratospheric clouds (PSC, figure 5.1) are observed in the stratosphere at altitudes of 15 km to 25 km during the winter. They are thought to contain cubic ice crystals, which is inferred from observations of Scheiner's halo[54] and the temperature regime at that altitude. Reactions which process HCl, $ClONO_2$ and HOCl into Cl_2, and subsequently dissociate Cl_2 homolytically to form the chlorine radicals implicated in ozone depletion are heterogeneously catalysed by the surfaces of ice crystals in these clouds[146].

Just as proton ordering affects the bulk cohesive energy of ice, it is known to affect the surface energy, albeit to a much greater extent[5]. When a hexagonal ice crystal is cleaved to reveal the [0001] basal plane, each surface molecule in the top half of the

Figure 5.1: Polar stratospheric clouds.

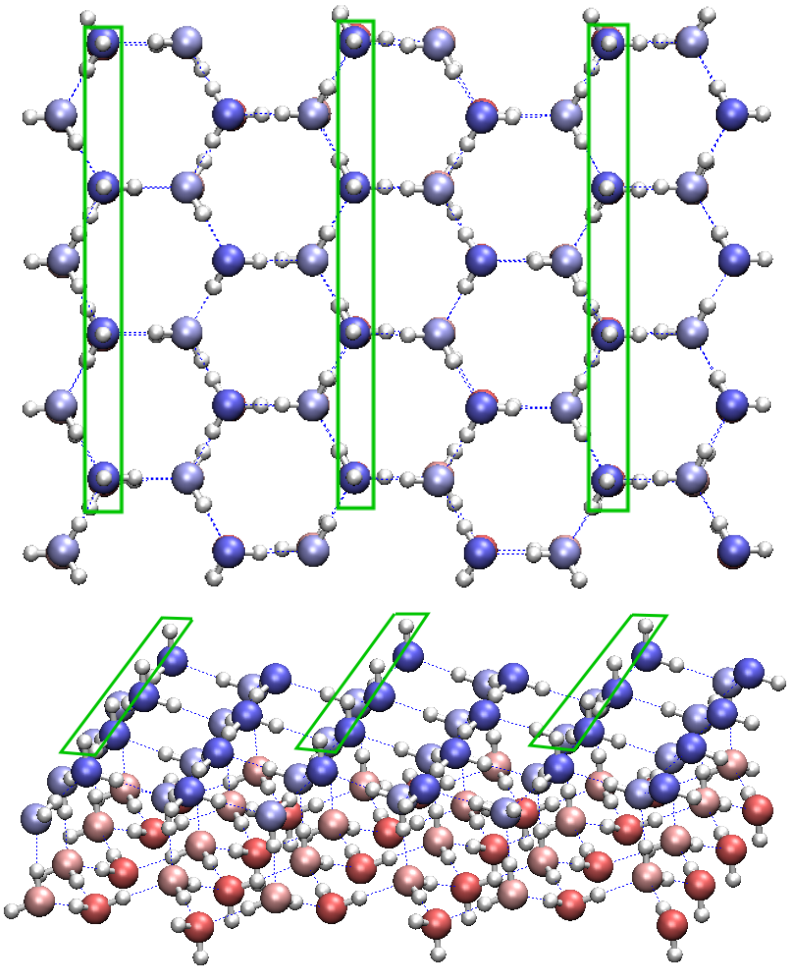

Figure 5.2: [0001] basal surface of a 2 bilayer hexagonal ice slab. Dark blue atoms are oxygens in the top half of the uppermost bilayer. The dangling OH bonds are ordered as in Fletcher's striped phase, with the stripes highlighted in green.

bilayer has one broken hydrogen bond; when the surface molecule is a hydrogen bond donor, it is said to have a "dangling OH bond." Each surface molecule has six surface nearest neighbours (figure 5.2); it has been shown that the orientation of a surface molecule relative to those of its six neighbours has a significant effect on the surface energy.

Experiments have shown that the ice surface is indeed the ideal full bilayer surface termination of the basal plane of hexagonal ice[147]. Although they were not able to resolve proton ordering, Glebov *et al*. observed "small domains of additional structure" with a periodicity of approximately twice the lattice constant of the ideally terminated

surface in helium atom scattering experiments[147]. Whilst Glebov *et al*. conclude that the most likely configuration of the ice surface is disordered (attributing the helium diffraction peaks mentioned above to boundaries between domains of different phase or orientation, Buch *et al*. suggest that they may be a result of the proton ordered striped phase[102].

Recently, Sazaki *et al.* optically imaged elementary steps on a hexagonal ice surface using laser confocal microscopy[6]. Such observations will in principle allow the experimental evaluation of the step ledge free energy of hexagonal ice, which may be important not only in the theory of two dimensional nucleation, but also in reaction chemistry, where these defects may be important in catalysis. For example, theoretical studies of HCl adsorption on ice have shown that ice surface defects can increase its adsorption energy, and possibly facilitate ionisation[148]. Bolton reports QM/MM simulations which indicate that step (and seven-ring) defects on a hexagonal ice surface facilitate that barrierless ionic dissociation of HCl molecules[146]. Batista and Jónsson used the TIP4P potential to form "island" defects on a hexagonal ice surface, their results suggesting that for one to five adsorbed water molecules, the molecules comprising the island occupy non-crystallographic positions, but become crystalline when a sixth molecule is added via a complicated restructuring with a low barrier[149]. The first stage in a study of surface defects is an analysis of step defects.

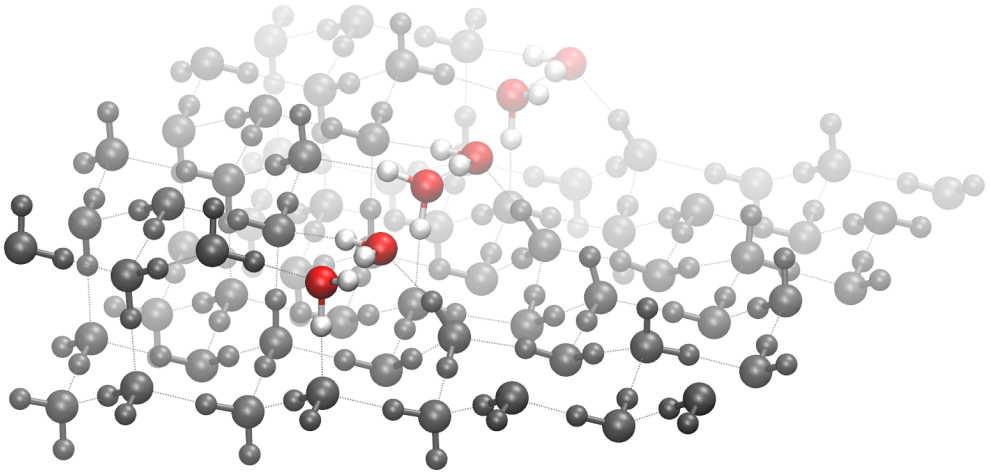

Figure 5.3: A *reconstructed* step feature on an ice I surface consisting of two visible bilayers. Molecules on the step edge are in colour.

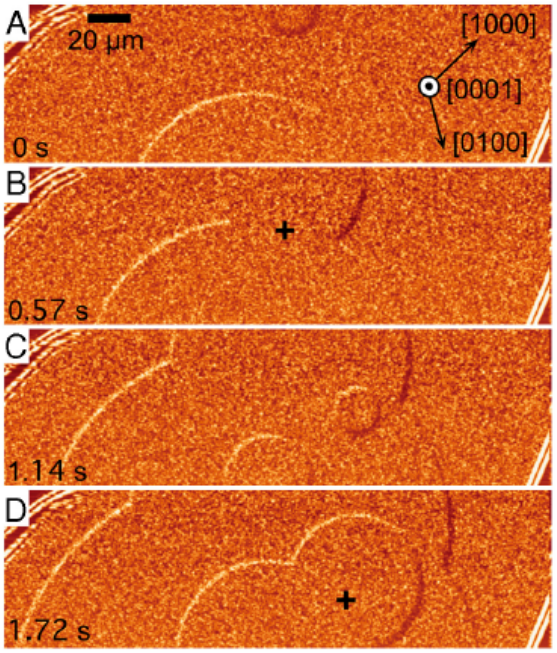

Figure 5.4: Optical images of a basal [0001] hexagonal ice surface taken using laser confocal microscopy (taken from Sazaki *et al.*[6]) They show the birth, growth and coalescence of elementary (single bilayer) step defects. The fact that no step contrast remains after the growth fronts merge indicates that the steps are indeed elementary. Note that the step growth is isotropic.

This chapter begins with an assessment of the effect of proton ordering on the hexagonal and cubic ice surfaces, followed by an attempt to characterise step defects on the

basal planes of cubic and hexagonal ice with a view to explaining the circular growth observed in figure 5.4.

5.2 Model and methods

5.2.1 Generating proton ordered cubic ice slabs

As mentioned previously, the surface energy of hexagonal ice is affected by proton ordering by an order of magnitude more than the bulk cohesive energy. With this in mind, we can fully randomise the bulk proton ordering in the slab, and only pay attention to the surface ordering whilst assuming that the bulk energy has not changed significantly. The surface ordering is defined by the following order parameter on the [0001] basal plane (of the hexagonal ice cell)[5],

$$C^B_{\mathrm{OH}} = \frac{1}{N_{\mathrm{OH}}} \sum_{i=1}^{N_{\mathrm{OH}}} c_i, \tag{5.1}$$

where N_{OH} is the total number of dangling OH bonds on the surface (both sides of the slab), and c_i is the number of dangling OH bonds adjacent to the i^{th} dangling OH. The B denotes the basal [0001] surface of hexagonal ice. In other words, the order parameter C_{OH} is defined as the average number of dangling OH bonds surrounding a dangling OH bond.

In principle, C^B_{OH} can vary between 2 and 6, where the Fletcher "striped phase" has an order parameter of 2 — although the order parameter is non-unique, for example, a "meandering" surface pattern will also have a surface order parameter of 2. A high order parameter represents a high degree of clustering of dangling OH bonds, while a random surface configuration will have an order parameter of 3. Note that C^B_{OH} is calculated by averaging over both sides of the slab in this work.

The analogous surface of cubic ice is the (111) plane. Cubic ice crystals are generally

described as having octahedral symmetry (for example, in the explanation of Scheiner's halo[54]), and all eight surfaces on an octahedral crystal will be topologically identical (ignoring proton disorder) due to the symmetry. Whilst the (111) surface may not be the only facet expressed during crystallisation, it is the natural starting point for a study of the surface energy of cubic ice, which has no equivalent to the prism face of hexagonal ice.

The cubic ice cells used in chapter 4 do not have bilayers normal to the faces of the cell, so it was necessary to construct a new cell with bilayers normal to the z-direction, analogous to those for hexagonal ice. Thus starting from the fully cell optimised cubic $P4_12_12$ cell (chosen because it is the highest symmetry antiferroelectric cell, and a non-polar slab is required for such calculations), a surface was constructed in the (111) plane, resulting in a 12 molecule cell that was three bilayers deep. This was used to construct a six-bilayer $5 \times 3 \times 2$ supercell containing 360 molecules, analogous to the six-bilayer hexagonal ice slabs used by Pan *et al.*[5]. The surfaces of the slab were defined at the extremities of the cell in the z-direction ($z = 0$ and $z = c$); the initial cell had an order parameter of 2.

Rick and Haymet describe an algorithm for randomising the proton ordering in an ice cell without violating the ice rules, called the "move" algorithm[89], summarised below.

1. Identify a closed loop of hydrogen bonds
   a) Randomly select a molecule in the lattice, i
   b) Randomly select one of its 4 nearest neighbours, j
   c) If j is a hydrogen bond donor to i, randomly pick one of the two neighbours of j that are donors to j; otherwise pick one of the two neighbours of j that are acceptors to j.
   d) Continue to walk randomly in this way until the next molecule has already

been visited on the walk. In a periodic cell, the walker may stop on a periodic image of the starting molecule.

2. Reorient the water molecules without violating the ice rules. For each molecule j on the N-molecule loop, rotate the molecule about the O_j–H_{1j} axis, where H_{1j} is the hydrogen atom in j *not* in the loop. The effect of this is to reverse the direction of all the hydrogen bonds that form the loop.

This scheme would normally be used in conjunction with a Monte Carlo/Metropolis algorithm, where the acceptance probability of a move is an exponential function of the energy change resulting from the move. In this case, however, the aim was to alter the proton ordering pattern on the surface, so only moves that (i) contained surface molecules and (ii) increased the order parameter were accepted; a configuration was saved after every such move. Although in principle the maximum value of C^B_{OH} is 6 in an infinite cell[5], no configurations were observed with values of more than ∼4.5 (with loose tolerances; it was assumed that no more configurations were to be found after 5000 "moves" with no increase in the order parameter). Some examples of the surfaces constructed by this algorithm are shown in figure 5.5.

As an additional step, after every move, the configuration was screened for a dipole moment. When performing slab calculations, it is necessary to ensure that the dipole moment of the slab is close to zero in the z-direction, otherwise there may be long range residual electrostatic forces between periodic images, which cause the slab to potentially drift through the vacuum gap during geometry optimisation. Any move which was found to increase the magnitude of the dipole in the cell was rejected. Hayward and Reimers describe three methods of imposing this constraint in an ice slab[85].

C0: No additional constraints; screen the cell for zero dipole moment after generation

C1: Constrain the number of each of the 36 OH bond orientations (24 for hexagonal ice) to be equal.

C2: Constrain the number of each of the 12 OH bond orientations per bilayer to be equal.

Constraint C0 is inefficient, since it will result in a vast majority of unusable configurations, whilst C2 is too strong and my introduce unwanted order into the lattice. Therefore, the cell was tested against the C1 constraint after every move.

5.2.2 Surface energy of ices Ih and Ic

Surface energy calculations were performed on five such configurations with different order parameters, and by way of comparison, on the five configurations used by Pan *et al.*[5] (surface energy calculations are extremely sensitive to the details of the computational setup, so it was decided that these calculations should be repeated using the same settings, rather than using the data acquired by Pan *et al.*)

The surface energy γ of a n bilayer slab is calculated as prescribed by Pan *et al*[5].:

$$\gamma = \frac{E_{\text{tot}}^{\text{slab}}(n) - nE_{\text{tot}}^{\text{bulk}}}{2A}, \tag{5.2}$$

where $E_{\text{tot}}^{\text{slab}}$ is the total energy of the slab, $E_{\text{tot}}^{\text{bulk}}$ is the bulk reference energy per bilayer and A is the surface area of one face of the slab. The bulk reference energy is defined as,

$$E_{\text{tot}}^{\text{bulk}} = E_{\text{tot}}^{\text{slab}}(n) - E_{\text{tot}}^{\text{slab}}(n-1), \tag{5.3}$$

i.e. the difference in energy between a n bilayer slab and a $n-1$ bilayer slab. Here, it is assumed that the slab is deeper than the critical thickness, such that the total energy increases uniformly with the number of bilayers. Figure 5.6 demonstrates that the surface energy converges rapidly with respect to the number of bilayer. The fact that cubic ice has a lower surface energy than hexagonal for the first column of this plot has no physical meaning, since a single bilayer of ice is neither hexagonal nor cubic. The difference in energy between the single bilayer data points arises from the difference in

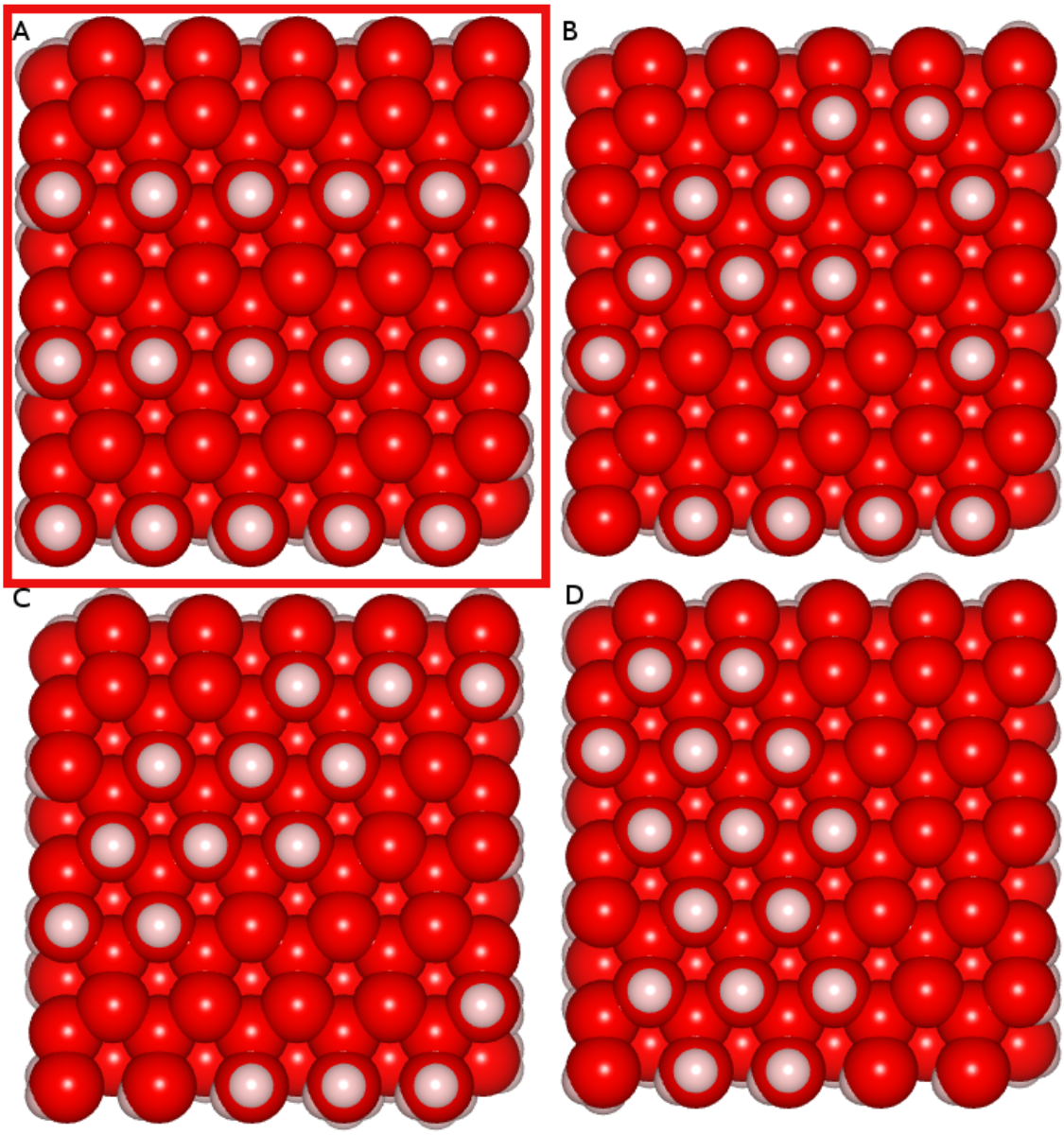

Figure 5.5: Illustration of proton ordering patterns on the (111) surface of ice Ic. Dangling hydrogens are shown in white; hydrogen atoms below the uppermost layer are hidden. The surfaces respectively have order parameters (C^B_{OH}) of A: 2.0, B: 2.8, C: 3.6, D: 4.4. Note that these numbers include dangling bonds on *both* sides of the slab, even though only one side of each slab is shown. Neighbouring dangling OH bonds correspond to the second nearest neighbour oxygen atoms (they are all on one half of the bilayer), hence the hexagonal pattern.

cell dimensions, since this was a geometry optimisation rather than a cell optimisation (the slabs were created by successively removing bilayers from a six bilayer hexagonal or cubic ice slab). Thus although in principle the structures for single bilayer slabs are

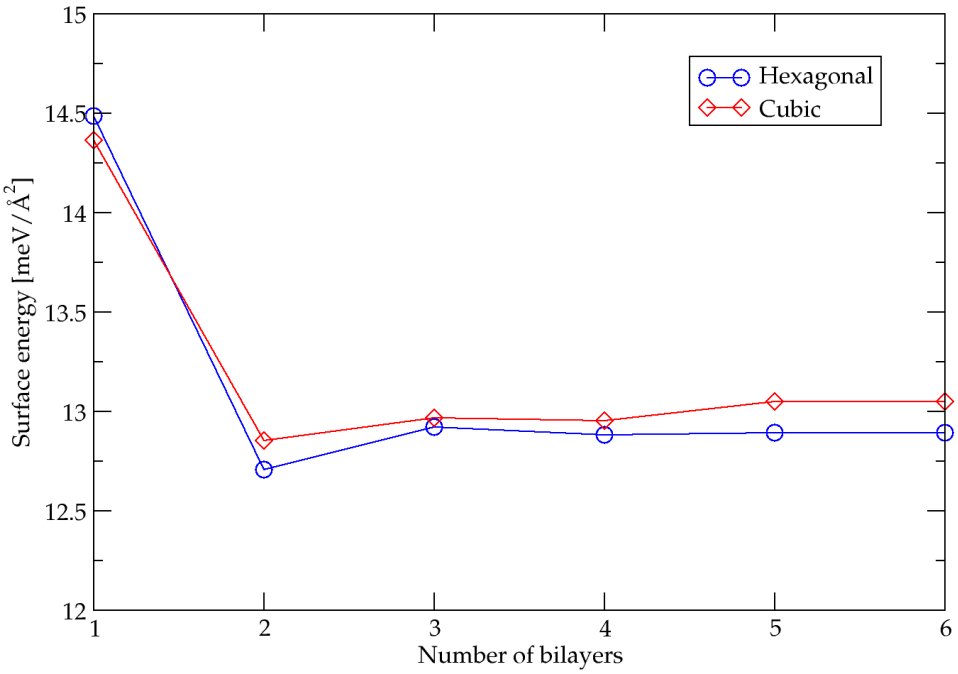

Figure 5.6: Graph of surface energy against number of bilayers. The surface energy has essentially converged at 3 bilayers.

identical, there is some residual stress caused by the unrelaxed cell, and there may be a different number of plane waves in each cell.

Five slabs with different surface order parameters were generated using the method described in section 5.2.1. The bulk structures were converted to slabs by inserting a vacuum gap of at least 20 Å extending in the z-direction; these were geometry optimised in CP2K using the PBE exchange-correlation functional, a 400Ry plane wave cutoff and the GTH TZV2P basis set. SCF cycles were assumed to have converged for energy changes of less than $1.0 \times 10^{-6}\, E_\mathrm{h}$. The geometry optimisation was assumed to be converged when the change in geometry was less than $3.0 \times 10^{-3}\, a_0$ and the forces were less than $5.0 \times 10^{-5}\, E_\mathrm{h}\, a_0{}^{-1}$.

5.2.3 Step formation energies of ices Ih and Ic

The grooved slab used to model steps is shown schematically in figure 5.7. Step forma-

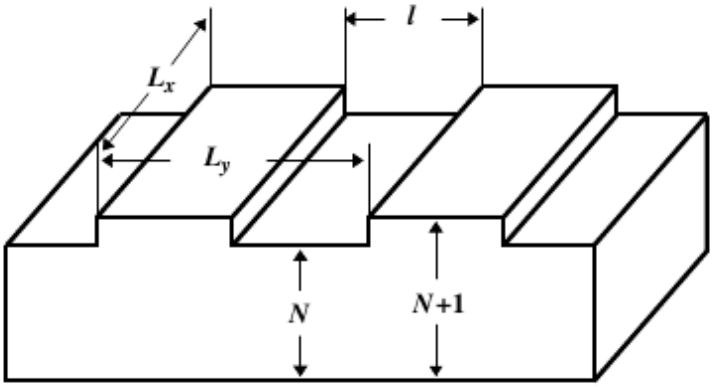

Figure 5.7: Schematic representation of the grooved slab used to model step defects (taken from Yu *et al.*[16]). A single layer step is formed on a N layer slab; the slab is 2D periodic with cell dimensions $a = L_x$ and $b = L_y$ (in the 3D periodic case a vacuum gap is used in the c-direction, and steps separated by a distance l.

tion energies were computed using a modified version of the method described by Li *et al*[150]. The surface energy γ is taken from equation (5.2), and the ledge energy is defined as,

$$E_{\text{ledge}} = \frac{(E_{\text{slab}} - E_{\text{bulk}} - \gamma A)}{2L_x}, \tag{5.4}$$

where the terms in parenthesis are respectively the energy of the grooved slab (E_{slab}), the bulk energy (E_{bulk}), and the surface energy over both sides of the slab (γA), i.e. the ledge energy is the excess energy when the bulk and surface energies are subtracted from the slab energy. L_x is the length of the step. Here, it is assumed that either the step is non-polar, or the separation l between periodic images of the step is sufficient such that there is no residual electrostatic interaction between steps. Interactions between steps can be incorporated using the following relation, which assumes an inverse square interaction between images:

$$E_{\text{ledge}} = E_{\text{step}} + \frac{B}{l^2}, \tag{5.5}$$

where B is a constant to be determined.

Thus for cases where there is interaction between steps, the ledge energy is calculated for slabs with different step separations (l), and equation (5.5) used to determine the form of the step energy. This is problematic in the case of the ice surface since for any proton disordered surface, there will be a different arrangement of dangling OH bonds on the step for different values of l — and it is impossible to decompose the final contribution into proton disorder and the Coulomb interaction between periodic step images. For this reason, we will only consider the ledge energy E_{ledge}, ensuring that only steps with a sufficiently large value of l are considered.

A variety of different slabs were used to calculate step energies; these were constructed using the eight-molecule hexagonal and twelve-molecule cubic cells described in section 5.2.1. A $10 \times 3 \times 3$ striped (order parameter 2) hexagonal ice slab was constructed to investigate step growth in the [1000] direction, and a $5 \times 6 \times 3$ slab to study growth in the perpendicular [0100] direction. Similarly, $10 \times 3 \times 2$ and $5 \times 6 \times 2$ slabs of cubic ice were constructed to study steps in analogous directions (they are not assigned Bravais-Miller indices due to the cubic cell). The top (or bottom) bilayer of the slab was cleaved as in figure 5.7 on either side to create a symmetrical "top hat" feature of varying widths, resulting in a set of configurations with different values of l. These configurations were geometry optimised using the same computational setup as in section 5.2.2. Vacancy energies (E_{vacancy}) were calculated by removing one molecule from the step and re-optimising; the vacancy energy is defined as:

$$E_{\text{vacancy}} = E_{\text{slab}} - E_{\text{step}} - E_{\text{H}_2\text{O}} \tag{5.6}$$

where E_{slab} is the total energy of the slab with a step defect and vacancy, E_{step} is the total energy with the step but no vacancy, and $E_{\text{H}_2\text{O}}$ is the *gas phase* total energy of a water molecule.

5.3 Results and discussion

5.3.1 Surface energy of ices Ih and Ic

The results of the surface energy calculations are presented in figure 5.8. This is in

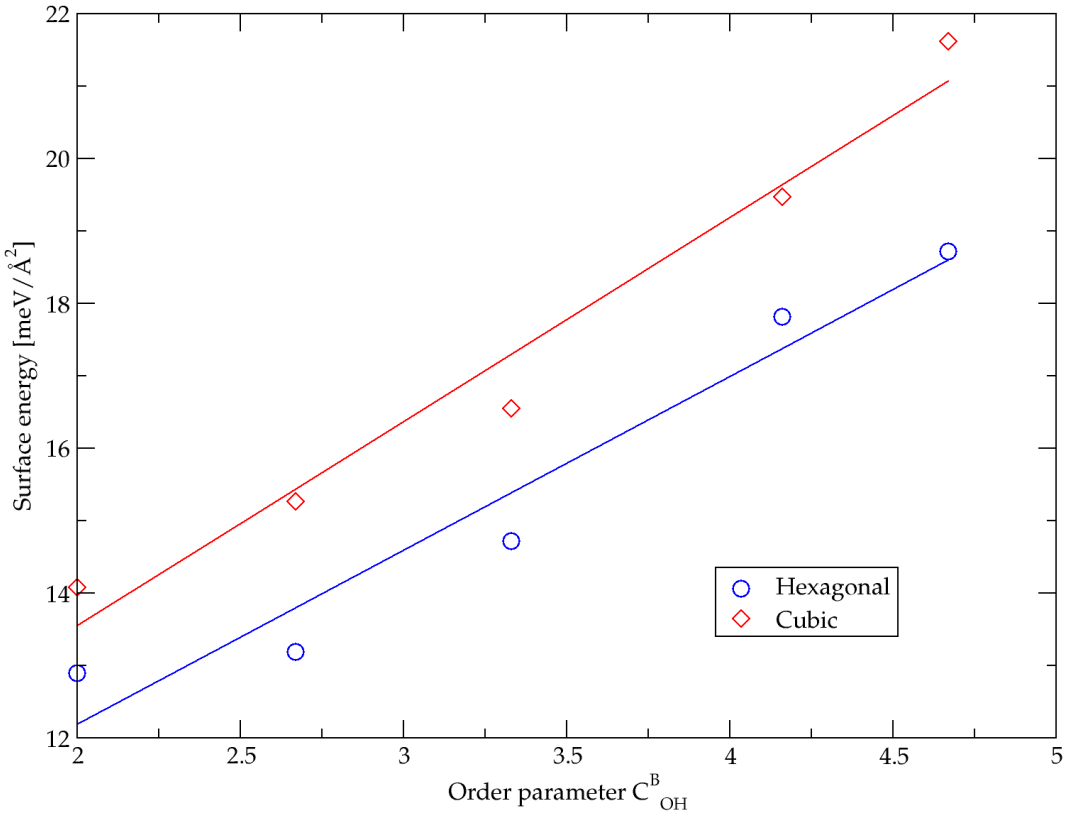

Figure 5.8: Surface energy of hexagonal and cubic ice as a function of the order parameter C^B_{OH}; a higher value of C^B_{OH} represents a higher degree of clustering of dangling OH bonds. Formally, it is the average number of dangling OH bond adjacent to each dangling OH bond.

broad agreement with the results of Pan *et al.*, who report a linear correlation between the surface energy and order parameter. The surface energy of the striped hexagonal phase is slightly higher at the PBE level (12.9 meV Å^{-2} compared with 12.5 meV Å^{-2} according to Pan). Unsurprisingly, the cubic ice surface displays the same trend, from which we can draw the same conclusion as Pan *et al.*: that the most favourable surface ordered configuration minimise electrostatic repulsion between dangling OH bonds,

subject to the constraint that the ice rules are not violated.

Crucially, the cubic ice surface has a higher surface energy by approximately 10% for all values of C_B^{OH}, although the physical meaning of this is a potential subject for debate. At the most fundamental level, cleaving a cubic crystal to expose the (111) plane is less facile than it is to form the basal [0001] plane of hexagonal ice. This means that the hexagonal ice surface is more stable, and therefore less reactive.

In order to explain these findings, we calculated the structural relaxation energy of the striped surfaces, which is defined as the difference in total energy between the final optimised structure and a single point on the initial structure. The relaxation energy turned out to be 0.15 eV higher for hexagonal ice, i.e. the hexagonal ice surface relaxes considerably more. An analysis of the structure revealed that both surfaces undergo reconstruction to roughly the same extent for both polytypes; the oxygen-oxygen separation in the surface bilayers changes from 2.691 Å to 2.704 Åfor cubic ice and from 2.694 Å to 2.707 Å for hexagonal. The standard deviation of surface bilayer oxygen-oxygen separation changed from 0.002 Å to 0.073 Å for cubic ice and 0.021 Å to 0.071 Å for hexagonal. The relative separation of surface protons changed very little, by less than 0.001 Å on average. The only outlying value in this case is the standard deviation surface oxygen-oxygen separation for hexagonal ice before reconstruction; it is almost an order of magnitude higher than for cubic, suggesting there is considerably less symmetry in the hexagonal surface (i.e. the oxygen atoms are further from their ideal lattice points).

The fact that the atoms in cubic ice are more constrained to their lattice points suggests that the curvature of potential energy surface is higher than for hexagonal ice. This is supported by the fact that the hexagonal ice slab took almost an order of magnitude more steps to reach the same convergence threshold (99, compared with 16 for the cubic slab). It is possible that when the surface is cleaved, the shallow potential energy surface for hexagonal ice facilitates further movement in phase space. Performing calculations

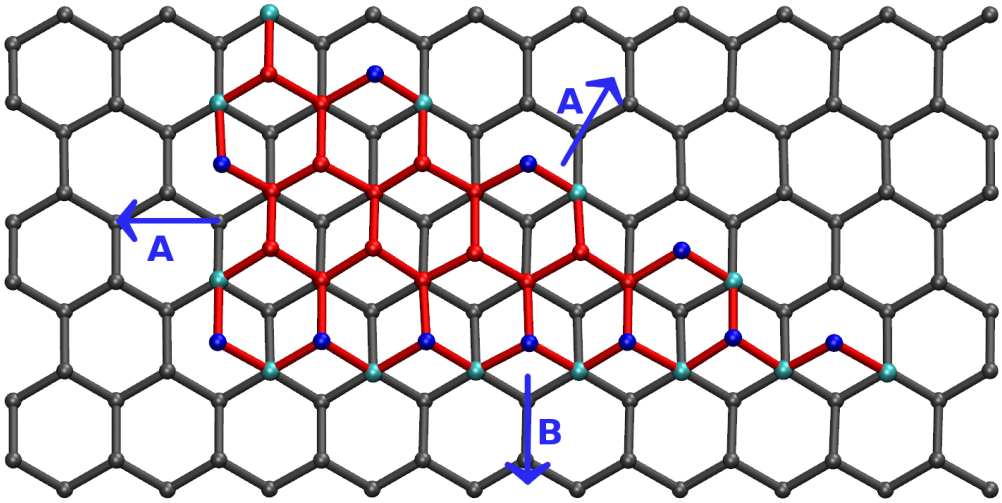

Figure 5.9: Definition of the two step types. Only oxygen atoms are shown; atoms in the uppermost bilayer are coloured red, and atoms in the lower bilayer are coloured grey. Oxygen atoms on step edges are coloured blue on the upper half of the top by layer and cyan on the lower half. The cubic ice surface is shown; on the hexagonal ice surface, there would be no offset between the layers (the hexagons in the two bilayers would coincide vertically), and the steps would grow in the [1000] and [01$\bar{1}$0] directions for the A-steps and in the [0100] direction for the B-step.

analogous to Watkins *et al.*[26] to determine vacancy energies for the cubic ice bulk and surface may be instructive.

5.3.2 Steps on striped surfaces

There are two contributions to the step formation energy on ice surfaces; this section focuses on the effect of the underlying oxygen lattice on the step energy, followed by the effect of proton ordering in section 5.3.3.

5.3.2.1 A, B_1 and B_2 steps

In order to simplify the notation, we define two distinct types of step: A and B (figure 5.9). Furthermore, B-steps are subdivided into two types: B_1, which are terminated with molecules in the upper half of the top bilayer (figure 5.10b), and B_2, which are terminated with molecules in the lower half (figure 5.10c).

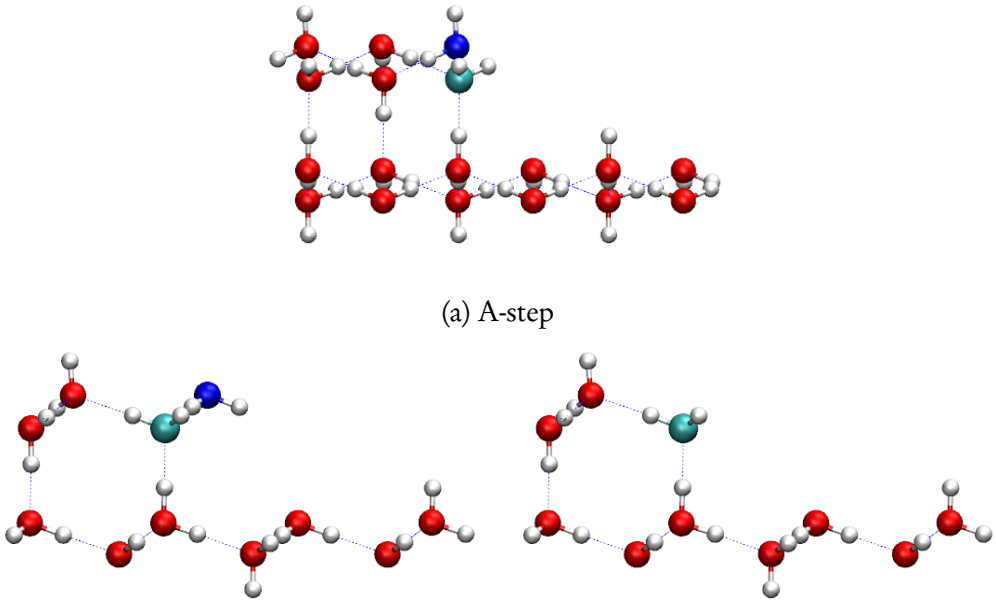

(a) A-step

(b) B_1-step

(c) B_2-step

Figure 5.10: The A-, B_1- and B_2-steps (unrelaxed). Oxygen atoms on the step edge on the upper half of the top bilayer are blue, and cyan on the lower half.

Step formation energies for the hexagonal and cubic A-steps are reported in table 5.1. The alternating value of the ledge energy for the A-steps as l increases is an artefact of the method by which the slab was created, but leads to an important insight into step formation. For the higher ledge energies, the proton ordering resulted in a major structural relaxation on one side of the striped slab, but not on the other, whilst for the lower ledge energies, reconstruction occurred on both sides.

When the basal plane of an ice crystal is cleaved, as in section 5.2.2, the water molecules that are normally four-coordinated in the bulk become three-coordinated at the surface. When a step defect is introduced, some molecules in the top half of the top bilayer on the step edge become two-coordinated, an energetically unfavourable situation. These two-coordinated molecules will sometimes relax to form a third hydrogen bond with a three-coordinated molecule on the bilayer below (figure 5.11), but in some cases the hydrogen bond topology makes this impossible. The lower ledge energies on table 5.1 correspond to surface proton ordering configurations where substantial recon-

A-step			B-step		
l (Å)	Hexagonal	Cubic	l (Å)	Hexagonal	Cubic
8.8	10.1	17.0	15.3	30.1	29.4
13.2	16.5	8.9	19.1	37.8	37.5
17.6	10.4	16.7	22.9	14.26	15.9
22.0	16.3	9.0	26.7	42.9	41.2
26.4	10.5	16.8	30.6	29.9	28.9
30.8	16.9	10.1	34.4	38.2	37.1
34.2	12.8	17.0	38.2	14.3	16.0

Table 5.1: Ledge energies (E_{ledge}) in eV Å^{-1} of hexagonal and cubic A- and B-steps on striped surfaces. l is the distance between steps (periodic images), i.e. a larger value of l represents a narrower step with a larger distance to the next periodic image (see figure 5.7). A single row of molecules is removed from the step edge in to create slabs with progressively larger values of l.

struction as in figure 5.11 occurs on both step defects (i.e. both sides of the "top hat" on the slab), whilst the higher energies correspond to a situation where there is reconstruction on one side only. Reconstruction can occur similarly on the B-step, as shown in figure 5.12.

Ledge energies for B-steps are almost invariably higher than for the A-steps, but spread is much larger, and there are four distinct energy "bands". As with the A-steps, it is possible for either side of the step feature to relax, but in addition there are two distinct ways of cleaving the surface to generate either a B_1-step or a B_2-step, compared with one for the A-steps. The ledge energies are considerably higher as a result of the topology of the surface — in all cases, only one of the two step edges was able to relax to form the third hydrogen bond mentioned above. On the A-step, there were up to three water molecules on the step edge that underwent major structural relaxation to form an extra hydrogen bond (figure 5.13), compared with up to five on the B_1-step (figure 5.14) and none on the B_2 step. The B_2 step undergoes minimal structural relaxation because all of the molecules on the step edge are in the lower half of the bilayer and are therefore three-coordinated.

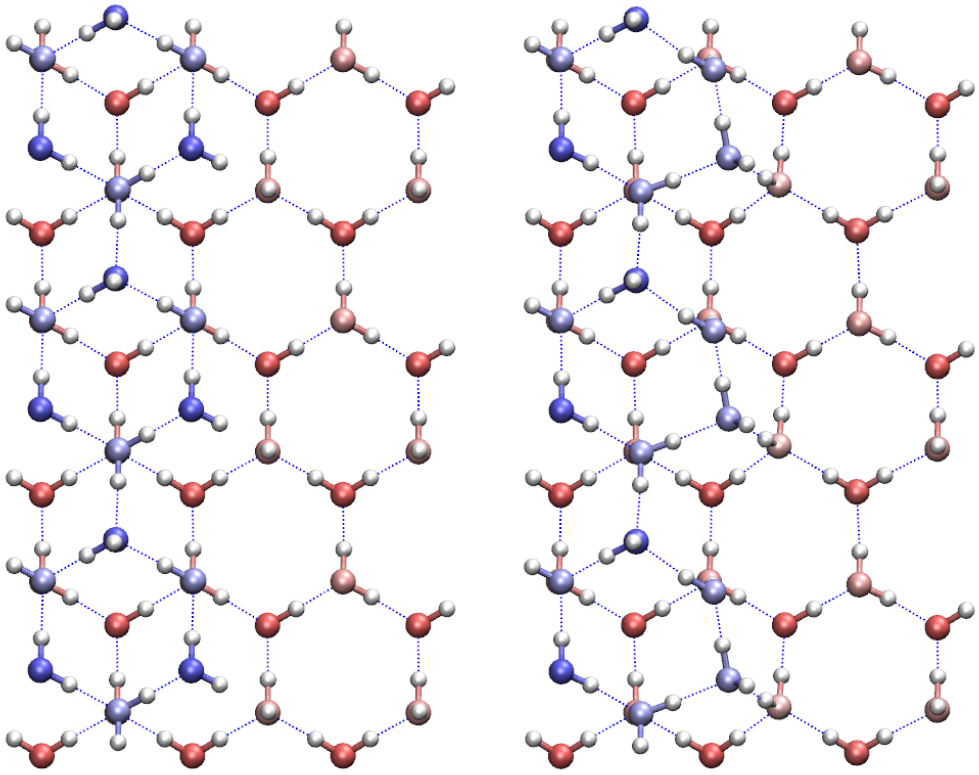

(a) Top view before reconstruction.

(b) Top view after reconstruction.

(c) Side view before reconstruction.

(d) Side view after reconstruction.

Figure 5.11: A step feature on the basal plane of a striped six bilayer $10 \times 3 \times 2$ cubic ice surface before and after reconstruction (only two bilayers shown). Oxygen atoms are coloured according to their "height" in the cell; dark blue atoms are in the top half of the upper bilayer, and dark red atoms are in the lower half of the bottom bilayer. Hydrogen bonds are indicated by blue broken lines. Note the formation of the new hydrogen bond to the two-coordinated molecules in the uppermost bilayer after relaxation.

5.3.2.2 B_1^* and B_2^* steps

The situation is complicated further by the lack of mirror symmetry for the two uppermost bilayers when a B-step forms. It is therefore necessary to define two further types

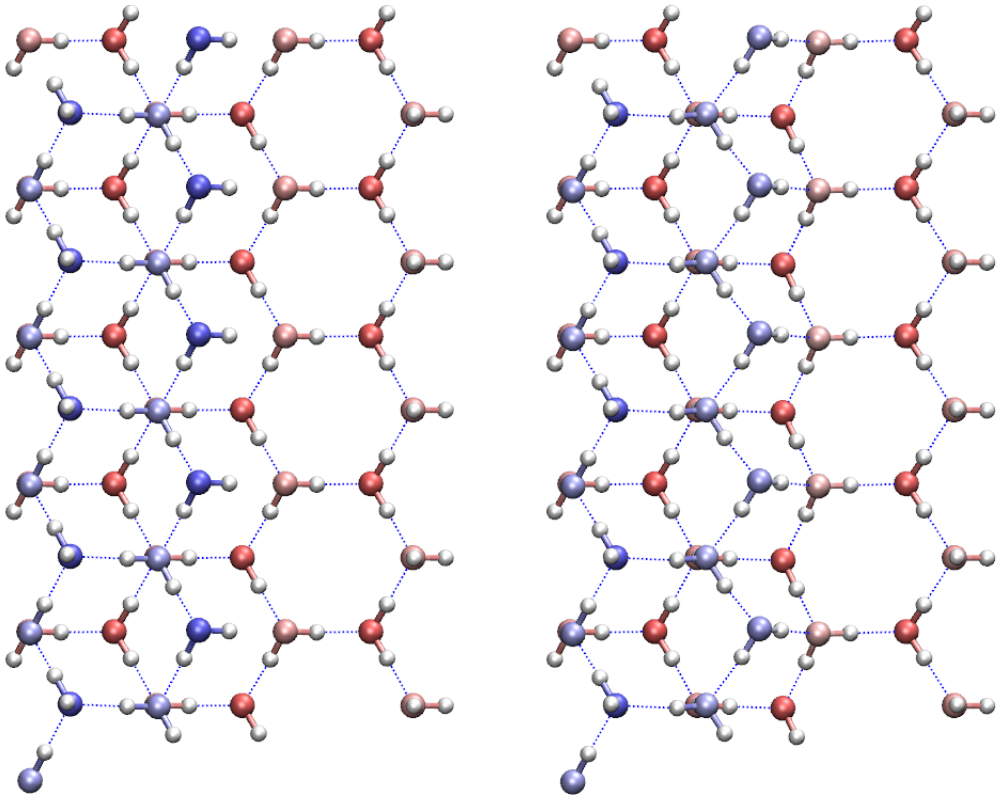

(a) Top view before relaxation.

(b) Top view after relaxation.

(c) Side view before relaxation.

(d) Side view after relaxation.

Figure 5.12: A step feature on the basal plane of a striped six bilayer $5 \times 6 \times 2$ cubic ice surface before and after relaxation (only two bilayers shown). Oxygen atoms are coloured according to their "height" in the cell; dark blue atoms are in the top half of the upper bilayer, and dark red atoms are in the lower half of the bottom bilayer. Hydrogen bonds are indicated by blue broken lines. Note the formation of the new hydrogen bond to the two-coordinated molecules in the uppermost bilayer after relaxation.

of B-step: B_1^* and B_2^*. The difference between B_1 and B_1^* is shown in figure 5.15. There are one-coordinated molecules on a B_1^*-step edge, thus even after major reconstruction, the edge molecules remain two-coordinated. The two-coordinated edge molecules on

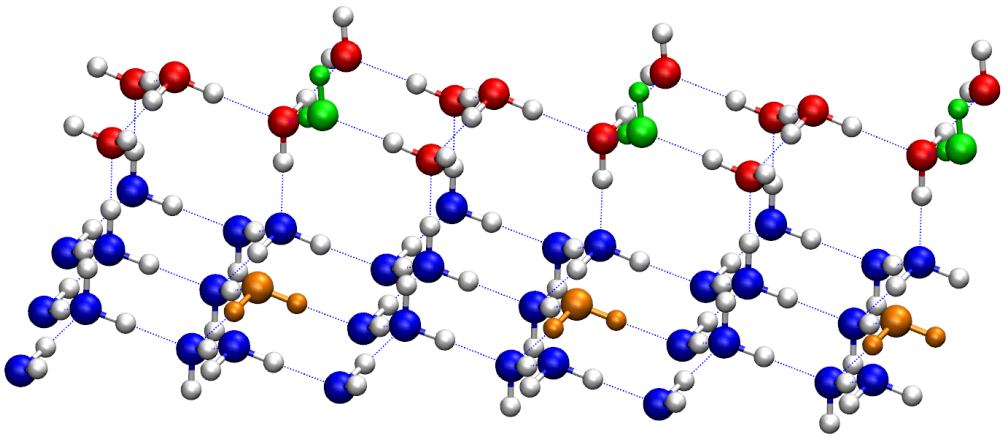

Figure 5.13: The "active" molecules in the reconstruction of the A-step in the top bilayer (green) and its only nearest neighbour in the lower bilayer (orange) on an A-step. Red oxygen atoms are in the upper terrace and blue ones are in the lower terrace.

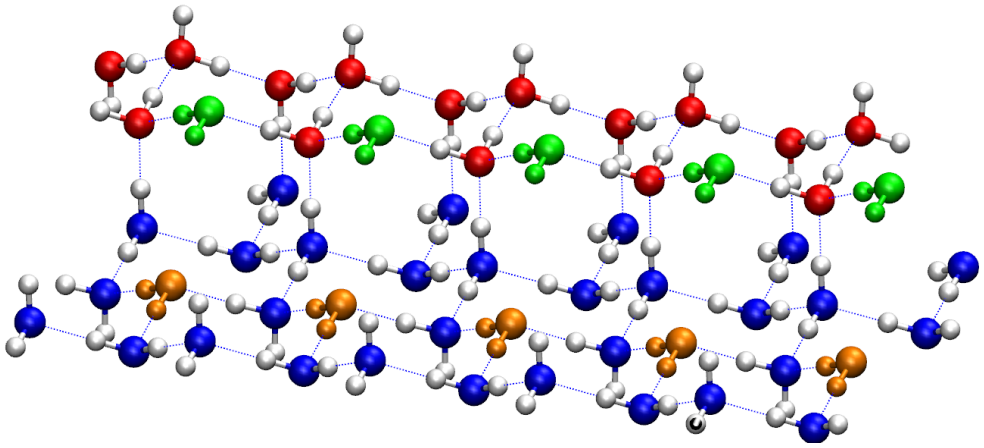

Figure 5.14: The "active" molecules in the reconstruction of the B_1-step in the top bilayer (green) and its nearest neighbours in the lower bilayer (orange) on an A-step. Red oxygen atoms are in the upper terrace and blue ones are in the lower terrace.

the B_1 step have two nearest neighbours on the lower terrace with which they can form a hydrogen bond, compared with only one for the B_1^*-step.

A similar situation arises for the B_2- and B_2^* steps; however, there is minimal structural relaxation for any B_2 step, so their step formation energies should be similar.

Due to the symmetry of the ice slab, it is impossible to form a grooved slab with only B_1 or B_1^* steps, there will always be one of each (and similarly for B_2 and B_2^*). Therefore the ledge energies presented for B-steps are not representative of a single type of step.

The five different types of step are summarised in table 5.2. Table 5.3 lists the lowest

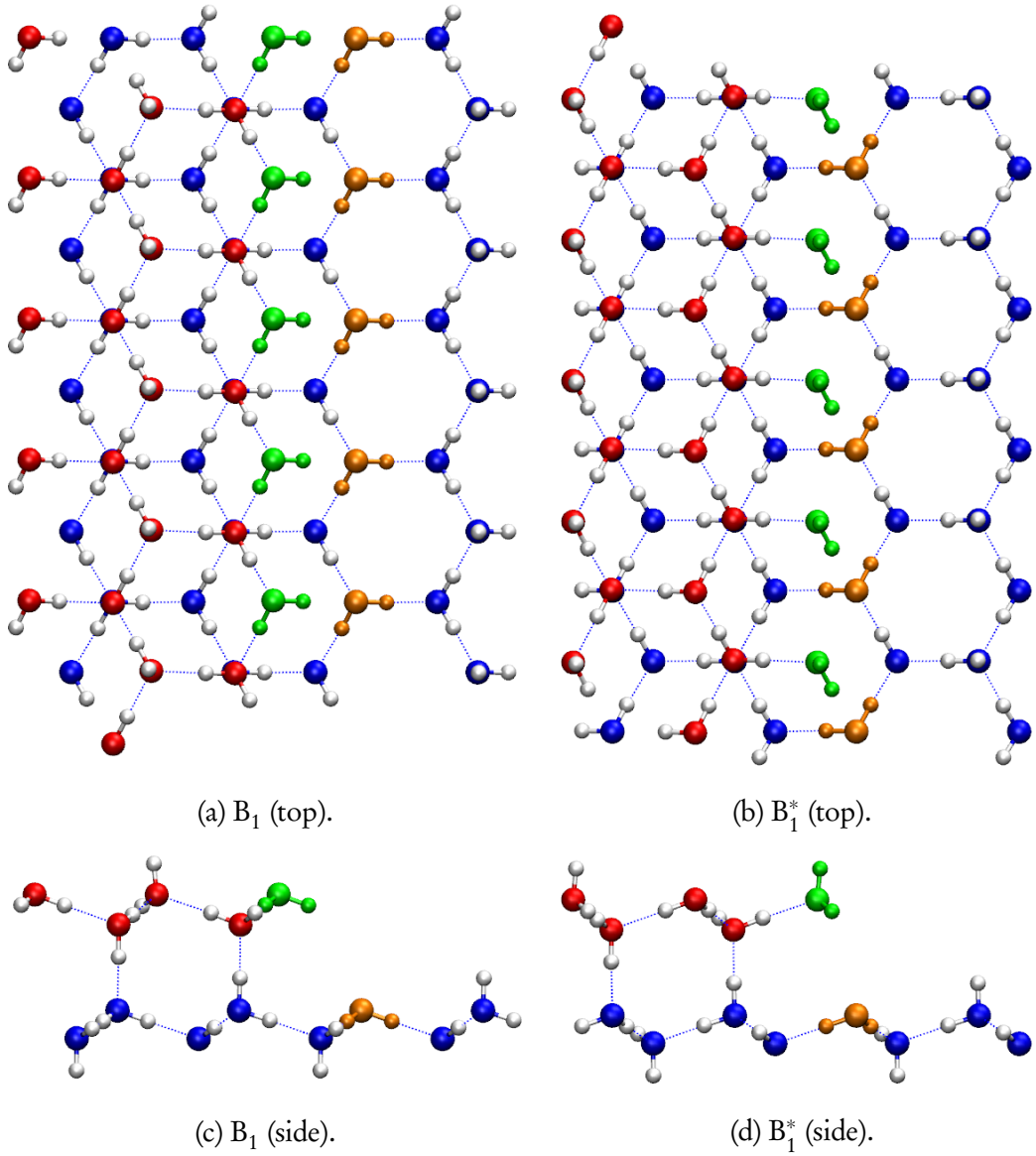

(a) B_1 (top). (b) B_1^* (top).

(c) B_1 (side). (d) B_1^* (side).

Figure 5.15: Difference between B_1- and B_1^* unreconstructed steps. Two-coordinated molecules are green, and the lower terrace molecules to which they form new hydrogen bonds are orange. Note that in the B_1^* step, the two-coordinated molecules each have two nearest neighbours in the lower terrace, compared with one for the B_1-step.

ledge energies for the cubic striped slabs. For these three cases, both sides of the terrace have the same step feature (i.e. a reconstructed A-step, a reconstructed B_1 step or an unreconstructed B_2 step on both sides), so based on the assumption that l is sufficiently high (approximately 20 Å in these cases) and the Coulomb interaction between step images is essentially zero, these are the step formation energies.

Step	Coordination number of step edge molecules	Number of nearest neighbours in lower terrace
A	2	1
B_1	2	1
B_1^*	1	2
B_2	3	—
B_2^*	3	—

Table 5.2: Summary of different step types.

	Ledge energy	
	meV/Å	eV/molecule
A	17.38	0.25
$B_1 + B_1^*$	22.81	0.10
$B_2 + B_2^*$	32.95	—
$B_1 + B_2$	15.97	—
$B_1^* + B_2^*$	41.22	—

Table 5.3: Lowest step formation energies for *proton ordered* (striped) surfaces. Due to the slab symmetry, there are always two types of step in the B-direction on each slab. Step energy per molecule refers to (notionally) two-coordinated molecules. Ledge energies per molecule are expressed as energy per *two-coordinated* molecule. Values for step combinations involving a B_2 step have not been included because they do have two-coordinated molecules on the step edge.

The bulk energy of hexagonal or cubic ice is 0.7 eV and in the bulk, there are two hydrogen bonds per molecule (in the bulk each molecule is involved in four hydrogen bonds, accepting and donating two each, but these are shared so there are only two bonds per molecule), resulting in an average energy of 0.35 eV per bond. The lowest ledge energy per molecule for an A-step on the cubic striped slab can be expressed as 0.25 eV per notionally two coordinated molecule, which corresponds approximately to the formation of one additional hydrogen bond during reconstruction. Similarly, the energy of the B_1 step can be expressed as 0.10 eV per two coordinated molecule, which is considerably lower. The B_1 step has a higher density of two coordinated molecules than the A-step (2.20 $Å^{-1}$ for the former compared with 3.81 $Å^{-1}$ for the latter), but the

ledge energy per Ångstrom is higher for the B_1 step. This is somewhat counterintuitive, since one might expect more reconstructions per unit length to lower the B_1 step energy more than for the A-step.

5.3.2.3 Formation energies of different step types

In order to explain these numbers, I have attempted to calculate the energy of each unique B-step type. The symmetry of the ice lattice normal to the surface and in the B-direction means that it is only possible to construct certain combinations of B-steps. This gives the sums of step energies in table 5.3. These can be regarded as four simultaneous equations with four unknowns, which can be written in matrix form:

$$\begin{pmatrix} 1 & 1 & 0 & 0 \\ 0 & 0 & 1 & 1 \\ 1 & 0 & 1 & 0 \\ 0 & 1 & 0 & 1 \end{pmatrix} \begin{pmatrix} E(B_1) \\ E(B_1^*) \\ E(B_2) \\ E(B_2^*) \end{pmatrix} = \begin{pmatrix} 22.81 \\ 32.95 \\ 15.97 \\ 41.22 \end{pmatrix} \tag{5.7}$$

This matrix is singular, as can be demonstrated by adding the first and second rows, and the third and forth rows, thus there are linear dependencies and this set of equations cannot be uniquely solved. If we assume that $B_2 = B_2^*$, the resulting equations can be solved to give step energies of $E(B_1) = -0.51$ meV Å^{-1}, $E(B_1^*) = 23.33$ meV Å^{-1} and $E(B_2) = 16.49$ meV Å^{-1}. The negative energy for the B_1 step suggests that the assumption that the B_2 steps have identical energies is not completely valid. It is not unreasonable, however, to assume they are similar, from which it follows that the B_1 step has the lowest energy of all steps (including A) due to the dense reconstruction. The high energy of the B_1^* step is a result of one-coordinated molecules reconstructing to become two coordinated, such that although they do undergo reconstruction, the edge molecules still have a lower coordination (2) than on the B_2 steps (3). Finally, in order to make the step formation energy of B_1 positive, the B_2-step must have a lower energy than B_2^*,

although the reasons for this are unclear, since both undergo minimal reconstruction.

Up to this point, we have not discussed the difference between steps on hexagonal and cubic ice surfaces. Table 5.1 suggests that A-step energies are about 5–10% higher for hexagonal ice on the cubic ice surface, and B-step energies are generally 5–10% higher for B-steps on the hexagonal ice surface. In a hexagonal ice crystal the bilayers are stacked such that in the z-direction, "channels" run through the hexagonal rings; in cubic ice, the layers are offset such that a molecule lies at the centre of a hexagonal ring on the layer below. The differences in step energy must be a combined result of the difference, and the subtly different proton ordering (even though both hexagonal and cubic surfaces are striped). At this stage, we do not have an explanation for the energy differences.

In the following sections, we use only proton disordered cubic ice surfaces; both hexagonal and cubic ices are of interest for different reasons, so the choice is somewhat arbitrary. We expect the same step formation model will be valid for both polytypes with subtle energetic differences, since in the first coordination sphere of a molecule, the structures are identical. After development of a model for cubic ice, we hope to revisit hexagonal ice in future work.

5.3.3 Steps on disordered surfaces

It is difficult to relate these numbers to the two-dimensional single bilayer crystal growth on the ice surface, firstly because the surfaces considered thus far are striped (having an order parameter of 2), and secondly because of topological variation when a single layer is cleaved from the step edge due to both the underlying ice lattice and the surface proton ordering. The lowest energy B-step on the hexagonal slab is more favourable than the lowest energy A-step, but a randomly cleaved B-step is less likely to have the lower energy due to topological variation. These considerations are however somewhat artificial, since one would expect the surface to be proton disordered, with an order parameter of 3.0.

l (Å)	A-step
13.2	20.0
17.6	28.4
22.0	25.0
26.4	25.5
30.8	17.4
35.2	30.1
39.6	18.5

Table 5.4: Ledge energies in meV Å^{-1} for proton disordered cubic ice A-steps ($C_B^{\mathrm{OH}} = 3.07$).

l (Å)	$B_1 + B_1^*$	$B_2 + B_2^*$
9.5	19.1	38.8
17.1	30.6	36.3
24.8	38.6	31.7
32.4	31.6	37.1

Table 5.5: Ledge energies in meV Å^{-1} for proton disordered cubic ice B-steps ($C_B^{\mathrm{OH}} = 3.07$).

The energies in section 5.3.2 only apply to a special case, the striped Ih/Ic surface; on a disordered surface, the step termination is unlikely to lead to a straight step defect since the relaxation must be dependent on the proton ordering on the top two bilayers. Surface disordered slabs were generated as in section 5.2.1; in the first instance, surfaces with an order parameter closest to three (the supposed order parameter of a real hexagonal ice surface) were considered. Tables 5.4 and 5.5 demonstrate the range of ledge energies for seven different proton disordered A-steps and eight different proton disordered B_1 and B_2 steps on surfaces with an order parameter of 3.07.

From this relatively small set of results, it can be seen that ledge energies range between 17.4 meV Å^{-1} and 30.1 meV Å^{-1} for A-steps, 19.1 meV Å^{-1} and 38.6 meV Å^{-1} for B_1-steps and 31.7 meV Å^{-1} and 38.8 meV Å^{-1} for B_2-steps. These numbers give the impression that disordered A-steps generally have the lowest ledge energies, followed by B_1 steps, and B_2 steps have the highest energies.

Considering first the A-step energies, those at the lower end of the range occur when all of the two-coordinated step edge molecules are in a favourable configuration to form the additional hydrogen bonds. As the number of under-coordinated molecules increases, the step energy increases. There are instances where a two-coordinated molecular configuration is so unfavourable due to Coulomb repulsion that it is almost forced out of the step, becoming part-way between a step molecule and a surface-adsorbed molecule; these have the highest step energy.

The energies above for B_1 steps are an average for the B_1-step on one side of the terrace, and a B_1^* on the other — and as demonstrated in section 5.3.2, the B_1 ordered step has the lowest formation energy and the B_1^* ordered step has the highest energy since after reconstruction B_1-step edge molecules are three-coordinated, whereas B_1^* molecules are two-coordinated. The outlying energy for the B_1-step at $l = 9.5$ has two possible causes. The first is the favourable, locally striped proton ordering on the B_1-step which allows full reconstruction of all two-coordinated edge molecules. The second is the fact that each edge molecule on the B_1^* step has two nearest neighbours on the lower terrace, which for the local proton ordered structure in this case, allowed one of the edge molecules to become three coordinated, lowering the step energy substantially.

The figures in tables 5.4 and 5.5 give an indication of the affect of proton ordering on cubic ice steps, but to get a statistical average for these energies requires far more calculations on surfaces of varying order parameter and the same periodic step separation. The surfaces used in this chapter are somewhat biased by the way they were constructed: the Move algorithm was used on a striped slab; although this randomises the surface over time, surfaces with low values of C_{OH}^{B} locally retain characteristics of the striped slab, which may result in slabs that are more ordered than intended. A possible solution would be to start with a high-C_{OH}^{B} slab, and run the algorithm in reverse, only accepting moves that reduce the order parameter.

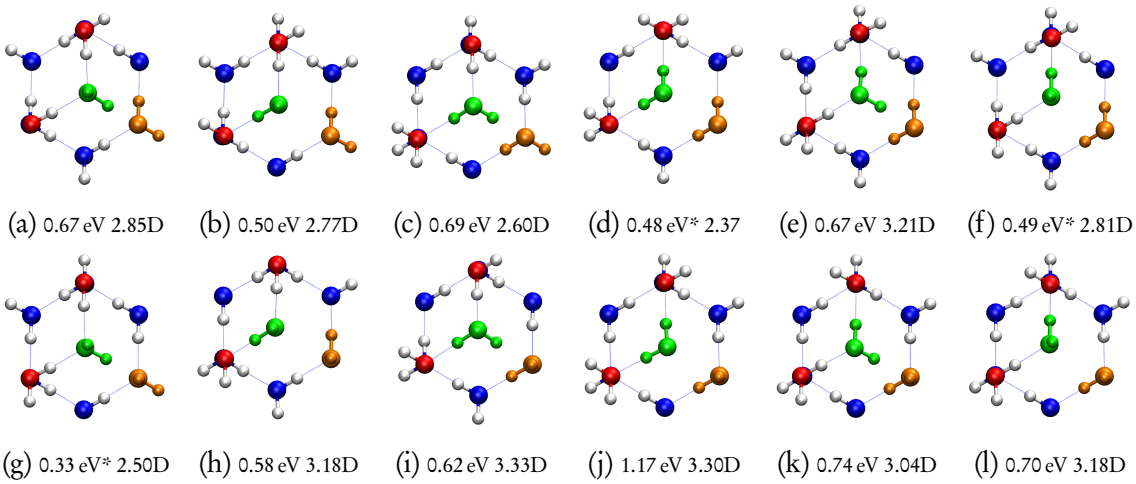

(a) 0.67 eV 2.85D (b) 0.50 eV 2.77D (c) 0.69 eV 2.60D (d) 0.48 eV* 2.37 (e) 0.67 eV 3.21D (f) 0.49 eV* 2.81D

(g) 0.33 eV* 2.50D (h) 0.58 eV 3.18D (i) 0.62 eV 3.33D (j) 1.17 eV 3.30D (k) 0.74 eV 3.04D (l) 0.70 eV 3.18D

Figure 5.16: The twelve possible configurations for the "active" molecules in a A-step edge termination on cubic ice, together with the vacancy energy of the molecule in the upper half-bilayer of the step (coloured green) and its dipole moment. The other upper bilayer molecules are coloured red, and lower bilayer molecules are coloured blue. The ledge energy depends on whether this molecule is unrestricted enough to relax and form a hydrogen bond with the closest molecule in the upper half-bilayer of the lower terrace (coloured yellow). The three configurations marked with an asterisk (*) do not undergo this reconstruction.

5.3.3.1 Vacancy energies for disordered steps

In the case of the A-step, it was observed that the ability of a two-coordinated molecule in the top half of the top bilayer (dark blue in figure 5.11) to relax is determined by its orientation and the orientation of its nearest three-coordinated neighbour in the top half of the bilayer below (pale red in figure 5.11). A molecule constrained by an ice lattice has six allowed orientations, and there are only two possible orientations of the molecule in the lower bilayer that can influence the relaxation, a dangling OH bond or a non-dangling OH. Thus there are $2 \times 6 = 12$ configurations of the two "active" molecules, pictured in figure 5.16. The vacancy energy of the upper bilayer molecule (in green) was evaluated in each case, along with the dipole moment of the molecule in question.

It is noteworthy that of the 12 configurations illustrated in figure 5.16, only three are incapable of the reconstruction to form an additional hydrogen bond. These con-

figurations have the lowest vacancy energies, which is unsurprising since they remain two-coordinated. Thus approximately one in four molecular sites on a step will have a high energy, onto which adsorption and therefore crystalline growth are easier. Adsorption onto one of these sites will result in two kinks on the step, which facilitate expansion of the growth front.

5.3.3.2 Molecular dipoles of step edge molecules

Watkins *et al*. established that surface molecules have a large and continuous range of vacancy formation energies, and that the vacancy energy is weakly correlated with the molecular dipole[26]. They note that in the bulk (a set comprised of all molecules below the surface bilayer), molecular dipoles have values in a narrow band around 3.5D, the bulk molecular dipole, and the surface molecules have dipoles in a wide band between roughly 2.7D and 4.5D. Figure 5.17 shows the frequency of molecular dipoles in a $10 \times 3 \times 2$ (6-bilayer) proton disordered cubic ice slab with an A-step. In agreement with the finding of Watkins *et al*. there is a strong peak in the range 3.4–3.7D which constitutes the bulk molecules, with a large spread for the surface molecules.

If we consider only molecules on the step edge that are two-coordinated when the surface is cleaved, the frequency distribution of dipoles is shown in figure 5.18. It can be seen that most edge molecules have a dipole between the bulk value (3.5D) and the gas phase value (1.85D). This is because the geometry of a molecule is less constrained at the step edge compared with the bulk, and the bond angle is allowed to relax to a conformation closer to the gas phase value.

In a similar analysis to Watkins *et al*[26]., figure 5.19 shows the molecular dipole plotted against the vacancy energy, but only for molecules on the step edge in the top half of the bilayer, i.e. molecules that are two coordinated instantaneously after the surface is cleaved to create the step feature. Note that the gas phase energy of a water molecule is used as the reference here (whereas Watkins *et al*. used a bulk phase reference). It shows

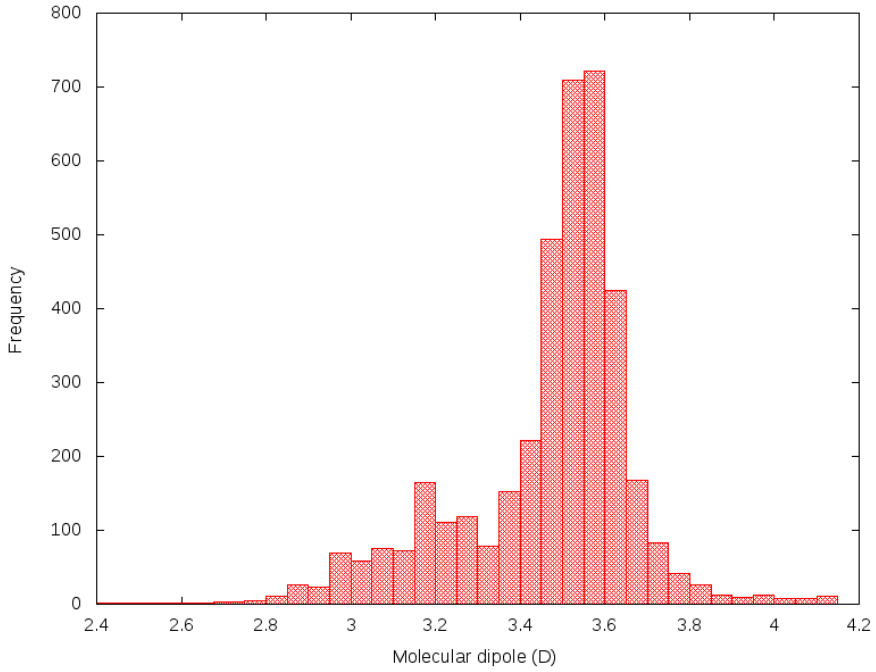

Figure 5.17: Histogram of molecular dipole moments for all molecules in seven different six-bilayer cubic ice slabs with a step feature. The sharp peak in the 3.5–3.6D range corresponds to the molecular dipole in bulk ice.

a weak positive correlation — higher dipoles are generally associated with a higher vacancy energy. This is consistent with the findings of Watkins *et al*. for a pristine surface. Thus in principle, it should be possible to identify the most weakly bound molecules by identifying the step molecules with the lowest dipole moment as the points on the step edge most susceptible to pre-melting. Thierfelder *et al.* report adsorption energies in the range 0.548 eV to 0.576 eV for a water monomer on a disordered hexagonal ice surface using VASP and the PBE functional[151]. The adsorption energy is therefore higher than the vacancy energy for the step edge molecules that do not undergo significant reconstruction in figure 5.16 (5.16d, 5.16f and 5.16g), and possibly one or two that do undergo reconstruction (5.16b, 5.16h). Molecules in these configurations must be metastable with respect to migration from the step to the terrace, but there must also be an activation barrier since they did not spontaneously move during geometry optimisation. It is possible that some of these molecule occupy local minima on the potential energy surface, and it should be emphasised that we have only performed *static*

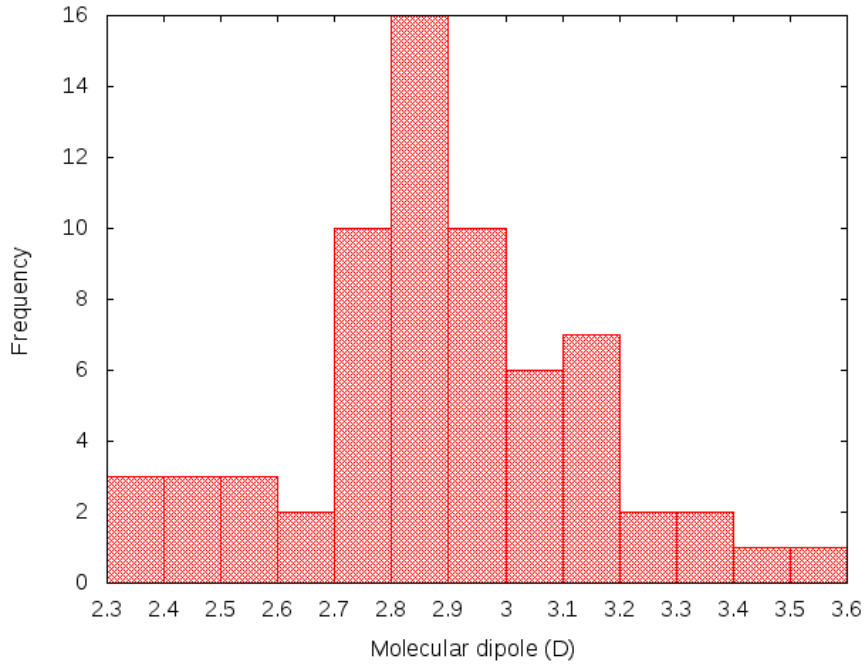

Figure 5.18: Frequency distribution of dipoles of molecules that are two-coordinated when the surface is cleaved to form a step defect (i.e. molecules in the top half of the bilayer). These molecules may or may not relax to form a third hydrogen bond with a molecule on the lower bilayer, as in figure 5.11d. This plot uses data from 12 different slabs, for a total of 76 data points.

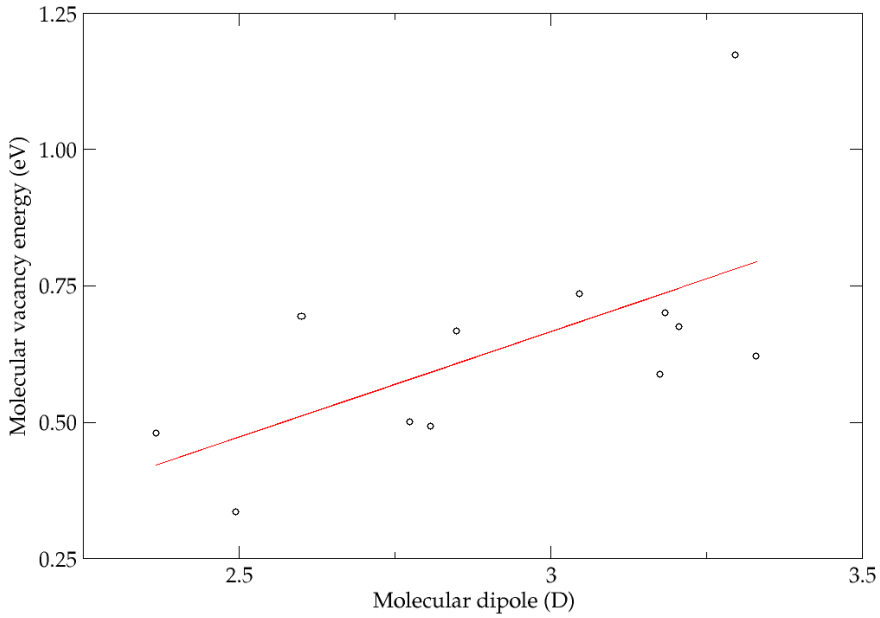

Figure 5.19: Plot of molecular dipole moments against vacancy energies for water molecules on the step edge in the top half of the uppermost bilayer. The red line shows the weak inverse correlation.

calculations at 0 K. In a molecular dynamics simulation, where the system is given thermal energy, it is quite possible that these loosely bound molecules will overcome low barriers and migrate to one of the terraces, manifesting pre-melting on the microscopic scale.

The ledge energies for ordered and disordered surfaces give us an important insight into the rate and direction of the two dimensional nucleation reported by Sazaki *et al*[6]. A low step energy represents a stable termination. After the crystal is cleaved to form a step, some of the molecules in the upper half of the top bilayer will be two-coordinated, i.e. they only form hydrogen bonds with two other molecules. This is an unstable arrangement — the lowest energy configuration in bulk ice consists of four-coordinated molecules which are topologically impossible at the surface — therefore molecules at the step edge prefer to relax, forming a third hydrogen bond with the lower terrace. The formation of such stable steps actually hinders the lateral growth of a bilayer because hydrogen bonds must be broken in order to adsorb additional molecules. Steps are more reactive relative to the surface or bulk because the molecular sites are undercoordinated, and are therefore particularly susceptible to adsorption and modify diffusion barriers[152]. Crystal growth is faster on "sticky" edges, that is, edges with a higher ledge energy where the energy will be lowered by the addition of a molecule from the liquid phase without a barrier. In the case of the three-coordinated step edge molecules, this might require the breaking of the newly formed hydrogen bond. Growth is therefore faster on a step where the structural relaxation has not occurred.

Sazaki *et al*. observed birth and *isotropic* growth of single ice bilayers — there was no preferred growth direction and no distinct flat step front. Steps in [1000] and [10$\bar{1}$0] directions are topologically identical (as illustrated in figure 5.9 when considering the oxygen sub-lattices, so one might expect to see the birth of hexagonal "islands" and their planar growth; the work of Sazaki demonstrates that this is not necessarily the case.

The formation of hexagonal islands is hindered by two effects. The first is that an

A-step may conditionally have a higher ledge energy than a B-step, due to the fact that a B-step may consist of only molecules in the upper half of the bilayer in the upper terrace, or only molecules in the lower half of the bilayer. The former will relax to create a low energy step due to the higher density of notionally two-coordinated molecules per unit length compared with A-steps, whilst the latter is a high energy and therefore "sticky" step since molecules in the lower half of the bilayer are invariably three-coordinated and cannot relax. This should presumably lead to a step growth with two distinct alternating rates: fast when the sticky high energy step is exposed, then low when the low energy relaxed step is formed.

The second effect is surface proton disorder. Watkins *et al*. demonstrated that the ice surface has a wide range of molecular vacancy energies, and figure 5.19 demonstrates that the same is true of step edge molecules in the upper half of the bilayer, suggesting that certain points on the step are more susceptible to pre-melting. The converse is also true: that there is a range of molecular adsorption energies at the step edge which will result in non-uniform two-dimensional crystal growth.

In conclusion, it would appear that the isotropic two-dimensional growth of single bilayers on the ice surface is a complicated superposition of three effects: firstly, the growth of A-steps in the direction of the prism faces which in principle would result in the formation of expanding hexagonal islands; secondly, growth of B-steps, which alternates between faster than growth in any other direction and slow depending on whether the step terminates in molecules in the bottom or top half of the bilayer respectively; and thirdly, proton disorder, which should be stochastic for the expected random dangling-OH distribution. It is not inconceivable that these three effects in conjunction could lead to the birth and growth of the expanding circular islands observed by Sazaki *et al*. but a more detailed characterisation requires further study.

5.4 Summary and conclusions

DFT calculations show that the cubic ice surface, like the hexagonal ice surface, undergoes reconstruction to minimise the energy due to electrostatic repulsion between dangling OH bonds. As with hexagonal ice, the surface energy is correlated with the order parameter C_B^{OH}, which describes the average number of dangling OH bonds adjacent to a dangling OH bond, such that clustering of dangling OH bonds is energetically unfavourable, whilst the Fletcher striped phase has the lowest energy. The surface energy of the cubic striped phase is approximately 10% higher than that of the hexagonal striped phase, so hexagonal ice is less reactive.

We have identified five distinct types of step on the ice I surface, and evaluated their energies on proton ordered and disordered surfaces. Some proton ordered configurations allow the undercoordinated molecules on a step edge to reconstruct, forming an additional hydrogen bond with the lower terrace, thereby reducing the step energy. B_1 steps have the lowest step formation energy since they undergo the most molecular reconstructions per unit length. B_1^* steps have the highest surface energy because the terminating molecules are one-coordinated, and reconstruct to become only two-coordinated. Only molecules in the upper half of the top bilayer at the step edge are capable of undergoing this relaxation, thus B_2 steps, where the step terminates on a three-coordinated molecule on the lower half of the bilayer will undergo minimal reconstruction (i.e. will not form new hydrogen bonds), and have a higher step energy. Proton disordered steps have a range of energies, and disordered A-steps generally have a lower energy than disordered B-steps for the reason detailed above.

Two-coordinated molecules on the step edge (prior to reconstruction) have a range of vacancy energies; these vacancy energies are weakly correlated with the molecular dipole moment, since the most weakly bound molecules have weaker hydrogen bonds, therefore their electron density is closer to that of the gas phase.

Two-dimensional bilayer ice growth is dependent on step energies: high energy steps

will result in a faster moving growth front since they are more reactive and therefore "sticky". Thus growth is fastest in the B-step direction, and has an alternating rate: fast when a B_2-step is exposed, and slow when a B_1 step is exposed. However, the overlapping range of energies for disordered A-steps means that growth in the direction of the A-step maybe conditionally favoured depending on the local proton ordered configuration. A range of molecular vacancy energies for two-coordinated molecules on the step edge means that certain sites on the step are more favourable for adsorption, resulting in non-uniform growth. These effects in part explain the lack of straight step fronts in the two-dimensional growth of elementary ice layers observed by Sazaki *et al*., but we cannot make strong inferences about the circular growth patterns observed.

Chapter 6

Formation of interstellar glycolaldehyde

6.1 Introduction

Glycolaldehyde is the simplest sugar, a monosaccharide containing two carbon atoms with the formula CH_2OHCHO. It is the subject of interest due to its implication in the formation of RNA and amino acids in terrestrial environments. The prebiotic synthesis of sugars on Earth was thought to occur via the formose reaction $2\,H_2CO \longrightarrow CH_2OHCHO$, which is autocatalytic after the first reaction catalysed by (for example) a clay surface, a base, or a photon[7]. The discovery of extraterrestrial glycolaldehyde in molecular clouds, where stars are born, casts doubt on this proposition.

It has been detected in significant quantities first in the Galactic Centre molecular cloud Sagittarius B2(N)[7] and more recently near the star-forming hot molecular core G31.41+0.31[8]. It is known that the reactions necessary to form glycolaldehyde cannot occur in the gas phase in the lifetime of a molecular cloud (roughly ten million years); although many reactions between hydrogen atoms and neutral molecules have low barriers, they cannot proceed at temperatures lower than 100 K[153]. Whilst the details of

the formation mechanism is unknown, it is assumed to proceed via a series of reaction starting with the hydrogenation of carbon monoxide, catalysed by icy "mantles" coating dust grains in the interstellar medium (ISM).

The interstellar formation of Glycolaldehyde is a potential future hot topic, since it has recently been observed using ALMA (the Atacama Large Millimeter Array) in the vicinity of the Sun-like protostar IRAS 16293-2422[9]. Crucially it was detected at distances roughly equivalent to the separation of the Sun and Uranus from the protostar, suggesting that the ingredients for life were present during the formation of the solar system.

Since it is impossible to simulate the long timescales and extremely low fluxes involved in astrochemistry experimentally, examining reaction barriers using computational modelling can give us great insight into the mechanisms of glycolaldehyde formation.

In this chapter we propose a potential mechanism for the formation of glycolaldehyde based on the astrophysical and chemical considerations in a recent paper by Woods *et al.*, and an alternative proposed by Goumans (private communication, 2011). The first part is a characterisation of the reactions comprising these mechanisms in the gas phase to high levels of theory including MP2 and CCSD(T). The second part models bare dust grains as hydroxylated silicate nanoclusters, assessing their effect on the reaction barriers. The third part examines the catalytic effect of a crystalline ice surface on these reactions, modelling icy mantles on interstellar dust grains.

6.2 The nature of interstellar dust grains

Glycolaldehyde has been observed in molecular clouds, cold and dense regions containing gas and dust which agglomerate to form stars and planets. Temperatures vary between 10 K and 100 K; the temperature is lowest at the core of the cloud, which is shielded from radiation by the surrounding dust grains. The collision rate between

gaseous atoms and molecules is less than once per year, with significant chemical evolution occurring over a timescale of 10^6 to 10^7 years[154]. At such low temperatures, reaction barriers are typically too high in the gas phase, and are therefore thought to occur on the surface of dust grains for the following three reasons[154]:

- At 10 K, most atoms and molecules deposited on the grain surface remain adsorbed for long periods of time.
- Excess energy from exothermic reactions can escape into the surface, allowing addition and recombination reactions to proceed without subsequent dissociation.
- The surface can be a catalyst, reducing reaction barriers and allowing the formation of complex molecules under unfavourable conditions.

The nano-particles comprising interstellar dust make up only 1% of the total mass of the interstellar medium, but play a vital role in its chemical evolution[155]. Dust grains form at ~1000 K from magnesium, silicon, oxygen and carbon surrounding dying stars and range in size from 1 nm to 1 μm[155]. Young molecular clouds of this type are sparse and easily penetrated by cosmic rays, and remain as bare siliceous or carbonaceous particles as volatile molecules are rapidly evaporated by incident radiation. As the cloud cools the density increases, and the core is shielded from radiation, thus allowing the deposition of molecules on the grains and the formation of mantles of molecular ices. The mantle consists mostly of water ice, but contains many other species such as CO, CO_2, H_2CO, CH_3OH, CH_4 and NH_3, as observed in the infrared spectrum of the molecular cloud surrounding protostar W33A (figure 6.1). The observed abundances of these species can only explained by reactions catalysed on icy dust grain surfaces[154].

Significantly, the broad H_2O peak in the 3 μm region suggests the presence of low density amorphous (LDA) ice, or amorphous solid water (ASW) (as denoted by the astronomical community; here, the latter abbreviation is used to avoid confusion with the local density approximation) instead of crystalline ice. The ASW mantle is doped

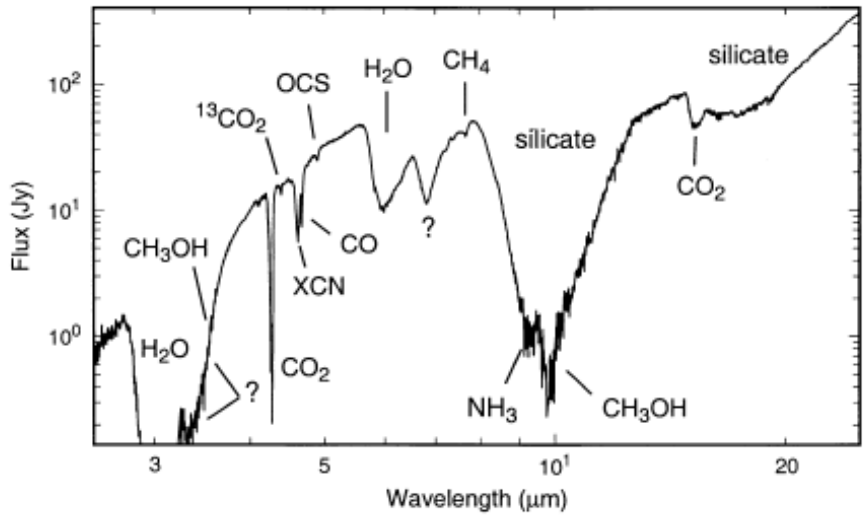

Figure 6.1: 2.4 μm–2.5 μm infrared spectrum of icy dust grains comprising the molecular cloud around the protostar W33A (taken from Gibb *et al.* (2000)[17]). W33A is unusual in having a 'rich solid-state molecular spectrum.'

with impurities including CO and CO_2. Crystalline cubic ice Ic forms at higher temperatures and remains crystalline even when cooled to 10 K since it is more stable, but can be transformed to ASW under certain conditions[154].

- Under bombardment from 100 keV electrons at temperatures below 80 K.
- Under incident ultraviolet photons at temperatures below 70 K.
- Under bombardment from 700 keV protons or 3 keV He^+ ions.

Note that although most water ice in interstellar dust grain mantles is thought to be amorphous, observations of crystalline ice are not unprecedented. Ice mantles formed above a threshold of ~110 K are crystalline, and those formed below are amorphous. In addition to experimental data, Maldoni *et al.* developed an astrophysical model which suggests that grain mantles in dust surrounding oxygen-rich stars are crystalline[156]. It has been suggested that slow water deposition rates may result in the formation of cubic ice, even at temperatures associated with amorphous ice formation[157;158]. However, it does not necessarily follow that grain mantles in molecular clouds are crystalline.

Amorphous ice undergoes a phase transition to ice Ic at ∼120 K, a process that occurs at a decreased rate as the temperature drops. Omont *et al.* therefore propose that amorphous mantles may transform to crystalline ice if left for long enough at sufficiently high temperatures below the transition point[159], but this is likely to result in ice consisting of the two coexisting phases. A crystalline "seeding" surface in amorphous ice will also greatly increase the transition rate.

6.3 Reactions on icy mantles

Reactions on the surface of interstellar dust grains broadly fall into two categories. The first type is energetic processes caused by incident cosmic rays, specifically ultraviolet radiation and ions in the keV–MeV range. The products are numerous and varied, and depend on the composition of the ice; CO, CO_2 and CH_3OH doped ices result in the formation of such species as H_2O_2, HO_2, HCO, H_2CO, HCOOH and CH_3CHO[154]. Energetic processes are generally suppressed by shielding of the molecular cloud core, leading to the second type, which includes non-energetic surface reactions involving abundant species such as hydrogen and oxygen atoms.

At low temperatures, only atoms are likely to be mobile on grain surfaces; in particular at 10 K, only hydrogen atoms are mobile.

Most atomic and molecular species present in the ISM adsorb onto ice at 10 K. Typically one hydrogen atom will adsorb onto a dust grain per day, and one carbon or oxygen atom every few days. The surface coverage of the grain is low, so the Langmuir-Hinshelwood mechanism (in which both reacting species are adsorbed onto the surface) dominates over the Eley-Rideal mechanism (one species is adsorbed, the other is incident from the gas phase). At 10 K, most thermally activated processes are impossible due to the size of the reaction barriers, therefore quantum tunnelling becomes important.

The de Broglie wavelength λ_{dB} of a particle of mass m is defined as,

$$\lambda_{\mathrm{dB}} = \frac{h}{\sqrt{2mkT}} \tag{6.1}$$

For a rectangular barrier of width a and height E, the tunnelling rate k_q is defined as approximately,

$$k_q \simeq \nu_0 e^{-\frac{2a}{\hbar}\sqrt{2mE}} \tag{6.2}$$

where ν_0 is the frequency of harmonic oscillation. It is clear that tunnelling is independent of temperature. This can be compared with the rate of thermal diffusion k_{th},

$$k_{\mathrm{th}} = \nu_0 e^{-\frac{E}{kT}} \tag{6.3}$$

Tunnelling is generally possible when the de Broglie wavelength of the reactant species is similar to the barrier width; this is only thought to be possible for light atoms (namely hydrogen) at low temperatures. It is also significant in surface diffusion. The tunnelling rate drops drastically as the mass of the species increases, and is acutely sensitive to the shape of the barrier — meaning its symmetry as well as its width a (tunnelling is facilitated by a symmetrical barrier).

6.4 The effect of grain surface morphology

There is no known viable mechanism for the formation of hydrogen molecules in the gas phase via recombination of hydrogen atoms at low temperatures. It is therefore generally accepted that this reaction happens on the surface of interstellar dust grains via the Langmuir-Hinshelwood or hot atom mechanism. This reaction releases 4.5 eV of energy, the partitioning of which could have a significant impact on the chemical and physical evolution of the molecular cloud. Hornekær *et al.* performed laboratory experiments in which hydrogen and deuterium recombined on porous and non-porous

amorphous ice films[160], reaching several important conclusions. Firstly, they found that hydrogen atoms are extremely mobile on the ASW surface at temperatures as low as 8 K. Secondly, H_2 molecules formed by recombination on *porous* ASW remained physisorbed for long periods since it is retained in the pores, with approximately one molecule desorbing per year (a short period on an astronomical scale). Most of the heat of recombination is transferred to the ASW in this case, facilitating thermal catalysis of grain surface reactions. Thirdly, in the case of non-porous ASW, the H_2 molecules desorb much sooner after recombination, and the energy released is transferred into the gas phase as translational and vibrational kinetic energy in the H_2 molecules. They conclude that in the case of dense or "dark" molecular clouds, the grain morphology is responsible for the energy distribution of gaseous H_2, and not the detailed chemical nature of the grain surface.

Al-Halabi and van Dishoeck examined the adsorption and diffusion of hydrogen atoms on an amorphous ice surface using classical trajectory calculations and the TIP4P water model with a H–H_2O pair potential[161]. They found that (somewhat counterintuitively) the adsorption rate is weakly dependent on whether the surface is crystalline or amorphous, but the atoms are much more tightly bound on the amorphous ice surface as a result of corrugations, which mean that adsorbed species have more nearest neighbours inside grooves. The binding energy distribution for crystalline ice is much narrower since amorphous ice has a diverse array of adsorbing potential wells in comparison. They calculate that the adsorption lifetime for a hydrogen atom at 10 K is approximately 1 day on crystalline surface, compared with 230 million years on an ASW surface. The vastly increased adsorption lifetime for ASW means that hydrogen recombination is much more efficient. Since the recombination reaction is barrierless, it is expected to be the dominant process on the grain surface, compared with hydrogenation of CO-derived species.

Interstellar ice is thought to have a larger range of hydrogen binding energies due to

the presence of molecules other than H_2O. A lower binding energy generally results in a higher diffusivity, but lowers the adsorption probability.

Hidaka *et al.* experimentally examined the effect of the morphology of the ice surface on the hydrogenation of CO[162]. Hydrogenation was allowed to occur on amorphous and crystalline (presumably cubic from the formation regime) ices in the following sequence,

$$CO \longrightarrow HCO \longrightarrow H_2CO \longrightarrow CH_3O \text{ or } H_2COH \longrightarrow CH_3OH \tag{6.4}$$

and the abundances of each species monitored using Fourier transform infrared spectroscopy. It is noteworthy that none of the radical species (HCO, CH_3O or H_2COH) were detecting, suggesting that the biradical reactions involved in their hydrogenation occurred extremely rapidly. It transpired that the rate of the $CO + H \longrightarrow HCO$ step was much higher on ASW, perhaps due to the lower hydrogen desorption rate on the amorphous surface caused by the trapping of atoms in pores and corrugations[161]. The rate constant was found to be the same on ASW and crystalline ice, suggesting that the enhanced rate on the ASW surface is purely a result of the greater hydrogen atom number density. CO doped ice has lower hydrogen adsorption rate than pure ice because it has a much smaller dipole; as a result, the reaction rate is decreased if the CO molecule coverage is too high.

6.5 Proposed glycolaldehyde formation mechanisms

Glycolaldehyde, methyl formate and acetic acid are isomers with the empirical formula $C_2H_4O_2$, and have all been detected in molecular cores. They appear with varying abundances as a result of their different formation mechanisms; glycolaldehyde and acetic acid have comparable abundances, whereas methyl formate is ubiquitous in comparison. Hollis *et al.* reported relative abundances (glycolaldehyde : acetic acid : methyl formate)

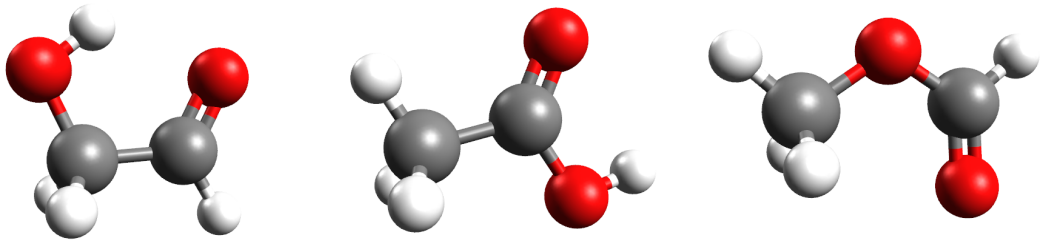

(a) Glycolaldehyde (b) Acetic acid (c) Methyl formate

Figure 6.2: Three isomers with the empirical formula $C_2H_4O_2$ detected in molecular clouds.

of 1 : 0.5 : 26 in the Large Molecule Heimat hot core in Sagittarius B2(N)[163].

Woods *et al.* list five possible mechanisms for the formation of glycolaldehyde[164]:

I Sorrell (2001)[165]

$$H_2O + h\nu \longrightarrow OH + H \tag{6.5}$$

$$CH_4 + h\nu \longrightarrow CH_3 + H \tag{6.6}$$

$$CH_3 + OH \longrightarrow CH_3OH \tag{6.7}$$

$$CO + H \longrightarrow HCO \tag{6.8}$$

$$CH_3OH + HCO \longrightarrow CH_2OHCHO + H \tag{6.9}$$

II Bennett & Kaiser (2007)[166]

$$CH_3OH + CRP \longrightarrow CH_2OH + H \tag{6.10}$$

$$CO + H \longrightarrow HCO \tag{6.11}$$

$$CH_2OH + HCO \longrightarrow CH_2OHCHO \tag{6.12}$$

III Halfen *et al.* (2006)[167]

$$H_3^+ + H_2CO \longrightarrow H_2COH^+ + H_2 \tag{6.13}$$

$$H_2COH^+ + H_2CO \longrightarrow CH_2OHCH_2O^+ \tag{6.14}$$

$$CH_2OHCH_2O^+ \longrightarrow CH_2OHCHOH^+ \tag{6.15}$$

$$CH_2OHCOH^+ \longrightarrow CH_2OHCHO + H^+ \tag{6.16}$$

IV Béltran *et al.* (2009)[8]

$$CO + H + H \longrightarrow H_2CO \tag{6.17}$$

$$CO + H \longrightarrow HCO \tag{6.18}$$

$$H_2CO + HCO + H \longrightarrow CH_2OHCHO \tag{6.19}$$

V Charnley & Rodgers (2005)[168]

$$CO + H \longrightarrow HCO \tag{6.20}$$

$$HCO + C \longrightarrow HC_2O \tag{6.21}$$

$$HC_2O + H \longrightarrow CH_2CO \tag{6.22}$$

$$CH_2CO + H \longrightarrow CH_2CHO \tag{6.23}$$

$$CH_2CHO + O \longrightarrow OCH_2CHO \tag{6.24}$$

$$OCH_2CHO + H \longrightarrow CH_2OHCHO \tag{6.25}$$

Note that "CRP" stands for cosmic ray particle. All of these mechanisms apart from III (which happens in the gas phase) occur on a grain surface, via the Langmuir-Hinshelwood or hot atom mechanisms. Woods *et al.* assess each of these models using astrophysical models, concluding that II and III can be dismissed since their rates would be too low to account for the observed abundance of glycolaldehyde, whilst V is only feasible if the

rate of the final step is enhanced. From a physical perspective, the chance of a three-body collision happening as in mechanism IV is vanishingly small, although these steps can be replaced with two separate hydrogenations.

It should be noted that during experimental observations of such reactions on amorphous ice surfaces, no radical species were detected[169–171] because it is assumed that biradical reactions that consume them occur at a much higher rate. It is therefore generally thought that the biradical reaction steps are barrierless on the grain surface.

They conclude that a modified version of I is the most likely scheme at 10 K:

$$CH_3 + OH \longrightarrow CH_3OH \tag{6.26}$$

$$CO + H \longrightarrow HCO \tag{6.27}$$

$$CH_3OH + HCO \longrightarrow CH_2OHCHO + H \tag{6.28}$$

Without performing any detailed quantum chemical calculations, Woods *et al.* attempt to assess the chemical viability of these reactions[164]. They suggest that reaction 6.28 is not viable, since one of the reactants is the stable methanol molecule, and one of the products is the extremely reactive hydrogen atom, so the reverse reaction would be favoured. Similarly, reaction 6.19 is unlikely to occur not only because formaldehyde (H_2CO) is a stable species, and a reaction between two formaldehyde molecules is unlikely to be facile. Instead, this reaction can be split in two parts; the formation of the hydroxymethyl radical (H_2COH) and a subsequent biradical reaction with HCO:

$$H_2CO + H \longrightarrow H_2COH \tag{6.29}$$

$$H_2COH + HCO \longrightarrow CH_2OHCHO \tag{6.30}$$

The crucial step in this sequence is the formation of the hydroxymethyl radical (H_2COH) which is in principle competitive with the formation of the methoxy radical (CH_3O). The latter is kinetically favoured in the gas phase, with a barrier that is lower by ~ 40 kJ mol^{-1} [172],

whilst the former is thermodynamically favoured, with an energy approximately 20 kJ mol^{-1} lower (at the MP3/6-31G**//HF/6-31G** level[173]).

Woods *et al.* suggest that mechanism V is unlikely since it involves carbon and oxygen addition reactions, when the hydrogen atom is the only mobile species on the ice surface at 10 K. In particular, reaction 6.21 is unlikely to compete with the formation of formaldehyde since atomic hydrogen is so much more abundant than atomic carbon. Hence from a chemical perspective, mechanism IV is identified as the best candidate of the two favoured by astrophysical considerations.

6.6 The characteristic (cross-over) temperature

For a generalised reaction A + B $\longrightarrow$ C, the rate of formation of C is expressed in the equation,

$$\frac{d[\mathrm{C}]}{dt} = k(T)[A][B], \tag{6.31}$$

where square brackets indicate the concentration of the enclosed species and $k(T)$ is a temperature dependent rate constant. The van 't Hoff equation describes the temperature-dependence of the equilibrium constant k for a reversible reaction:

$$\frac{d\ln k}{dT} = \frac{\Delta U}{k_B T^2} \tag{6.32}$$

Here, k_B is the Boltzmann constant and ΔU is the change in internal energy, which is equivalent to the activation (reaction) barrier V_0. This expression can be integrated to give the Arrhenius equation, which allow the calculation of the *classical* rate constant as a function of temperature.

$$k(T) = k_0 e^{-\frac{V_0}{k_B T}} \tag{6.33}$$

The pre-exponential factor k_0 expresses the probability of a reaction occurring through the frequency of collisions between reactants, and is determined via transition state the-

ory. It can be expressed as a function of the vibrational modes of the system, thus calculating the rate constant requires both a barrier height and vibrational frequencies; whilst the first can be obtained for systems of hundreds of atoms using DFT, the second is intractable for the systems considered in section 6.9. Moreover, the Arrhenius equation only describes reactions classically; in the regime of interest, it is thought that transitions across the activation barrier will be more frequent due to quantum mechanical tunnelling.

Whilst it is not possible to calculate a rate constant using only the reaction profile, it is possible to calculate the characteristic (or crossover) temperature T_c, which is defined as the temperature at which the probabilities of classical thermal transitions over the barrier and quantum mechanical tunnelling transition through the barrier are equal[174]. Benderskii *et al.* simplify the problem to give the following expression for T_c[175]:

$$T_c = \frac{\hbar\omega^*}{2\pi k_B} \tag{6.34}$$

Here, ω^* is the imaginary frequency associated with the transition state. If the cartesian reaction coordinate is rescaled to normal mode coordinates in atomic units, this quantity is given by the curvature (second derivative) of the reaction profile at the transition state. The transformation into normal coordinates can be achieved by multiplying the cartesian by the atomic mass for each atom in the system.

6.7 Gas phase reactions

The formation barriers and relative stability of the methoxy (CH_3O) and hydroxymethyl (H_2COH) radicals may have an important role in the mechanism or products. For the

reactions,

$$H_2CO + H \longrightarrow CH_3O \tag{6.35}$$

$$H_2CO + H \longrightarrow H_2COH \tag{6.36}$$

Saebø *et al.* report barriers of 51.9 kJ mol^{-1} and 84.2 kJ mol^{-1}, and that the H_2COH species is more stable by 20.9 kJ mol^{-1}, at the MP3/6-31G**//HF/6-31G** level[173]. Sosa *et al.* conducted extensive studies on the same reactions using large basis sets, finding the barriers to be 27.97 kJ mol^{-1} and 57.11 kJ mol^{-1} at the CISD-SCC/6-311G(d,p)//HF/6-31G(d) level (where SCC stands for size consistency correction). They observed that barriers calculated using perturbation theory are consistently 25 kJ mol^{-1}–50 kJ mol^{-1} too high due to spin contamination in the transition state. They estimate the difference in energy between the two radical species is 27.2 kJ mol^{-1}.

Woon examines two steps in the hydrogenation of carbon monoxide, terminating with methanol; these are also important reactions in the glycolaldehyde mechanism[172;176]: the addition of hydrogen to carbon monoxide to form the formyl radical (HCO) and the addition of hydrogen to formaldehyde to form the methoxy radical (CH_3O). At the QCISD(T) level, his calculations indicate a barrier of 19.16 kJ mol^{-1} for HCO formation, and a barrier of 20.75 kJ mol^{-1} for CH_3O formation. An experimental derivation of the activation energy based on the Arhenius equation for the formation of the formyl radical at 10 K yielded (8.3 ± 1.7) kJ mol^{-1}, although this is likely to be significantly lower than the actual barrier since it implicitly includes rate effects such as quantum tunnelling.

Woon attempts to simulate the effect of an ice surface using cluster calculations consisting of the reacting species and between one and four water molecules embedded in a dielectric field which simulates the long range effect of an ice surface[172]. This has a minimal effect on the barrier for formyl radical formation, with three water molecules

increasing it by $\sim$1 kJ mol^{-1} at the QCISD//MP2 level.

The barrier for the formation of the methoxy radical is analogously 20.75 kJ mol^{-1} at the QCISD(T) level. Unlike the previous reaction, the addition of one to four water molecules results in a significant (but perhaps insufficient) reduction in the barrier. The reduction is attributed to the fact that formaldehyde has a dipole moment similar to that of the water molecule, whereas the dipole moment of the carbon monoxide molecule is twenty times lower than that of water. The addition of four H_2O molecules reduces the barrier by 3.60 kJ mol^{-1} at the QCISD level, which is a clear improvement over the the other reaction. The dielectric field only reduces the barrier by 0.96 kJ mol^{-1} in the gas phase, which would seem to suggest that the effect of the bulk ice on the barrier is minimal. Woon initially suggests that abstraction of the formyl radical ($H_2CO + H \leftrightharpoons HCO + H_2$) will compete with the hydrogenation of formaldehyde, but the calculations indicate that the presence of water molecules hinders the formation fo the hydrogen molecule.

This leads him to conclude that formyl radical formation may not be efficient on grain mantles unless tunnelling has a greater effect than experiments suggest, and that icy grains only play a minor role in formaldehyde and methanol formation.

6.7.1 Choice of density functional for surface reactions

One of the main drawbacks of DFT is that the approximated exchange-correlation functionals available are not derived *ab initio*; the exact form of the density functional in the Kohn-Sham equations is unknown, and there is no systematic method for developing new functionals. In the absence of a universal density functional that describes all systems, new functionals are continually developed to model a small subset of systems or phenomena, thus choosing the right functional is critical.

For the calculations in this chapter, it is necessary to use a hybrid density functional, i.e. one that mixes a certain fraction of Hartree-Fock exchange in with the Kohn-Sham

exchange. The reason for this is essentially that a fundamental flaw of approximate exchange-correlation functional is the self interaction error, the interaction of an electron with its own charge distribution, which causes barriers to be grossly underestimated; incorporating exact exchange goes some way towards mitigating this. Although self interaction corrections are available for GGAs, they are costly and impractical.

Andersson and Grüning conducted a detailed survey of available density functional and attempted to assess their suitability for studying astrophysically relevant reactions[153]. They achieved this by calculating gas phase barrier heights and reaction energies for 10 reactions, notably including hydrogen addition ($H + X \leftrightharpoons HX$) and hydrogen abstraction ($X + H_2 \leftrightharpoons HX + H$), using 39 different functionals including LDA, GGA, meta-GGA, and hybrids with low and high exact exchange fractions.

Their general conclusions relevant to this work are summarised as follows:

1. Hybrids with a high exact exchange fractions (e.g. BHandHLYP, MPW1K) work well for calculating barrier heights, but less so for atomisation and reaction energies.

2. Some hybrids with modest exact exchange fractions (notably B1B95-28, B97-1, B97-2 and B98) result in barriers that are almost as good as with a high exact exchange fraction (in most cases), and give better atomisation and reaction barriers.

3. Meta-GGAs can potentially perform almost as well as hybrids for barriers, notably VS98 and OLAP3. Functionals with OPTX exchange (e.g. OLYP) tend to outperform those with B88 exchange (e.g. BLYP).

4. The HCTH family of GGA functionals performs almost as well the meta-GGAs, but not as well as hybrids. In particular, the HCTH/120 functional has the water dimer in its training set, and may be suitable for modelling ice.

5. The best hybrids for modelling the low barrier hydrogen addition reactions are B1B95-25 and B1B95-28.

6. BHandHLYP performs best (including reaction energies) for the abstraction-type reactions.

7. For the general class of reaction where a hydrogen atom is a reactant, the best functionals are MPW1K, B97-1, MPW58/60, BHandHLYP, KMLYP-mod and B98, all of which have a mean average error of $\sim$4 kJ mol^{-1} for their barrier heights (i.e. chemical accuracy).

8. The results achieved with double-ζ and triple-ζ basis sets are comparable to those obtained with quadruple-ζ; this bodes well for work on larger systems that rely on smaller basis sets.

They conclude that the best overall functional with respect to barrier heights is MPW1K, and the best overall description (including atomisation and reaction energies) is provided by B1B95-28.

Obviously the choice of functional for this work is reliant on what has been implemented in CP2K. The BHandHLYP functional was chosen since many of the semi-empirical functionals have not been implemented, and in any case, the model used is too crude to expect anything approaching chemical accuracy.

6.7.2 Model and methods

We first characterise the reactions of interest in the gas phase in order to gauge the reaction barriers at high levels of theory.

All gas phase calculations were performed using the NWChem[177] and Orca[178] quantum chemistry codes. Both are electronic structure codes that employ Gaussian basis sets and are capable of performing (non-periodic) high level post Hartree-Fock calculations. NWChem was mainly used to characterise the larger systems since the parallelisation is more extensive.

Initial and final geometries for gas phase products and reactants were determined

at the hybrid DFT PBE0/DZVP level. The resulting structures were reoptimised at the frozen core MP2/cc-pVDZ level using Orca, and for the cases where there was an obvious reaction coordinate, constrained optimisation was used to locate the transition state, if any. Starting from the reacting species in the initial configuration, the reaction coordinate was constrained using z-matrix notation, and all other degrees of freedom were fully relaxed. The reaction coordinate was reduced, bringing the reactant species closer together, and the process repeated until the product was reached. The MP2 method suffers heavily from spin contamination near the transition state, so there were frequently convergence problems, which were solved by reducing the reaction coordinate step size in the constrained optimisation (this worked because the wavefunction from a completed constrained optimisation was used as the initial guess for the next step). Tight SCF convergence criteria were used in all cases, namely an energy change of $1 \times 10^{-8}\,E_\mathrm{h}$ and a gradient of $1 \times 10^{-5}\,E_\mathrm{h}\,{a_0}^{-1}$ for single points, and energy change of $5 \times 10^{-6}\,E_\mathrm{h}$ with a maximum gradient of $3 \times 10^{-4}\,E_\mathrm{h}\,{a_0}^{-1}$ and a maximum displacement of $4 \times 10^{-3}\,a_0$ for geometry optimisations.

Upon generation of a reaction profile along the coordinate, the configuration closest to the energy maximum (in cases where there was a maximum) was used as the input structure for a saddle point optimisation. The initial, final and transition state configurations were re-optimised at the MP2/cc-pVTZ level (*without* the frozen core approximation), and the resulting energies used to compute the barriers and heats of reaction.

This method was appropriate for radical reactions (systems with a multiplicity of 2). Singlet state biradical reactions, on the other hand would not work in the same way since for the forward reaction, the codes were unable to generate an initial wavefunction guess with the correct spin density distribution (opposing spins on each of the reactants), and for the reverse reaction, the UHF calculation was unable to homolytically dissociate the bond, resulting in an incorrect spin distribution. As a solution, a

single point UHF calculation in the *triplet* state was performed on the initial configuration in order to introduce a bias into the wavefunction, and this was used as an initial guess for a singlet state single point calculation. The resulting wavefunction was used as the initial guess for the first configuration in the constrained optimisation. Obviously this method will not work for the reverse reaction, and is therefore not quite as thorough; however, we expect the biradical reactions to be barrierless in the gas phase, so we do not have to characterise the transition state.

MP2 calculations in general provide good geometries, but the transition state energies are generally grossly overestimated due to spin contamination. For this reason, coupled cluster with singles, doubles and perturbative triples single points were taken at the initial, final and transition states, and used to recompute the barriers and heats of reaction. Thus our best estimate for the energies in the gas phase are at the CCSD(T)/aug-cc-pVTZ//MP2/aug-cc-pVTZ level. It was necessary to use NWChem for these accurate calculations. The following convergence criteria were used: for single points, an energy change of $1 \times 10^{-8}\,E_\mathrm{h}$, and for geometry optimisations an energy change of $1 \times 10^{-7}\,E_\mathrm{h}$ between ionic steps, with a maximum gradient threshold of $1.5 \times 10^{-5}\,E_\mathrm{h}\,{a_0}^{-1}$ and a maximum step size of $6 \times 10^{-5}\,a_0$.

The reactions that will be examined in the section are:

$$CO + H \longrightarrow HCO \tag{6.37}$$

$$HCO + H \longrightarrow H_2CO \tag{6.38}$$

$$H_2CO + H \longrightarrow CH_3O \tag{6.39}$$

$$H_2CO + H \longrightarrow H_2COH \tag{6.40}$$

$$H_2COH + HCO \longrightarrow CH_2OHCHO \tag{6.41}$$

$$2\,HCO \longrightarrow HOCCOH \tag{6.42}$$

$$HOCCOH + H \longrightarrow CH_2OCHO \tag{6.43}$$

$$CH_2OCHO + H \longrightarrow CH_2OHCHO \tag{6.44}$$

$$\tag{6.45}$$

The following mechanism proposed by Charnley and Rodgers[168] will not be considered for two main reasons. Firstly, as observed by Woods *et al.*, atomic carbon and oxygen are only likely to be present in significant quantities relative to atomic hydrogen during early times. The second problem arises primarily from the first reaction in the chain, 6.46.

$$HCO + C \longrightarrow HC_2O \tag{6.46}$$

$$HC_2O + H \longrightarrow CH_2CO \tag{6.47}$$

$$CH_2CO + H \longrightarrow CH_2CHO \tag{6.48}$$

$$CH_2CHO + O \longrightarrow CH_2OCHO \tag{6.49}$$

Reaction (6.46) is notable because it has significant multireference character (see section 3.5.1). It can be regarded as a combination of two non-identical resonance structures: one with a C≡C triple bond and the unpaired electron localised on the oxygen, and the other with a C=C double bond and the electron localised on the carbon which is

bonded to the hydrogen.

In this study, we will examine two possible mechanisms; the first (A) is the most likely candidate (from a chemical perspective) identified by Woods *et al.*[164]; the second (B) was independently proposed by Goumans.

A Similar to the mechanism proposed by Beltrán *et al.*[8]

$$CO + H \longrightarrow HCO \tag{6.50}$$

$$HCO + H \longrightarrow H_2CO \tag{6.51}$$

$$H_2CO + H \longrightarrow H_2COH \tag{6.52}$$

$$H_2COH + HCO \longrightarrow CH_2OHCHO \tag{6.53}$$

B Alternative mechanism proposed by Goumans

$$CO + H \longrightarrow HCO \tag{6.54}$$

$$2\,HCO \longrightarrow HOCCOH \tag{6.55}$$

$$HOCCOH + H \longrightarrow CH_2OCHO \tag{6.56}$$

$$CH_2OCHO + H \longrightarrow CH_2OHCHO \tag{6.57}$$

6.7.3 Results and discussion

A full geometry optimisation on the simplest structures, the final and transition states of the HCO molecule, confirmed that structures relaxed at the MP2 level were almost identical to those optimised at the CCSD(T) level, with the bond lengths and angle varying by less than 1%. Although this may not hold for more complex structures, the resources were not available to perform full coupled cluster geometry optimisations, thus it was assumed that the MP2 geometries were essentially the same.

According to table 6.1 The forward barriers for the reactions studied indicate that

in general, MP2 greatly overestimates barriers as a result of spin contamination in the transition state structures. For example, in the reaction $H_2CO + H \longrightarrow H_2COH$, the MP2 barrier is almost double the height of the CCSD(T) barrier. In principle, the ideal value of $S(S+1)$ is 0.75 for a single unpaired electron (with $S = 0.5$); however, the expectation value of $< S^2 >$ was calculated to be 0.92, a deviation of 0.17. Woon eliminated spin contamination from his gas phase calculation by employing the PMP2 method[172], in which "intruder" states are projected out at the expense of computational cost. It was decide that this was unnecessary for this work in light of the CCSD(T) results.

The second noteworthy point is that the DFT barriers are all underestimates. The B3LYP barriers in particular are gross underestimates, compared with the BHandHLYP and M05-2x barriers, emphasising the importance of a large exact exchange fraction; the Hartree-Fock exchange somewhat mitigates the self interaction error inherent in DFT, reducing barrier underestimates. It is less clear why the only GGA tested, HCTH/120 gives such reasonable barriers; it can only be assumed that the empirical fitting results in some error cancellation.

A potentially important comparison is the different products of the reaction between formaldehyde (H_2CO) and an hydrogen atom: the methoxy radical (CH_3O) is not involved in any glycolaldehyde-forming mechanisms, and may form the basis of competing mechanism for species such as methanol and methyl formate. The hydroxymethyl radical (H_2COH) could potentially form methanol or glycolaldehyde. It can be seen that whilst the methoxy radical is *kinetically* favourable, with a barrier that is lower by 28.8 kJ mol^{-1}, the hydroxymethyl radical is *thermodynamically* favourable with a reaction heat that is more exothermic by 34.57 kJ mol^{-1} (see table 6.3) at the CCSD(T) level. This is a moot point under the conditions of the ISM, however, since neither reaction will be activated at temperatures of 10 K.

	Forward barrier (kJ mol^{-1})					
Reaction	MP2	CCSD(T)	BHandHLYP	B3LYP	M05-2x	HCTH/120
$CO + H \longrightarrow HCO$	25.66	14.24	8.96	1.29	21.16	12.23
$HCO + H \longrightarrow H_2CO$	0.00	—	—	—	—	—
$H_2CO + H \longrightarrow CH_3O$	59.12	21.11	10.49	4.57	22.87	16.20
$H_2CO + H \longrightarrow H_2COH$	91.80	49.91	36.58	21.24	45.45	31.95
$H_2COH + HCO \longrightarrow CH_2OHCHO$	0.00	—	—	—	—	—
$2\,HCO \longrightarrow HOCCOH$	0.00	—	0.00	—	—	—
$HOCCOH + H \longrightarrow CH_2OCHO$	70.77	28.88	8.09	2.70	19.46	13.33
$CH_2OCHO + H \longrightarrow CH_2OHCHO$	0.00	—	—	—	—	—

Table 6.1: Forward barriers for gas phase reactions. MP2 calculations were performed at the cc-pVTZ level; CCSD(T) figures are single points at the cc-pVTZ level on MP2 geometries. Four different exchange-correlation functionals are evaluated at the DFT/TZVP level: two hybrids with a high exact exchange fraction (BHandHLYP and M05-2x), one with a moderate exact exchange fraction (B3LYP) and one semi-empirical GGA (HCTH/120). All of the biradical reactions were found to be barrierless at the MP2/cc-pVDZ level; this was deemed sufficient to assume that these reactions were therefore barrierless at all other levels, hence the dashes in the respective columns.

	Reverse barrier (kJ mol^{-1})					
Reaction	MP2	CCSD(T)	BHandHLYP	B3LYP	M05-2x	HCTH/120
$CO + H \longrightarrow HCO$	91.80	89.57	101.26	114.17	110.68	127.02
$HCO + H \longrightarrow H_2CO$	0.00	—	—	—	—	—
$H_2CO + H \longrightarrow CH_3O$	59.75	128.58	146.86	5.52	154.29	134.34
$H_2CO + H \longrightarrow H_2COH$	218.78	191.95	198.27	162.24	210.58	183.03
$H_2COH + HCO \longrightarrow CH_2OHCHO$	0.00	—	—	—	—	—
$2\,HCO \longrightarrow HOCCOH$	0.00	—	—	—	—	
$HOCCOH + H \longrightarrow CH_2OCHO$	145.879	144.286	151.27	141.21	157.80	151.06
$CH_2OCHO + H \longrightarrow CH_2OHCHO$	0.00	—	—	—	—	—

Table 6.2: Reverse barriers for gas phase reactions. MP2 calculations were performed at the cc-pVTZ level; CCSD(T) figures are single points at the cc-pVTZ level on MP2 geometries. Four different exchange-correlation functionals are evaluated at the DFT/TZVP level: two hybrids with a high exact exchange fraction (BHandHLYP and M05-2x, one with a moderate exact exchange fraction (B3LYP)) and one semi-empirical GGA (HCTH/120). All of the biradical reactions were found to be barrierless at the MP2/cc-pVDZ level; this was deemed sufficient to assume that these reactions were therefore barrierless at all other levels, hence the dashes in the respective columns.

	Reaction energy (kJ mol^{-1})					
Reaction	MP2	CCSD(T)	BHandHLYP	B3LYP	M05-2x	HCTH/120
$CO + H \longrightarrow HCO$	−66.14	−75.33	−92.30	−112.87	−89.52	−114.79
$HCO + H \longrightarrow H_2CO$	−390.00	−397.22	−373.46	−395.15	−400.13	−387.73
$H_2CO + H \longrightarrow CH_3O$	−0.63	−107.48	−136.37	−0.95	−131.42	−118.14
$H_2CO + H \longrightarrow H_2COH$	−126.97	−142.05	−161.70	−141.01	−165.13	−151.08
$H_2COH + HCO \longrightarrow CH_2OHCHO$	−521.98	−399.24	−347.85	−357.23	−368.08	−337.64
$2\,HCO \longrightarrow HOCCOH$	−322.11	−313.34	−284.96	−278.12	−419.48	−279.72
$HOCCOH + H \longrightarrow CH_2OCHO$	−75.102	−115.405	−143.18	−138.51	−138.34	−137.73
$CH_2OCHO + H \longrightarrow CH_2OHCHO$	−520.14	−162.65	−455.81	−476.76	−493.95	−458.97

Table 6.3: Reaction energies for gas phase reactions. MP2 calculations were performed at the cc-pVTZ level; CCSD(T) figures are single points at the cc-pVTZ level on MP2 geometries. Four different exchange-correlation functionals are evaluated at the DFT/TZVP level: two hybrids with a high exact exchange fraction (BHandHLYP and M05-2x), one with a moderate exact exchange fraction (B3LYP) and one semi-empirical GGA (HCTH/120).

6.8 Reactions on hydroxylated silicate nanoclusters

6.8.1 Introduction

In section 6.2, it was mentioned that ISM dust grains are thought to consist of a siliceous core surrounded by low density amorphous ice. Such inferences are generally made by analysing their mid-IR (2.5 μm to 15 μm) to far-IR spectra (15 μm to 100 μm). The dominant form of silicate in the ISM is amorphous, with crystalline polymorphs such as olivine and pyroxene comprising <2%[179].

Concrete evidence of the composition of certain types of dust grain was provided by NASA's "Stardust" mission, in which more than 10000 particles in the size range 1 μm to 300 μm were collected from the comet Wild 2 by high speed capture in silica aerogel and physically returned to Earth. A 'major portion' of the particles larger than 1 μm were found to be olivine and pyroxene[180].

To date, catalysis of interstellar reactions by bare siliceous surfaces has been studied in some detail. Goumans *et al*. use an embedded cluster QM/MM approach to evaluate the catalytic activity of the edingtonite ($BaAl_2Si_3O_{10}$) on methanol (one of the most abundant ISM molecules) formation[181]. The proposed mechanism is similar to the initial stages of glycolaldehyde formation, with the repeated hydrogenation of a carbon monoxide molecule — the difference being that in methanol formation, the methoxy radical (CH_3O) is formed instead of the hydroxymethyl radical (CH_2OH) — thus methanol and glycolaldehyde may follow competitive pathways. Whilst a negatively charged SiO^- surface defect is shown to lower the activation barriers, the effect is insufficient to enable the reaction at temperatures of 10 K to 20 K without tunnelling[182].

Here we examine a limited subset of the glycolaldehyde-forming reactions on hydroxylated silicate nanoclusters, which represent bare interstellar dust grains.

6.8.2 Model and methods

The details of the DFT calculations were chosen to be consistent with the work of Jelfs *et al.*[18] All cluster calculations were carried out using NWChem, the 6-31G** basis set and the B3LYP and BHandHLYP hybrid functionals, but in this case the DFT-D3 dispersion correction[119] was employed in addition in order to more accurately describe the reaction chemistry. The reacting species and product molecules were adsorbed onto the clusters at a variety of different binding sites in order to find the most favourable; in order to minimise the number of such calculations, the symmetry of the cluster was used to avoid redundant configurations. The initial and final configurations were then used as the end points in a NEB calculation containing 8 images. Single points were considered to be converged for energy changes of less than $1 \times 10^{-6}\,E_\mathrm{h}$ and gradients of less that $5 \times 10^{-4}\,E_\mathrm{h}\,{a_0}^{-1}$. The respective tolerances for the energy, gradient and step sizes between geometry optimisation steps were $5 \times 10^{-6}\,E_\mathrm{h}$, $4.5 \times 10^{-4}\,E_\mathrm{h}\,{a_0}^{-1}$ and $3 \times 10^{-4}\,a_0$. NEB calculations had a convergence threshold of $1 \times 10^{-5}\,E_\mathrm{h}$ for the total band energy.

It was our intention to evaluate a limited subset of the reactions comprising mechanisms A and B (page 174) on clusters of varying size and with varying degrees of hydroxylation, allowing us to gauge the effects of curvature (related to cluster size) and the nature of the substrate on the reaction barriers. However, time constraints meant that it was only possible to study in detail three reactions on two fully hydroxylated (i.e. every silicon atom has a hydroxyl group) clusters.

The smallest cluster considered is the 8-silicon double four-ring, consisting of only four-rings (pictured in figure 6.3[18]). Of the two possible 16-silicon clusters available, only cage 1 (figure 6.4a) was used due to time constraints. Whilst both are fully hydroxylated, cage 2 (figure 6.4b) contains 4-, 5- and 6-rings, whereas cage 1 contains only 4- and 5-rings. A larger structure is required for larger rings, so in principle, the largest ring size can be considered a rough measure of curvature. Of the two 16-silicon clusters, cage 2 has a lower curvature in the vicinity of the 6-ring.

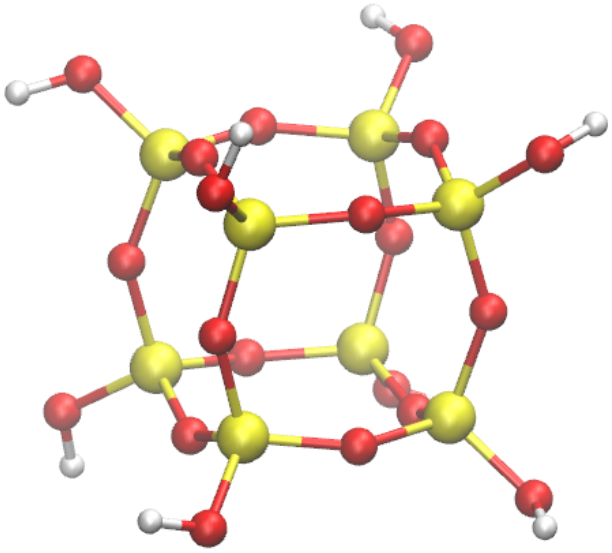

Figure 6.3: the 8-silicon hydroxylated cluster, the double four-ring[18]. Silicon atoms are yellow, oxygens red and hydrogens white.

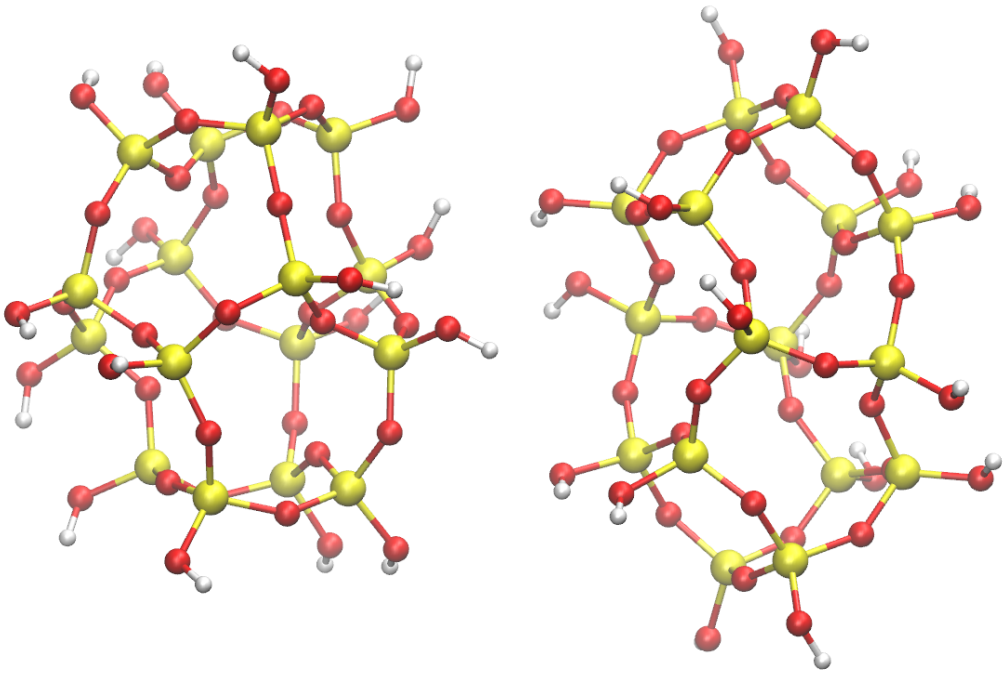

(a) Cage 1: 4- and 5-rings.

(b) Cage 2: 4-, 5- and 6-rings.

Figure 6.4: The two 16-silicon fully hydroxylated clusters. Silicon atoms are yellow, oxygens red and hydrogens white.

6.8.3 The nudged elastic band (NEB) method

The nudged elastic band (NEB) is a convenient method for locating saddle points on a potential energy surface. A sequence of "images," system configurations along the reaction path, are linked together using springs with a spring constant k, such that when atoms on images along the band are acted on by two elastic forces which "pull" them towards the configuration of the adjacent images, ensuring an equal separation of images in phase space. When all forces perpendicular to the band are minimised, the sequence of images represents the minimum energy path between the reactants and products, and contains at least one first order saddle point. In order to locate the saddle point, the band is optimised by minimising the total force acting on each image.

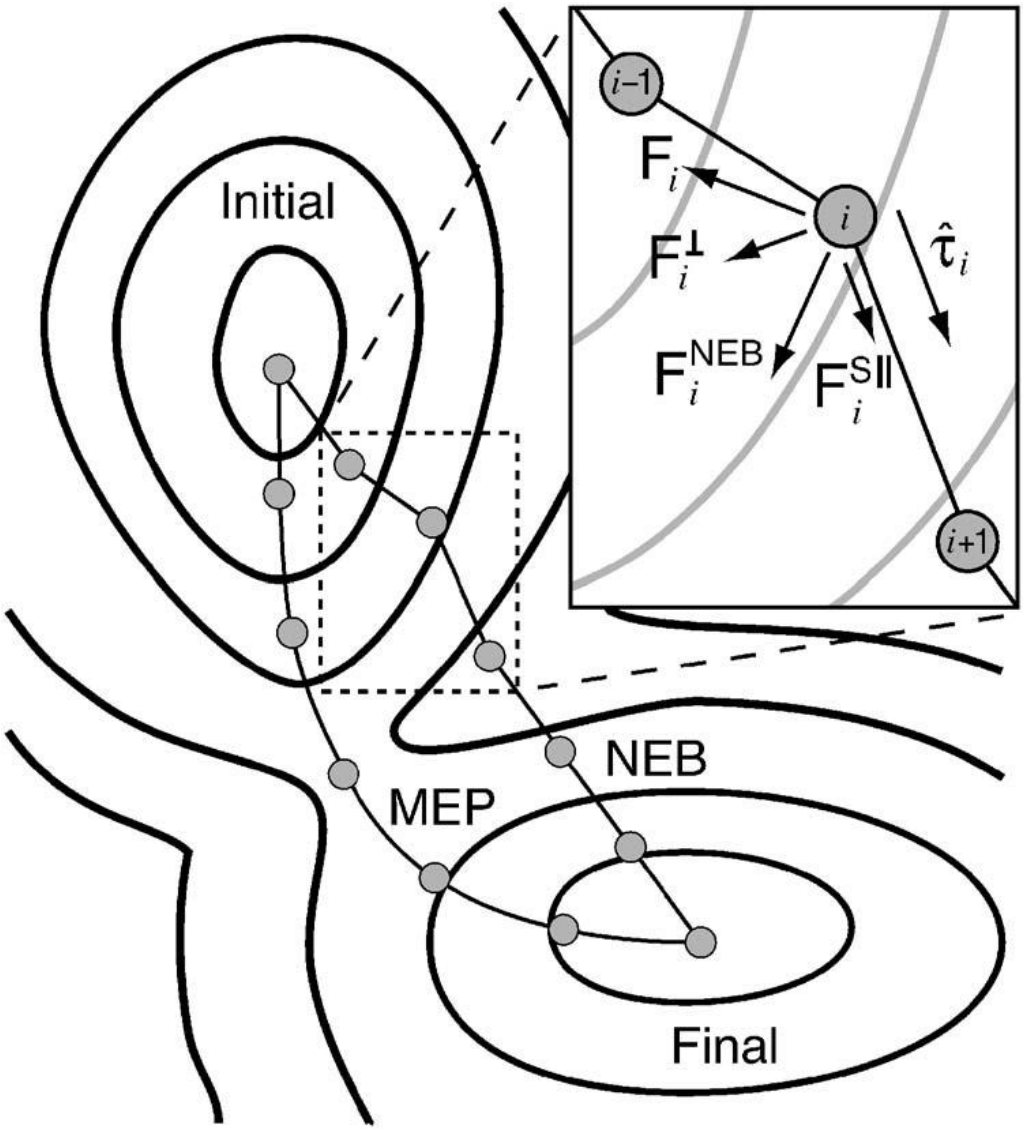

Figure 6.5: Schematic representation of the nudged elastic band method (taken from Sheppard *et al.*[19])

In this work, the fixed endpoints (vectors $\vec{R}_0$, the reactant configuration, and $\vec{R}_{n+1}$, the product configuration, in phase space) were created by relaxing the reactant molecules and the product molecules on the substrate to their equilibrium configurations. The intervening images (vectors $(\vec{R}_1, \vec{R}_2, \ldots, \vec{R}_n)$ are generated using a linear interpolation of the coordinates between the initial and final states.

In the state described above, the method has two major problems: firstly, the geometry optimisation for each image results in a net force which pushes all of the images

towards their nearest local minimum (the reactant and product states), resulting in a sparser distribution of images around the saddle point; this is known as the "sliding down" phenomenon. Secondly, in regions where the minimum energy path is curved in phase space, local decreases in the potential energy surface can cause corners to be cut, with images in these "concave" regions being forced into spurious minima. These problems can be avoided by introducing the "nudge," or projecting out the components of the *true* force parallel to the chain, and the components of the *spring* force perpendicular to the chain [183].

The adjusted force acting on an image i is,

$$\vec{F}_i^{\mathrm{NEB}} = \vec{F}_i^{S\parallel} + \vec{F}_i^{t\perp} \tag{6.58}$$

where $\vec{F}_i^{S\parallel}$ is the spring force parallel to the tangent (The unit vector τ_i in figure 6.5) and $\vec{F}_i^{t\perp}$ is the true force perpendicular to the tangent. The spring component in this expression is the projection of the spring force onto the unit tangent vector.

$$\vec{F}_i^{S\parallel} = \{k[(\vec{R}_{i+1} - \vec{R}_i) - (\vec{R}_i - \vec{R}_{i-1})] \cdot \hat{\tau}_i\}\hat{\tau}_i \tag{6.59}$$

Similarly, the true force component is the projection of the true force onto the normal to the tangent, where the true force is simply the gradient of the image potential E_i.

$$\vec{F}_i^{t\perp} = \vec{F}_i^{t} - (\vec{F}_i^{t} \cdot \hat{\tau}_i)\hat{\tau}_i \tag{6.60}$$

$$= \vec{\nabla} E_i - (\vec{\nabla} E_i \cdot \hat{\tau}_i)\hat{\tau}_i \tag{6.61}$$

The unit tangent vector τ_i can be estimated either by normalising the vector connecting images $i-1$ and $i+1$, or by normalising the sum of the two unit vectors between $i-1$ and i, and i and $i+1$ (see figure 6.5). The latter method of calculating the tangent is generally better, since it ensures that the images are equally spaced; however, in cases

where the perpendicular component of the force is small compared with the parallel, kinks may develop in the band particularly near the saddle points on the minimum energy path. In a variant of the NEB method designed by Henkelman and Jónsson[184], the tangent is given by,

$$\tau_i = \tau_i^+ F(E_1) + \tau_i^- G(E_2) \tag{6.62}$$

where τ_i^+ is the vector connecting images i and $i+1$, and τ_i^- is the vector connecting images $i-1$ and i. The magnitudes of the vectors are determined by switching functions F and G which are dependent on the relative energies of the three images. This formulation of the tangent, together with a modified expression for the spring force parallel to the tangent, called the "improved tangent" NEB, and used in this work, reduces errors in the minimum energy path caused by kinks in the band.

In addition many variants of the NEB method involve some implementation of a "climbing image" (including the one used in this work), where the image with the highest true energy is allowed to move uphill on the potential energy surface, thereby locating the transition state.

6.8.4 Results and discussion

Looking first at results for the reactions on the double four-ring (tables 6.4 and 6.5 for BHandHLYP/6-31G** and B3LYP/6-31G** respectively), it is clear that B3LYP, whilst being a good functional for describing the geometry and formation energies of hydroxylated silicate clusters, is inappropriate for calculating reaction barriers of interest; compared with BHandHLYP, it grossly underestimates barriers.

Although the double four-ring seems to catalyse the hydrogenation of carbon monoxide, resulting in a barrier that is lower by a factor of almost two, it actually hinders the hydrogenation of formaldehyde, increasing the barriers of both competing reactions by a factor of 2–3.

The calculations involving sixteen-silicon clusters were far more expensive, so we

Table 6.4: Barriers and heats in kJ mol^{-1} for glycolaldehyde-forming reactions on the hydroxylated double four-ring at the BHandHLYP/6-31G** level.

	Cluster surface			Gas phase		
	Forward barrier	Reverse barrier	Heat	Forward barrier	Reverse barrier	Heat
$H + CO \longrightarrow HCO$	4.62	127.74	−123.12	8.13	97.67	−89.54
$H_2CO + H \longrightarrow CH_3O$	30.88	175.44	−144.56	11.37	148.40	−137.03
$H_2CO + H \longrightarrow H_2COH$	67.30	232.86	−165.56	36.24	189.84	−153.60

Table 6.5: Barriers and heats in kJ mol^{-1} for glycolaldehyde-forming reactions on the hydroxylated double four-ring at the B3LYP/6-31G** level.

	Cluster surface			Gas phase		
	Forward barrier	Reverse barrier	Heat	Forward barrier	Reverse barrier	Heat
$H + CO \longrightarrow HCO$	2.91	119.98	−117.08	0.24	110.79	−110.55
$H_2CO + H \longrightarrow CH_3O$	39.57	167.26	−127.70	5.16	5.73	—-0.55
$H_2CO + H \longrightarrow H_2COH$	25.05	159.37	−134.32	20.44	151.09	−130.65

	Forward barrier	Reverse barrier	Heat
$H_2CO + H \longrightarrow CH_3O$	6.90	153.52	−146.62
$H_2CO + H \longrightarrow H_2COH$	18.91	193.72	−174.81

Table 6.6: Reaction barriers and heats in kJ mol^{-1} for two reactions on the sixteen-silicon hydroxylated nanocluster (cage 1) at the BHandHLYP/6-31G** level. Gas phase reactions at the same level of theory are listed in table 6.4.

limited ourselves to a comparison of two the competing reactions forming CH_3O and H_2COH. A variety of H_2CO binding sites were used in the NEB, most of which yielded a viable reaction path for CH_3O, but not for H_2COH. The energies of the paths with the lowest barriers are listed in table 6.6. Compared with reactions on the double four-ring reactions on cage 1 are far more favourable: the barriers are actually reduced, and they are a factor of approximately two lower than in the gas phase. This seems to support the earlier assertion that a lower curvature has an enhanced catalytic effect on these reactions.

Figure 6.6 shows the NEB paths for these reactions on cage 1. In the case of CH_3O, the hydrogen atom follows a direct path to the carbon, whereas for H_2COH, the hydrogen is somewhat hindered by overly acute $H\hat{O}C$ angle and the hydrogen atom to which the formaldehyde is hydrogen bonded. It can be seen that over the course of the reaction, the H_2CO fragment moves much further in the case of H_2COH; initially it is on the boundary between the four- and five-rings, but by the end it is obviously over the four-ring. The movement of the formaldehyde fragment is the only way that the reactants can overcome the steric hindrance inherent in the point at which they are bound to the cluster. It can be concluded that this reaction is only feasible if the formaldehyde molecule is physisorbed onto the cluster between two rings and by comparing the results for the reactions on the double four-ring (where the reaction occurs on the boundary between two four-rings) and cage 1 (where it occurs between a four-ring and a five-ring), supports the earlier claim that a lower curvature on the cluster surface results in a lower barrier.

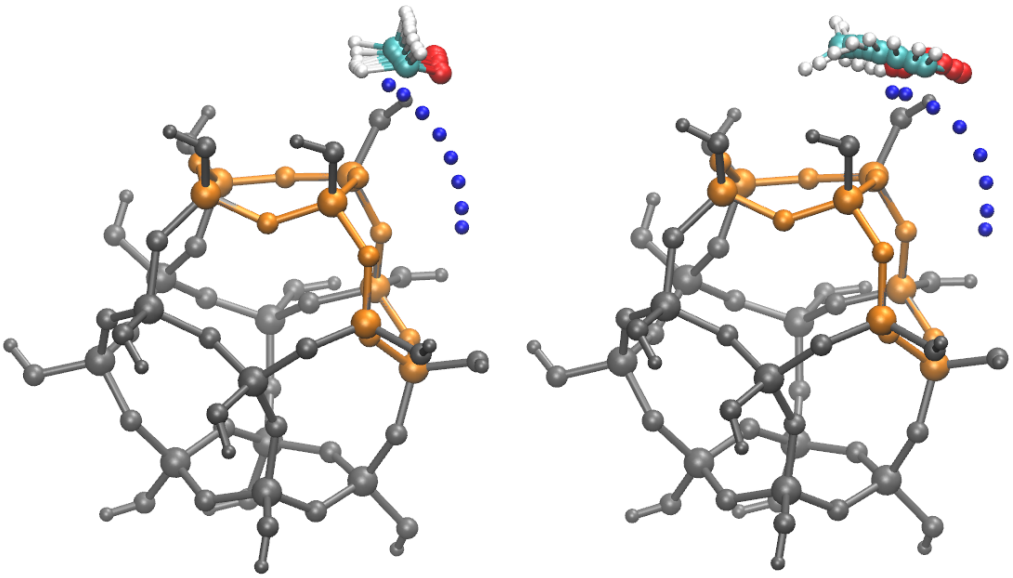

(a) CH_3O (b) H_2COH

Figure 6.6: NEB paths for a hydrogen atom reacting with a H_2CO molecule on a hydroxylated silicate cluster (cage 1, figure 6.4a) to form CH_3O (left) and H_2COH (right). The reactant hydrogen atom is coloured blue and the five- and four-rings on which the reaction occurs are coloured orange for clarity.

6.9 Reactions on icy mantles

6.9.1 Introduction

The conditions in the dense molecular clouds in which interstellar glycolaldehyde has been detected place strong constraints on the mechanism of its formation. It has already been established that at 10 K, the barrier for the simplest reaction ($CO + H \longrightarrow HCO$) is too high to feasibly occur in the gas phase. As demonstrated in section 6.7.3, the other activated reactions have even higher barriers in the gas phase.

The composition of the mineral core of ISM dust grains is difficult to generalise; with the only available physical samples collected from the comet Wild 2[180], we are forced to rely on spectroscopic observations, which suggest various polymorphs of carbonaceous and silicate materials. What is more certain is that 60-70% of the interstellar ice coating the grains is H_2O, most likely in the form of impure ASW[155]. The observed

abundance of interstellar glycolaldehyde can only be accounted for by the catalysis on the surface of icy dust grains.

Owing to the difficulty in representing a highly disordered structure in a relatively small scale periodic model, our first step is the evaluation of the viability of glycolaldehyde-formation reactions on a crystalline ice surface, with a view to refining the method to include an amorphous surface in the future.

6.9.2 Model and methods

The main aim of this work has been to evaluate the likelihood of these reaction occurring on an ice surface representative of an interstellar dust grain mantle. There have been some attempts to characterise some of these reactions on ice, but these have been limited to nanoscale cluster models which lack the long range order of a true surface[172]. To this end, we have used a 3D periodic slab model of ice, on top of which the reactions occur. The main problem with this type of calculation is the cost: in order to get reasonable reaction barriers, it is necessary to use (at the minimum) hybrid DFT, which is prohibitively expensive for a periodic cell containing hundreds of water molecules. CP2K offers a convenient solution to this problem; the recently implemented ADMM method[185] allows such calculations to be completed in about two or three times the time taken for a similar GGA calculation, an improvement of orders of magnitude over other hybrid DFT methods. It is important to note, however, that this is improvement relies on error cancellation and the use of more limited basis sets, thus we do not expect to achieve chemical accuracy.

It was originally our intention to model reactions on a six-bilayer cubic ice slab for which the surface energy is converged with respect to addition or removal of bilayers. In order to be large enough to avoid image interactions between surface species, the slab would need to contain at least 288 water molecules. However, we soon realised that this would be too difficult given the time and resources available, and scaled it down to a

two bilayer slab containing 96 water molecules. This is a fairly coarse model, but allows us to gauge the relative barriers to the reactions which form glycolaldehyde. Figure 5.6 demonstrates that the surface energy of an ice slab converges rapidly with respect to the number of bilayers, justifying the choice of model. All calculations were performed using the BHandHLYP hybrid density functional (which includes 50% Hartree-Fock exchange), Goedecker-Teter-Hutter (GTH) double-ζ (DZVP) basis sets and pseudopotentials[129], a plane wave cutoff of 400Ry and Grimme's DFT-D3 dispersion correction[119] potential with a dispersion cutoff of 10 Å. The convergence tolerances were set at and energy change of $1 \times 10^{-6}\,E_\mathrm{h}$ for single points, and for geometry optimisations, a maximum displacement of $1 \times 10^{-3}\,a_0$ and a maximum force of $5 \times 10^{-5}\,E_\mathrm{h}\,{a_0}^{-1}$. For the ADMM method the cpFIT3 auxiliary basis set was employed, and a truncated Coulomb potential was employed to facilitate periodic Hartree-Fock calculations. The Coulomb truncation radius was set to 5 Å.

In order to generate the ice slabs, a proton ordered bulk cell containing 288 water molecules with surface order parameter of 2.0 for the surfaces at the top and bottom of the cell ($z = 0$ and $z = c$) was used as a starting point. A computer code employing the Hayward-Reimers algorithm[85] was used to alter the order parameter on the surfaces whilst maintaining the integrity of the ice lattice. This was achieved by finding random loops of hydrogen bonds and rotating them such that the ice rules remained inviolate; only moves that increased the surface order parameter were allowed, thereby resulting in a series of slabs with increasing order parameters between 2 and 4.5 (approximately). A slab with an order parameter of 3.33 was chosen as the most representative of a real ice surface, and as having the largest variety of adsorption points for molecules. This configuration was reduced to a two bilayer, 96 molecule slab approximately 10 Å thick, and the cell extended to 45 Å in the z-direction. At 35 Å, the vacuum gap in this case was perhaps excessive, but was retained such that there would be a sufficiently large vacuum gap for a six bilayer slab with the same cell parameters. The cell parameters were fixed,

and the two bilayer slab was allowed to fully relax, forming the slab to be used in the majority of the calculations below.

In previous experimental work, biradical reactions have been assumed to be barrierless because radical species other than hydrogen atoms were not observed; it was concluded that the were being consumed in biradical reactions too rapidly to be detected[154]. Here, this has not been assumed, and these reactions have received the same explicit treatment, allowing for the eventuality that DFT model is not representative of the experimental reality, or that the surface somehow inhibits the recombination of radicals.

For the single radical reactions, the reactants were placed on the surface and allowed to fully relax. This was repeated for binding sites that obviously constituted a different immediate environment (although an exhaustive survey of binding sites was not conducted due to limited resources), and for the products. The relaxed initial and final configurations were then used as the fixed endpoints for a seven-replica improved tangent[184] nudged elastic band calculation.

Owing to the necessity of manually specifying an initial guess for the biradical reactions, it proved impossible to adapt the nudged elastic band method for them. A variation of the constrained optimisation method was used in these cases; as for the gas phase calculations, the code was unable to generate an initial guess wavefunction with the correct spin density distribution. To remedy this, an initial guess was formed using a single point on the starting configuration with the spin on the reactant fragments constrained to be either 1 or -1 using Blöchl's density-derived atomic point charges (DDAPC) scheme[186], resulting in a singlet state.

6.9.3 Results and discussion

In many ways, the model used was less than optimal. Although crystalline ice has been detected in the ISM, the vast majority of water ice, including the mantle of interstellar

dust grains is expected to be low density amorphous ice. Whilst periodic models of amorphous ice do exist, an extremely (prohibitively, in the case of hybrid functionals) large unit cell is required to adequately model the disorder in such systems. However, a crystalline ice surface is suitable as a first approximation.

It was found that the HCTH/120 GGA functional recovers reaction barriers almost as well as the chosen hybrid functional, BHandHLYP[153]. However, at the time of writing, an open shell version of HCTH/120 has not been implemented in CP2K. At the start of this project, it was our intent to extend our somewhat crude two-bilayer model to a six-bilayer model (the bulk energy is converged with respect to surface energy at four bilayers or more using the PBE functional, according to Pan *et al.*[5]); however, this would have proven too computationally expensive using a hybrid functional with the resources available.

We were also limited in our choice of hybrid functional to those available in CP2K, the only code capable of making such hybrid supercell calculations tractable. Whilst BHandHLYP gives good barrier heights, it is less convincing with respect to reaction energies[153]. Ideally, we would have chosen a semi-empirical "tuned" hybrid functional with a high Hartree-Fock exchange fraction, such as MPW1K, or a modest Hartree-Fock exchange fraction with an improved correlation form, such as B97-1. In addition, the use of the double zeta basis set introduces a significant BSSE, of the order of a few kJ mol^{-1}. This is the same order of magnitude as the barrier heights calculated for many of the reactions; however, a larger basis set would be computationally intractable.

Owing to the inaccuracies inherent in the model, the figures in table 6.7 should not be regarded as absolute values, but should instead be used as a comparison with gas phase calculations at the same level of theory as an indication of the extent to which the reaction barriers are lowered, if at all.

A comparison of the reaction barriers in the gas phase (table 6.1) and on the ice surface (table 6.7) suggests that the ice surface greatly facilitates three of the four rate

determining reactions in the mechanisms considered. For this reason, barriers and reaction energies in the gas phase were recomputed using at the BHandHLYP/DZVP level, i.e. with a congruent (but not identical) basis set.

The reaction barrier for H+CO $\longrightarrow$ HCO is reduced by almost a factor of two. This reaction has been studied in some detail in the gas phase, at high levels of theory[173], and to a limited extent on small water clusters embedded in a dielectric field representative of ice by Woon[172]. This result clearly conflicts with Woon's; he found that a four-water molecule cluster reduced the barrier by 3.6 kJ mol^{-1} from a gas phase value of 20.75 kJ mol^{-1}; a significant but insufficient reduction. Moreover, the dielectric field intended to replace the long range influence of an ice surface reduced the barrier by less than 1 kJ mol^{-1}. Although his model is less sophisticated, Woon's calculations are performed at a higher level of theory, PMP2 and QCISD.

Of greater significance is the effect of the ice surface on the addition of hydrogen to formaldehyde. At the BHandHLYP/DZVP level, the barrier of the methoxy radical formation reaction is reduced by a factor of four (from 12.36 kJ mol^{-1} to 4.67 kJ mol^{-1}), whilst the effect on the hydroxymethyl radical formation reaction is more pronounced, displaying a barrier reduction of a factor of six (from 41.00 kJ mol^{-1} to 7.35 kJ mol^{-1}). Without performing path integral molecular dynamics calculations, it is impossible to quantify the effects of tunnelling on these barriers, but given that tunnelling of hydrogen atoms at 10 K is thought to be significant, it is possible to envisage these barriers being overcome since they are the same order of magnitude as the barrier for the hydrogenation of carbon monoxide. Taking into account BSSE and the inherent uncertainties associated with the functional, the barriers can be considered to be essentially the same; in addition, the formation of the hydroxymethyl radical is more exothermic by an insignificant amount (0.64 kJ mol^{-1}), from which we can conclude that both reactions are approximately equally likely to occur.

Given that all of the biradical reactions are barrierless as suggested by experimental-

	Ice surface			Gas phase		
Reaction	Barrier	Reverse	Heat	Barrier	Reverse	Heat
$CO + H \longrightarrow HCO$	6.25	125.56	−119.31	10.15	101.27	−91.12
$HCO + H \longrightarrow H_2CO$	—	—	−5.48	—	—	−373.95
$H_2CO + H \longrightarrow CH_3O$	4.67	168.20	−163.53	12.36	136.74	−1.31
$H_2CO + H \longrightarrow H_2COH$	7.35	171.52	−164.17	41.00	168.69	−127.69
$H_2COH + HCO \longrightarrow CH_2OHCHO$	—	—	−342.96	—	—	−370.64
$2\,HCO \longrightarrow HOCCOH$	—	—	−282.23	—	—	−290.45
$HOCCOH + H \longrightarrow CH_2OCHO$	9.18	167.48	−158.30	10.87	151.63	−140.76
$CH_2OCHO + H \longrightarrow CH_2OHCHO$	—	—	−460.75	—	—	−441.06

Table 6.7: Reaction barriers and heats (in kJ mol^{-1}) on a two-bilayer crystalline ice slab, compared with the gas phase at the same level of theory. Calculations were performed at the BHandHLYP/DZVP level. A dash in the barrier/reverse barrier columns indicates that the reaction is barrierless. The basis sets are *not* identical; CP2K calculations used the GTH variant.

Species	Adsorption energy (kJ mol^{-1})
H	−1.39
CO	−10.90
HCO	−15.59
H_2CO	−50.12
CH_3O	−28.05
H_2COH	−36.50
HOCCOH	−102.32
CH_2OCHO	−93.30
CH_2OHCHO	−117.84

Table 6.8: Adsorption energies (in kJ mol^{-1}) for all species involved in mechanisms A and B on the two bilayer crystalline ice surface (at the BHandHLYP/DZVP level). The adsorbed configurations are shown in figure 6.7.

ists[154], there is a clear rate determining step for each of the two mechanisms. In the case of mechanism A (page 174), it is the hydrogenation of formaldehyde, and in the case of mechanism B, it is the hydrogenation of the HOCCOH species. The reaction barrier for the latter is marginally higher (by 1.83 kJ mol^{-1}), but not sufficiently to be sure that the difference is not a result of BSSE or self interaction. It seems more likely that the respective rates are limited by the ease with which the HCO and H_2COH radicals can migrate across the ice surface.

It was found to be extremely difficult to calculate a migration barrier for a hydrogen atom because the potential energy landscape of a proton disordered ice surface is so irregular. Hydrogen atoms can physisorb either to the "flat" surface water molecules (i.e. molecules without a dangling OH) or sit above the centre of a six-ring, depending on the proton ordering in the local environment. Two attempts to calculate the barrier using the nudged elastic band approach yielded energies of 2 kJ mol^{-1} to 4 kJ mol^{-1}; taking into account BSSE, hydrogen migration therefore has either a low or zero barrier.

The situation is more complicated for molecules: a specific proton ordering pattern is required for a polar molecule to bind to the ice surface, and on a disordered surface, the most favourable binding sites require a specific proton ordered configuration

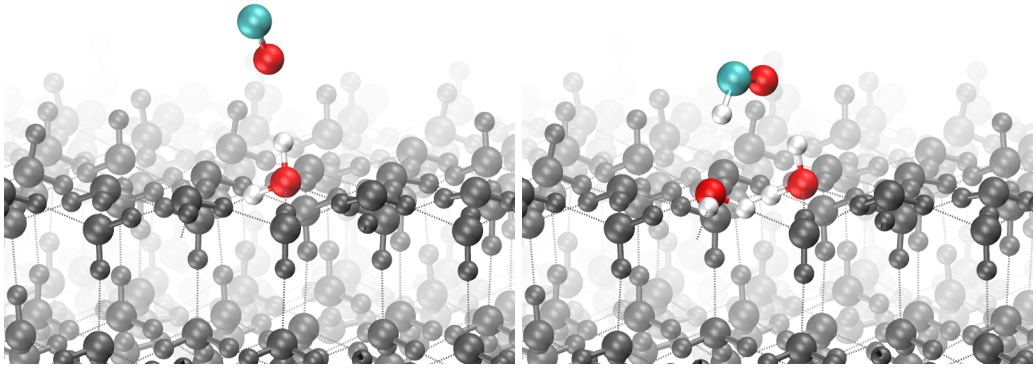

(a) CO (b) HCO

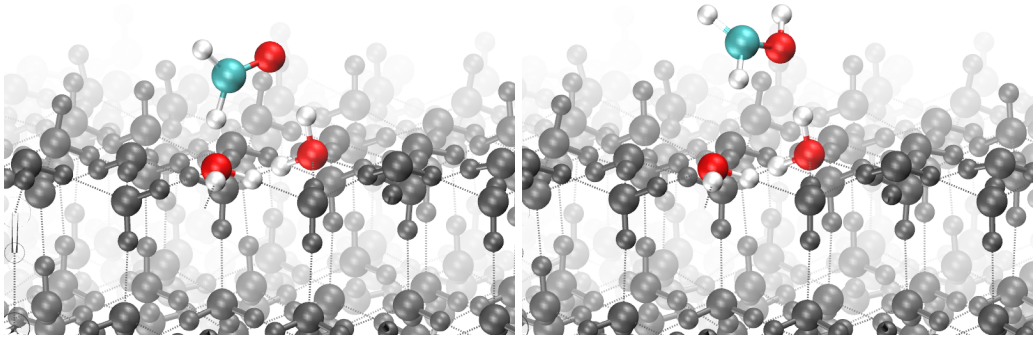

(c) H_2CO (d) H_2COH

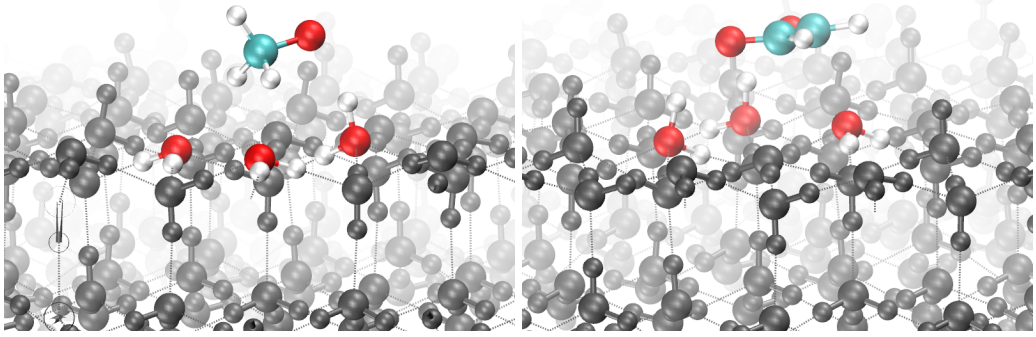

(e) CH_3O (f) HOCCOH

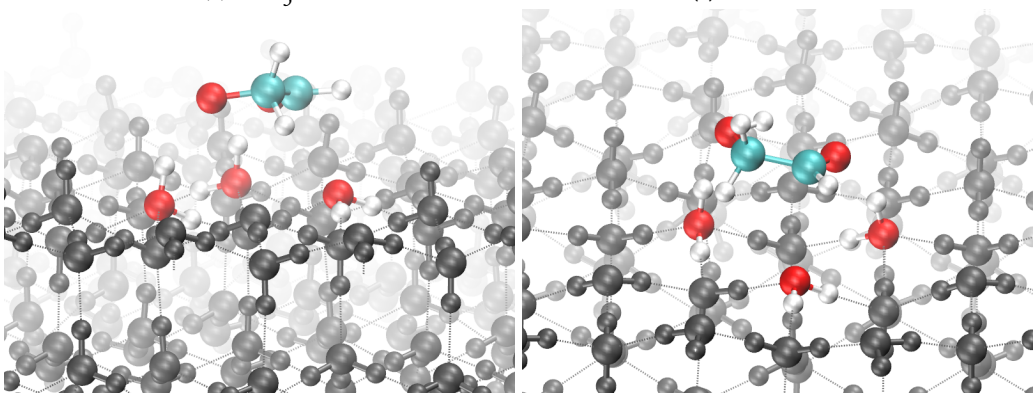

(g) CH_2OCHO (h) CH_2OHCHO

Figure 6.7: Binding of various species to the ice surface. Water molecules that are not involved in physisorption are coloured grey.

coupled with a specific molecular orientation; it is expected that this, in conjunction with the larger mass, will hinder migration. Since we have neither the time nor computational resources to perform an extensive survey of migration barriers, as a first approximation, adsorption energies for the species involved in both mechanisms were calculated, and are presented in table 6.8. It should be noted that these values correspond to only one local proton ordered environment of many on the ice surface, so in fact there will be a range of energies. The environment on which to calculate was chosen on the following basis: a survey of adsorption sites was performed for carbon monoxide (this proved to include a relatively small number of calculations, since for a bound CO molecule, the "local environment" constitutes only three surface water molecules, one of which must have a dangling OH. The site with the largest adsorption energy was chosen to sequentially hydrogenate the CO molecule in order to construct molecules up to CH_3O and H_2COH. For the two-carbon molecules, the situation was more complicated; it was necessary to find sensible adsorption sites for both reactants and products on a finite slab, so the case of reactions (6.53) and (6.55), there was only one possible location for the reaction to occur. The adsorption energy of CO ranged between $-10.90\,\mathrm{kJ\,mol^{-1}}$ and $-4.70\,\mathrm{kJ\,mol^{-1}}$.

The low barrier for hydrogen migration calculated using the NEB method supports the proposition that adsorption energies and migration barriers are generally correlated; the adsorption energy for hydrogen is almost negligible, and considerably less than the largest potential error caused by BSSE and the self-interaction error. The adsorption energy of the HCO molecule is an order of magnitude larger, at $-15\,\mathrm{kJ\,mol^{-1}}$, which supports the notion that only hydrogen atoms are mobile on the *crystalline* ice surface. The potential energy surface on ASW is far more irregular, and it is therefore conceivable that in areas that are locally "flat," it will be possible for these larger species to overcome the migration barrier by tunnelling.

One reaction that has not been studied is the formation of methyl formate, CH_3O+

$HCO \longrightarrow CH_3OCHO$. It is likely to be barrierless on the ice surface, considering all of the other biradical reactions on the ice surface were found to be barrierless; if anything, the lower barrier to the formation of the CH_3O radical should make it more favourable than the competing glycolaldehyde-forming reaction (6.53). On the other hand, H_2COH is essentially planar, whilst CH_3O is tetrahedral, therefore taking steric hindrance into account, HCO can attack H_2COH from two angles (either side of the plane), whereas it can only attack CH_3O from one direction (the side of the oxygen atom). It is impossible to draw a strong conclusion from this in the absence of rate constants for these reactions, but these conclusions may go some way to explaining the higher abundance of methyl formate.

We now attempt to estimate the characteristic temperature using the method described in section 6.6 for the reaction $H_2CO + H \longrightarrow CH_3O$. We assume that the form of the function used to fit the profile of the reaction on the ice surface is qualitatively similar to the gas phase profile. Thus a detailed dataset from the gas phase reaction is used to determine the functional form that will be fit to the ice surface data (figure 6.8). The coordinates for the ice surface reaction were converted from Ångström to atomic units (Bohr), and rescaled to normal mode coordinates by multiplying each coordinate by the square root of the atomic mass. This new basis was used to recompute the reaction coordinate.

The function $f(x)$ that was found to fit the gas phase data is a linear combination of a Morse function and a Gaussian function:

$$f(x) = a[(1 - e^{-b(x-c)})^2 - 1] + pe^{-\frac{(x-q)^2}{r^2}} + s \tag{6.63}$$

$$f''(x) = 2ab^2[-e^{-b(x-c)} - 2e^{2b(x-c)}] + \frac{2p}{r^4} e^{-\frac{-(x-q)^2}{r^2}} [(x-q)^2 - r^2] \tag{6.64}$$

The fit for this function with the ice surface data for the reactions $H_2CO + H \longrightarrow CH_3O$ and $H_2CO + H \longrightarrow H_2COH$ is shown in figure 6.9, and is used to determine the param-

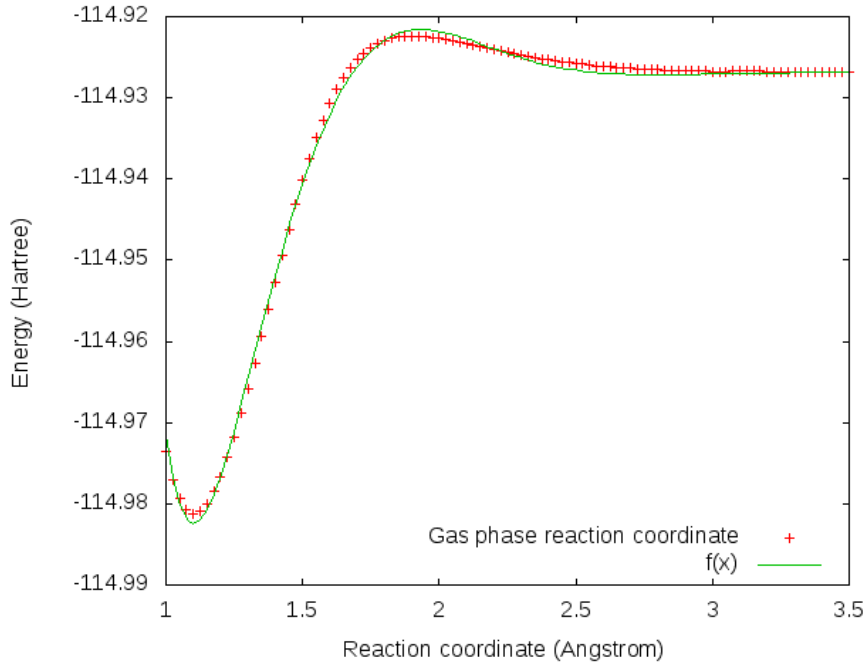

Figure 6.8: Function $f(x)$ fit to the gas phase (Cartesian) reaction coordinate for $H_2CO + H \longrightarrow CH_3O$.

eters a, b, c, p, q, r and s in each case. The second derivative $f''(x)$ is taken at the transition state to calculate the curvature. The curvature at the transition state for the formation of CH_3O in figure 6.9a is -0.01 atomic units, which translates to an imaginary frequency of $-2300\,cm^{-1}$ and a characteristic temperature of 3300 K. In contrast, the imaginary frequency for the $H_2CO + H \longrightarrow H_2COH$ reaction was calculated from figure 6.9b as $-440\,cm^{-1}$, corresponding to a characteristic temperature of 640 K. The first value is perhaps surprisingly high; Goumans and Kästner used harmonic quantum transition state theory (HQTST) to predict the characteristic temperature of hydrogen abstraction from methanol ($H + H_3COH \longrightarrow H_2 + H_2COH$ or CH_3O)[187] in the gas phase, which is a similar class of reaction to the type studied here. HQTST is a semi-classical method that has been shown to perform well at low temperatures. They report values of $T_c = 331$ K for H_2COH formation and 396 K for CH_3O formation, i.e. an order of magnitude smaller than for the CH_3O-forming reaction considered above. The exceptionally high characteristic temperature calculated suggests that on the ice surface,

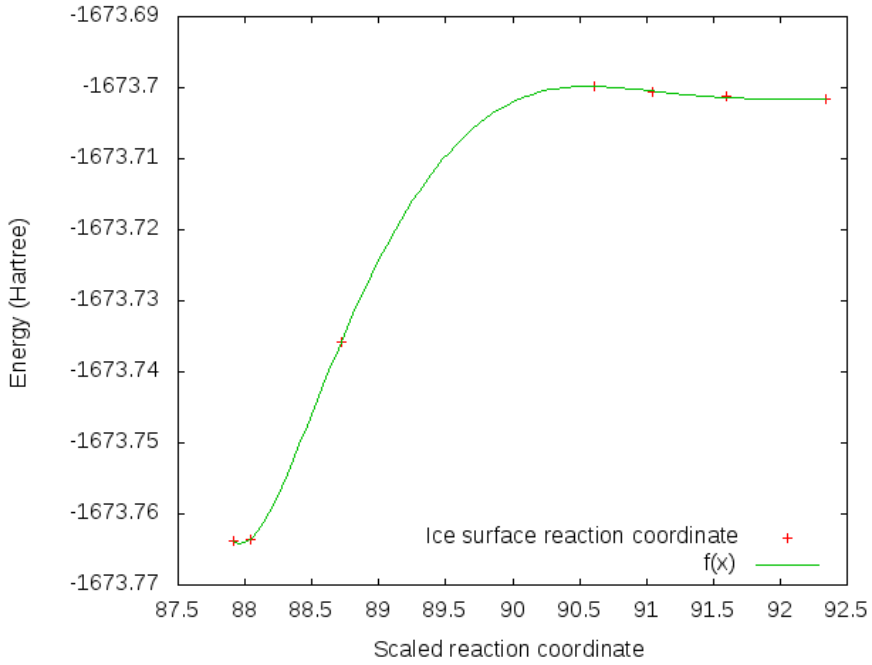

(a) Function $f(x)$ fit to the ice surface reaction coordinate (normal mode coordinates) for $H_2CO + H \longrightarrow CH_3O$.

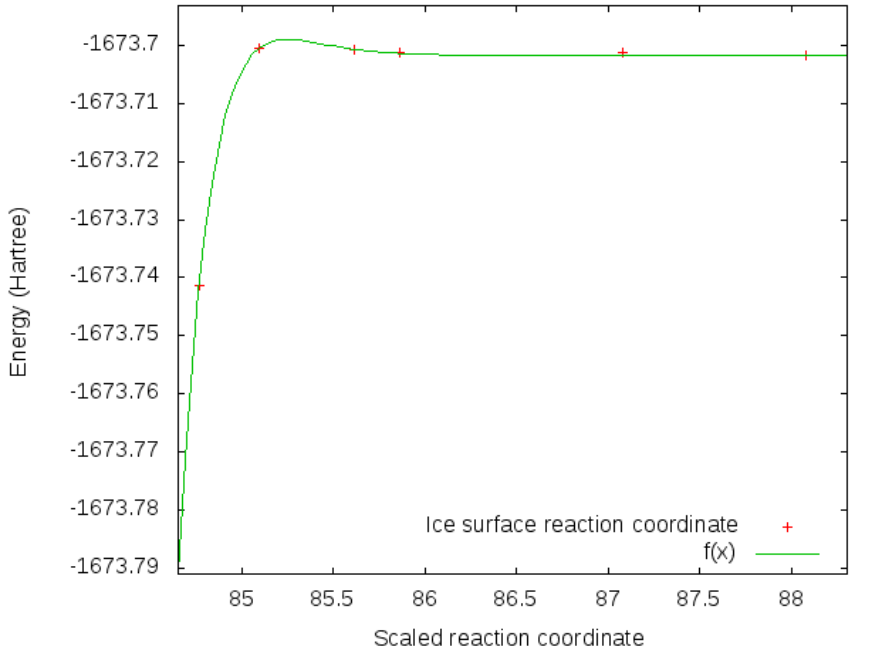

(b) Function $f(x)$ fit to the ice surface reaction coordinate (normal mode coordinates) for $H_2CO + H \longrightarrow H_2COH$.

Figure 6.9: Demonstration of fitting procedure to obtain curvature at the transition state for two ice surface reactions. Note that the D3 dispersion correction was used in neither calculation due the resulting introduction of numerical noise.

quantum mechanical tunnelling happens is by far the dominant barrier-crossing process at all temperatures of physical interest, and that it is more important on the ice surface than it is in the gas phase. It is perhaps a sign that the ice alters the form and curvature of the potential energy surface of the reactants such that tunnelling is far more favourable than in the gas phase, by making the barrier narrower, and perhaps more symmetrical.

The characteristic temperature for the H_2COH-forming reaction is much lower, and is of the same order of magnitude as the frequencies reported by Goumans *et al*. When a hydrogen atom approaches a formaldehyde molecule on the ice surface, the approach vector is more favourable for the formation of CH_3O because in the case of H_2COH, the COH bond angle is acute, and far from the angle in the product molecule. The NEB paths for these reactions are shown in figure 6.10. Whilst the hydrogen atom has a direct path in the case of CH_3O (figure 6.10a), its path is clearly modified by the presence of the ice surface hydrogen atom to which the oxygen in the formaldehyde molecule is hydrogen bonded (figure 6.10b). When forming the H_2COH radical, the path of the hydrogen atom is deflected both vertically and laterally by the potential energy surface. It is possible that this makes the potential energy surface for the latter reaction more complicated, with a more distorted barrier that is less favourable for tunnelling: the reaction barrier is superimposed onto the torsional barrier on the H–CO–H axis. However, these conclusions assume that the curvature estimates (not to mention the model) are accurate enough; this may not be the case.

There were two problems which prevented the calculation of T_c for all of the ice surface reactions, both of which made the fitting process impossible in the majority of cases. The first was the sparsity of data points, especially in the vicinity of the transition states. The use of a harmonic approximation with a finite difference approximation of the curvature was rendered impossible for this reason, and also results in a large margin of error for the curvature, as can be seen in figure 6.9a. The second reason is numerical noise, which we believe is primarily a result of the D3 dispersion correction. D3 is a

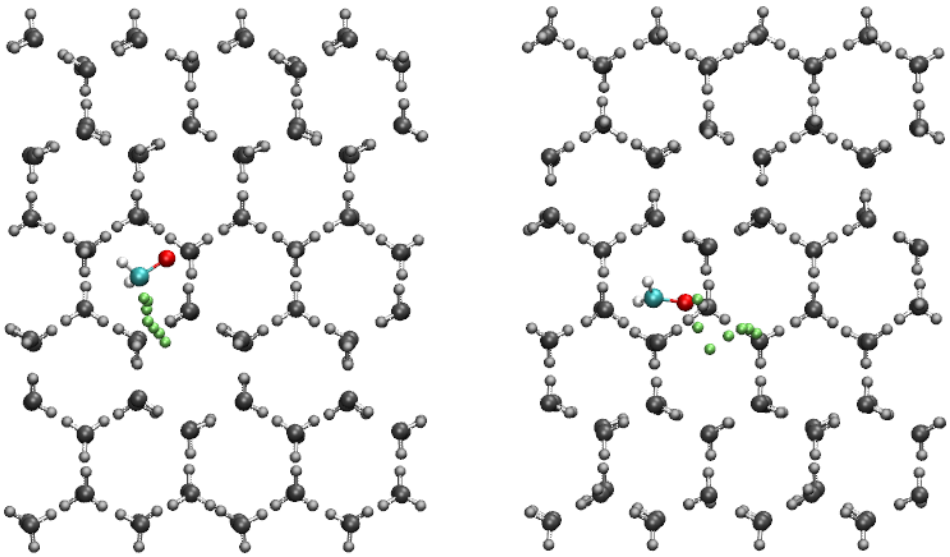

(a) CH_3O (b) H_2COH

Figure 6.10: NEB paths for a hydrogen atom reacting with H_2CO to form CH_3O (left) and H_2COH (right) on an ice surface. Only the path of the hydrogen atom is shown for clarity.

semiempirical method. The problems with D3 are twofold. Firstly, in attempting to empirically improve long range correlation using a c_6 term, it employs a method which, while appropriate for describing *inter*molecular interactions, is part of a completely different paradigm to DFT and therefore deteriorates the *intra*molecular and interatomic description. Secondly, the corrections are parameterised using gas phase data from neutral atoms, which behave very differently to atoms in the solid state, including water ice. For example, the polarisability and dipole moment of water molecules change by a factor of two in the transition from the gas phase to the solid state. In summary, whilst a long range dispersion correction is necessary to describe reaction catalysed by a surface, the implementation is far from perfect.

6.10 Summary and conclusions

On the basis of astrophysical and chemical models, two mechanisms for the formation of glycolaldehyde were examined; the first involving hydrogenation of carbon monoxide to form formyl and hydroxymethyl radicals which combine to produce glycolaldehyde, and the second requiring the formation and reaction of formyl radicals to form the HOCCOH species, which is subsequently hydrogenated to form glycolaldehyde. These reactions have been characterised in detail up to a high level of theory, and it is apparent that none of the activated reactions are feasible in the gas phase at 10 K.

It was found that hydroxylated silicate nanoclusters will catalyse the hydrogenation of formaldehyde, and the barrier reduction from the gas phase is related to the curvature of the substrate cluster; larger clusters result in a greater reduction.

Reactions simulated on an ice surface were found to have their barriers reduced considerably. In particular, the difference in barrier between the hydrogenation of formalydehyde to the methoxy and hydroxymethyl radicals was reduced from 28 kJ mol^{-1} in the gas phase to 3 kJ mol^{-1} on the ice surface. That is, the formation of the hydroxymethyl radical is only slightly less kinetically favourable than the methoxy radical, which may be responsible for the abundance of methyl formate.

The rate determining steps are the hydrogenation of formaldehyde and the hydrogenation of HOCCOH respectively. The latter has a higher barrier by 2 kJ mol^{-1}, therefore the first mechanism is the more likely (although this may change if BSSE is significant). Both reactions are contingent on the ability of the formyl radical to migrate across the ice surface; the adsorption energy of HCO is about an order of magnitude higher than that of the hydrogen atom which has a zero migration barrier, so in the regime of quantum tunnelling and considering the long timescales involved in astrochemistry, migration should be possible.

Chapter 7

Conclusions and future work

7.1 Conclusions

In this thesis, computational models were employed to improve the characterisation of cubic ice, which to date remains incomplete. We generated an exhaustive set of symmetry-unique proton ordered bulk configurations for hexagonal (16 configuration) and cubic (11 configurations) lattices, and were able to determine their unambiguous ground states, independent of functional recipe. In the case of hexagonal ice, the calculated $Cmc2_1$ ground state is in agreement with previous work[12], and experimental evidence[82]. Similarly the ground state configuration of cubic ice was found to have $I4_1md$ symmetry and named ice XIc[4]. High precision DFT calculations and comparison with reference DMC calculations suggest that ices XI and XIc are essentially degenerate. It may be possible to prepare ice XIc in the laboratory using a similar method to XI, using slow cooling in the presence of a KOH dopant.

As with hexagonal ice, the cubic ice surface reconstructs to minimise electrostatic repulsion between dangling OH bonds. The Fletcher "striped" phase achieves the lowest surface energy for cubic ice by minimising the average number of dangling OH bonds adjacent to a dangling OH bond. The surface energy increases as the degree of clustering of dangling OH bonds increases. Both hexagonal and cubic ice surfaces have the

same relation between surface energy and dangling OH bond clustering; however, cubic ice surfaces of any order parameter are approximately 10% higher in energy than their hexagonal counterparts.

Elementary steps on the ice surface can undergo major reconstruction to lower step formation energies. Two-coordinated molecules on the step edge can form an additional hydrogen bond with the lower terrace, but this process is contingent on local proton ordering on the step and lower terrace. When a molecule forms a third hydrogen bond, it stabilises the step locally, and when the reconstruction is not possible, it forms a high energy site which is "sticky" and facilitates adsorption and therefore step growth. Of the five step types considered, A-steps appear at the lower end of the step formation energy spectrum. The B_1-step has a higher density of two-coordinated molecules and can therefore reconstruct to form more hydrogen bonds, resulting in the lowest step energy. Molecules on the B_1^* step edge are one-coordinated, and reconstruct to become two-coordinated; their lower coordination results in B_1^* steps having the highest formation energy. There are no two-coordinated molecules on the B_2-step, so it undergoes a minimal reconstruction and generally has a high energy (but not the highest). Thus we expect two-dimensional bilayer growth the be fast in the direction of the B-steps (but with a staggered rate due to the difference between the B_1-, B_1^* and B_2 steps) and slow in the A-step direction, but also non-uniform due to proton disorder. This may go some way to explaining the isotropic two-dimensional growth observed by Sazaki *et al*[6].

In the chapters 4 and 5, the physics of structural features of the cubic ice surface was discussed; in chapter 6, surfaces were used to assess their catalytic impact on the formation of glycolaldehyde, the simplest sugar in the interstellar medium. Glycolaldehyde has been detected in the dense molecular clouds[7;8] and more recently in the vicinity of a Sun-like protostar[9], but calculations show that its formation is not feasible in the gas phase at 10 K. By modelling bare interstellar dust grains as hydroxylated silicate nanoclusters, and their ice mantles as a crystalline ice surface, we find that surfaces are

capable of reducing barriers to the point where reactions may happen (albeit over long time scales, and with the aid of quantum tunneling) at low temperatures. It was found that the barrier height for reactions occurring on the silicate clusters is related to the curvature of the cluster; larger clusters with a flatter surface reduce the barrier more. The ice surface causes a more substantial barrier reduction, and of the two mechanisms studied, the reaction between H_2COH and HCO radicals, which themselves are formed by hydrogenation of carbon monoxide, is the more favourable.

7.2 Future work

It was recognised that in the bulk, the atoms in hexagonal ice are on average further from their ideal lattice points than in cubic ice, highlighting the difference in the potential energy surfaces for these polytypes. The atoms in cubic ice are more confined to their lattice points, suggesting a higher curvature on the potential energy surface, which apparently allows less reconstruction on the cubic ice surface. It would be interesting perform a similar analysis to Watkins *et al.*[26], and calculate vacancy energies on the cubic ice surface, comparing them with vacancies in the hexagonal ice surface.

There is an enormous amount of scope for further study on the topic of elementary steps on the ice surface. Although static DFT calculations at 0 K give us a lot of insight into the energetics of step formation, the situation is very different at finite temperatures: due to the lower coordination, thermal excitations are much less costly on the edge of a step than they are on a pristine surface, so it is impossible to simply extrapolate from zero-temperature simulations[152]. Additionally, surface and step formation energies are only relevant to a surface-vacuum interface, when the situation of genuine interest is an interfacial energy between the surface and liquid water. It may therefore be instructive perform dynamic calculations, either *ab initio*, or more likely using classical forcefields such as TIP4P, to simulate the time evolution of the crystal.

One of the primary motivations for this work was to investigate the impact of cubic

ice on atmospheric reactions implicated in ozone depletion. Bolton used a QM/MM approach to demonstrate that step defects enable the barrierless homolytic dissociation of HCl, a reaction important in ozone destruction[146]; his calculations used the semiempirical PM3 method, and may benefit from a higher level of theory. It would also be interesting (if costly) to compare reaction barriers for such atmospheric reactions between cubic and hexagonal ice surfaces and steps.

The NEB calculations on glycolaldeyde in chapter 6 would benefit from an improved model. As previously mentioned, the HCTH/120 GGA functional yields barriers that are comparable to BHandHLYP[153] at a fraction of the cost, but an open shell version has not been implemented in CP2K. It would allow the use of thicker (up to six bilayers), larger surface areas (and therefore a wider variety of environments), steps, and most importantly the use of low density amorphous ice slabs which are intractable using hybrid functionals. In order to estimate reaction rates, it is necessary to perform vibrational frequency calculations which are intractable for the numbers of atoms used since each atom in the system requires three single point calculations in the central difference approximation, multiplied by three spatial degrees of freedom. This issue can be sidestepped by a fairly coarse approximation, using a reduced Hessian calculation and only calculating the vibrational modes for the "important" atoms, ignoring the ice substrate — but open shell vibrational frequency calculations have not yet been implemented in CP2K. An alternative is to take a cut from the ice slab, containing the reacting species and a small number of substrate molecules, freezing the substrate atoms, and doing a transition state optimisation on the reactant atoms using non-periodic boundary conditions. The vibrational frequencies of this cluster can then be calculated at a lower cost.

Bibliography

[1] W. Zhang, C. He, J. Lian, and Q. Jiang. Selected crystallization of water as a function of size. *Chem. Phys. Lett.*, 421:251, 2006.

[2] B. J. Murray and A. K. Bertram. Formation and stability of cubic ice in water droplets. *Phys. Chem. Chem. Phys.*, 8:186, 2006.

[3] M. Dunn and J. C. Dore. Structural studies of ice formation in porous silicas by neutron diffraction. *J. Cryst. Growth*, 92:233, 1988.

[4] Z. Raza, D. Alfè, C. G. Salzmann, J. Klimeš, A. Michaelides, and B. Slater. Proton ordering in cubic ice and hexagonal ice; a potential new ice phase — XIc. *Phys. Chem. Chem. Phys.*, 13:19788, 2011.

[5] D. Pan, L. M. Liu, G. A. Tribello, B. Slater, A. Michaelides, and E. Wang. Surface energy and surface proton order of the ice Ih basal and prism surfaces. *J. Phys. Cond. Mat*, 22:074209, 2010.

[6] G. Sazaki, S. Zepeda, S. Nakatsubo, E. Yokoyama, and Y. Furukawa. From the Cover: Elementary steps at the surface of ice crystals visualized by advanced optical microscopy. *PNAS*, 107:19702, 2010.

[7] J. M. Hollis, F. J. Lovas, and P. R. Jewell. Interstellar Glylcolaldehyde: the first sugar. *Astrophys. J.*, 540:107, 2000.

[8] M. T. Beltrán, C. Codella, S. Viti, R. Neri, and R. Cesaroni. First Detection of Glycolaldehyde Outside the Galactic Center. *Astrophys. J.*, 690:L93, 2009.

[9] J. K. Jø rgensen, C. Favre, S. E. Bisschop, T. L. Bourke, E. F. van Dishoeck, and M. Schmalzl. Detection of the simplest Sugar, glycolaldehyde, in a solar-type protostar with ALMA. *Astrophys. J. Lett.*, 757:1, 2012.

[10] *Yellowcloud*. *Yellowcloud*'s Flickr stream (accessed 08/2012). `http://www.flickr.com/photos/yellowcloud`.

[11] C. G. Salzmann, P. G. Radaelli, B. Slater, and J. L. Finney. The polymorphism of ice: five unresolved questions. *Phys. Chem. Chem. Phys.*, 13:18468, 2011.

[12] T. K. Hirsch and L. Ojamäe. Quantum-chemical and force-field investigations of ice Ih: computation of proton-ordered structures and prediction of their lattice energies. *J. Phys. Chem. B*, 108:15856, 2004.

[13] Giacomo. Tag digital photography (accessed 09/2012). http://tagdigitalphotography.com/archives/179.

[14] E. R. Davidson and K. Morokuma. A proposed antiferroelectric structure for proton ordered ice Ih. *J. Chem. Phys.*, 81:3741, 1984.

[15] T. M. Klapötke. Research group website (accessed 05/2012). http://www.chemie.uni-muenchen.de/ac/klapoetke/content/klapoetke/research/computational_chemistry.html.

[16] B. D. Yu and M. Scheffler. Ab initio study of step formation and self-diffusion on Ag(100). *Phys. Rev. B*, 55:10, 1996.

[17] E. L. Gibb, D. C. B. Whittet, W. A. Schutte, A. C. A. Boogert, J. E. Chiar, P. Ehrenfreund, P. A. Gerakines, J. V. Keane, A. G. G. M. Tielens, E. F. van Dishoeck, and O. Kerkhof. An inventory of interstellar ices toward the embedded protostar W33A. *Astrophys. J.*, 536:347, 2000.

[18] K. E. Jelfs, E. Flikkema, and S. T. Bromley. Evidence for atomic mixing via multiple intermediates during the dynamic interconversion of silicate oligomers in solution. *Chem. Comm.*, 48:46, 2012.

[19] D. Sheppard, R. Terrell, and G. Henkelman. Optimization methods for finding minimum energy paths. *J. Chem. Phys.*, 128:134106, 2008.

[20] C. Huang, K. T. Wikfeldt, T. Tokushima, D. Nordlund, Y. Harada, U. Bergmann, M. Niebuhr, T. M. Weiss, Y. Horikawa, M. Leetmaa, M. P. Ljungberg, O. Takahashi, A. Lenz, L. Ojamäe, A. P. Lyubartsev, S. Shin, L. G. M. Pettersson, and A. Nilsson. The inhomogeneous structure of water at ambient conditions. *PNAS*, 106:15214, 2009.

[21] C. Huang, K. T. Wikfeldt, T. Tokushima, D. Nordlund, Y. Harada, U. Bergmann, M. Niebuhr, T. M. Weiss, Y. Horikawa, M. Leetmaa, M. P. Ljungberg, O. Takahashi, A. Lenz, L. Ojamäe, A. P. Lyubartsev, S. Shin, L. G. M. Pettersson, and A. Nilsson. Reply to Soper et al.: Fluctuations in water around a bimodal distribution of local hydrogen-bonded structural motifs. *PNAS*, 107:E45, 2010.

[22] A. K. Soper, J. Teixeira, and T. Head-Gordon. Is ambient water inhomogeneous on the nanometer-length scale? *PNAS*, 107:E44, 2010.

[23] M. Chaplin. Water structure and science (accessed 06/2011). http://www1.isbu.ac.uk/water/.

[24] D. Kennedy and C. Norman. What don't we know? *Science*, 309:78, 2005.

[25] D. Ehre, E. Lavert, M. Lahav, and I. Lubomirsky. Water freezes differently on positively and negatively charged surfaces of pyroelectric materials. *Science*, 327:672, 2010.

[26] M. Watkins, D. Pan, E. G. Wang, A. Michaelides, J. VandeVondele, and B. Slater. Large variation in ice surface dipoles and vacancy formation energies — why the ice surface is like an old mattress. *submitted*, 2011.

[27] C. G. Salzmann, P. Radaelli, E. Mayer, and J. Finney. Ice XV: a new thermodynamically stable phase of ice. *Phys. Rev. Lett.*, 103:15701, 2009.

[28] J. Jelassi, H. L. Castricum, M. Bellissent-Funel, J. Dore, J. B. W. Webber, and R. Sridi-Dorbez. Studies of water and ice in hydrophilic and hydrophobic mesoporous silicas: pore characterisation and phase transformations. *Phys. Chem. Chem. Phys.*, 12:2838, 2010.

[29] E. B. Moore, E. de la Llave, K. Welke, D. A. Scherlis, and V. Molinero. Freezing, melting and structure of ice in a hydrophilic nanopore. *Phys. Chem. Chem. Phys.*, 12:4124, 2010.

[30] O. Yamamuro. Heat capacity and glass transition of pure and doped cubic ices. *J. Phys. Chem. Sol.*, 48:935, 1987.

[31] Y. P. Handa, D. D. Klug, and E. Whalley. Difference in energy between cubic and hexagonal ice. *J. Chem. Phys.*, 84:7009, 1986.

[32] Y. P. Handa, D. D. Klug, and E. Whalley. Energies of the phases of ice at low temperature and pressure relative to ice Ih. *Canadian Journal of Chemistry*, 66:919, 1988.

[33] E. Mayer and A. Hallbrucker. Cubic ice from liquid water. *Letters to Nature*, 325:601, 1987.

[34] J. A. McMillan and S. C. Los. Vitreous ice: irreversible transformations during warm-up. *Nature*, 206:806, 1965.

[35] H. Sugisaki, H. Suga, and S. Seki. Calorimetric study of the glassy state IV: Heat capacities of glassy water and cubic ice. *Bull. Chem. Soc. Jpn.*, 41:2591, 1968.

[36] J. E. Shilling, M. A. Tolbert, O. B. Toon, E. J. Jensen, B. J. Murray, and A. K. Bertram. Measurements of the vapor pressure of cubic ice and their implications for atmospheric ice clouds. *Geo. Res. Lett.*, 33:0, 2006.

[37] C. G. Salzmann, E. Mayer, and A. Hallbrucker. Thermal properties of metastable ices IV and XII: comparison, isotope effects and relative stabilities. *Phys. Chem. Chem. Phys.*, 6:1269, 2004.

[38] B. J. Murray, S. L. Broadley, T. W. Wilson, S. J. Bull, R. H. Wills, H. K. Christenson, and E. J. Murray. Kinetics of the homogeneous freezing of water. *Phys. Chem. Chem. Phys.*, 12:10380, 2010.

[39] B. J. Murray, D. A. Knopf, and A. K. Bertram. The formation of cubic ice under conditions relevant to Earth's atmosphere. *Nature*, 434:202, 2005.

[40] D. M. Murphy. Dehydration in cold clouds is enhanced by a transition from cubic to hexagonal ice. *Geophys. Res. Lett.*, 30:2230, 2003.

[41] B. J. Murray. Enhanced formation of cubic ice in aqueous organic acid droplets. *Environ. Res. Lett.*, 3, 2008.

[42] B. J. Murray and A. K. Bertram. Inhibition of solute crystallisation in aqueous h^+-nh_4^+-so_4^{2-}-h_2o droplets. *Phys. Chem. Chem. Phys.*, 10:3287, 2008.

[43] B. J. Murray and J. M. C. Plane. Uptake of Fe, Na and K atoms on low-temperature ice: implications for metal atom scavenging in the vicinity of polar mesospheric clouds. *Phys. Chem. Chem. Phys.*, 7:3970, 2005.

[44] P. Mehl and P. Boutron. Cryoprotection of red blood cells by 1,3-butanediol and 2, 3-butanediol. *Cryobiology*, 25:44, 1988.

[45] G. Malenkov. Liquid water and ices: understanding the structure and physical properties. *J. Phys. Cond. Mat.*, 21:283101, 2009.

[46] V. F. Petrenko and R. W. Whitworth. *Physics of Ice*. Oxford University Press, 1999.

[47] N. Bjerrum. Structure and Properties of Ice. *Science*, 115:385, 1952.

[48] V. Buch, P. Sandler, and J. Sadlej. Simulations of H2O Solid, Liquid, and Clusters, with an Emphasis on Ferroelectric Ordering Transition in Hexagonal Ice. *J. Phys. Chem. B*, 102:8641, 1998.

[49] T. L. Malkin, B. J. Murray, A. V. Brukhno, J. Anwar, and C. G. Salzmann. Structure of ice crystallized from supercooled water. *PNAS*, 109:1041, 2012.

[50] E. B. Moore and V. Molinero. Is it cubic? Ice crystallization from deeply supercooled water. *Phys. Chem. Chem. Phys.*, 13:20008, 2011.

[51] W. F. Kuhs, D. V. Bliss, and J. L. Finney. High-resolution neutron powder diffraction study of ice Ic. *Journal de Physique Colloque*, 3:631, 1987.

[52] G. P. Johari. On the coexistence of cubic and hexagonal ice between 160 and 240 K. *Phil. Mag. B*, 78:375, 1998.

[53] C. G. Salzmann, P. G. Radaelli, A. Hallbrucker, E. Mayer, and J. L. Finney. The preparation and structures of hydrogen ordered phases of ice. *Science (New York, N.Y.)*, 311:1758, 2006.

[54] E. Whalley. Cubic ice in nature. *J. Phys. Chem.*, 87:4174, 1983.

[55] M. Riikonen, L. V. Sillanpaa, L. Virta, D. Sullivan, J. Moilanen, and I. Luukonen. Halo observations provide evidence of airborne cubic ice in the Earth's atmosphere. *Applied Optics*, 39:6090, 2000.

[56] T. Kobayashi. Cubic structure models at the junctions in polycrystalline snow crystals. *J. Cryst. Growth*, 35:262, 1976.

[57] T. Takahashi. On the role of cubic structure in ice nucleation. *J. Cryst. Growth*, 59:441, 1982.

[58] L. G. Dowell and A. P. Rinfret. Low temperature forms of ice as studied by X-Ray diffraction. *Nature*, 188:1144, 1960.

[59] J. E. Bertie, L. D. Calvert, and E. Whalley. Transformations of Ice II, Ice III, and Ice V at Atmospheric Pressure. *J. Chem. Phys.*, 38:840, 1963.

[60] D. C. Steytler, J. C. Dore, and C. J. Wright. Neutron diffraction study of cubic ice nucleation in a porous silica network. *J. Phys. Chem.*, 87:2458, 1983.

[61] G. P. Johari. Water's size-dependent freezing to cubic ice. *J. Chem. Phys.*, 122:194504, 2005.

[62] L. Pauling. The structure and entropy of ice and of other crystals with some randomness of atomic arrangement. *J. Am. Chem. Soc.*, 57:2680, 1935.

[63] P. V. Hobbs. *Ice Physics*. Oxford University Press, 1974.

[64] J. D. Bernal and R. H. Fowler. A theory of water and ionic solution, with particular reference to hydrogen and hydroxyl ions. *J. Chem. Phys.*, 1:515, 1933.

[65] A. Bartok and A. Baranyai. Disorder in ice polymorphs: A Monte Carlo simulation study. *J. Non-Cryst. Solids*, 353:2698, 2007.

[66] B. Silvi. Importance of electrostatic interactions between nonbonded molecules in ice. *Phys. Rev. Lett.*, 73:842, 1994.

[67] J. Lekner. Electrostatics of proton arrangements in ice Ic. *Physica B*, 240:263, 1997.

[68] J. Lekner. Energetics of hydrogen ordering in ice. *Physica B*, 252:149, 1998.

[69] S. Casassa, M. Calatayud, K. Doll, C. Minot, and C. Pisani. Proton ordered cubic and hexagonal periodic models of ordinary ice. *Chem. Phys. Lett.*, 409:110, 2005.

[70] B. Guillot. A reappraisal of what we have learnt during three decades of computer simulations on water. *J. Mol. Liq.*, 101:219, 2002.

[71] J. L. F. Abascal, E. Sanz, R. García Fernández, and C. Vega. A potential model for the study of ices and amorphous water: TIP4P/Ice. *J. Chem. Phys.*, 122:234511, 2005.

[72] H. J. C. Berendsen, J. P. M. Postma, W. F. van Gunsteren, and J. Hermans. Interaction models for water in relation to protein hydration. *FEMS Immunology*, 11:237, 1996.

[73] C. Vega, J. L. F. Abascal, M. M. Conde, and J. L. Aragones. What ice can teach us about water interactions: a critical comparison of different water models. *Faraday Discussions*, 141:9, 2009.

[74] W. L. Jorgensen, J. Chandrasekhar, J. D. Madura, R. W. Impey, and M. L. Klein. Comparison of simple potential functions for simulating liquid water. *J. Chem. Phys.*, 79:926, 1983.

[75] M. W. Mahoney and W. L. Jorgensen. A five-site model for liquid water and the reproduction of the density anomaly by rigid, nonpolarizable potential functions. *J. Chem. Phys.*, 112:8910, 2000.

[76] J. L. F. Abascal and C. Vega. A general purpose model for the condensed phases of water: TIP4P/2005. *J. Chem. Phys.*, 123:234505, 2005.

[77] C. McBride, C. Vega, E. G. Noya, R. Ramírez, and L. M. Sesé. Quantum contributions in the ice phases: the path to a new empirical model for water-TIP4PQ/2005. *J. Chem. Phys.*, 131:024506, 2009.

[78] S. W. Rick. Simulations of proton order and disorder in ice Ih. *J. Chem. Phys*, 122:094504, 2005.

[79] H. Nada and J. P. J. M. van der Eerden. An intermolecular potential model for the simulation of ice and water near the melting point: A six-site model of H[sub 2]O. *J. Chem. Phys.*, 118:7401, 2003.

[80] Y. Tajima, T. Matsuo, and H. Suga. Phase transition in KOH-doped hexagonal ice. *Nature*, 299:810, 1982.

[81] R. Howe and R. W. Whitworth. A determination of the crystal structure of ice XI. *J. Chem. Phys.*, 90:4450, 1989.

[82] A. J. Leadbetter, R. C. Ward, J. W. Clark, P. A. Tucker, T. Matsuo, and H. Suga. The equilibrium low-temperature structure of ice. *J. Chem. Phys.*, 82:424, 1985.

[83] S. M. Jackson and R. W. Whitworth. Thermally-Stimulated Depolarization Studies of the Ice XI—Ice Ih Phase Transition. *J. Phys. Chem. B*, 101:6177, 1997.

[84] R. Howe. The possible ordered structures of ice Ih. *Le Journal de Physique Colloques*, 48:599, 1987.

[85] J. A. Hayward and J. R. Reimers. Unit cells for the simulation of hexagonal ice. *J. Chem. Phys.*, 106:1518, 1997.

[86] J. L. Kuo, J. V. Coe, S. J. Singer, Y. B. Band, and L. Ojamäe. On the use of graph invariants for efficiently generating hydrogen bond topologies and predicting physical properties of water clusters and ice. *J. Chem. Phys.*, 114:2527, 2001.

[87] J. L. Kuo and S. J. Singer. Graph invariants for periodic systems: Towards predicting physical properties from the hydrogen bond topology of ice. *Phys. Rev. E*, 67:16114, 2003.

[88] C. Knight, S. J. Singer, J. L. Kuo, T. Hirsch, L. Ojamäe, and M. Klein. Hydrogen bond topology and the ice VII/VIII and Ih/XI proton ordering phase transitions. *Phys. Rev. E*, 73:056113, 2006.

[89] S. W. Rick and A. D. J. Haymet. Dielectric constant and proton order and disorder in ice Ih: Monte Carlo computer simulations. *J. Chem. Phys.*, 118:9291, 2003.

[90] S. W. Rick, S. J. Stuart, and B. J. Berne. Dynamical fluctuating charge force fields: Application to liquid water. *J. Chem. Phys.*, 101:6141, 1994.

[91] A. Baranyai, A. Bartók, and A. A. Chialvo. Computer simulation of the 13 crystalline phases of ice. *J. Chem. Phys.*, 123:054502, 2005.

[92] A. Baranyai, A. Bartók, and A. A. Chialvo. Limitations of the rigid planar nonpolarizable models of water. *J. Chem. Phys.*, 124:74507, 2006.

[93] C. Pisani. Proton-ordered ice structures at zero pressure. A quantum-mechanical investigation. *Chem. Phys. Lett.*, 253:201, 1996.

[94] A. Erba, S. Casassa, L. Maschio, and C. Pisani. DFT and local-MP2 periodic study of the structure and stability of two proton-ordered polymorphs of ice. *J. Phys. Chem. B*, 113:2347, 2009.

[95] C. Pisani, L. Maschio, S. Casassa, M. Halo, and A. Erba. A local-MP2 approach to the ab initio study of electron correlation in crystals and to the simulation of vibrational spectra: the case of Ice XI. *Theor. Chem. Acc.*, 123:327, 2009.

[96] A. Erba, S. Casassa, R. Dovesi, L. Maschio, and C. Pisani. Periodic density functional theory and local-MP2 study of the librational modes of Ice XI. *J. Chem. Phys.*, 130:074505, 2009.

[97] G. A. Tribello and B. Slater. Proton ordering energetics in ice phases. *Chem. Phys. Lett.*, 425:246, 2006.

[98] F. Labat, C. Pouchan, C. Adamo, and G. E. Scuseria. Role of Nonlocal Exchange in Molecular Crystals : The Case of Two Proton-ordered Phases of Ice. *J. Comput. Chem.*, 32:2177, 2011.

[99] E. R. Batista, S. S. Xantheas, and H. Jónsson. Electric fields in ice and near water clusters. *J. Chem. Phys.*, 112:3285, 2000.

[100] N. H. Fletcher. Reconstruction of ice crystal surfaces at low temperatures. *Phil. Mag. B*, 66:109, 1992.

[101] J. P. Devlin and V. Buch. Evidence for the surface origin of point defects in ice: control of interior proton activity by adsorbates. *J. Chem. Phys.*, 127:091101, 2007.

[102] V. Buch, H. Groenzin, I. Li, M. J. Shultz, and E. Tosatti. Proton order in the ice crystal surface. *PNAS*, 105:5969, 2008.

[103] S. Kuwajima and A. Warshel. Incorporating electric polarizabilities in water-water interaction potentials. *J. Phys. Chem.*, 94:460, 1990.

[104] D. Pan, L. M. Liu, G. A. Tribello, B. Slater, A. Michaelides, and E. Wang. Surface Energy and Surface Proton Order of Ice Ih. *Phys. Rev. Lett.*, 101:155703, 2008.

[105] A. R. Leach. *Molecular Modelling: Principles and Applications*. Pearson Education Limited, 2001.

[106] E. G. Lewars. *Computational Chemistry*. Springer, 2011.

[107] P.-O. Löwdin. *Correlation problem in many-electron quantum mechanics I. Review of different approaches and discussion of some current ideas*, pages 207–322. John Wiley & Sons, 2007.

[108] F. Jensen. *Introduction to Computational Chemistry*. John Wiley & Sons, 1999.

[109] P. Hohenberg and W. Kohn. Inhomogeneous Electron Gas. *Phys. Rev.*, 136:B864, 1964.

[110] R. M. Martin. *Electronic Structure: Basic Theory and Practical Methods*. Cambridge University Press, 2008.

[111] W. Kohn and L. Sham. Self-consistent equations including exchange and correlation effects. *Phys. Rev.*, 140:1133, 1965.

[112] J. P. Perdew and K. Schmidt. Jacob's ladder of density functional approximations for the exchange-correlation energy. In *Density Functional Theory and Its Application to Materials vol CP577, ed V Van Doren et al (Melville, NY: American Institute of Physics)*, page 1. Aip, 2001.

[113] J. P. Perdew, A. Ruzsinszky, J. Tao, V. N. Staroverov, G. E. Scuseria, and G. Csonka. Prescription for the design and selection of density functional approximations: more constraint satisfaction with fewer fits. *J. Chem. Phys.*, 123:62201, 2005.

[114] A. D. Becke. Density-functional thermochemistry. IV. A new dynamical correlation functional and implications for exact-exchange mixing. *J. Chem. Phys.*, 104:1040, 1996.

[115] J. P. Perdew, M. Ernzerhof, and K. Burke. Rationale for mixing exact exchange with density functional approximations. *J. Chem. Phys*, 105:9982, 1996.

[116] P. J. Feibelman. Lattice match in density functional calculations: ice Ih vs. beta-AgI. *Phys. Chem. Chem. Phys.*, 10:4688, 2008.

[117] R. J. Needs, M. D. Towler, N. D. Drummond, and P. López Ríos. Continuum variational and diffusion quantum Monte Carlo calculations. *J. Phys. Cond. Mat.*, 22:023201, 2010.

[118] S. Grimme. Semiempirical GGA-type density functional constructed with a long-range dispersion correction. *J. Comp. Chem.*, 27:1789, 2006.

[119] S. Grimme, J. Antony, S. Ehrlich, and H. Krieg. A consistent and accurate *ab initio* parametrization of density functional dispersion correction (DFT-D) for the 94 elements H-Pu. *J. Chem. Phys.*, 132:154104, 2010.

[120] D. C. Langreth, M. Dion, H. Rydberg, E. Schroder, P. Hyldgaard, and B. I. Lundqvist. Van der Waals density functional theory with applications. *Int. J. Quantum Chem.*, 101:599, 2005.

[121] M. Dion, H. Rydberg, E. Schröder, D. Langreth, and B. Lundqvist. Van der Waals Density Functional for General Geometries. *Phys. Rev. Lett.*, 92:22, 2004.

[122] X. Wu, M. C. Vargas, S. Nayak, V. Lotrich, and G. Scoles. Towards extending the applicability of density functional theory to weakly bound systems. *J. Chem. Phys.*, 115:8748, 2001.

[123] D. J. Lacks and R. G. Gordon. Pair interaction of rare-gas atoms as a test of exchange-energy-density functionals in regions of large density gradients. *Phys. Rev. A*, 47:4681, 1993.

[124] J. Klimeš, D. R. Bowler, and A. Michaelides. Chemical accuracy for the van der Waals density functional. *J. Phys.: Condens. Matter*, 22:022201, 2010.

[125] J. Vandevondele, M. Krack, F. Mohamed, M. Parrinello, T. Chassaing, and J. Hutter. Quickstep: Fast and accurate density functional calculations using a mixed Gaussian and plane waves approach. *Comp. Phys. Comm.*, 167:103, 2005.

[126] S. F. Boys. Electronic Wave Functions. I. A General Method of Calculation for the Stationary States of Any Molecular System. *Proceedings of the Royal Society A: Mathematical, Physical and Engineering Sciences*, 200:542, 1950.

[127] M. C. Payne, M. P. Teter, D. C. Allan, T. A. Arias, and J. D. Joannopoulos. Iterative minimization techniques for ab initio total-energy calculations: molecular dynamics and conjugate gradients. *Rev. Mod. Phys.*, 64:1045, 1992.

[128] G. Lippert, J. Hutter, and M. Parrinello. A hybrid Gaussian and plane wave density functional scheme. *Mol. Phys.*, 92:477, 1997.

[129] S. Goedecker, M. Teter, and J. Hutter. Separable dual-space Gaussian pseudopotentials. *Phys. Rev. B*, 54:1703, 1996.

[130] D. R. Hamann. H_2O hydrogen bonding in density-functional theory. *Phys. Rev. B*, 55:R10157, 1997.

[131] B. Santra, A. Michaelides, and M. Scheffler. On the accuracy of density-functional theory exchange-correlation functionals for H bonds in small water clusters: benchmarks approaching the complete basis set limit. *J. Chem. Phys.*, 127:184104, 2007.

[132] E. Whalley. Scheiner's Halo: Evidence for Ice Ic in the Atmosphere. *Science*, 211:389, 1981.

[133] C. Knight and S. J. Singer. Hydrogen bond ordering in ice V and the transition to ice XIII. *J. Chem. Phys.*, 129:164513, 2008.

[134] B. Santra, A. Michaelides, M. Fuchs, A. Tkatchenko, C. Filippi, and M. Scheffler. On the accuracy of density-functional theory exchange-correlation functionals for H bonds in small water clusters. II. The water hexamer and van der Waals interactions. *J. Chem. Phys.*, 129:194111, 2008.

[135] G. Kresse and D. Joubert. From ultrasoft pseudopotentials to the projector augmented-wave method. *Phys. Rev. B*, 59:1758, 1999.

[136] J. Klimeš, D. Bowler, and A. Michaelides. Van der Waals density functionals applied to solids. *Phys. Rev. B*, 83:195131, 2011.

[137] J. R. Trail and R. J. Needs. Smooth relativistic Hartree-Fock pseudopotentials for H to Ba and Lu to Hg. *J. Chem. Phys.*, 122:174109, 2005.

[138] P. Giannozzi, S. Baroni, N. Bonini, M. Calandra, R. Car, C. Cavazzoni, D. Ceresoli, G. L. Chiarotti, M. Cococcioni, I. Dabo, A. Dal Corso, S. de Gironcoli, S. Fabris, G. Fratesi, R. Gebauer, U. Gerstmann, C. Gougoussis, A. Kokalj, M. Lazzeri, L. Martin-Samos, N. Marzari, F. Mauri, R. Mazzarello, S. Paolini, A. Pasquarello, L. Paulatto, C. Sbraccia, S. Scandolo, G. Sclauzero, A. P. Seitsonen, A. Smogunov, P. Umari, and R. M. Wentzcovitch. QUANTUM ESPRESSO: a modular and open-source software project for quantum simulations of materials. *J. Phys. Cond. Mat.*, 21:395502, 2009.

[139] D. Alfè and M. Gillan. Efficient localized basis set for quantum Monte Carlo calculations on condensed matter. *Phys. Rev. B*, 70:161101, 2004.

[140] B. Santra, J. Klimeš, D. Alfè, A. Tkatchenko, B. Slater, A. Michaelides, R. Car, and M. Scheffler. Hydrogen bonds and van der Waals forces in ice at ambient and high pressures. *submitted*, 2011.

[141] L. Mitáš, E. L. Shirley, and D. M. Ceperley. Nonlocal pseudopotentials and diffusion Monte Carlo. *J. Chem. Phys.*, 95:3467, 1991.

[142] L. M. Fraser, W. M. C. Foulkes, G. Rajagopal, R. J. Needs, S. D. Kenny, and A. J. Williamson. Finite-size effects and Coulomb interactions in quantum Monte Carlo calculations for homogeneous systems with periodic boundary conditions. *Phys. Rev. B*, 53:1814, 1996.

[143] B. Hess, C. Kutzner, D. van der Spoel, and E. Lindahl. GROMACS 4: Algorithms for Highly Efficient, Load-Balanced, and Scalable Molecular Simulation. *J. Chem. Theor. Comput.*, 4:435, 2008.

[144] G. A. Tribello, B. Slater, M. A. Zwijnenburg, and R. G. Bell. Isomorphism between ice and silica. *Phys. Chem. Chem. Phys.*, 12:8597, 2010.

[145] K. Kobayashi and H. Yasuda. Phase transition of ice Ic to ice XI under electron beam irradiation. *Chem. Phys. Lett.*, page 5, 2012.

[146] K. Bolton. A QM/MM study of HCl adsorption at ice surface defect sites. *J. Mol. Struct.: Theochem*, 632:145, 2003.

[147] A. Glebov, A. P. Graham, A. Menzel, and J. P. Toennies. A helium scattering study of the structure and phonon dynamics of the ice surface. *J. Chem. Phys.*, 112:11011, 2000.

[148] D. C. Clary and L. Wang. Influence of surface defects on the adsorption of HCl on ice. *Faraday Trans.*, 93:2763, 1997.

[149] E. R. Batista and H. Jonsson. Diffusion and island formation on the ice Ih basal plane surface. *Comp. Mat. Sci.*, 20:325, 2001.

[150] B. Li, A. Michaelides, and M. Scheffler. Density functional theory study of flat and stepped NaCl(001). *Phys. Rev. B*, 76:1, 2007.

[151] C. Thierfelder, A. Hermann, P. Schwerdtfeger, and W. G. Schmidt. Strongly bonded water monomers on the ice Ih basal plane: density-functional calculations. *Phys. Rev. B*, 74:45422, 2006.

[152] E. D. Williams. Surface steps and surface morphology: understanding macroscopic phenomena. *Surf. Sci.*, 299:502, 1994.

[153] S. Andersson and M. Grüning. Performance of Density Functionals for Calculating Barrier Heights of Chemical Reactions Relevant to Astrophysics. *J. Phys. Chem. A*, 108:7621, 2004.

[154] N. Watanabe and A. Kouchi. Ice surface reactions: A key to chemical evolution in space. *Prog. Surf. Sci.*, 83:439, 2008.

[155] D. J. Burke and W. A. Brown. Ice in space: surface science investigations of the thermal desorption of model interstellar ices on dust grain analogue surfaces. *Phys. Chem. Chem. Phys.*, 12:5947, 2010.

[156] M. M. Maldoni, M. P. Egan, R. G. Smith, G. Robinson, and C. M. Wright. Crystalline water ice in OH32.8-0.3. *Mon. Not. R. Astron. Soc.*, 345:912, 2003.

[157] A. Kouchi, T. Yamamoto, T. Kozasa, T. Kuroda, and J. M. Greenberg. Conditions for condensation and preservation of amorphous ice and crystallinity of astrophysical ices. *Astronomy and Astrophysics*, 290:1009, 1994.

[158] P. Jenniskens and D. F. Blake. Crystallisation of amorphous water ice in the solar system. *Astrophys. J.*, 473:1104, 1996.

[159] A. Omont, S.H. Moseley, T. Forveille, W. J. Glaccum, P. M. Harvey, L. Likkel, R. F. Loewenstein, and C. M. Lisse. Observations of 40-70 micron bands of ice in IRAS 09371+1212 and other stars. *Astrophys. J.*, 355:L27, 1990.

[160] L. Hornekær, A. Baurichter, V. V. Petrunin, D. Field, and A. C. Luntz. Importance of surface morphology in interstellar H_2 formation. *Science*, 302:1943, 2003.

[161] A. Al-Halabi and E. F. van Dishoeck. Hydrogen adsorption and diffusion on amorphous solid water ice. *Mon. Not. R. Astron. Soc.*, 1656:1648, 2007.

[162] H. Hidaka, N. Miyauchi, a. Kouchi, and N. Watanabe. Structural effects of ice grain surfaces on the hydrogenation of CO at low temperatures. *Chem. Phys. Lett.*, 456:36, 2008.

[163] J. M. Hollis, S. N. Vogel, L. E. Snyder, P. R. Jewell, and F. J. Lovas. The spatial scale of glycolaldehyde in the galactic centre. *Astrophys. J.*, 554:81, 2001.

[164] P. M. Woods, G. Kelly, S. Viti, B. Slater, W. A. Brown, F. Puletti, D. J. Burke, and Z. Raza. On the Formation of Glycolaldehyde in Dense Molecular Cores. *Astrophys. J.*, 750:19, 2012.

[165] W. H. Sorrell. Origin of amino acids and organic sugars in interstellar clouds. *Astrophys. J.*, 555:129, 2001.

[166] C. J. Bennett and R. I. Kaiser. On the formation of glycolaldehyde ($HCOCH_2OH$) and methyl formate ($HCOOCH_3$) in interstellar ice analogs. *Astrophys. J.*, 661:899, 2007.

[167] D. T. Halfen, A. J. Apponi, N. Woolf, R. Polt, and L. M. Ziurys. A systematic study of glycolaldehyde in Sagittarius B2(N) at 2 and 3mm: criteria for detecting large interstellar molecules. *Astrophys. J.*, 639:237, 2006.

[168] S. B. Charnley and S. D. Rodgers. Pathways to Molecular Complexity. *Proc. Int. Astron. Union*, 1:237, 2006.

[169] H. Hidaka, N. Watanabe, T. Shiraki, A. Nagaoka, and A. Kouchi. Conversion of H_2CO to CH_3OH by reactions of cold atomic hydrogen on ice surfaces below 20K. *Astrophys. J.*, 614:1124, 2004.

[170] N. Watanabe, T. Shiraki, and A. Kouchi. The dependence of H_2CO and CH_3OH formation on the temperature and thickness of H_2O-CO ice duringthe successive hydrogenation of CO. *Astrophys. J.*, 588:121, 2003.

[171] K. Hiraoka, T. Sato, S. Sato, N. Sogoshi, T. Yokoyama, H. Takashima, and S. Kitagawa. Formation of formaldehyde by the tunneling reaction of H with solid CO at 10K revisited. *Astrophys. J.*, 577:265, 2002.

[172] D. E. Woon. Modeling gas-grain chemistry with quantum chemical cluster calculations. I. heterogeneous hydrogenation of CO and H_2CO on icy grain mantles. *Astrophys. J.*, 569:541, 2002.

[173] S. Saebø, L. Radom, and H. F. Schaefer. The weakly exothermic rearrangement of methoxy radical (CH_3O) to the hydroxymethyl radical (CH_2OH). *J. Chem. Phys.*, 78:845, 1983.

[174] S. G. Christov. The characteristic (crossover) temperature in the theory of thermally activated tunneling processes. *Mol. Eng.*, 7:109, 1996.

[175] V. A. Benderskii, V. I. Goldanskii, and D. E. Makaraov. Quantum dynamics in low-temperature chemistry. *Phys. Rep.*, 233, 1993.

[176] D. E. Woon. An ab initio benchmark study of the H + CO -> HCO reaction. *J. Chem. Phys.*, 105:9921, 1996.

[177] M. Valiev, E.J. Bylaska, N. Govind, K. Kowalski, T.P. Straatsma, H.J.J. Van Dam, D. Wang, J. Nieplocha, E. Apra, T.L. Windus, and W.a. de Jong. NWChem: A comprehensive and scalable open-source solution for large scale molecular simulations. *Comp. Phys. Comm.*, 181:1477, 2010.

[178] F. Neese. The ORCA program system. *WIREs Comput. Mol. Sci.*, 2:73, 2012.

[179] L. P. Keller, S. Bajt, G. a Baratta, J. Borg, J. P. Bradley, D. E. Brownlee, H. Busemann, J. R. Brucato, M. Burchell, L. Colangeli, L. D'Hendecourt, Z. Djouadi, G. Ferrini, G. Flynn, I. A. Franchi, M. Fries, M. M. Grady, G. A. Graham, F. Grossemy, A. Kearsley, G. Matrajt, K. Nakamura-Messenger, V. Mennella, L. Nittler, M. E. Palumbo, F. J. Stadermann, P. Tsou, A. Rotundi, S. A. Sandford, C. Snead, A. Steele, D. Wooden, and M. Zolensky. Infrared spectroscopy of comet 81P/Wild 2 samples returned by Stardust. *Science*, 314:1728, 2006.

[180] D. Brownlee, P. Tsou, J. Aléon, C. M. O'd Alexander, T. Araki, S. Bajt, G. A. Baratta, R. Bastien, P. Bland, P. Bleuet, J. Borg, J. P. Bradley, A. Brearley, F. Brenker, S. Brennan, J. C. Bridges, N. D. Browning, J. R. Brucato, E. Bullock, M. J. Burchell, H. Busemann, A. Butterworth, M. Chaussidon, A. Cheuvront, M. Chi, M. J. Cintala, B. C. Clark, S. J. Clemett, G. Cody, L. Colangeli, G. Cooper, P. Cordier, C. Daghlian, Z. Dai, L. D'Hendecourt, Z. Djouadi, G. Dominguez, T. Duxbury, J. P. Dworkin, D. S. Ebel, T. E.

Economou, S. Fakra, S. A. J. Fairey, S. Fallon, G. Ferrini, T. Ferroir, H. Fleckenstein, C. Floss, G. Flynn, I. A. Franchi, M. Fries, Z. Gainsforth, J.-P. Gallien, M. Genge, M. K. Gilles, P. Gillet, J. Gilmour, D. P. Glavin, M. Gounelle, M. M. Grady, G. A. Graham, P. G. Grant, S. F. Green, F. Grossemy, L. Grossman, Jeffrey N. Grossman, Y. Guan, K. Hagiya, R. Harvey, P. Heck, G. F Herzog, P. Hoppe, F. Hörz, J. Huth, I. D. Hutcheon, K. Ignatyev, H. Ishii, M. Ito, D. Jacob, C. Jacobsen, S. Jacobsen, S. Jones, D. Joswiak, A. Jurewicz, A. T. Kearsley, L. P. Keller, H. Khodja, A. L. D. Kilcoyne, J. Kissel, A. Krot, F. Langenhorst, A. Lanzirotti, L. Le, L. A. Leshin, J. Leitner, L. Lemelle, H. Leroux, M.-C. Liu, K. Luening, I. Lyon, G. Macpherson, M. A. Marcus, K. Marhas, B. Marty, G. Matrajt, K. McKeegan, A. Meibom, V. Mennella, K. Messenger, S. Messenger, T. Mikouchi, S. Mostefaoui, T. Nakamura, T. Nakano, M. Newville, L. R. Nittler, I. Ohnishi, K. Ohsumi, K. Okudaira, D. A. Papanastassiou, R. Palma, M. E. Palumbo, R. O. Pepin, D. Perkins, M. Perronnet, P. Pianetta, W. Rao, F. J. M. Rietmeijer, F. Robert, D. Rost, A. Rotundi, R. Ryan, S. A. Sandford, C. S. Schwandt, T. H. See, D. Schlutter, J. Sheffield-Parker, A. Simionovici, S. Simon, I. Sitnitsky, C. J. Snead, M. K. Spencer, F. J. Stadermann, A. Steele, T. Stephan, R. Stroud, J. Susini, S. R. Sutton, Y. Suzuki, M. Taheri, S. Taylor, N. Teslich, K. Tomeoka, N. Tomioka, A. Toppani, J. M. Trigo-Rodríguez, D. Troadec, A. Tsuchiyama, A. J. Tuzzolino, T. Tyliszczak, K. Uesugi, M. Velbel, J. Vellenga, E. Vicenzi, L. Vincze, J. Warren, I. Weber, M. Weisberg, A. J. Westphal, S. Wirick, D. Wooden, B. Wopenka, P. Wozniakiewicz, I. Wright, H. Yabuta, H. Yano, E. D. Young, R. N. Zare, T. Zega, K. Ziegler, L. Zimmerman, E. Zinner, and M. Zolensky. Comet 81P/Wild 2 under a microscope. *Science*, 314:1711, 2006.

[181] T. P. M. Goumans, A. Wander, C. R. A. Catlow, and W. A. Brown. Silica grain catalysis of methanol formation. *Mon. Not. R. Astron. Soc.*, 382:1829, 2007.

[182] T. P. M. Goumans, C. R. A. Catlow, and W. A. Brown. Hydrogenation of CO on a silica surface: an embedded cluster approach. *J. Chem. Phys.*, 128:134709, 2008.

[183] N. González-García, J. Pu, À. González-Lafont, J. M. Lluch, and D. G. Truhlar. Searching for saddle points by using the nudged elastic band method: an implementation for gas-phase systems. *J. Chem. Theor. Comput.*, 2:895, 2006.

[184] G. Henkelman and H. Jónsson. Improved tangent estimate in the nudged elastic band method for finding minimum energy paths and saddle points. *J. Chem. Phys.*, 113:9978, 2000.

[185] M. Guidon, J. Hutter, and J. VandeVondele. Auxiliary density matrix methods for Hartree-Fock exchange calculations. *J. Chem. Theor. Comput.*, 6:2348, 2010.

[186] P. E. Blöchl. Electrostatic decoupling of periodic images of plane-wave-expanded densities and derived atomic point charges. *J. Chem. Phys.*, 103:7422, 1995.

[187] T. P. M. Goumans and J. Kästner. Deuterium enrichment of interstellar methanol explained by atom tunneling. *J. Phys. Chem. A*, 115:10767, 2011.